

Track simulation and reconstruction in LHCb

Cover: Condensation trails (contrails) in the sky.

ISBN: 90-6464-244-3

Printed by Ponsen & Looijen b.v., Wageningen.

Copyright © 2005 by Jeroen van Tilburg. All rights reserved.

The work described in this thesis is part of the research program of 'het Nationaal Instituut voor Kernfysica en Hoge-Energiefysica' (NIKHEF) in Amsterdam, the Netherlands. The author was financially supported by the 'Stichting Fundamenteel Onderzoek der Materie' (FOM).

VRIJE UNIVERSITEIT

Track simulation and reconstruction in LHCb

ACADEMISCH PROEFSCHRIFT

ter verkrijging van de graad Doctor aan
de Vrije Universiteit Amsterdam,
op gezag van de rector magnificus
prof.dr. T. Sminia,
in het openbaar te verdedigen
ten overstaan van de promotiecommissie
van de faculteit der Exacte Wetenschappen
op dinsdag 11 oktober 2005 om 13.45 uur
in het auditorium van de universiteit,
De Boelelaan 1105

door

Jeroen Ashwin Niels van Tilburg

geboren te 's-Gravenhage

promotor: prof.dr. M.H.M. Merk

Contents

1	Introduction	1
2	B physics	5
2.1	Standard Model	5
2.2	CP violation in the Standard Model	7
2.3	B mesons	10
2.3.1	Mixing of neutral B mesons	10
2.3.2	Decay of B mesons	14
2.3.3	CP violation with neutral B mesons	15
3	LHCb experiment	21
3.1	Large Hadron Collider	21
3.2	General layout	26
3.3	Vertex Locator	28
3.4	Trigger Tracker	31
3.5	Inner Tracker	32
3.6	Outer Tracker	32
3.7	RICH detector	35
3.8	Calorimeters	37
3.9	Muon system	40
3.10	Trigger	41
3.10.1	Level-0	42
3.10.2	Level-1	43
3.10.3	High Level Trigger	44
4	Monte Carlo simulation	47
4.1	Introduction to LHCb simulations	47
4.2	Framework and applications	48
4.3	Event generation	50
4.3.1	Pythia	51
4.3.2	B production	52
4.3.3	Multiple parton interactions	54
4.3.4	Fragmentation	57
4.3.5	B decay simulation	58

4.3.6	Pile-up and spill-over	58
4.4	Detector simulation	59
4.4.1	Geant	59
4.4.2	Passage of particles through matter	60
5	Outer Tracker simulation	67
5.1	Detector description	67
5.2	Particle distributions	71
5.3	Detector response	73
5.3.1	General overview	73
5.3.2	Digitisation processes	74
5.4	Detector performance	83
5.4.1	Occupancy	83
5.4.2	Efficiency	84
5.4.3	Resolution	85
6	Track reconstruction	87
6.1	Track fit	87
6.1.1	Kalman formalism	89
6.1.2	Resolution and pull	92
6.1.3	Extended Kalman filter	92
6.1.4	Propagation	93
6.1.5	Projection	96
6.1.6	Outlier removal and refit	97
6.2	Pattern recognition	100
6.2.1	Track types	100
6.2.2	General strategy	101
6.2.3	Matching tracks	103
6.3	Overall tracking performance	108
6.4	Track visualisation	116
7	Selection and sensitivity studies	119
7.1	Decays of interest	119
7.2	Particle identification	122
7.3	Event selection	124
7.3.1	Overview of the selection variables	124
7.3.2	Preselection	127
7.3.3	Optimisation of final selection	127
7.3.4	Event yield	132
7.3.5	B decay times	135
7.4	Flavour tagging	135
7.5	Sensitivity studies	139
7.5.1	Likelihood fit	139
7.5.2	Sensitivity on Δm_s	141

7.5.3 Sensitivity on $\gamma - 2\chi$	142
7.6 Conclusion	144
A Kalman filter derivation	147
References	155
Summary	157
Samenvatting	161
Dankwoord	165

Contents

Chapter 1

Introduction

Since many decades physicists have been intrigued by Nature's preference for matter over antimatter. Matter is what everything around us is made of, as for instance people, the Earth, the Moon, and all the stars. Antimatter, on the other hand, is not so common. The reason that it is uncommon in our daily lives is that it cannot survive in a matter-dominated environment. Nevertheless, it is regularly created by Nature — and exists for short periods of time — in radioactive decays and in collisions of cosmic particles with the atmosphere. Today, antimatter is also created in particle accelerators, and even in hospitals when making PET scans.

There is no evidence for the presence of large quantities of antimatter in the Universe [1]. So why does the Universe consist of only matter, and not of antimatter? This question arose after the discovery of antimatter in cosmic rays in the 1930s. Apparently, there must be a fundamental difference between matter and antimatter.

Shortly after the Big Bang, when the Universe was created, there was a hot and dense phase. Cosmologists believe that in this phase there was an equal amount of matter and antimatter. Somehow, the Universe must have developed an excess of particles over antiparticles. In 1967, Sakharov [2] posed three conditions needed to explain this imbalance. One of them is the violation of CP symmetry.

Symmetry is an important concept in physics. The laws of physics are invariant under certain symmetry transformations. According to Noether's theorem, a continuous symmetry leads to a conservation law. For instance, time invariance leads to conservation of energy and spatial translation invariance leads to conservation of momentum. In general, physicists want to investigate whether the laws of physics obey certain symmetry principles. In 1956, Lee and Yang [3] pointed out that the discrete symmetry of space inversion, also called parity (denoted by P), may not be conserved in all fundamental interactions. Soon thereafter, the first experimental evidence [4] showed that parity is indeed violated in the weak interaction. It was a striking result that the weak interaction would behave totally differently in a mirror-world. Other fundamental, discrete symmetries are charge inversion (C), i.e., particle–antiparticle transformations, and time reversal (T). Until 1964, it was thought that — instead of P symmetry — the combined CP operation was a good symmetry. That year, violation of the CP symmetry was observed [5] in the weak decay of neutral K mesons.

Nowadays, the phenomenon of CP violation is described in the Standard Model of particle physics. It is incorporated in the Cabibbo-Kobayashi-Maskawa (CKM) matrix, which describes the quark transitions in the weak interaction. The aim for many particle physicists is to accurately measure the matrix elements using the decay of B mesons. CP violation can be observed when there is a difference between the decay of a B to some final state, f , and the decay of an anti- B to the CP -conjugated state, \bar{f} . Some decay channels are expected to exhibit large CP -violating effects, which can theoretically be interpreted in a clean and model-independent way. Measurements of these B decays will provide insight into the question whether the observed CP violation is sufficient to explain the current excess of matter in the Universe.

The first observation of CP violation with B mesons has already been made by the two B factory experiments (*BABAR* and *BELLE*) using the decay $B^0 \rightarrow J/\psi K_s^0$ and similar modes. Other experiments (*CDF* and *DØ*) have started running and also plan to measure CP violation in the B system.

At the Large Hadron Collider (LHC), B mesons will be created abundantly in the high-energy proton–proton collisions. This collider is currently being constructed at CERN (European Organisation for Nuclear Research) in Geneva. One of the experiments located around a collision point is LHCb, which is designed to detect these B mesons. The aim of LHCb is to study CP violation and find rare decays using a high-statistics sample of B decays. The two advantages of LHCb, compared to the B factories, are the higher statistics of B decays, giving access to decay modes with small branching fractions, and the possibility to study the heavier types of B hadrons, most notably the B_s meson.

In the harsh hadronic environment of proton–proton collisions, not only B mesons, but also many other particles are created, leaving many tracks in the detector. One of the main challenges of LHCb is to find the B decays among the tracks emerging from the collision. Therefore, LHCb requires a fast track reconstruction with high efficiency.

Simulation studies play a prominent role in the optimisation of the design of the detector, as well as in the determination of the expected performance. Ultimately, the performance is measured in terms of the sensitivity to the CP -violating parameters. This requires both a realistic simulation and an efficient reconstruction of an event after a proton–proton collision.

The remainder of this thesis is divided into the following chapters:

In Chapter 2, an overview of CP violation in the Standard Model is presented. Also, the method to extract the CP -violating parameters in the CKM matrix using benchmark B decay channels is explained.

In Chapter 3, the LHCb detector is discussed. First, the characteristics of proton–proton collisions in the LHC are summarised. Thereafter, the detector itself, its main components, and their functionality are described.

In Chapter 4, the simulation procedure of proton collision events is explained. After a brief introduction to the software framework, the B production mechanism and the different types of particle interaction with the detector are explained.

In Chapter 5, the detection of particles in one of LHCb’s components, namely the

Outer Tracker, is presented. This subdetector is an essential part of the track reconstruction system. Using the simulations described in Chapter 4, the expected particle flux and momentum distribution in the Outer Tracker are determined. Also, the electronics' response to traversing particles is modelled in detail.

In Chapter 6, the reconstruction of tracks in LHCb is described. A comprehensive overview of the track fit procedure is given. Afterwards, the pattern recognition algorithms, which search for tracks, are discussed. Special attention is given to the track matching algorithm, which combines the track segments found by two other track search algorithms. Next, the overall performance of the combined pattern recognition algorithms and track fit is presented. Finally, the visualisation procedure of tracks and their hits in the LHCb event display is explained.

In Chapter 7, the method to select $B_s^0 \rightarrow D_s^- \pi^+$ and $B_s^0 \rightarrow D_s^{(*)\mp} K^{(*)\pm}$ decays is discussed. First, the selection cuts are optimised to obtain a high efficiency and low background rate. In turn, the decays that pass the final selection are the input for a fast Monte Carlo simulation to determine the sensitivity of LHCb to the CP -violating parameters.

Introduction

Chapter 2

B physics

The Standard Model describes the known elementary particles and their mutual interactions. Elementary particles are — by definition — the smallest (i.e., indivisible) constituents of matter. B mesons contain one of the heaviest elementary particles, namely the b quark. The decay of B mesons is well suited to measure the phenomenon of CP violation. Some decay channels allow a theoretically clean measurement of the CP -violating parameters in the Standard Model.

In this chapter, an overview of CP violation in the Standard Model and its relation to the decay of B mesons is given. First, a brief introduction to the Standard Model is offered in Section 2.1. Then, in Section 2.2 the CKM matrix, describing the quark transitions in the weak interaction, is discussed. The CKM matrix is the source of CP violation in the Standard Model. Finally, in Section 2.3 the physics of B mesons and the methods to extract the CP -violating parameters are presented.

Furthermore, many excellent textbooks exists, offering a complete overview on these topics. For instance, for an introductory review on particle physics and the Standard Model, the reader is referred to Ref. [6]. For a detailed overview of CP violation, including many phenomenological aspects, Ref. [7] is advised.

2.1 Standard Model

For many decades the Standard Model has proven to provide a very accurate description of the interactions between elementary particles. Two types of elementary particles can be distinguished: fermions, which have half-integer spin, and bosons, which have integer spin. The fermions in the Standard Model are quarks and leptons. They form the building blocks of matter. The bosons are the force-carriers, responsible for the interaction between the fermions. The Standard Model accommodates the electromagnetic, the strong, and the weak force. The corresponding bosons and coupling constants are listed in Table 2.1. The fourth and weakest force in Nature, gravitation, is not accommodated in the Standard Model.

Both quarks and leptons can be divided into three generations with increasing mass. Each generation contains again two types of fermions. For the quarks this results in six flavours: up, down, strange, charm, bottom, and top. For the leptons, each generation

Table 2.1: Standard Model forces, the mediating bosons, and their relative strength.

Force	Boson	Relative strength
Strong	g (8 gluons)	$\alpha_s \sim \mathcal{O}(1)$
Electromagnetic	γ (photon)	$\alpha \sim \mathcal{O}(10^{-2})$
Weak	Z^0, W^\pm (weak bosons)	$\alpha_W \sim \mathcal{O}(10^{-6})$

Table 2.2: The fundamental fermions in the Standard Model: quarks and leptons. They are divided into three generations. For each particle listed there is a corresponding antiparticle with opposite charge. Also, each quark comes in three different colours, resulting that the electric charge in each generation (quarks plus leptons) adds up to zero. The quark masses are determined in the $\overline{\text{MS}}$ scheme. Values are obtained from Ref. [8].

charge	Quarks			
$\frac{2}{3}$	u (up) 1.5–4 MeV	c (charm) 1.15–1.35 GeV	t (top) (174.3 ± 5.1) GeV	
$-\frac{1}{3}$	d (down) 4–8 MeV	s (strange) 80–130 MeV	b (bottom) 4.1–4.4 GeV	
charge	Leptons			
0	ν_e (e neutrino) < 3 eV	ν_μ (μ neutrino) < 0.19 MeV	ν_τ (τ neutrino) < 18.2 MeV	
-1	e (electron) 0.511 MeV	μ (muon) 106 MeV	τ (tau) 1.78 GeV	

contains a charged lepton and a (neutral) neutrino. They can be of type electron, muon, or tau. The Standard Model fermions are summarised in Table 2.2. Today, all listed fermions and their antiparticles have been observed. According to *CPT* invariance, which is a fundamental invariance in quantum gauge theory, particles and antiparticles must have equal masses and decay times.

The strong force acts on a quantum number of the quark called colour. Accordingly, the theory of the strong force is often referred to as Quantum Chromodynamics (QCD). The quarks listed in Table 2.2 come in three different colours: red, green, and blue. The corresponding antiquarks have the opposite anticolours: antired, antigreen, and antiblue. The colour of a quark can change by exchanging a gluon with another quark. Quarks can only occur in bound states, because QCD only allows colour neutral objects. Therefore, quarks are confined inside hadrons. There are two types of hadrons: baryons and mesons.

Baryons are built from three quarks (or three antiquarks), each having a different colour quantum number. Protons and neutrons, the building blocks of atomic nuclei, are well-known examples of baryons that contain the two lightest quarks (up and down). It is interesting to note that their masses (~ 940 MeV) are governed by the scale of the

strong force, Λ_{QCD} , and not by the masses of the constituent quarks (cf. Table 2.2). This scale basically sets the size of the hadrons and thus the kinetic energy of quarks confined inside hadrons.

In contrast to baryons, mesons are built from a quark and an antiquark of opposite colour. Kaons and pions are well-known examples of mesons. This thesis focuses on the physics of mesons containing either a b quark or an anti- b quark: B mesons. An important aspect of the strong interaction is that quarks are always created in quark–antiquark pairs of the same flavour. This also implies that B hadrons are produced in pairs, where one B hadron contains a b quark and the other an anti- b quark, denoted by \bar{b} .

The electromagnetic force acts on all charged particles through the exchange of a (massless) photon. The weak force acts on all fermions through the exchange of a massive W^\pm or Z^0 boson (see Table 2.1). W^\pm bosons change the quark flavour from *up-type* to *down-type* and vice versa. They are referred to as the charged current of the weak interaction. In contrast, the neutral weak current, mediated by the Z^0 boson, cannot change flavour, just as the photon in the electromagnetic interaction. The absence of any flavour-changing neutral current is described by the Glashow-Iliopoulos-Maiani (GIM) mechanism [9].

In the Standard Model, the electromagnetic and weak interaction are unified into a single electroweak interaction. This unification can be made at the cost of introducing a new and yet unobserved particle: the Higgs boson. The Higgs field is responsible for the broken symmetry between the *massive* weak bosons and the *massless* photon. The mechanism that gives masses to the W^\pm and Z^0 is called spontaneous symmetry breaking (SSB). After SSB, also the quarks and leptons obtain their mass from the Yukawa coupling to the Higgs field. However, the resulting mass eigenstates are not the same as the eigenstates in the weak base. In other words, the weak interaction couples to the quarks in a rotated (mixed) base. In order to describe this base transformation between the quark mass eigenstates and weak eigenstates, Kobayashi and Maskawa [10] introduced in 1973 the Cabibbo-Kobayashi-Maskawa (CKM) quark mixing matrix.

2.2 CP violation in the Standard Model

In perturbation theory, the quantum mechanical transition amplitude for a given process can be written in terms of currents which describes the exchange of a boson. After SSB, the charged current of a W^- exchange can be written as

$$J^{\mu-} = (\bar{u}_L, \bar{c}_L, \bar{t}_L) \gamma^\mu V_{\text{CKM}} \begin{pmatrix} d_L \\ s_L \\ b_L \end{pmatrix}, \quad (2.1)$$

where V_{CKM} is the CKM matrix and γ^μ are the Dirac matrices. The subscript L denotes left-handedness of the Dirac spinors. Similarly, the exchange of a W^+ is obtained from the hermitian conjugate. The parity-violating character of the weak interaction is manifest in (2.1): it acts only on left-handed quarks or right-handed antiquarks.

Equation (2.1) shows explicitly that the W^\pm does not couple directly to the mass eigenstates (d, s, b), but instead to the weak interaction eigenstates, which can be defined by

$$\begin{pmatrix} d' \\ s' \\ b' \end{pmatrix} = V_{\text{CKM}} \begin{pmatrix} d \\ s \\ b \end{pmatrix} . \quad (2.2)$$

The CKM matrix is a unitary matrix, which is written as

$$V_{\text{CKM}} = \begin{pmatrix} V_{ud} & V_{us} & V_{ub} \\ V_{cd} & V_{cs} & V_{cb} \\ V_{td} & V_{ts} & V_{tb} \end{pmatrix} . \quad (2.3)$$

The complex matrix elements represent 18 parameters: 9 real plus 9 imaginary numbers. Unitarity, i.e., $V_{\text{CKM}}^\dagger V_{\text{CKM}} = \mathbb{1}$, implies 9 constraints. In addition, 5 arbitrary phases can be absorbed by redefining the quark fields. As a result the CKM matrix is described by only 4 physical parameters: 3 rotation angles and 1 phase. This phase is the source of all CP -violating effects in the flavour sector of the Standard Model. Without this phase the CKM matrix would become a real 3×3 orthogonal matrix, which can be described by 3 rotation (Euler) angles. A popular form of the CKM matrix is the Wolfenstein parameterisation as it exhibits a hierarchical structure:

$$V_{\text{CKM}} = \begin{pmatrix} 1 - \frac{1}{2}\lambda^2 & \lambda & A\lambda^3(\rho - i\eta) \\ -\lambda & 1 - \frac{1}{2}\lambda^2 & A\lambda^2 \\ A\lambda^3(1 - \rho - i\eta) & -A\lambda^2 & 1 \end{pmatrix} + \mathcal{O}(\lambda^4) . \quad (2.4)$$

It is obtained from an expansion around the sine of the ‘‘Cabibbo angle’’, $\lambda = \sin \theta_C \simeq 0.22$. Furthermore, A, ρ, η are real parameters of order unity. CP violation implies that $\eta \neq 0$. The higher-order terms up to $\mathcal{O}(\lambda^5)$ read

$$\begin{pmatrix} -\frac{1}{8}\lambda^4 & 0 & 0 \\ A^2\lambda^5(\frac{1}{2} - \rho - i\eta) & -\frac{1}{8}\lambda^4(1 + 4A^2) & 0 \\ \frac{1}{2}A\lambda^5(\rho + i\eta) & A\lambda^4(\frac{1}{2} - \rho - i\eta) & -\frac{1}{2}A^2\lambda^4 \end{pmatrix} . \quad (2.5)$$

One of the constraints following from the unitarity of the CKM matrix is obtained by multiplying the first column with the complex conjugates of the third column, yielding

$$V_{ud}V_{ub}^* + V_{cd}V_{cb}^* + V_{td}V_{tb}^* = 0 . \quad (2.6)$$

This constraint can be visualised as a triangle in the complex plane (see Fig. 2.1). Since all three terms in (2.6) are of order λ^3 , the sides of the triangle are of comparable size. The unitarity triangle, as shown in Fig. 2.1, is obtained by dividing all terms by $V_{cd}V_{cb}^*$. The apex of the triangle lies at $(\bar{\rho}, \bar{\eta}) = (1 - \frac{1}{2}\lambda^2)(\rho, \eta)$. In total, six of these unitarity triangles can be constructed. Only two have sides of the same order; the others are squashed. An interesting observation is that the area within each triangle is the same for all six unitarity triangles and is a direct measure for the amount of CP violation in

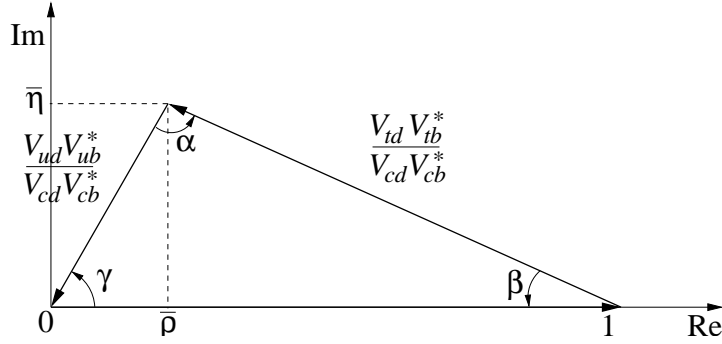


Figure 2.1: The unitarity triangle in the complex plane.

the Standard Model [11]. The three angles in Fig. 2.1 are defined as counter-clockwise rotations of

$$\alpha = \arg \left(-\frac{V_{td} V_{tb}^*}{V_{ud} V_{ub}^*} \right) \quad , \quad \beta = \arg \left(-\frac{V_{cd} V_{cb}^*}{V_{td} V_{tb}^*} \right) \quad , \quad \gamma = \arg \left(-\frac{V_{ud} V_{ub}^*}{V_{cd} V_{cb}^*} \right) \quad . \quad (2.7)$$

In the Wolfenstein parameterisation to $\mathcal{O}(\lambda^3)$, it follows that $-\beta$ is the phase of V_{td} , and $-\gamma$ is the phase in V_{ub} .

One of the squashed triangles comes from the product of the second and third column,

$$V_{ub} V_{us}^* + V_{cb} V_{cs}^* + V_{tb} V_{ts}^* = 0 \quad . \quad (2.8)$$

Conveniently, the small angle of $\mathcal{O}(\lambda^2)$ of this triangle is defined as

$$\chi = \arg \left(-\frac{V_{cb} V_{cs}^*}{V_{tb} V_{ts}^*} \right) \quad . \quad (2.9)$$

It represents the phase of V_{ts} in the Wolfenstein parameterisation.

The goal in B physics is to find out whether the CKM matrix describes all flavour changing interactions. Many extensions to the Standard Model predict new effects in flavour physics which may be observable by measuring (CP -violating) decays of B mesons. The Standard Model already survived its first experimental test. The value of $\sin 2\beta$ has been measured by the experiments *BABAR* [12] and *BELLE* [13] in the decay of $B^0 \rightarrow J/\psi K_S^0$ and other $b \rightarrow c\bar{s}s$ modes. The current world average is $\sin 2\beta = 0.731 \pm 0.056$ [8]. It agrees well with the constraints from other, indirect measurements.

Nevertheless, more measurements are required to overconstrain the CKM matrix. Especially, the measurements with a clean theoretical (i.e., model-independent) interpretation determine the accuracy to which the Standard Model is tested. An accurate knowledge of the CKM matrix might give sensitivity to New Physics.

Table 2.3: Neutral *B* meson parameters. The measured values are taken from Ref. [8]. The entries denoted with (th) are theoretical estimates. The subscript q distinguishes between the B_d and B_s system.

	B_d system	B_s system
m_q (MeV)	5279.4 ± 0.5	5369.6 ± 2.4
$1/\Gamma_q = \tau_q$ (ps)	1.536 ± 0.014	1.461 ± 0.057
Δm_q (ps $^{-1}$)	0.502 ± 0.007	> 14.4 (CL > 95%)
$x_q = \Delta m_q/\Gamma_q$	0.771 ± 0.012	> 20.6 (CL > 95%)
$\Delta\Gamma_q/\Gamma_q$	$< 10^{-2}$ (th)	~ 0.1 (th)
$1 - q/p ^2$	$< 10^{-2}$ (th)	$< 10^{-2}$ (th)

2.3 *B* mesons

There are four types of neutral *B* mesons, which have a quark content of

$$\begin{aligned} |B^0\rangle &= |\bar{b}d\rangle , \quad |\bar{B}^0\rangle = |\bar{b}\bar{d}\rangle , \\ |B_s^0\rangle &= |\bar{b}s\rangle , \quad |\bar{B}_s^0\rangle = |\bar{b}\bar{s}\rangle . \end{aligned} \quad (2.10)$$

These are also called the *B* flavour eigenstates. It follows that the B^0 and \bar{B}^0 are antiparticles of each other. According to the CPT theorem they have the same mass and lifetime. Together they form the B_d system. Similarly, the B_s^0 and \bar{B}_s^0 form the B_s system. In the remainder of this chapter most equations are written in terms of B^0 and \bar{B}^0 ; they equally hold for B_s^0 and \bar{B}_s^0 .

In 1983, the lifetime of the *B* meson (τ_B) was measured for the first time by the MAC and MARK-II collaborations [14, 15]. The long lifetime of the *B* meson came as a surprise. Before that time it was thought that V_{cb} , which determines the decay amplitude, was of order λ , just as V_{us} and V_{cd} . However, it was found that V_{cb} was much smaller, namely $\mathcal{O}(\lambda^2)$, which results in a longer lifetime for the *B* meson. A long lifetime is useful in the detection and identification of *B* mesons, as their decay vertices can be separated from the primary production vertex.

Another useful characteristic of the *B* meson is its large mass, due to the constituting *b* quark. The large mass difference between the heavy *b* quark and the much lighter *d* or *s* quarks in neutral *B* mesons makes it possible to approximate many QCD effects, which cannot be calculated with perturbation theory, using heavy quark effective theory (HQET). In the decay through the weak interaction, the light *d* or *s* quark can effectively be regarded as a spectator quark. This allows a factorisation of the full process into a short-distance electroweak decay and a long-distance QCD process. The mass and decay times of the B^0 and B_s^0 are listed in Table 2.3.

2.3.1 Mixing of neutral *B* mesons

Another surprising characteristic of neutral *B* mesons is their large mixing, which was first measured in 1987 in the B_d system by the ARGUS collaboration [16]. It means

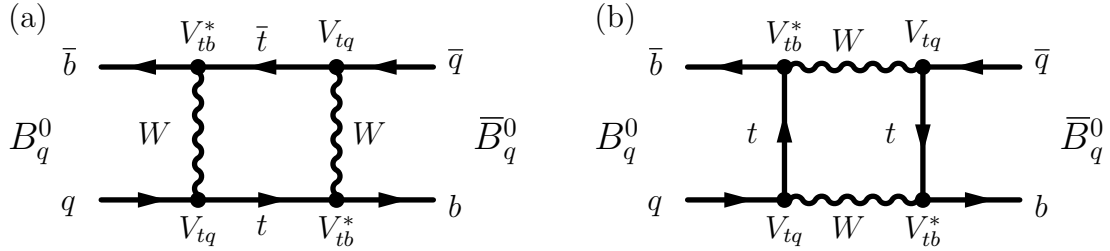


Figure 2.2: Feynman box diagrams for B mixing, contributing to the amplitude M_{12} . The q quark can be either a d or s quark. The charge-conjugated process for $\bar{B}^0 \rightarrow B^0$ is obtained by replacing all quarks by antiquarks (and vice versa) and taking the complex-conjugates of the CKM elements.

that a B^0 can evolve in time into a \bar{B}^0 and vice versa. The B mixing — or better, B oscillation — occurs because the mass eigenstates of the B meson are different from the flavour eigenstates as given in (2.10).

In general, the state of a neutral B meson can be written as a linear combination (superposition) of B^0 and \bar{B}^0 by

$$a|B^0\rangle + b|\bar{B}^0\rangle . \quad (2.11)$$

The time evolution of this state is governed by the Schrödinger equation. In the matrix notation, the Hamiltonian, H , is represented by a 2×2 matrix. An effective, non-hermitian Hamiltonian is used to include the loss of B mesons through decay. The Schrödinger equation then becomes

$$i\frac{d}{dt} \begin{pmatrix} a(t) \\ b(t) \end{pmatrix} = H \begin{pmatrix} a(t) \\ b(t) \end{pmatrix} = (M - \frac{i}{2}\Gamma) \begin{pmatrix} a(t) \\ b(t) \end{pmatrix} , \quad (2.12)$$

where M and Γ are two hermitian matrices. From CPT symmetry it follows that B^0 and \bar{B}^0 have equal masses ($M_{11} = M_{22}$) and equal decay times ($\Gamma_{11} = \Gamma_{22}$). The off-diagonal elements satisfy $M_{12} = M_{21}^*$ and $\Gamma_{12} = \Gamma_{21}^*$, because M and Γ themselves are hermitian. The off-diagonal amplitude M_{12} arises from virtual intermediate states, while Γ_{12} arises from real, on-shell intermediate states. The amplitude M_{12} is dominated by processes with top (t) quarks in the intermediate states. These processes are illustrated by Feynman diagrams in Fig. 2.2. The large B mixing follows from the large mass of the top quark.

The eigenstates of the Schrödinger equation (2.12) are the mass eigenstates of neutral B mesons, defined as

$$|B_{H,L}\rangle = p|B^0\rangle \mp q|\bar{B}^0\rangle , \quad (2.13)$$

where B_H is the *heavy* eigenstate and B_L is the *light* eigenstate. Their time dependence is written as

$$|B_{H,L}(t)\rangle = e^{-(im_{H,L}+\Gamma_{H,L}/2)t}|B_{H,L}(0)\rangle , \quad (2.14)$$

where $m_{H,L}$ and $\Gamma_{H,L}$ are the masses and decay rates of the B_H and B_L .

The difference in mass and decay rate is defined as

$$\begin{aligned}\Delta m &= m_H - m_L \quad , \\ \Delta\Gamma &= \Gamma_H - \Gamma_L \quad ,\end{aligned}\tag{2.15}$$

such that Δm is positive by definition. The sign of $\Delta\Gamma$ is determined experimentally. Similarly, the average mass and decay time are:

$$\begin{aligned}m &= \frac{m_H + m_L}{2} \quad , \\ \Gamma &= \frac{\Gamma_H + \Gamma_L}{2} \quad .\end{aligned}\tag{2.16}$$

Solving the Schrödinger equation (2.12) gives the relation between the ratio q/p and the off-diagonal matrix elements, M_{12} and Γ_{12} :

$$\frac{q}{p} = -\sqrt{\frac{M_{12}^* - i\Gamma_{12}^*/2}{M_{12} - i\Gamma_{12}/2}} \quad .\tag{2.17}$$

The production of B mesons is governed by the strong interaction. This implies that B mesons are always produced in a flavour eigenstate as given by (2.10). Substituting (2.13) into (2.14), the time evolution of a B meson initially produced as B^0 or \bar{B}^0 can be expressed as

$$\begin{aligned}|B_{\text{phys}}^0(t)\rangle &= g_+(t)|B^0\rangle + \frac{q}{p}g_-(-t)|\bar{B}^0\rangle \quad , \\ |\bar{B}_{\text{phys}}^0(t)\rangle &= g_+(-t)|\bar{B}^0\rangle + \frac{p}{q}g_-(t)|B^0\rangle \quad ,\end{aligned}\tag{2.18}$$

where the time dependence is given by

$$g_\pm(t) = \frac{1}{2}(e^{-(im_L+\Gamma_L/2)t} \pm e^{-(im_H+\Gamma_H/2)t}) \quad .\tag{2.19}$$

After a time t , the probabilities to observe a B^0 or \bar{B}^0 for a B meson that is originally produced as either B^0 or \bar{B}^0 are

$$\begin{aligned}|\langle B^0|B_{\text{phys}}^0(t)\rangle|^2 &= |g_+(t)|^2 \quad , \\ |\langle \bar{B}^0|B_{\text{phys}}^0(t)\rangle|^2 &= \left|\frac{q}{p}\right|^2 |g_-(t)|^2 \quad , \\ |\langle B^0|\bar{B}_{\text{phys}}^0(t)\rangle|^2 &= \left|\frac{p}{q}\right|^2 |g_-(t)|^2 \quad , \\ |\langle \bar{B}^0|\bar{B}_{\text{phys}}^0(t)\rangle|^2 &= |g_+(t)|^2 \quad ,\end{aligned}\tag{2.20}$$

with

$$|g_\pm(t)|^2 = \frac{1}{4}(e^{-\Gamma_H t} + e^{-\Gamma_L t} \pm 2e^{-\Gamma t} \cos \Delta m t) \quad .\tag{2.21}$$

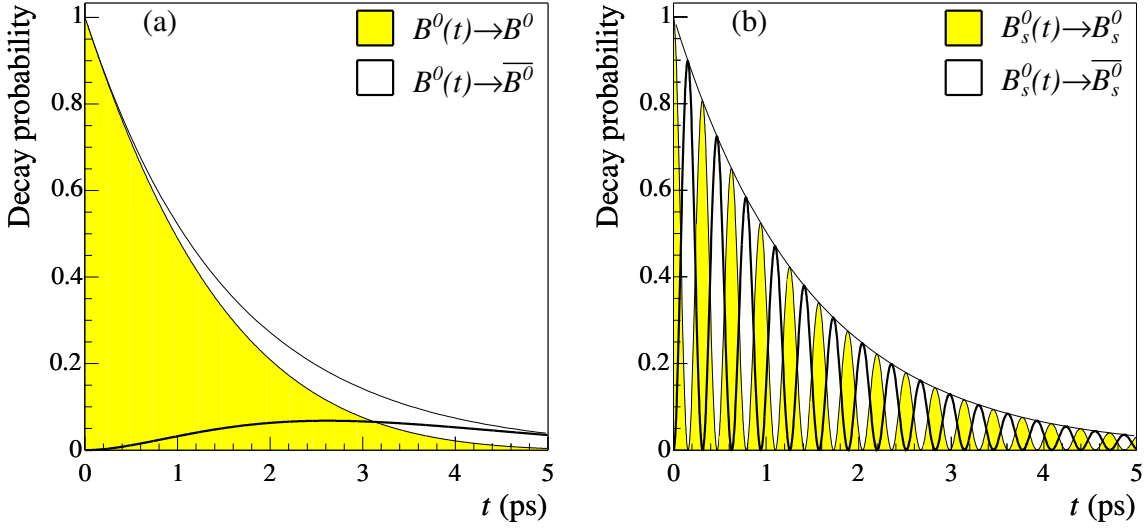


Figure 2.3: Probability for a B meson produced as B^0 to decay as B^0 or \bar{B}^0 , applied to the B_d system (a) and the B_s system (b). The values for $\Gamma_{d,s}$, $\Delta\Gamma_s$, and Δm_d are taken from Table 2.3. The value for Δm_s is assumed to be 20 ps^{-1} . $\Delta\Gamma_d$ is assumed to be zero. A large $\Delta\Gamma$ would result in an additional damping of the oscillation amplitude.

The form of (2.21) is governed by the decay terms of the heavy and light component and by an oscillation term which decreases exponentially with the average decay rate. Figure 2.3 shows the decay probabilities for the B_d and B_s systems.

In the B_d system, $\Delta\Gamma_d/\Gamma_d \approx 0$ (see Table 2.3) is a good approximation for the expectation value in the Standard Model. This is not the case for the B_s system where $\Delta\Gamma_s/\Gamma_s \approx 0.1$. Consequently, $\Delta\Gamma_s$ cannot be neglected. An estimate [17] based on lattice calculations predicts $\Delta\Gamma_s/\Gamma_s = 0.12 \pm 0.06$. Recently, the CDF collaboration measured a value as large as $\Delta\Gamma_s/\Gamma_s = 0.65^{+0.22}_{-0.33} \pm 0.01$ [18] using the decay $B_s^0 \rightarrow J/\psi\phi$.

The oscillation frequency is given by Δm_q . A useful quantity is the ratio $x_q = \Delta m_q/\Gamma_q$, which gives the average number of oscillations before decay. In the B_d system this value is measured to be $x_d = 0.771 \pm 0.012$ (see Table 2.3). The oscillations in the B_s system are much more rapid. The current lower limit is $x_s > 20.6$ with a CL > 95%.

The oscillations can be observed in decays of B mesons to a flavour-specific final state. This means that the charge of the final-state particles unambiguously determines the flavour of the B meson at the time of decay. For instance, the decay $B_s^0 \rightarrow D_s^- \pi^+$ (and the charge-conjugated decay $\bar{B}_s^0 \rightarrow D_s^+ \pi^-$) can be used to extract Δm_s using the four rate equations in (2.20). The two Feynman diagrams for this decay channel are given in Fig. 2.4. The LHCb detector is well suited to measure this decay and to resolve the oscillations. In Chapter 7, the experimental sensitivity on Δm_s is presented. In order to measure Δm_s , the decay time needs to be determined accurately, requiring a reconstruction of all decay products. In addition, the initial flavour of the B meson needs to be determined. This is accomplished by a method called flavour tagging, which

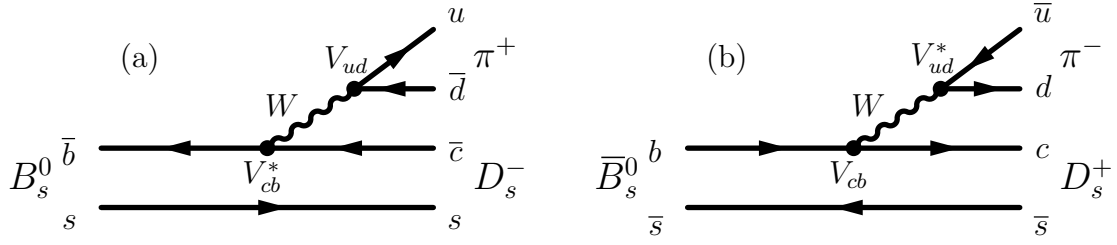


Figure 2.4: Feynman diagrams for the decays \$B_s^0 \rightarrow D_s^- \pi^+\$ (a) and \$\bar{B}_s^0 \rightarrow D_s^+ \pi^-\$ (b).

will also be discussed in Chapter 7.

Finally, in case \$|q/p| \neq 1\$, it follows from (2.20) that the oscillation probabilities of \$B^0 \rightarrow \bar{B}^0\$ and \$\bar{B}^0 \rightarrow B^0\$ are different. This asymmetry is called *CP violation in mixing*. In the limit \$|\Gamma_{12}| \ll |M_{12}|\$, which is a good approximation in both the \$B_d\$ and \$B_s\$ systems, Eq. (2.17) becomes \$q/p = -\sqrt{M_{12}^*/M_{12}}\$. In terms of the CKM elements this equals (see Fig. 2.2)

$$\left(\frac{q}{p}\right)_{B_d} = \frac{V_{tb}^* V_{td}}{V_{tb} V_{td}^*} = e^{-2i\beta} \quad \text{and} \quad \left(\frac{q}{p}\right)_{B_s} = \frac{V_{tb}^* V_{ts}}{V_{tb} V_{ts}^*} = e^{2i\chi} , \quad (2.22)$$

where \$\beta\$ and \$\chi\$ are the angles from the unitarity triangles. Accordingly, \$\beta\$ is also called the \$B^0\$ mixing phase, and \$\chi\$ the \$B_s^0\$ mixing phase. Since \$|q/p| \approx 1\$ in both the \$B_d\$ system and the \$B_s\$ system, it follows that \$B_H\$ and \$B_L\$ are \$CP\$ eigenstates and that \$CP\$ violation in mixing is expected to be very small (\$< 10^{-2}\$: see Table 2.3). The decay channel \$B_s^0 \rightarrow D_s^- \pi^+\$ is well suited to search for \$CP\$ violation in \$B_s\$ mixing.

2.3.2 Decay of B mesons

There are many possible decay channels for \$B\$ mesons. The Particle Data Group (PDG) [8] lists more than 200 different decay modes. Each decay channel typically has a tiny branching fraction of \$\mathcal{O}(10^{-4}-10^{-5})\$. Only few of them have a final state common to both \$B^0\$ and \$\bar{B}^0\$. This is the reason that \$\Delta\Gamma\$ is small compared to \$\Delta m\$, since \$\Delta\Gamma\$ arises from real intermediate states to which both the \$B^0\$ and \$\bar{B}^0\$ can decay. A few examples of these channels are given later.

The decay amplitudes of a pure \$B^0\$ or \$\bar{B}^0\$ state into a final state \$f\$ are defined as

$$A_f = \langle f | T | B^0 \rangle , \quad \bar{A}_f = \langle f | T | \bar{B}^0 \rangle , \quad (2.23)$$

where \$T\$ is the transition matrix element. Analogously, for the charge-conjugated final state \$\bar{f}\$ the decay amplitudes \$A_{\bar{f}}\$ and \$\bar{A}_{\bar{f}}\$ are defined. When \$|A_f| \neq |\bar{A}_{\bar{f}}|\$, it means that the decay rate of a \$B^0\$ into a final state \$f\$ is different from that of a \$\bar{B}^0\$ into the \$CP\$-conjugated state \$\bar{f}\$. This is called *CP violation in decay*, which can occur when (at least) two decay amplitudes contribute to the same final state. In general, any observable \$CP\$-violating effect originates from the phase difference between two interfering amplitudes.

The decay amplitudes A_f and $\bar{A}_{\bar{f}}$ can be written as a sum

$$A_f = \sum_k A_k e^{i\delta_k} e^{i\phi_k} , \quad \bar{A}_{\bar{f}} = \sum_k A_k e^{i\delta_k} e^{-i\phi_k} , \quad (2.24)$$

where A_k is a real number and equal for both the B^0 and the \bar{B}^0 . Since the strong interaction conserves CP symmetry, the strong phase, δ_k , is the same for the decay of both the B^0 and the \bar{B}^0 . In contrast, the weak phase, ϕ_k , changes sign under CP transformation. Clearly, when only one amplitude A_k contributes, then $|A_f| = |\bar{A}_{\bar{f}}|$ and there is no CP violation in decay. For that, at least two amplitudes with different strong phases as well as different weak phases are required. The interference terms yield an observable CP -violating effect. In contrast with CP violation in mixing, CP violation in decay can also arise in charged meson and baryon decays.

2.3.3 CP violation with neutral B mesons

There is a third type of CP violation, apart from CP violation in mixing and in decay. CP violation may also occur in the *interference* between mixing and decay — even in the absence of CP violation in mixing and in decay. The interference between mixing and decay occurs when a B^0 can either decay directly to some final state f , or first oscillate into a \bar{B}^0 and then decay into this final state f . In case there is a relative phase between q/p (mixing) and $A_f/\bar{A}_{\bar{f}}$ (decay), this third type of CP violation can be observed. Conveniently, two parameters, λ_f and $\lambda_{\bar{f}}$ (not to be confused with the λ in the Wolfenstein parameterisation), are introduced as

$$\lambda_f = \frac{q}{p} \frac{\bar{A}_f}{A_f} , \quad \lambda_{\bar{f}} = \frac{q}{p} \frac{\bar{A}_{\bar{f}}}{A_{\bar{f}}} . \quad (2.25)$$

For convenience, two additional parameters are defined as $\bar{\lambda}_f \equiv 1/\lambda_f$ and $\bar{\lambda}_{\bar{f}} \equiv 1/\lambda_{\bar{f}}$. CP violation in the interference between mixing and decay implies that $\arg(\lambda_f) + \arg(\lambda_{\bar{f}}) \neq 0$.

Using the definition of the λ parameters, a general expression for the time-dependent decay rates can now be constructed. The decay rate of a B^0 to a final state f is defined as

$$\Gamma_{B \rightarrow f}(t) = |\langle f | T | B_{\text{phys}}^0(t) \rangle|^2 , \quad (2.26)$$

with similar expressions for \bar{B}^0 and \bar{f} . Using the equations (2.18), (2.23), and (2.25), the four decay rates, known as master equations, are given by

$$\begin{aligned} \Gamma_{B \rightarrow f}(t) &= |A_f|^2 (|g_+(t)|^2 + |\lambda_f|^2 |g_-(t)|^2 + 2\text{Re}[\lambda_f g_+^*(t) g_-(t)]) , \\ \Gamma_{B \rightarrow \bar{f}}(t) &= |\bar{A}_{\bar{f}}|^2 \left| \frac{q}{p} \right|^2 (|g_-(t)|^2 + |\bar{\lambda}_{\bar{f}}|^2 |g_+(t)|^2 + 2\text{Re}[\bar{\lambda}_{\bar{f}} g_+(t) g_-^*(t)]) , \\ \Gamma_{\bar{B} \rightarrow f}(t) &= |A_f|^2 \left| \frac{p}{q} \right|^2 (|g_-(t)|^2 + |\lambda_f|^2 |g_+(t)|^2 + 2\text{Re}[\lambda_f g_+(t) g_-^*(t)]) , \\ \Gamma_{\bar{B} \rightarrow \bar{f}}(t) &= |\bar{A}_{\bar{f}}|^2 (|g_+(t)|^2 + |\bar{\lambda}_{\bar{f}}|^2 |g_-(t)|^2 + 2\text{Re}[\bar{\lambda}_{\bar{f}} g_+^*(t) g_-(t)]) , \end{aligned} \quad (2.27)$$

where the interference terms probe the phases of λ_f and $\lambda_{\bar{f}}$. The time-dependent terms follow from (2.19) and can be written as

$$\begin{aligned} |g_{\pm}(t)|^2 &= \frac{1}{4} (e^{-\Gamma_H t} + e^{-\Gamma_L t} \pm 2e^{-\Gamma t} \cos \Delta m t) \\ &= \frac{e^{-\Gamma t}}{2} \left(\cosh \frac{\Delta \Gamma t}{2} \pm \cos \Delta m t \right) , \\ g_+^*(t)g_-(t) &= \frac{1}{4} (-e^{-\Gamma_H t} + e^{-\Gamma_L t} + 2ie^{-\Gamma t} \sin \Delta m t) \\ &= \frac{e^{-\Gamma t}}{2} \left(\sinh \frac{\Delta \Gamma t}{2} + i \sin \Delta m t \right) , \end{aligned} \quad (2.28)$$

while $g_+(t)g_-^*(t)$ is obtained by taking the complex conjugate of $g_+^*(t)g_-(t)$. Using (2.28), the master equations become

$$\begin{aligned} \Gamma_{B \rightarrow f}(t) &= |A_f|^2 (1 + |\lambda_f|^2) \frac{e^{-\Gamma t}}{2} \cdot \\ &\quad \left(\cosh \frac{\Delta \Gamma t}{2} + D_f \sinh \frac{\Delta \Gamma t}{2} + C_f \cos \Delta m t - S_f \sin \Delta m t \right) , \\ \Gamma_{\bar{B} \rightarrow f}(t) &= |A_f|^2 \left| \frac{p}{q} \right|^2 (1 + |\lambda_f|^2) \frac{e^{-\Gamma t}}{2} \cdot \\ &\quad \left(\cosh \frac{\Delta \Gamma t}{2} + D_f \sinh \frac{\Delta \Gamma t}{2} - C_f \cos \Delta m t + S_f \sin \Delta m t \right) \end{aligned} \quad (2.29)$$

where

$$D_f = \frac{2\text{Re}\lambda_f}{1 + |\lambda_f|^2} , \quad C_f = \frac{1 - |\lambda_f|^2}{1 + |\lambda_f|^2} , \quad S_f = \frac{2\text{Im}\lambda_f}{1 + |\lambda_f|^2} . \quad (2.30)$$

The other two decay rates into the charge-conjugated final state are obtained by substituting f by \bar{f} . The factors D_f ($D_{\bar{f}}$) and S_f ($S_{\bar{f}}$) are sensitive to the phase of λ_f ($\lambda_{\bar{f}}$), and thus to CP violation.

Decay to a CP eigenstate: $B^0 \rightarrow J/\psi K_S^0$

The most simple case where a B^0 and a \bar{B}^0 can decay to the same final state, is the decay to a CP eigenstate. In that case it follows that $\lambda_f = \lambda_{\bar{f}}$. Hence, only two decay rates need to be considered.

A famous example is the decay $B^0 \rightarrow J/\psi K_S^0$, also known as the “golden” decay channel. As mentioned before this decay has been used by *BABAR* [12] and *BELLE* [13] to measure $\sin 2\beta$. The final state is (almost) a CP eigenstate. The Feynman tree diagrams for this decay are shown in Fig. 2.5. In addition, there are also higher-order “penguin” diagrams contributing to this decay. Fortunately, the dominant penguin contributions have the same weak phase as the tree diagram, which implies that $|A_f/\bar{A}_f| = 1$. Since to good approximation $|q/p| = 1$, therefore also $|\lambda_f| = 1$. It should be noted, however, that

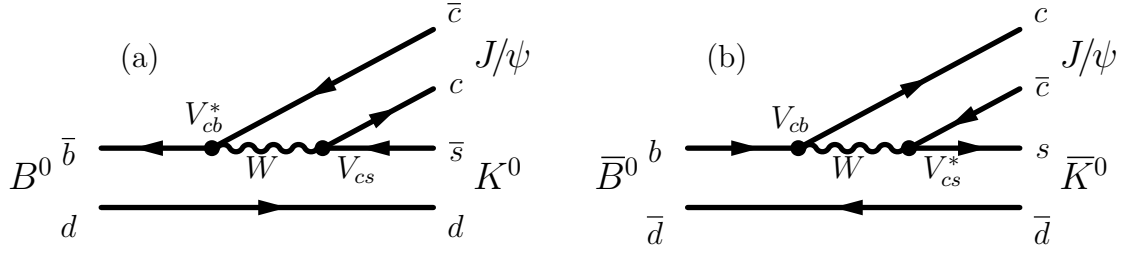


Figure 2.5: Feynman tree diagrams for $B^0 \rightarrow J/\psi K^0$ and $\bar{B}^0 \rightarrow J/\psi \bar{K}^0$. The K^0 and \bar{K}^0 in the final state oscillate into K_L^0 and K_S^0 . The K_S^0 is more easy to detect.

a phase still remains in λ_f . Neglecting also $\Delta\Gamma$ in the B_d system, the time-dependent asymmetry is simply

$$\mathcal{A}_{CP}(t) = \frac{\Gamma_{\bar{B} \rightarrow f}(t) - \Gamma_{B \rightarrow f}(t)}{\Gamma_{\bar{B} \rightarrow f}(t) + \Gamma_{B \rightarrow f}(t)} = \text{Im}\lambda_f \sin \Delta m t . \quad (2.31)$$

In other words, the amplitude of the time-dependent asymmetry equals $\text{Im}\lambda_f$.

Now, using the CKM elements in Fig. 2.5 and in (2.22), $\lambda_{J/\psi K_S^0}$ can be calculated as

$$\lambda_{J/\psi K_S^0} = \left(\frac{q}{p}\right)_{B_d} \frac{\bar{A}_{J/\psi K_S^0}}{A_{J/\psi K_S^0}} = \left(\frac{q}{p}\right)_{B_d} \frac{\bar{A}_{J/\psi \bar{K}^0}}{A_{J/\psi K^0}} \left(\frac{p}{q}\right)_K = - \left(\frac{V_{tb}^* V_{td}}{V_{tb} V_{td}^*}\right) \left(\frac{V_{cb} V_{cs}^*}{V_{cb}^* V_{cs}}\right) \left(\frac{V_{cs} V_{cd}^*}{V_{cs}^* V_{cs}}\right), \quad (2.32)$$

where $(p/q)_K$ corrects for the fact that the B^0 (\bar{B}^0) first decays to a K^0 (\bar{K}^0) and then oscillates to a K_S^0 . The minus sign arises from the fact that the final state is CP odd. In the end, all CKM factors cancel and only the phases of V_{td} and V_{td}^* remain. Using (2.22) this results in

$$\text{Im}\lambda_{J/\psi K_S^0} = \sin 2\beta . \quad (2.33)$$

Decay to a CP eigenstate: $B_s^0 \rightarrow J/\psi \phi$

The decay $B_s^0 \rightarrow J/\psi \phi$ is very similar to the decay $B^0 \rightarrow J/\psi K_S^0$. The Feynman diagrams are obtained from Fig. 2.5 by substituting the spectator quark $d \rightarrow s$. The λ parameter is given by

$$\lambda_{J/\psi \phi} = \left(\frac{q}{p}\right)_{B_s} \frac{\bar{A}_{J/\psi \phi}}{A_{J/\psi \phi}} = \left(\frac{V_{tb}^* V_{ts}}{V_{tb} V_{ts}^*}\right) \left(\frac{V_{cb} V_{cs}^*}{V_{cb}^* V_{cs}}\right) . \quad (2.34)$$

Using (2.9) it follows that the imaginary part equals

$$\text{Im}\lambda_{J/\psi \phi} = \sin 2\chi , \quad (2.35)$$

where χ is the phase in B_s mixing.

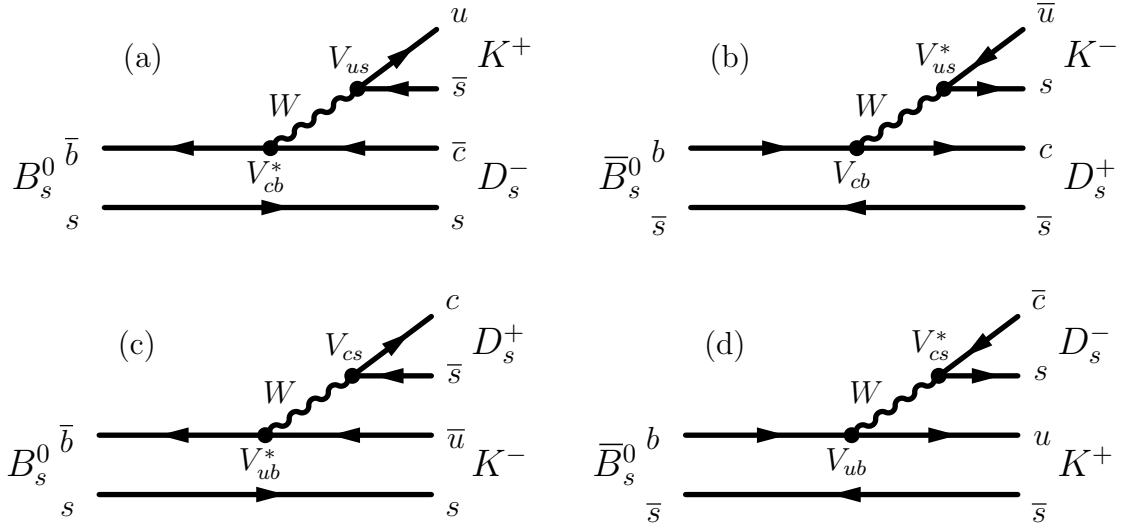


Figure 2.6: Feynman diagrams for $B_s^0 \rightarrow D_s^- K^+$ (a), $\bar{B}_s^0 \rightarrow D_s^+ K^-$ (b), $B_s^0 \rightarrow D_s^+ K^-$ (c), and $\bar{B}_s^0 \rightarrow D_s^- K^+$ (d).

A difference with the decay $B^0 \rightarrow J/\psi K_s^0$ is that in the decay of $B_s^0 \rightarrow J/\psi \phi$ the two final state particles are both vector mesons. Therefore, there can be contributions from both the CP even and CP odd decay amplitudes. In order to extract the CP -violating phase χ , an angular analysis is required to disentangle both contributions.

Decay to a non- CP eigenstate: $B_s^0 \rightarrow D_s^\mp K^\pm$

In general, the final state f need not be a CP eigenstate (i.e., $f \neq \bar{f}$). The interference occurs when both the B^0 and the \bar{B}^0 can decay — with different decay amplitudes — to the same final state. Together with the charge-conjugated decays they give rise to four distinct, time-dependent decay rates, as described by the master equations (2.29).

In the decay $B_s^0 \rightarrow D_s^\mp K^\pm$, the final state is a non- CP eigenstate to which both the B_s and \bar{B}_s can decay. The four decay rates can be used to extract λ_f and $\bar{\lambda}_{\bar{f}}$. This time, the sinh and cosh terms in (2.29) must be taken into account, because $\Delta\Gamma$ may be sizable in the B_s system. The four corresponding Feynman diagrams are drawn in Fig. 2.6. Since each decay is dominated by a single diagram, Eq. (2.24) implies that $|A_f| = |\bar{A}_{\bar{f}}|$ and $|A_{\bar{f}}| = |\bar{A}_f|$. Using also the approximation $|q/p| = 1$, it follows that $|\lambda_f| = 1/|\lambda_{\bar{f}}|$. The terms λ_f and $\bar{\lambda}_{\bar{f}} \equiv 1/\lambda_{\bar{f}}$ are calculated as

$$\begin{aligned}\lambda_{D_s^- K^+} &= \left(\frac{q}{p}\right)_{B_s} \frac{\bar{A}_{D_s^- K^+}}{A_{D_s^- K^+}} = \left(\frac{V_{tb}^* V_{ts}}{V_{tb} V_{ts}^*}\right) \left(\frac{V_{ub} V_{cs}^*}{V_{cb}^* V_{us}}\right) \left|\frac{A_2}{A_1}\right| e^{i\Delta_s} = |\lambda_{D_s^- K^+}| e^{i(\Delta_s - (\gamma - 2\chi))}, \\ \bar{\lambda}_{D_s^+ K^-} &= \left(\frac{p}{q}\right)_{B_s} \frac{A_{D_s^+ K^-}}{\bar{A}_{D_s^+ K^-}} = \left(\frac{V_{tb} V_{ts}}{V_{tb}^* V_{ts}^*}\right) \left(\frac{V_{ub}^* V_{cs}}{V_{cb} V_{us}^*}\right) \left|\frac{A_2}{A_1}\right| e^{i\Delta_s} = |\lambda_{D_s^- K^+}| e^{i(\Delta_s + \gamma - 2\chi)},\end{aligned}\tag{2.36}$$

where $|A_2/A_1|$ is the ratio of the *hadronic* amplitudes, which is expected to be of order

unity, and Δ_s is the *strong* phase difference between A_1 and A_2 . The value of $|\lambda_{D_s^- K^+}|$ is proportional to the ratio between $|V_{ub} V_{cs}^*|$ and $|V_{cb}^* V_{us}|$, which are both of order λ^3 in the Wolfenstein parameterisation. For this reason, this channel is expected to exhibit large CP -violating effects. By measuring the phase of $\lambda_{D_s^- K^+}$ and $\lambda_{D_s^+ K^-}$, both the strong phase, Δ_s , and the weak phase, $\gamma - 2\chi$, can be extracted. Hence, this decay channel provides an important method to probe the CKM angle γ as first pointed out in Ref. [19].

The small angle 2χ originates from B_s mixing and can be measured directly using, e.g., the decay $B_s^0 \rightarrow J/\psi \phi$. This angle is expected to be of order λ^2 in the Wolfenstein parameterisation. Combining the weak angles in the two decay channels results in a clean way to extract γ . The reconstruction of the decay channel $B_s^0 \rightarrow D_s^\mp K^\pm$ in LHCb and the sensitivity to measure the angle $\gamma - 2\chi$ are the subjects of Chapter 7.

Chapter 3

LHCb experiment

The LHCb detector will be an excellent facility to study B physics. This chapter presents the experimental setup as it is currently under construction. It explains the design of LHCb, the chosen detector technologies, and why it is suited for the study of B decays. First, Section 3.1 introduces the Large Hadron Collider (LHC) [20], providing the proton–proton (pp) collisions. Then, Section 3.2 gives an overview of the LHCb detector setup. The subsequent sections (Sects. 3.3–3.9) describe each of the subdetectors and their specific technologies in more detail. Finally, this chapter concludes with a summary of the trigger systems in Section 3.10.

3.1 Large Hadron Collider

The aim of the LHC project is to test the Standard Model, and, even more, to look for signals of physics beyond it. In the LHC, protons collide at a centre-of-mass energy of $\sqrt{s} = 14\text{ TeV}$, the highest ever achieved in pp collisions. At these energies new discoveries, as, e.g., the existence of supersymmetry (SUSY), are likely to be made. Also, the only unobserved particle in the Standard Model, the Higgs-boson, is expected to be produced and detected. The LHC provides a perfect facility to search for these new particles. Other research topics concern high-precision B physics, and the study of a new phase of matter produced in heavy-ion collisions. For the latter, the LHC is filled in dedicated runs with heavy ions (e.g., Pb) instead of protons.

The proton beams in the circular ring are accelerated in opposite directions to an energy of 7 TeV. Before reaching that energy, they have passed through a chain of preaccelerators. At the last stage of the preacceleration, the Super Proton Synchrotron (SPS) delivers 450 GeV protons to the LHC, where they are boosted to the final energy.

The LHC is installed underground in a tunnel of 27 km in circumference that previously housed the Large Electron Positron collider (LEP). April 1st, 2007 marks the start-up of this new collider. After a pilot run with only a single beam, the first pp collisions are expected a few months later.

At an energy of 7 TeV, protons require an 8.33 T magnetic field to maintain their orbit. This field is provided by superconducting magnets. As the two proton beams travel in opposite directions through the ring, separate beam pipes with opposite magnetic

field directions are needed. A two-in-one solution is chosen, where the magnet coils surrounding the two beam channels are firmly embodied inside the same iron yoke. The whole superconducting magnet is placed inside a cryostat, containing superfluid helium with a temperature of 1.9 K.

The four experiments at the LHC are located at each of the four interaction points. Here, the beams cross over to the other beam pipe and collide under a small angle. After filling, both beams consist of 2808 bunches with 10^{11} protons each. The time between two consecutive bunch crossings is 25 ns, which sets the basic clock frequency for the detector electronics to 40 MHz. As a consequence of the filling procedure, however, some bunches are empty.¹ Therefore, the average bunch crossing frequency of filled bunches, ν_{filled} , is somewhat lower, namely 30 MHz.

The luminosity is an important measure for the performance of the collider and determines the number of pp collisions at each crossing point. It includes the compactness of the beams, the ability of the magnets to focus the beams at the interaction point, the number of particles in the bunches, and the number of bunch crossings per second (see Ref. [20]). The maximal luminosity is $\mathcal{L}_{\max} = 10^{34} \text{ cm}^{-2}\text{s}^{-1}$. During the first year after the startup, however, the LHC runs at the lower luminosity of $10^{33} \text{ cm}^{-2}\text{s}^{-1}$.

The number of pp collisions also depends on the cross section. The total cross section is usually divided into an elastic and an inelastic part. Elastic collisions, which leave the colliding protons intact, are rarely seen in the detectors as the protons mainly escape through the beam pipe. The more violent, inelastic collisions often *do* emit particles that pass through the detector. Therefore, it is appropriate to consider only the inelastic cross section. In this thesis the inelastic cross section also includes diffractive collisions, which are soft scatterings where one or both of the protons break up.

The total number of inelastic collisions over a given period of time $[t_1-t_2]$ equals

$$N_{pp} = \sigma_{\text{inel}} \int_{t_1}^{t_2} \mathcal{L} \, dt \quad , \quad (3.1)$$

where $\sigma_{\text{inel}} = 80 \text{ mb}$ is the inelastic cross section expected for pp collisions at a centre-of-mass energy of 14 TeV [21]. The beams are stored for the duration of 7 hours, while the experiments take their data. Then, the beams are dumped and the LHC is refilled. During storage the luminosity exponentially decreases with a characteristic lifetime of 10 hours. For a given instantaneous luminosity \mathcal{L} , the number of inelastic collisions per filled bunch crossing follows a Poisson distribution with a mean of

$$\bar{n}_{pp} = \frac{N_{pp}}{N_{\text{bx}}} = \frac{\mathcal{L}\sigma_{\text{inel}}}{\nu_{\text{filled}}} \quad , \quad (3.2)$$

in which N_{bx} is the number of bunch crossings. At the maximal design luminosity, \mathcal{L}_{\max} , the average number of inelastic collisions in a beam crossing is expected to be 27. It should be noted that the luminosity at the interaction point of LHCb is maintained at a more modest luminosity to reduce the number of pp collisions per beam crossing, as will be explained below. The main machine parameters of the LHC are listed in Table 3.1.

¹The bunch structure does not have a simple pattern due to a complicated filling procedure. Details can be found in Ref. [20].

Table 3.1: Main LHC parameters.

Circumference	26659 m
Energy	7 TeV
Injection energy	0.45 TeV
Dipole field at 450 GeV	0.535 T
Dipole field at 7 TeV	8.33 T
Helium temperature	1.9 K
Coil aperture	56 mm
Distance between apertures	194 mm
Luminosity	$10^{34} \text{ cm}^{-2}\text{s}^{-1}$
Luminosity lifetime	10 h
Time between 2 fills	7 h
Bunch spacing	25 ns
Particles per bunch	10^{11}
Bunches per beam	2808

Figure 3.1 shows the location of the four experiments along the LHC ring. ATLAS [22] and CMS [23] are two general-purpose experiments. Both are central detectors constructed by large, international collaborations. Their main physics goals are the search for the Higgs boson and for SUSY particles. In addition, these experiments plan to study B physics, heavy-ion collisions, and many other interesting phenomena.

The ALICE [24] experiment focuses on studying strongly interacting matter at the extreme energy densities in heavy-ion collisions, and performing measurements of the phase transition between hadronic matter and the quark-gluon plasma. The ALICE detector is designed to cope with the higher particle multiplicities that are characteristic for heavy-ion collisions.

The fourth LHC detector is designed to study B physics: LHCb. As explained in the previous chapter, CP violation can be measured by analysing B decay events. For that purpose LHCb has an excellent vertex detector, which is able to resolve the fast B_s oscillations and to accurately determine the proper decay time. LHCb has extensive particle identification capabilities for the distinction between the different decay modes. And, LHCb has a tracking system that provides a good mass resolution, allowing a separation of true B decays from background events.

In the LHCb detector, the mean flight distance of B hadrons before decay is expected to be (11.8 ± 0.2) mm (see Fig. 3.2). Consequently, a good vertex resolution allows to separate most B decay vertices from the production vertex. This feature is essential in the identification of fake background decays which typically come directly from the primary pp collision. Other pp collisions within the same bunch crossing, also called pile-up, can significantly reduce the ability to identify the B decay vertex and its corresponding production vertex, especially when there are on average 27 collisions in the event of a bunch crossing. For this reason, the luminosity at the LHCb interaction point is limited to $2 \times 10^{32} \text{ cm}^{-2}\text{s}^{-1}$ by defocusing the beams, resulting in $\bar{n}_{pp} = 0.53$ inelastic collisions

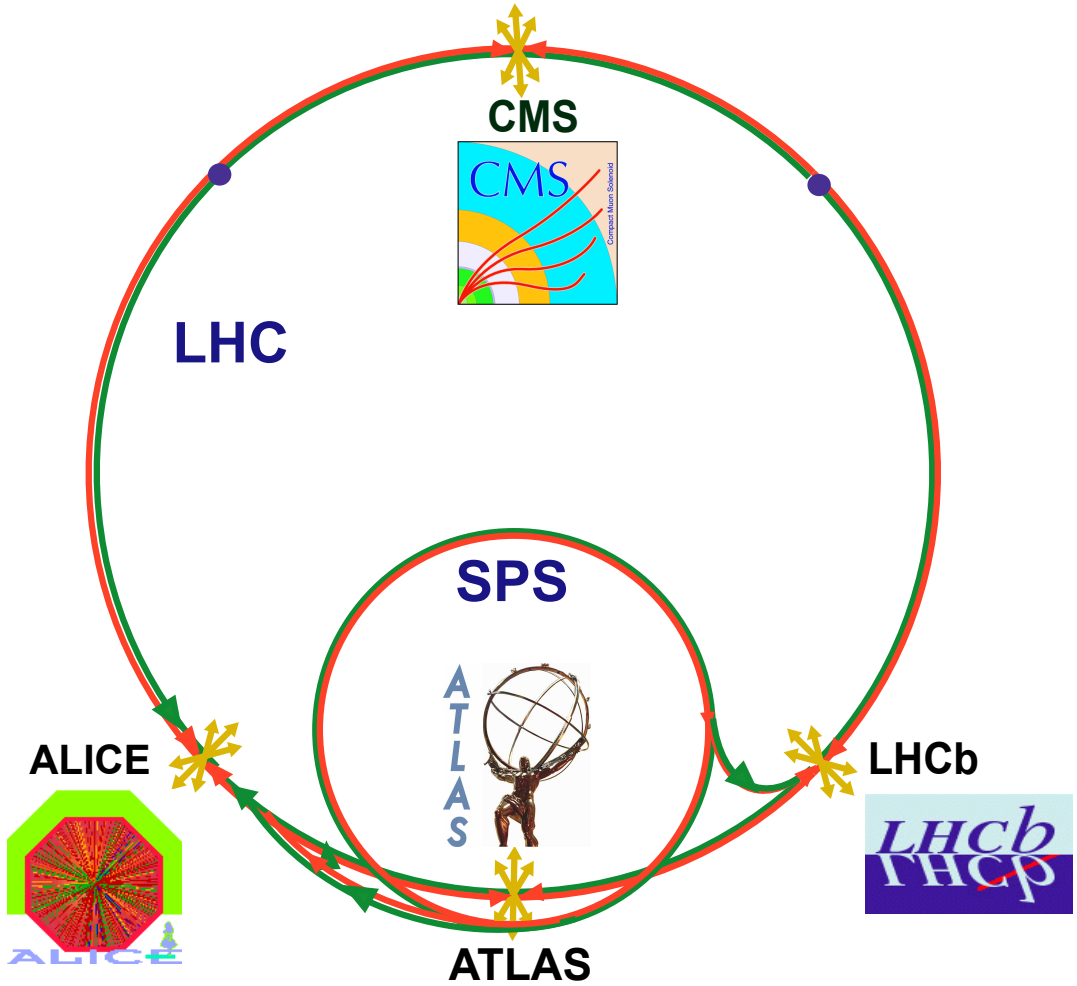


Figure 3.1: The LHC complex with its four experiments.

per filled bunch crossing (see Eq. (3.2)). The optimal luminosity for LHCb depends on several parameters, as, for instance, the ability to distinguish single-collision events from multiple-collision events. In a dedicated study [21] these considerations were taken into account and the optimal luminosity was found. Figure 3.3 shows the probabilities for single and multiple pp collisions as a function of the luminosity. Clearly, the optimal luminosity is close to the point where the number of single collisions is maximal. Likewise, the expected number of $b\bar{b}$ events without any pile-up collision is highest around the optimal luminosity as can be seen in Fig. 3.4.

The moderate luminosity requirement of LHCb implies that the optimal luminosity can already be obtained in the first year of LHC operation when the collider runs at $\mathcal{L} = 10^{33} \text{ cm}^{-2}\text{s}^{-1}$. In addition, there are two other benefits of running at a moderate luminosity. First, the particle multiplicity is lower, making the reconstruction of particle trajectories easier. And second, the radiation damage to the detector parts is less, which is especially important for the readout electronics. All subdetectors are designed to cope

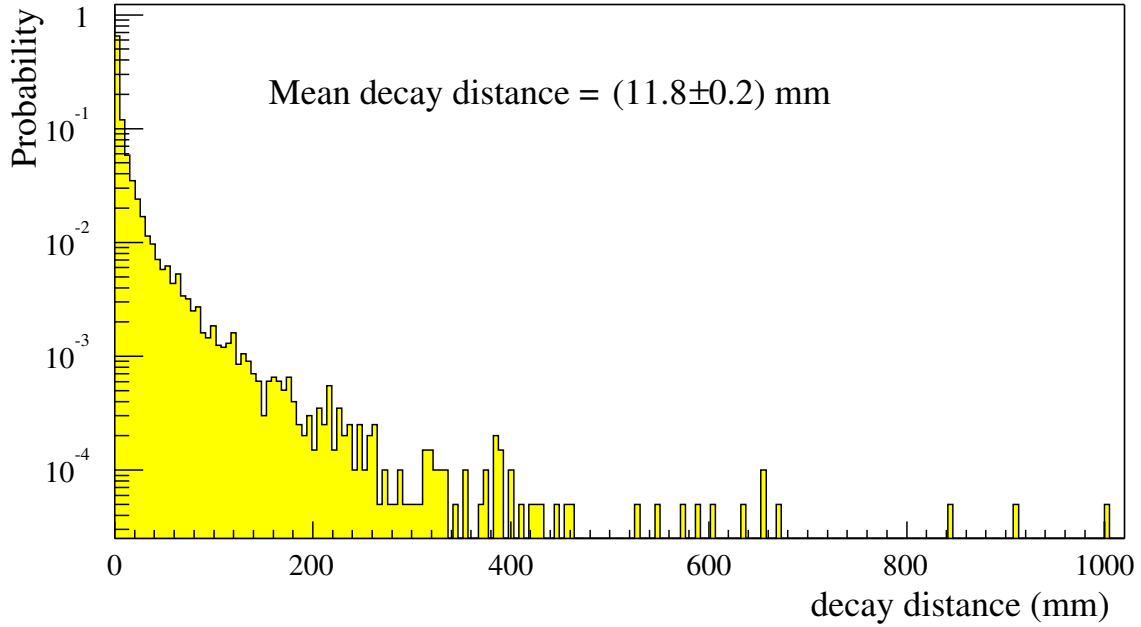


Figure 3.2: Distribution of the decay distance of B hadrons in LHCb. In contrast to the lifetime distribution, this distribution is not exponential due to the different momenta of the B hadrons.

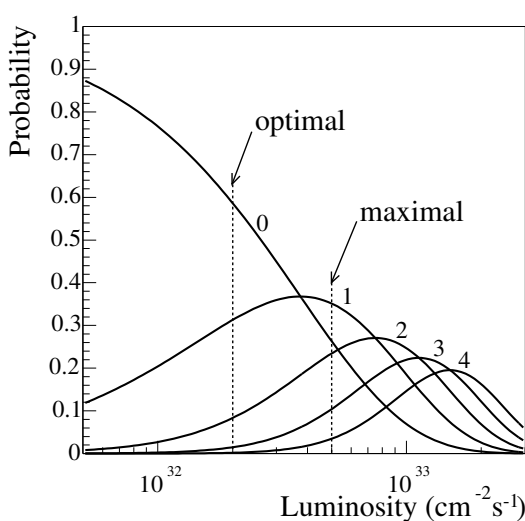


Figure 3.3: Probability for 0, 1, 2, 3, or 4 inelastic collisions per bunch crossing versus the luminosity.

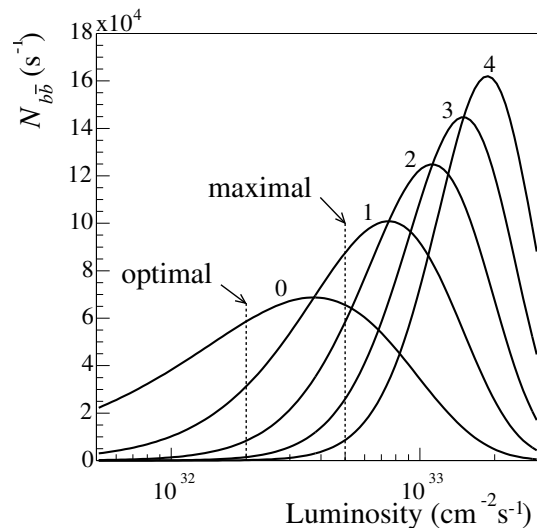


Figure 3.4: The number of $b\bar{b}$ events per second with 0, 1, 2, 3, or 4 pile-up collisions.

with a maximal luminosity of at least $5 \times 10^{32} \text{ cm}^{-2}\text{s}^{-1}$, leaving some freedom in the final choice for the optimal luminosity.

The $b\bar{b}$ cross section at a pp centre-of-mass energy of 14 TeV is assumed to be $\sigma_{b\bar{b}} = 500 \mu\text{b}$ in this thesis.² Compared to the inelastic cross section of 80 mb, this indicates that 1 in every 160 pp collisions produces a $b\bar{b}$ pair. The other collisions are considered to produce background, which must be rejected. Table 3.2 summarises the production cross section used in the simulation studies. Using Eq. (3.1), $10^{12} b\bar{b}$ pairs are expected to be produced per year (a year corresponds to $\sim 10^7$ s). However, the branching fractions for the B decay channels used to measure CP violation range between 10^{-4} – 10^{-6} .

Although the expected number of B events depends on $\sigma_{b\bar{b}}$, the actual value is not important in a precision measurement of the CP asymmetry. Of course, the error on the CP asymmetry depends on the number of reconstructed B decays, but this does not require a precise knowledge on $\sigma_{b\bar{b}}$. More important is the ratio $\sigma_{b\bar{b}}/\sigma_{\text{inel}}$, which basically determines the ratio of signal over background. As long as this ratio does not change, the luminosity can be tuned such that the number of $b\bar{b}$ pairs produced stays constant without damaging the detector.

Table 3.2: Assumed production cross sections.

Total	100 mb
Inelastic	80 mb
$c\bar{c}$	3.5 mb
$b\bar{b}$	500 μb

3.2 General layout

At the LHC, the two B hadrons from the $b\bar{b}$ pair produced in a pp collision are likely to fly in the same forward or backward cone. The next chapter explains in more detail this angular correlation in B production, which drives the design of the detector. Namely, LHCb is designed as a single-arm forward spectrometer, thus having a large acceptance for B events with a relatively small detection surface. It is housed in the underground pit located at one of the interaction points (IP8) along the LHC ring. The experimental setup is shown in Fig. 3.5.

Throughout this thesis, a right-handed coordinate system is adopted in which the positive z axis is defined as pointing from the Vertex Locator towards the muon detector, and the positive y axis is pointing upwards. Looking into the negative z direction, this leaves the x axis pointing to the right such that a right-handed system is made. Hence, in Fig. 3.5 the y axis is pointing upwards, out of the paper. A full description of the coordinate system can be found in Ref. [27].

The acceptance of the detector is defined by the polar angle with respect to the z axis. In the horizontal plane (i.e., the bending plane of the magnet) the acceptance lies between 10–300 mrad and in the vertical plane (non-bending plane) between 10–

²Estimates for $b\bar{b}$ cross section at $\sqrt{s} = 14$ TeV have large uncertainties [25]. This value is taken as a conservative estimate. Recent studies [26] indicate a cross section of $\sigma_{b\bar{b}} = 633 \mu\text{b}$.

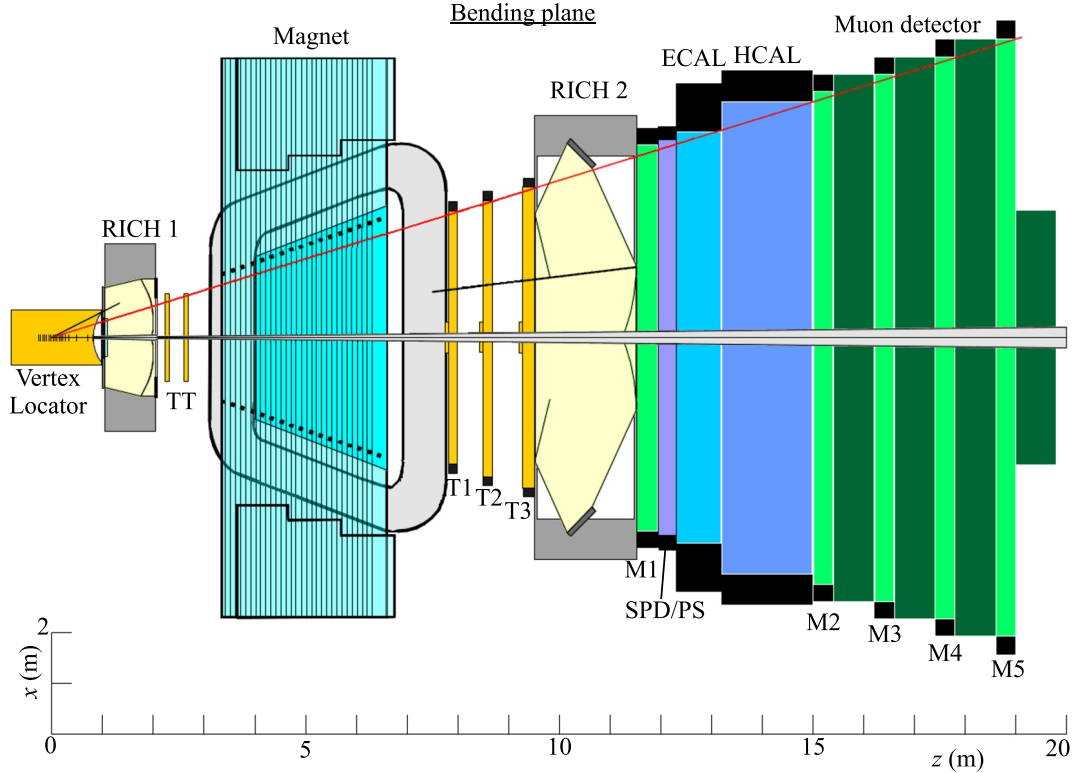


Figure 3.5: The LHCb setup with the different subdetectors shown in the horizontal plane — also referred to as the bending plane of the magnet.

250 mrad. The detector has a length of 20 m, giving it an overall dimension of roughly 6 m × 5 m × 20 m.

In the following sections each of the subdetectors is described in turn. They can be categorised into tracking detectors and particle identification (PID) detectors:

- **Tracking detectors:** Vertex Locator (VELO), Trigger Tracker (TT), Inner Tracker (IT), and Outer Tracker (OT).
- **PID detectors:** First and second Cherenkov detectors (RICH 1 and RICH 2), the electromagnetic and hadronic calorimeter (ECAL and HCAL), and the muon detector.

As it is impossible to write the event data from all collisions to tape, a trigger system is used to select events online. It is designed to identify events that contain a B decay. The goal is to reduce the number of events efficiently at an input rate of 16 MHz. The trigger uses information from the subdetectors to separate signal events from background events. For this purpose, it is subdivided into three independent levels, historically denoted as Level-0, Level-1, and High-Level Trigger. The trigger is discussed in Section 3.10.

The tracking system can be divided globally into three sub-systems. First, there is the Vertex Locator, which is installed around the interaction point. Second, there is the

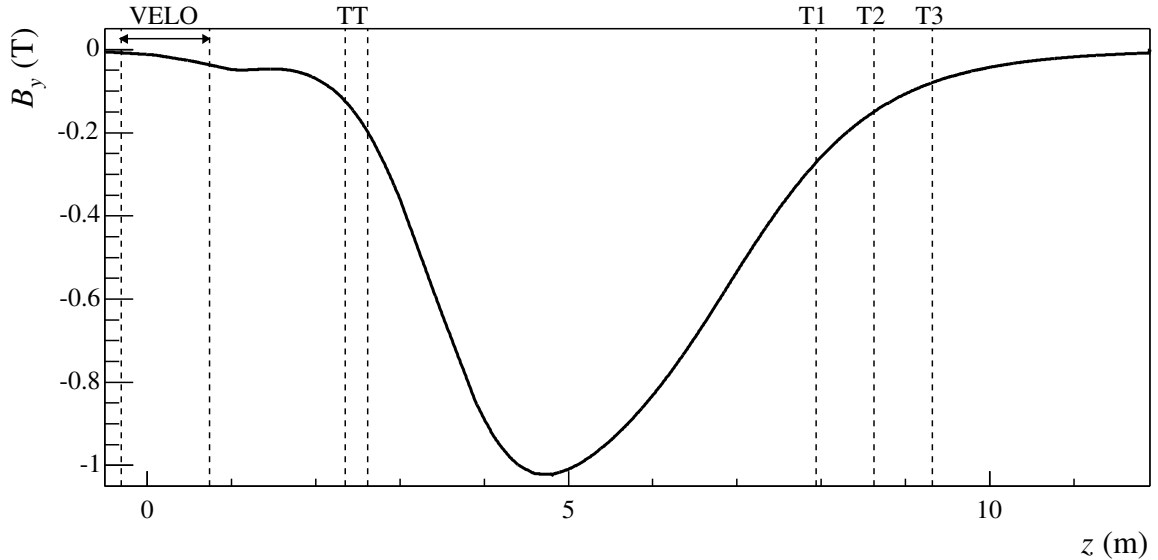


Figure 3.6: The main component of the magnetic field strength (B_y) along the z axis.

Trigger Tracker, which is placed after RICH 1 and just in front of the magnet. Third, after the magnet three tracking stations are located: T1, T2, and T3. The inner part of these stations, close to the beam pipe, is referred to as the Inner Tracker; the outer part covers the remaining acceptance and is called the Outer Tracker. The Outer Tracker is constructed from straw tube drift chambers; the other tracking detectors are all silicon strip detectors.

Charged particles are bent in the B field of the magnet [28]. Their momentum is measured from the deflection of the trajectories as the particles traverse the magnet. The difference between the track slope in the VELO and the track slope in the T stations is inversely proportional to the particle's momentum. In Chapter 6, this relation will be discussed. The bending power of the magnet is represented by the total integrated field, which is $\int B dl = 4.2 \text{ T m}$. The strength of the main component of the magnetic field along the z axis is shown in Fig. 3.6.

The detector design has gone through a number of optimisation phases. These changes are referred to as the “reoptimisation” [26]. The detector setup described in this thesis refers to this reoptimised design.

3.3 Vertex Locator

The Vertex Locator (VELO) [26, 29] contains 21 stations, positioned along and perpendicular to the beam axis. Figure 3.7 shows a cross section of the VELO and the interaction region as seen from above. Two types of silicon sensors are used: one measures the r coordinate with circular strips centred around the beam axis, the other measures the ϕ coordinate with straight, radial strips. The half-disc sensors, shown in

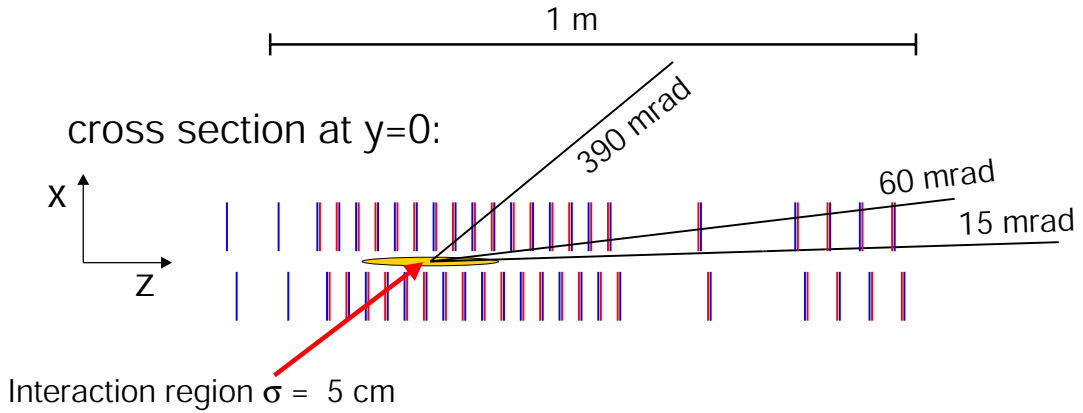


Figure 3.7: Setup of the stations in the VELO.

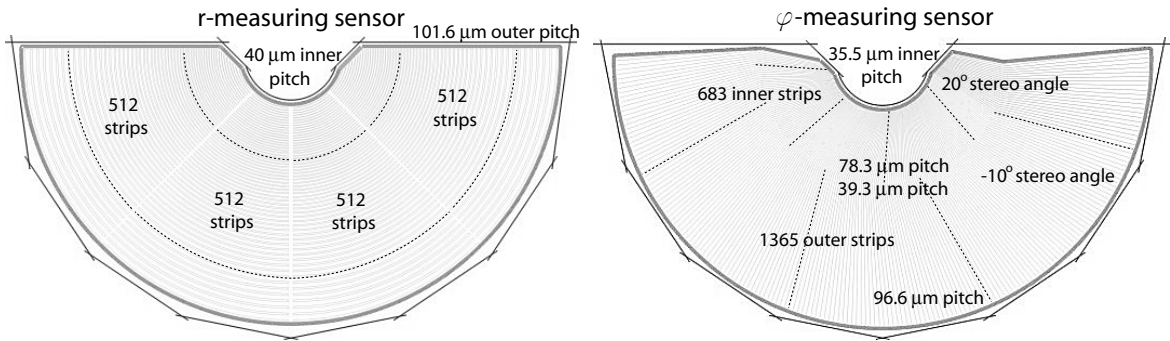


Figure 3.8: Layout of the r - and ϕ -measuring sensors.

Fig. 3.8, are arranged in pairs of r and ϕ sensors and mounted back-to-back.

The r - ϕ geometry has the advantage that it directly gives a projection in the r - z plane by using only r measurements. In this projection, forward-going tracks with a high impact parameter with respect to the production vertex are easily identified. The trigger exploits this idea by first reconstructing all tracks in the r - z projection, before reconstructing only the ones with a large impact parameter in three dimensions.

The $220 \mu\text{m}$ thick sensors are based on single-sided, n-on-n technology. The ϕ -measuring sensors have an inner section with strips under a stereo angle of 20° and an outer section with strips under a stereo angle of -10° . The strip pitch automatically increases from $35.5 \mu\text{m}$ to $78.3 \mu\text{m}$ in the inner section, and from $39.3 \mu\text{m}$ to $96.6 \mu\text{m}$ in the outer section. The r -measuring sensors are divided into four sections of 45° . The pitch between two r strips increases linearly from $40 \mu\text{m}$ on the inside to $101.6 \mu\text{m}$ on the outside. The varying strip pitch provides a more homogeneous occupancy throughout the sensor, since the particle flux is highest close to the beam axis, where the strip pitch is small, and decreases away from the beam, where the pitch is larger. The average occupancy per channel is well below 1% [29].

The sensitive area of the sensors starts at 8 mm from the beam axis, such that the first measurement of the track is as close to the primary vertex as possible. The shorter the

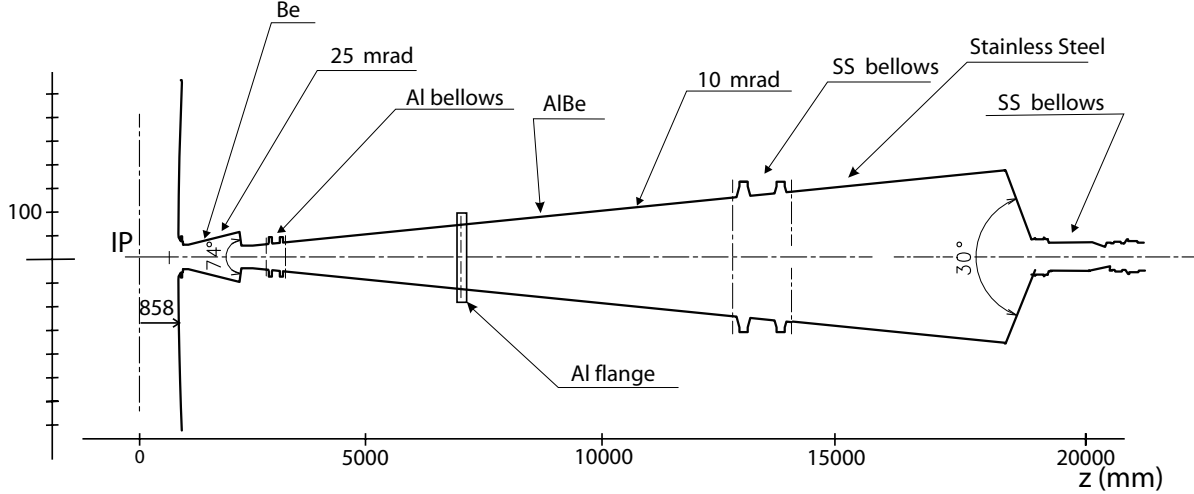


Figure 3.9: Layout of the beam pipe. It starts at the VELO exit window ($z = 858$ mm) and runs through the whole experiment. The bellows and flanges connect the different sections of the beam-pipe.

extrapolation of a track from its first measurement to the interaction region, the smaller is the error on the reconstructed position of the vertex. This proximity requirement implies that the sensors must be retractable during beam injection. In order to avoid severe radiation damage, a minimal distance of 3 cm is required when LHC is being filled. Consequently, the VELO is designed so that the two detector halves can be moved away from the beam in the horizontal direction.

The sensors are separated from the beam vacuum by a thin aluminium foil, which prevents outgassing of the sensors into the beam vacuum and also shields the electronics against RF pickup from the beams. This so-called RF foil has a complex shape, which is optimised such that a particle encounters a minimum amount of material before reaching the first sensor. In stable running conditions, the RF foil has a clearance of 5 mm from the beam line. The whole vertex detector is contained inside a vacuum vessel. The forward-going particles leave this vacuum vessel through a thin exit window, before continuing their journey through the detector. The LHCb beam pipe is attached to this exit window.

The beam pipe [26] is designed to minimise the creation of secondary particles, while resisting the air pressure from outside. The layout of the beam pipe is shown in Fig. 3.9. The first part of the beam pipe is made out of the light-weighted materials beryllium (1.8 m long) and beryllium-aluminium alloy (10 m long). After $z = 13$ m, where the amount of material is not critical anymore, the beam pipe is constructed from stainless steel. The thickness of the beam pipe ranges between 1.0 and 2.4 mm. The beam pipe roughly consists of two conical sections. The first one, starting after the VELO, is 1.3 m long with a 25 mrad opening angle; the second one is 16 m long with a 10 mrad opening angle.

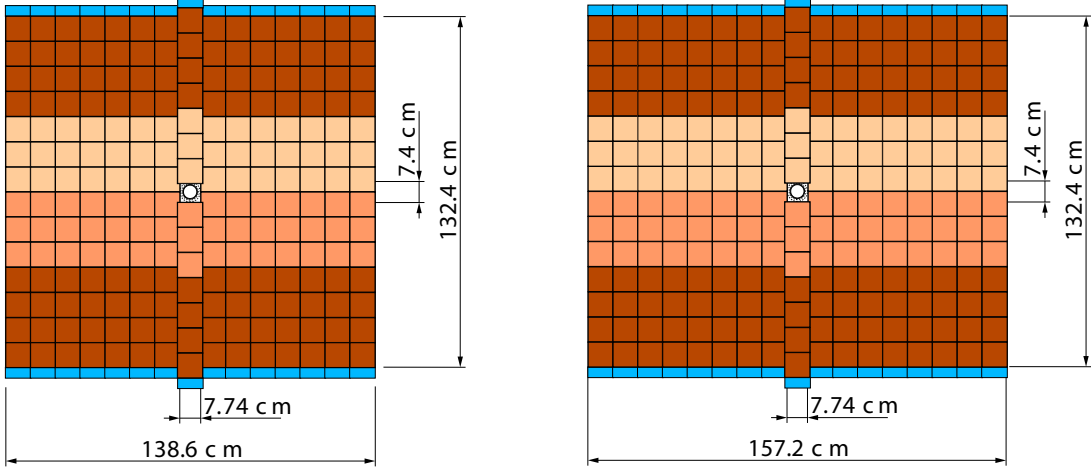


Figure 3.10: Layout of first (left) and last (right) TT layers. The shadings indicate strip connections.

3.4 Trigger Tracker

Just in front of the magnet, the Trigger Tracker (TT) [26] is located (see Fig. 3.5). It consists of two stations separated by a distance of 27 cm. As the name indicates, data from the TT is used to make the trigger decision. The presence of a low integrated magnetic field of $\sim 0.15 \text{ T m}$ between the VELO and the TT (see Fig. 3.6) is sufficient to assign a rough momentum estimate with a resolution of 20%–40% to the tracks. The trigger selects events with high-momentum tracks. Since the deflection of these high-momentum tracks is small, a good spatial resolution is required. Therefore, to resolve the deviation from a straight line, it is chosen to build the TT as a silicon strip detector.

Apart from its use in the trigger, the TT also serves to reconstruct long-living, neutral particles (mainly K_s^0 's) which may decay outside the acceptance of the VELO. Furthermore, it provides a momentum estimate for slow particles that are bent out of the LHCb acceptance before reaching the T stations, and it improves the momentum estimate for particles that do reach the T stations.

Each TT station has two layers of silicon covering the full acceptance. The strips in the four layers are arranged in stereo views, x - u and v - x , corresponding to angles with the vertical y axis of 0° , -5° , $+5^\circ$, and 0° . The stereo views allow a reconstruction of tracks in three dimensions. The vertical orientation of the strips is chosen to obtain a better spatial resolution in the horizontal plane (bending plane of the magnet), resulting in a more accurate momentum estimate.

A layer is built out of $11 \text{ cm} \times 7.8 \text{ cm}$ sensors as depicted in Fig. 3.10. In total, the silicon sensors cover a surface of about 8.4 m^2 . Depending on their distance from the horizontal plane, the strips of three or four neighbouring sensors are connected so that they can share a single readout. The layout is explained in detail in Ref. [30].

The capacitance per readout channel increases as more sensors are connected. This

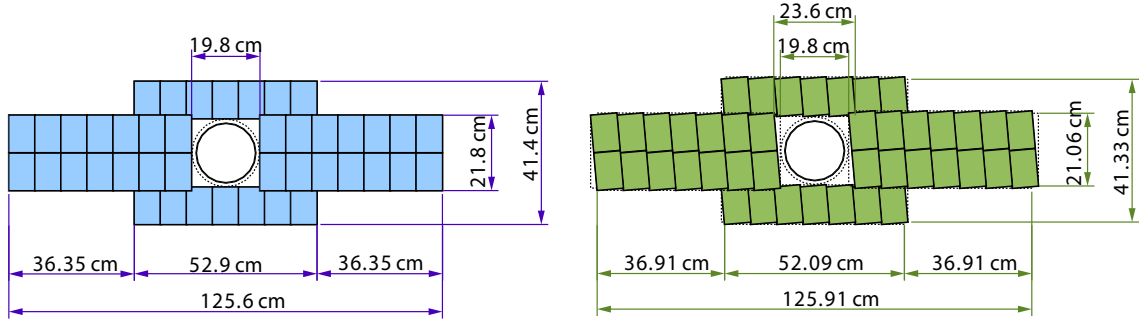


Figure 3.11: Layout of an IT *x* and *u* layer with the silicon sensors in the cross-shaped configuration. In the middle a cross section of the beam pipe is drawn.

gives rise to a higher noise rate. The signal-over-noise performance can be recovered by using thicker sensors. In order to connect up to four TT sensors, the sensors require a thickness of $500\,\mu\text{m}$. The strip pitch is $183\,\mu\text{m}$, which results, after clustering with neighbouring strips, in a spatial resolution of $\sim 50\,\mu\text{m}$ [31]. Due to their similar technologies, the development and construction of the TT is combined with the Inner Tracker into a common project named Silicon Tracker.

3.5 Inner Tracker

The Inner Tracker (IT) [32] covers the innermost region of the T stations, which receives the highest flux of charged particles. An IT station consists of four boxes of silicon sensors, placed around the beam pipe in a cross-shape. It spans about 125 cm in width and 40 cm in height (see Fig. 3.11). Each station box contains four layers in an *x-u-v-x* topology similar to that in the TT.

The silicon sensors have the same dimensions as in the TT. In the IT, however, not more than two sensors are connected. Therefore, they can be thinner due to the lower noise rate. The single sensors are $320\,\mu\text{m}$ thick, while the double sensors are $410\,\mu\text{m}$ thick. The strip pitch is $198\,\mu\text{m}$, resulting in a resolution of approximately $50\,\mu\text{m}$ [31].

The cross-shape has been chosen as the optimal shape for the IT. This was done to limit the occupancy in the hottest regions of the Outer Tracker. In Chapter 5, the simulation studies justifying this shape are discussed. The average hit occupancy in IT itself is expected to be less than 2% [31].

3.6 Outer Tracker

In the T stations, the Outer Tracker (OT) [33] covers the large region outside the acceptance of the Inner Tracker. Chapter 5 discusses in detail the simulation programme of the OT in LHCb. This section introduces the hardware design of the OT. As it is

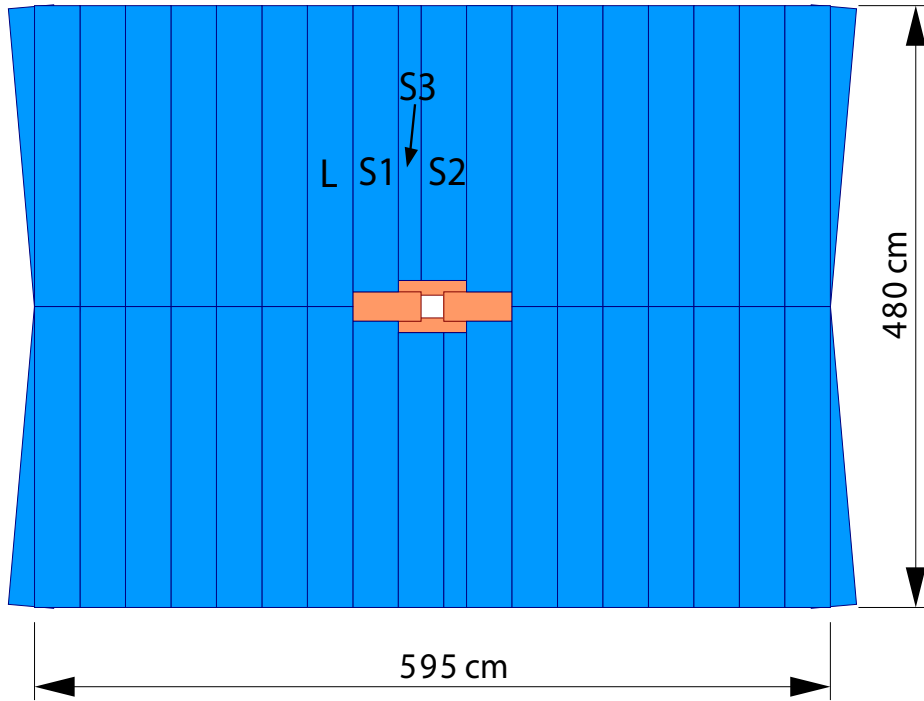


Figure 3.12: Layout of OT station (front view). In the centre the four boxes of the IT station are depicted.

relevant for the simulation studies in Chapter 5, there is an emphasis on the configuration of the readout system and on the choice of used materials. The use of light materials is important for the minimisation of scattering and hadronic interactions. These topics will recur in the next chapters.

Charged particles are detected in the OT with gas-filled straw tubes serving as drift cells. Each station contains four detection layers in the same $x-u-v-x$ configuration as in the IT and TT. Modules are the building blocks of the detection layers. Adjacent to each side of the IT station, seven long modules (L) are situated. Eight shorter modules — named S1, S2, and S3 — fill up the area above and below the IT. The layout is shown in Fig. 3.12. All three stations are of equal size, which is determined by the acceptance requirement at the last station of $250\text{ mrad} \times 300\text{ mrad}$ (see Ref. [34]). This fixes the length of the long modules to 4.8 m and that of the short modules to 2.3 m (S1) and 2.2 m (S2 and S3).

All modules, except S3, contain 128 straws, staggered in two monolayers of 64 straws each. As can be seen in Fig. 3.12, the two S3 modules have only half the normal width, corresponding to 32 straws per monolayer. In Fig. 3.13, the arrangement of the straws in a module is depicted. The inner diameter of the straws is 5.0 mm, and the pitch between two straws is 5.25 mm. The cathode cell wall is wound from two foils: the inner windings are made of a $40\text{ }\mu\text{m}$ thick, carbon-doped polymer foil (Kapton-XC); the outer windings are made of a $25\text{ }\mu\text{m}$ Kapton-XC foil with a $12.5\text{ }\mu\text{m}$ aluminium coating. In

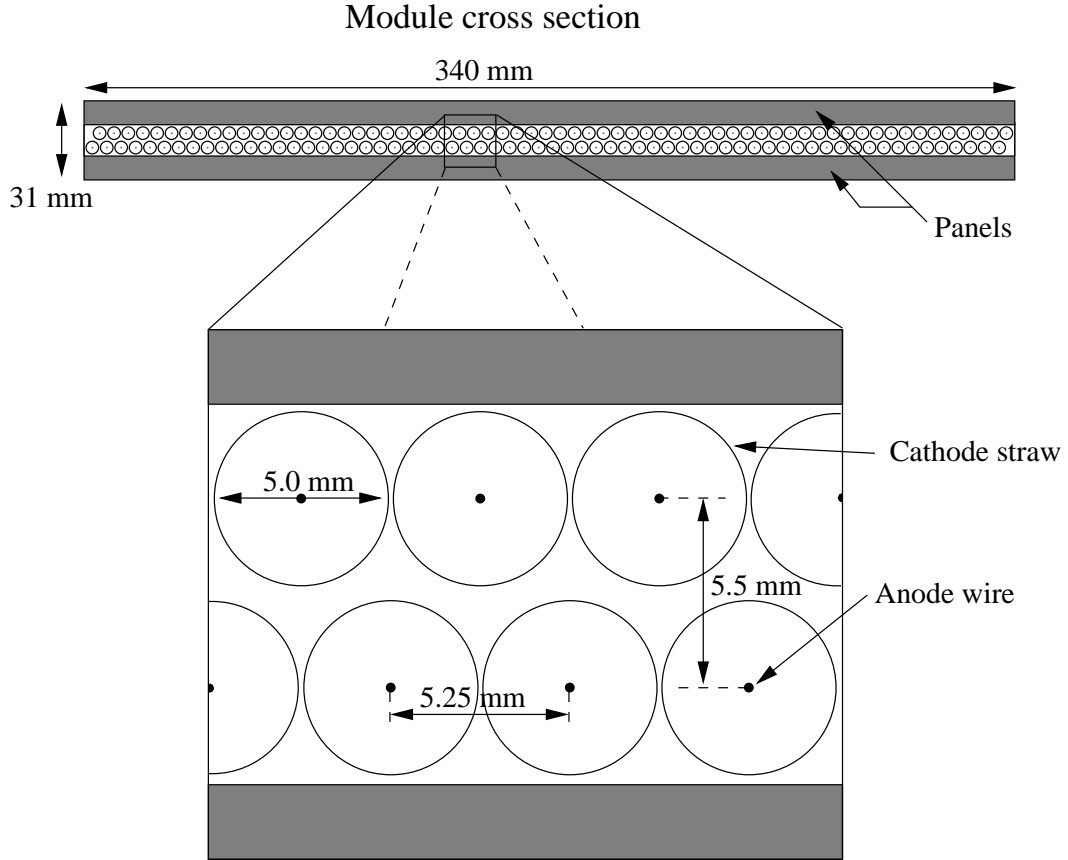


Figure 3.13: Cross section of an OT module (128 straws). A small region containing a few straws is magnified.

the centre of a straw a $24\text{ }\mu\text{m}$ thick, gold-coated, tungsten wire operates as the anode. Wire locators are placed every 80 cm to keep the wires in their central position.

The straws in a module are sandwiched between two panels, which form, together with the side panels, a stiff and gas-tight box. The panels are constructed from carbon-fibre skins glued onto a core of 10 mm thick polymethacrylimide rigid foam (Rohacell). The inside of the box is laminated with $25\text{ }\mu\text{m}$ Kapton foil for gas tightness and with $12\text{ }\mu\text{m}$ of aluminium for grounding of the straws. The full specification for the module elements is given in Ref. [35].

The straws in the long modules are physically split halfway in the module to limit the occupancy of hits. The splitting requires that the readout electronics are mounted on the top of every long module as well as on the bottom. The short modules require readout at only one side, located either at the top or at the bottom of the station.

The choice of the drift gas is driven by the requirement that it should provide a fast signal collection. In the Technical Design Report (TDR) [33], the constraint is put that the signal is collected within the time of two LHC bunch crossings, i.e., 50 ns. The selected drift gas is the mixture Ar(75)/CF₄(15)/CO₂(10), which has a maximum drift time of 32.5 ns. Including a propagation time of the electrical signal of about 10 ns, this

results in a total signal collection time well within two bunch crossings. The spatial resolution obtained in a test beam experiment [36] with this gas is 200 µm.

However, the use of CF₄, which provides a fast signal collection, might cause ageing effects [37]. This effect is still under study, and the option to leave out the CF₄ component is considered. For Ar(80)/CO₂(20) the maximum drift time is 41.2 ns [38]. In this case the total signal collection time exceeds the 50 ns limit, so that a 75 ns readout time window must be used.

The main components of the OT readout chain can be summarised as follows. The signal pulse from the anode wire is first transmitted to a preamplifier-shaper-discriminator chip (ASDBLR) [39, 40], which cancels out the slow-ion tail and shapes the signal on the leading edge of the input pulse. Next, the time digitiser chip (OTIS) [41] converts the signal into a digital time. For each 25 ns bunch crossing, the digitiser chip records maximally one 6-bit TDC time. When the LHCb Level-0 trigger accepts an event, the TDC times from two bunch crossings are transmitted to the central data acquisition system. For a 75 ns readout window, maximally three TDC times per readout channel are transmitted. This multiple hit capacity of the OTIS chip increases the detection efficiency. The effect on the efficiency is discussed in Chapter 5. Finally, four OTIS boards are connected to one Gigabit Optical Link (GOL) board [42]. Together with the high-voltage board all of these components are housed inside front-end (FE) electronics boxes, which are mounted at each end of a module.

3.7 RICH detector

The Ring Imaging Cherenkov detectors (RICH) [26, 43] provide particle identification. The RICH system is divided into two detectors: RICH 1 is located between the VELO and the TT, and RICH 2 is located between the last T station and the calorimeters (see Fig. 3.5). This combined system achieves a good π - K separation in the momentum range of 2–100 GeV, which is indispensable in the selection of many B decay channels. For instance, as is presented in Chapter 7, RICH information is essential to distinguish the $B_s^0 \rightarrow D_s^\mp K^\pm$ decay from the almost identical $B_s^0 \rightarrow D_s^- \pi^+$ decay.

Cherenkov radiation is emitted when a charged particle traverses a medium with a velocity greater than the velocity of light in that medium. The RICH principle is based on a measurement of the particle's velocity. Using the momentum of the reconstructed tracks, the mass and thus the particle type can be determined. The velocity of the particles is found by measuring the emission angle of Cherenkov photons with respect to the particle's trajectory. This angle, θ_C , depends on the particle's velocity $\beta = v/c$ as

$$\cos \theta_C = \frac{1}{n\beta} , \quad (3.3)$$

with n being the refraction index of the radiator medium. Particles start to radiate Cherenkov light above a threshold $\beta_t = 1/n$. A large refractive index allows to identify particles in the low-momentum range, while a small index is useful in the high-momentum range. The different radiators are chosen such that a large momentum range is covered over which particle identification is possible.

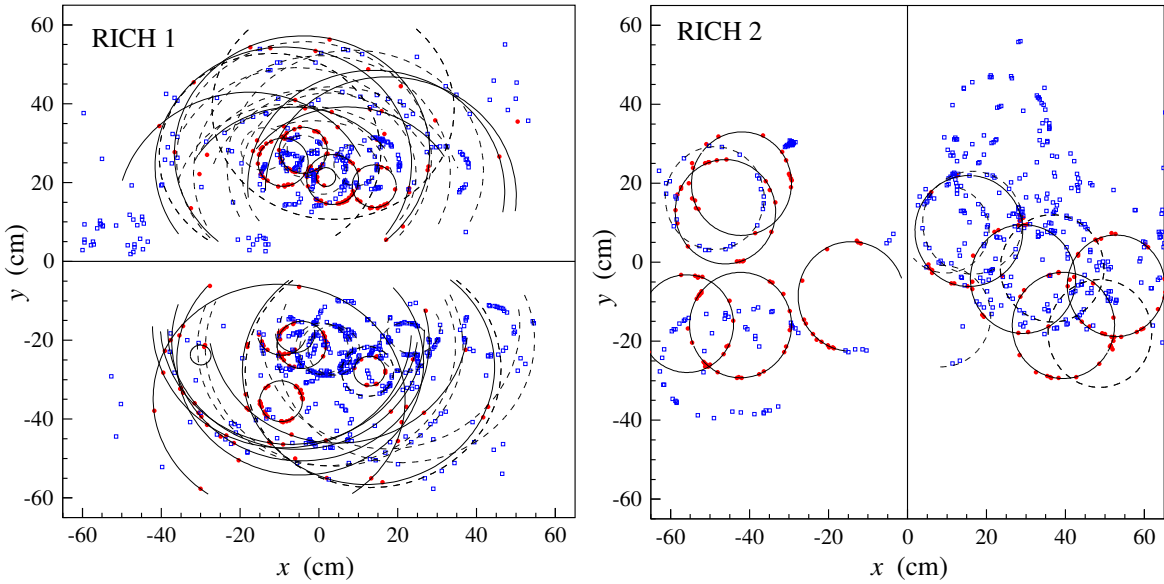


Figure 3.14: A typical event in the detection planes of RICH 1 (left) and RICH 2 (right). The horizontal (vertical) line separates the two detection planes in RICH 1 (RICH 2). Superimposed are the reconstructed rings for tracks which extend from the VELO up to the last T station (solid) and all other tracks (dashed).

In the RICH detectors the Cherenkov light is directed out of the LHCb acceptance via spherical and flat mirrors which have a reflectivity above 85%. The light cones are projected as circles (rings) onto a plane of photon detectors. The radius of each ring is a measure for the Cherenkov angle, θ_C . In addition, also the number of radiated photons contributes to sensitivity on the Cherenkov angle. The rings are simultaneously reconstructed in a global log-likelihood analysis. In the first iteration, this method assumes a pion hypothesis for each reconstructed track. A likelihood is calculated by comparing the expected pattern of photons to the observed pattern. Then, the particle hypotheses are varied one-by-one and the likelihood is recalculated, until the observed pattern matches best with the expected pattern. Figure 3.14 displays for both detectors the observed photons with the reconstructed rings in a typical event.

In RICH 1, two radiators cover a momentum range between 2 and 60 GeV. The first radiator is a 5 cm thick silica aerogel with a refractive index $n = 1.03$. It is suited for particle identification up to 10 GeV. The second radiator is a 85 cm long volume of C_4F_10 gas with $n = 1.0014$, providing particle identification from 10 to 60 GeV. RICH 1 covers almost the full acceptance, extending from 25 mrad to 250 mrad vertically and from 25 mrad to 300 mrad horizontally. A sketch of RICH 1 is depicted in Fig. 3.15. Hybrid Photon Detectors (HPD's) with integrated 1024-channel binary readout are placed at the upper and lower detection planes. The projected image has a granularity of $2.5 \text{ mm} \times 2.5 \text{ mm}$. The magnetic field at the detection planes in the shielding boxes is expected to be $\sim 2.5 \text{ mT}$. This is further decreased by local shielding

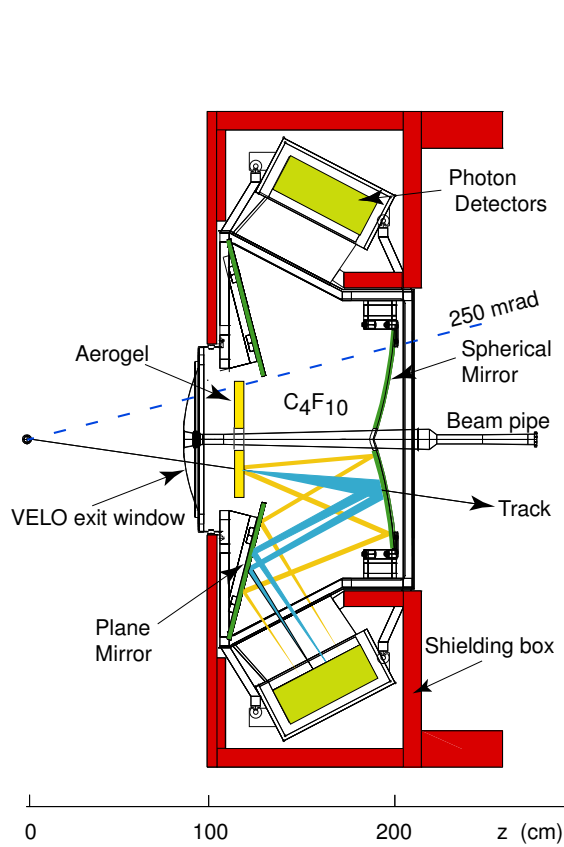


Figure 3.15: Vertical cross section of the RICH 1 detector.

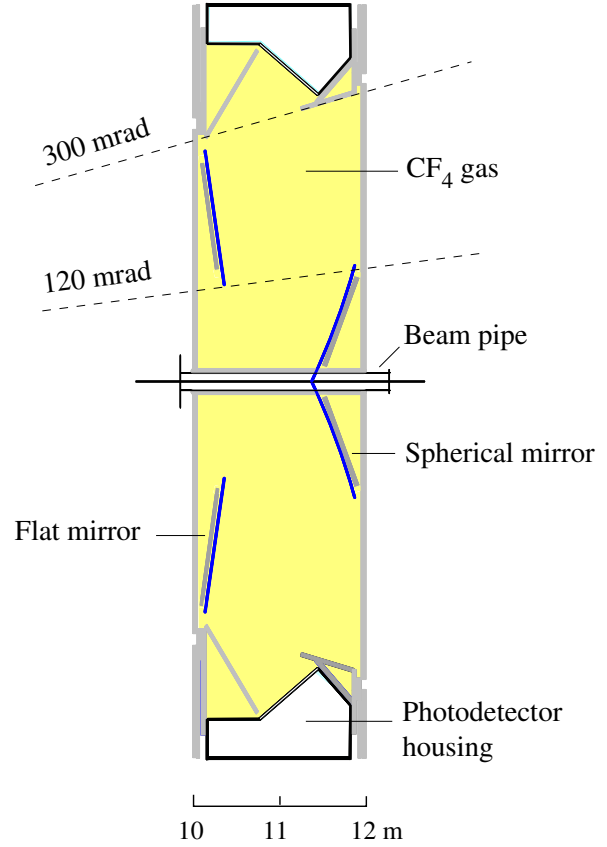


Figure 3.16: Horizontal cross section of the RICH 2 detector.

of the individual HPD tubes. Although photoelectrons are still affected in this stray field, the image is only distorted and there is no loss in efficiency. In fact, when the field is known, the image can be recovered in the reconstruction.

Figure 3.16 shows the layout of RICH 2. In contrast to RICH 1, it has a reduced acceptance, covering up to 120 mrad in the bending plane and up to 100 mrad in the non-bending plane. The radiator is CF_4 gas with $n = 1.0005$. RICH 2 is designed to provide particle identification up to 100 GeV. Similar to RICH 1, a system of spherical and flat mirrors guides the Cherenkov light outside the LHCb acceptance. This time, however, the mirror system is oriented horizontally. Again, HPD's are used for photon detection.

3.8 Calorimeters

All particles, except muons, are absorbed in the calorimeters [44]. Through their interaction with the bulk material, incident particles produce a cascade of secondary particles, which are finally absorbed. The ionisations induced by this particle shower excite atoms in the scintillator material, which emit scintillation light as they return to their ground

state. The total amount of scintillation light in the shower is a measure for the (deposited) energy of the particle.

The calorimeters are used in the Level-0 trigger to select events containing particles with a high transverse energy, E_T . The presence of a high- E_T particle is a sign for the decay of the heavy B meson. The transverse energy is defined as the energy component transverse to the beam axis and is calculated from the deposited energy and the position of this deposit with respect to the z axis. Apart from their use in the trigger, the calorimeters also allow identification of electrons and reconstruction of photons and neutral pions, which are important in the reconstruction of many B decays. Neutral pions ($\pi^0 \rightarrow \gamma\gamma$) are reconstructed by selecting those photon pairs with the correct invariant mass.

The calorimeter system in LHCb can be divided into an electromagnetic calorimeter (ECAL) and a hadronic calorimeter (HCAL). The ECAL measures the electromagnetic showers of electrons and photons. In addition, two separate detection layers are positioned in front of the ECAL, namely a scintillator pad detector (SPD) and a preshower detector (PS). They provide useful information on the longitudinal evolution of the electromagnetic shower. The HCAL measures the hadronic showers of pions, kaons, and protons. It is placed behind the ECAL (see Fig. 3.5). In the following the design and characteristics of the calorimeters are described. Note that all calorimeter systems use a polystyrene plastic as scintillator material.

The SPD and PS provide valuable information on the initial electromagnetic shower development, thereby improving the particle identification of the ECAL. First, before they start to shower, charged particles are identified by the SPD, since they produce ionisation, as opposed to neutral particles. This detector is used to distinguish electrons from photons. Then, between the SPD and PS a 12 mm thick lead wall initiates an electromagnetic shower. The PS detects this shower to discriminate between electrons and hadrons.

Both detection planes of the SPD and PS consist of 15 mm thick scintillator pads. The scintillation light is collected in each pad by a wavelength shifting (WLS) fibre and directed to multianode photomultipliers (MAPMT's), located outside the acceptance. The total thickness in z of the SPD/PS system is 180 mm.

The SPD and PS are laterally segmented into three sections with different granularity as depicted in Fig. 3.17. Being closest to the beam pipe, and thus receiving the highest particle flux, the inner section has the smallest pad size of 40.4 mm \times 40.4 mm. This corresponds roughly to the characteristic size of an electromagnetic shower, given by the Molière radius. Hence, the total energy is localised within a cluster with a maximal size of 2 \times 2 pads. The middle section has pads of 60.6 mm \times 60.6 mm and the outer section of 121.2 mm \times 121.2 mm. The ECAL follows the same segmentation as the SPD and PS.

The remaining shower from electrons and photons is detected in the “shashlik” type modules of the ECAL, which consists of 4 mm thick scintillating tiles alternated with 2 mm thick lead sheets. A full module counts 66 scintillation layers, located behind each other and oriented perpendicular to the z axis. The scintillation light is captured and transported to photomultipliers by WLS fibres, which run through holes in the module.

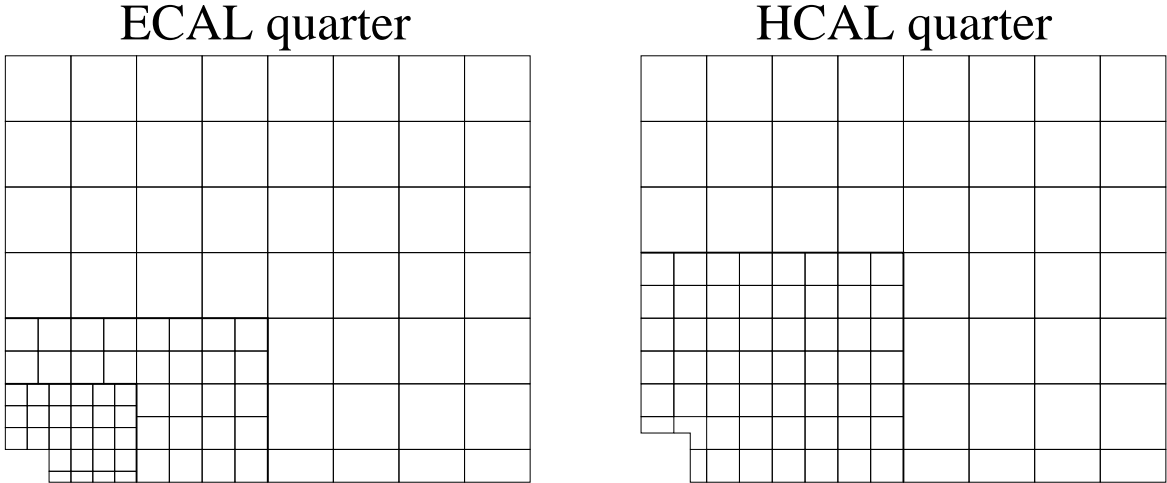


Figure 3.17: Front view of an ECAL (left) and HCAL (right) quarter showing the lateral segmentation. Each square in the ECAL represents 16 pads; each square in the HCAL represents 4 pads. The SPD/PS detectors have the same segmentation as the ECAL.

The modules in the inner and middle section have a fibre density of 144 per module, while those in the outer section have a fibre density of 64 per module. The energy (E) is measured with a resolution given by

$$\frac{\sigma(E)}{E} = \frac{10\%}{\sqrt{E}} \oplus 1.5\% \quad , \quad (3.4)$$

where E is expressed in GeV and \oplus means addition in quadrature.

Although hadrons may develop an initial shower already in the ECAL, they are fully absorbed inside the HCAL, where they deposit most of their energy. The HCAL is constructed out of 4 mm thick scintillator tiles, oriented perpendicular to the x axis and alternated with 16 mm thick iron plates. The scintillation light is guided to the photomultipliers at the rear of the HCAL by WLS fibres, which are fixed to the edge of the tiles. The long contact between the fibre and the scintillator tile provides efficient light collection. The fibres from a stack of tiles are connected to a single photomultiplier, hence defining the cell granularity of the HCAL. In the inner section 131.3 mm square cells are used and in the outer section 262.6 mm square cells (see Fig. 3.17), resulting in a modest energy resolution of

$$\frac{\sigma(E)}{E} = \frac{80\%}{\sqrt{E}} \oplus 10\% \quad , \quad (3.5)$$

where E is expressed again in GeV.

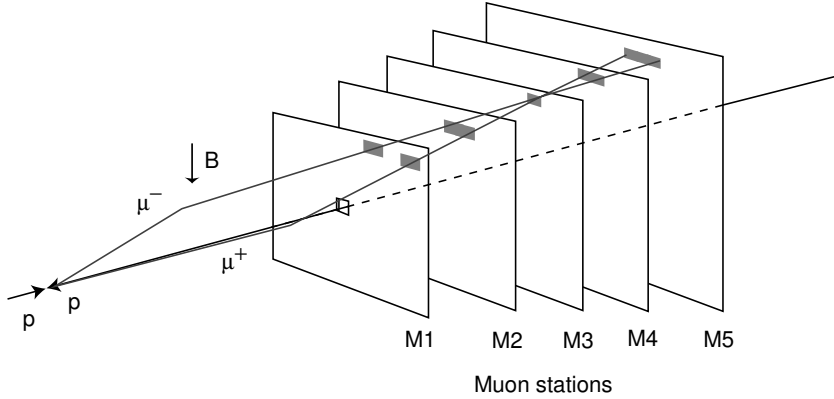


Figure 3.18: Concept of track finding in the muon trigger. The algorithm starts with hits in M_3 and then searches for additional hits in fields of interest in the other stations (highlighted). The muon tracks are assumed to originate from the interaction point. The corresponding kink obtained in the magnet is used to estimate p_T .

3.9 Muon system

Since muons are the only particles³ which penetrate the full calorimeter system, they need to be detected by a separate system. For this purpose the muon detector [45] is placed behind the calorimeters to identify the muons (see Fig. 3.5).

The muon system is used both in the Level-0 trigger to select muons with a high transverse momentum (p_T) and in the offline reconstruction to identify muons. In the trigger algorithm, high- p_T muons are found by a fast and standalone track reconstruction selecting particles which traverse all 5 muon stations. The slope of the track between M_1 and M_2 is used to estimate the momentum assuming that the particle originated from the interaction point. Hereby, a 20% resolution on p_T is obtained. Figure 3.18 displays the concept of the muon trigger. In the offline reconstruction, the muon system is used to identify the muons in the sample of tracks found in the tracking stations. In the corresponding algorithm, offline tracks are extrapolated to the muon stations to search for a confirmation of the muon hypothesis. In contrast with the trigger algorithm, this approach also finds muons with momenta below 8 GeV.

The first muon station, M_1 , is placed before the calorimeter system. The other four stations, M_2 – M_5 , are located directly behind the HCAL and are separated by 80 cm thick iron plates, which act as filters for the hadronic background. An additional iron shield protects M_5 against particles emerging from the opposite LHC beam. All stations cover the full LHCb acceptance. The position of M_1 in front of the SPD/PS is chosen to decrease the error on the momentum measurement due to scattering of the particles in the calorimeter material.

³Of course, also neutrinos penetrate the calorimeter, but their cross section is so small that they cannot be detected at all in the LHCb detector.

A pad readout structure provides binary space point measurements of the muon tracks, allowing a fast track finding in the trigger. Each station is divided into four regions with different pad granularity. The granularity in each region is adjusted to the particle flux. The regions and their pads increase in size from M1 to M5 so that they are mutually projective towards the interaction point, hereby simplifying the track search. The dimensions of the pads decrease towards the inner regions such that their hit occupancy stays roughly constant. In addition, the size in x is smaller than that in y , giving a more accurate momentum measurement.

The detectors are instrumented with multiwire proportional chambers (MWPC's), which fulfil both the requirement from the trigger to collect the signal within 20 ns and the requirement for radiation hardness. In the innermost region of M1, the MWPC's need to be equipped with a triple-GEM foil to deal with the higher particle flux. The required granularity is obtained by grouping the anode wires and the cathode pads of the MWPC's.

3.10 Trigger

Events cannot be written to permanent storage at the 40 MHz bunch crossing rate. This would create too much data volume, and in addition, these events cannot be fully reconstructed at this input rate. Therefore, a trigger system [46] is developed to reduce the event rate that is written to tape and available for a full offline reconstruction.

The initial data volume can be drastically reduced, since only a small fraction of the events actually contains a B decay of interest. Hence, the main strategy of the trigger is to look for the two signatures of B decays: the large B mass produces decay products with a high transverse momentum, and the long B lifetime produces tracks with a high impact parameter with respect to the primary interaction vertex. The trigger algorithms are optimised to give the highest efficiency for B decays, while removing a huge fraction of the background events. The trigger efficiency is calculated with respect to events containing B decays that pass the offline selection cuts.

In the trigger algorithms, there is not enough time available for a full event reconstruction. For this reason, events are selected (triggered) in successive stages (levels). First, at an initial stage, loose cuts on a few available reconstructed variables are applied, with an emphasis on reducing the obvious background events. Then, at a later stage, more time is available to distinguish the more difficult (signal-like) background events from the real B events. In addition to cuts on B signatures, cuts on the hit multiplicity are applied to remove hot events, as they demand a disproportional fraction of the reconstruction time. The trigger system is divided into three distinct levels (L0, L1, and HLT) which process an increasing amount of information from the subdetectors. Their input and output rates are summarised in Table 3.3, and they are discussed below.

Table 3.3: Trigger input and output rates for the three trigger levels.

Level	input rate	output rate	event size	suppression factor
0	16 MHz	1 MHz	5 kB	16
1	1 MHz	40 kHz	50 kB	25
HLT	40 kHz	200 Hz	100 kB	200

3.10.1 Level-0

The input rate for the Level-0 trigger is the rate of inelastic pp collisions, which is expected to be $\mathcal{L}\sigma_{\text{inel}} = 16 \text{ MHz}$ (see Eq. (3.1)). The purpose of this first level is to reduce the event rate to 1.0 MHz, while keeping a high efficiency for B events. It should be kept in mind that the rate for $b\bar{b}$ collisions is only $\mathcal{L}\sigma_{b\bar{b}} = 100 \text{ kHz}$. Level-0 is implemented in hardware residing at the detector. The L0-trigger decision is taken after a fixed latency of $4 \mu\text{s}$. During that time, equivalent to 160 bunch crossings, the FE electronics store the events in a pipeline memory. The maximum output rate for Level-0 is fixed to 1.1 MHz, which demands that the accepted events are transmitted to the L1 buffer within 900 ns. There are four L0 subsystems: the calorimeter trigger, the muon trigger, the pile-up trigger, and the decision unit. The latter collects reconstructed information of the other three and makes the L0 trigger decision.

The calorimeter trigger selects high- E_T deposits of 2×2 cells in the ECAL and HCAL. The ECAL clusters are identified as either electron, photon, or π^0 using the SPD/PS system. For hadrons, the E_T in the ECAL is added to the deposit in HCAL to correct for the energy loss in the ECAL. For each particle type only the highest E_T cluster is selected and sent to the decision unit, along with the total hit multiplicity in the SPD.

The muon trigger looks for muon tracks with a high p_T , as explained in Section 3.9. For each quadrant, the two muon candidates with the highest p_T are sent to the decision unit.

The pile-up trigger consists of two dedicated silicon stations located upstream of the VELO. These two stations, containing r sensors only, have a fast readout that allows them to be used in the L0 trigger. The purpose of the pile-up trigger is to veto bunch crossings with multiple collisions (see Fig. 3.3). Therefore, a histogramming method locates the primary vertices by combining the hits of both stations into track candidates in the r - z plane and subsequently calculating the corresponding z position of the vertex. The number of tracks in the second vertex and the total hit multiplicity are transmitted to the decision unit. It should be noted that since the pile-up veto is located upstream of the interaction region, it will not mistake a B vertex in the forward acceptance for a second primary vertex.

The decision unit receives information from the calorimeter, muon, and pile-up trigger to determine whether to select an event or discard it. First, events are vetoed on the basis of four global event variables. This means that events are discarded when the number of tracks in the second vertex is more than 3, when the pile-up multiplicity is larger than 112, when the SPD multiplicity is more than 280, or when the total E_T is

Table 3.4: Trigger efficiencies for $B_s^0 \rightarrow D_s^- \pi^+$ and $B_s^0 \rightarrow D_s^\mp K^\pm$ for Level-0, Level-1, and the combined efficiency (Level-0 and Level-1). All efficiencies are calculated with respect to events passing the offline selection (see Chapter 7).

	Level-0	Level-1	Combined
$B_s^0 \rightarrow D_s^- \pi^+$	$(50.1 \pm 0.6)\%$	$(60.8 \pm 0.8)\%$	$(30.4 \pm 0.5)\%$
$B_s^0 \rightarrow D_s^\mp K^\pm$	$(45.5 \pm 0.3)\%$	$(62.3 \pm 0.4)\%$	$(28.3 \pm 0.3)\%$

below 5 GeV. Second, an event is accepted when it contains a calorimeter cluster with E_T larger than 3.6 GeV (hadrons), 2.8 GeV (electrons), 2.6 GeV (photons), or 4.0 GeV (π^0), or when it contains a muon with $p_T > 1.1$ GeV. Furthermore, when the sum of the two muons with the largest p_T exceeds 1.3 GeV, the event is accepted irrespective of any veto trigger. Depending on the decay channel, the L0 trigger efficiency ranges between 40–90%. The efficiencies for $B_s^0 \rightarrow D_s^- \pi^+$ and $B_s^0 \rightarrow D_s^\mp K^\pm$ are given in Table 3.4.

3.10.2 Level-1

The Level-1 trigger is the first of two software triggers running on a commodity CPU farm. The 1800 CPU’s are shared with the High-Level Trigger. The trigger algorithms run in the same software environment as the offline algorithms, which is presented in the next chapter. On a L0 accept, the data from the FE boards of the subdetectors is shipped to the Trigger Electronics and Level-1 (TELL1) boards [47]. Here, the data is buffered for 58254 events, resulting in a maximum latency for the L1 trigger of more than 50 ms. In contrast to the fixed latency of the Level-0 trigger, this is variable latency. The maximum output rate is 40 kHz.

The L1 trigger decision is based on data from the VELO, TT, and the L0 decision unit, which amounts to an event size of 50 kB. Scenarios which increase the L1 data size by adding IT, OT, and M2–M5 are still under study (this is referred to as the scalability of the L1). The average execution time to process an event on a single CPU is tuned to be below 1 ms.

The L1 scheme is to search for B decay tracks having a high impact parameter (d) in combination with a large transverse momentum (p_T). The p_T requirement serves to reject low-momentum particles which have obtained a high impact parameter due to multiple scattering. In the following the L1 trigger algorithm is described.

First, the impact parameter is measured. A fast track reconstruction algorithm [48] searches for VELO tracks in the r - z projection using hits in the r sensors only. Figure 3.19 displays a typical event in the VELO. On average, about 60 tracks are reconstructed per event. The majority of these 2-D tracks points back directly to the primary vertex, which is reconstructed with a resolution of 60 μm in z . Tracks with a high impact parameter, in the range of 0.15–3.00 mm, and the ones matching a high- p_T L0 muon are reconstructed in three dimensions by including the hits from the ϕ sensors. On average only 8.5 tracks are selected by this requirement.

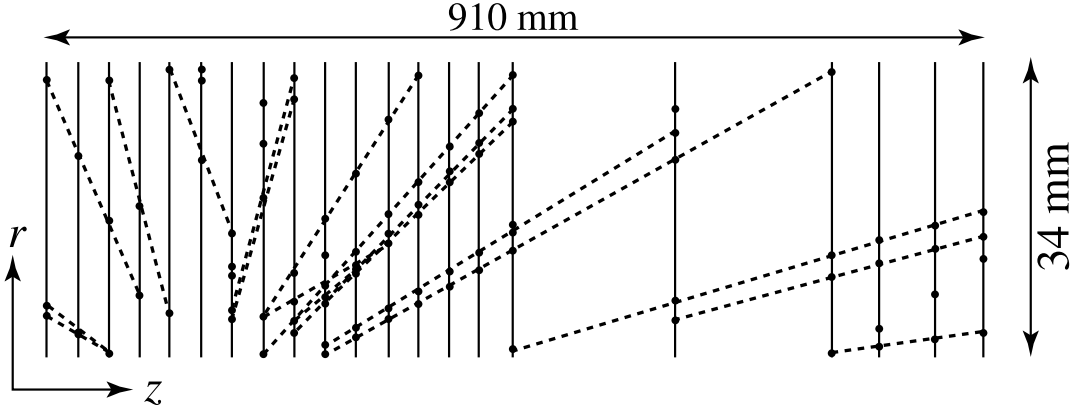


Figure 3.19: Event display showing the hits and reconstructed 2-D tracks in a 45° section of the VELO.

Second, the momentum of these 3-D tracks is measured. This is done by extrapolating them to the TT stations and using the deflection of the trajectory in the magnetic field to estimate the momentum. This results in a 20–40% momentum resolution. Another momentum estimate can be obtained by matching the 3-D tracks to L0 objects. A successful match improves the resolution to 6% (muons), 12% (electrons), and 15% (hadrons). Unfortunately, the reconstruction efficiency for L0 objects is not high enough to disregard the TT information in the Level-1 trigger, but this method does enhance the selection of decay channels containing muon pairs (dimuons) from $J/\psi \rightarrow \mu^+\mu^-$.

Finally, the trigger decision is taken using the two tracks with the highest p_T and a large impact parameter (d). A simultaneous cut is applied on the two variables $\sum \ln(p_T)$ and $\sum \ln(d/\sigma_d)$, where σ_d is the uncertainty on the impact parameter. For most channels, the L1 efficiency for L0 accepted events is 50–80%. The L1 efficiencies for $B_s^0 \rightarrow D_s^-\pi^+$ and $B_s^0 \rightarrow D_s^\mp K^\pm$ are given in Table 3.4.

3.10.3 High Level Trigger

At the final trigger stage, the High-Level Trigger (HLT) reduces the event rate to 200 Hz, nominally. The final output rate is configurable and depends mainly on the available storage space. The HLT algorithms run concurrently on the same CPU nodes as the L1 algorithm, but with a lower priority. They utilise the 25% remaining processing power, which can be translated into a time budget of about 10 ms per event. As the HLT is executed at the final step of the data acquisition (DAQ) [49] (DAQ), the data from all subdetectors is available at this trigger level, which corresponds to approximately 100 kB per event.

The first step in the HLT strategy is to re-evaluate the L1 decision using the hits in the tracking stations T1–T3 instead of those in TT, resulting in an improved momentum resolution of 0.6%. This step reduces the event rate with a factor two without a significant loss in signal events.

Before a further reduction of the event rate is possible, more reconstruction infor-

mation must be added to the events. Therefore, not only the ones with a high impact parameter, but all VELO tracks are reconstructed in 3-D. Then, these tracks are extrapolated to find hits in the TT and T stations using fast algorithms [48] resembling the pattern recognition algorithms used offline (see Chapter 6). Information on the particle identity is added to these tracks when they are matched to muon or electron candidates.

After the L1 confirmation, the event sample is already largely enriched with B decays. About 1 in every 7 events contains a $b\bar{b}$ pair. Nonetheless, to further reduce the event rate, inclusive and exclusive selections on specific decay channels are needed. Preliminary studies show that the rate for exclusive selections on the prominent decay channels of LHCb can be well below a few hundred Hz [46]. This part of the HLT, the event selection, is still under development and different ideas are studied. One of them is the option to include a fast RICH reconstruction, which would facilitate the selection of many decay channels.

Chapter 4

Monte Carlo simulation

A detailed simulation and reconstruction programme is used to estimate the performance of the LHCb detector. Many detector parameters described in the previous chapter have been tuned by running simulations with different settings. Hence, a realistic simulation is of major importance during the design phase of the experiment. Moreover, during the running phase of the experiment, many efficiency studies rely on comparisons of simulated data with real data from the detector. As the detector is currently in its construction phase most design parameters are fixed. Smaller adjustments not affecting the production of the detector parts, however, can still be considered.

First, in Section 4.1 the subject of simulations in LHCb is introduced. Then, in Section 4.2 the software framework and its applications are briefly described. In Section 4.3, the first step in the simulation chain, the event generation, is explained. The subsequent step, the simulation of particles inside the detector, is presented in Section 4.4.

4.1 Introduction to LHCb simulations

A good example in which simulations proved to be of major importance is the reoptimisation process in which the LHCb detector was redesigned in many places. At that time, simulations showed that the amount of material in the detector had become so much that the detection of particles had significantly degraded. It became clear that the total material budget had to be reduced drastically. Therefore, it was decided, for instance, to remove the tracking stations inside the magnet. The total number of tracking stations was reduced from 11 to only 4 (3 T stations plus Trigger Tracker). Other simulations showed the positive effect of these changes on the performance of the detector. More information and a detailed comparison of the old and the new, “light” design can be found in Refs. [26, 50].

The simulation of an event resulting from a pp collision is based on the Monte Carlo technique. These generated, Monte Carlo (MC) events are treated completely equivalent to real events. Thus, the same reconstruction programme used to reconstruct MC data will be used to reconstruct particles in real data as well. In absence of real data, MC data is the only way to estimate the performance of the detector. The final physics sensitivity depends on performance indicators such as the detection and reconstruction

efficiencies of signal as well as background events, and the precision on the reconstructed parameters, most notably the precision on the decay time of the B meson.

When LHC turns on, many events will be produced. Assuming a total cross section of 100 mb, every second about 20 million pp collisions are expected. Although most of these events are rejected by the trigger, a reasonable number still needs to be simulated, for instance, to tune the trigger. These events are commonly referred to as minimum-bias events, as they would be recorded when the trigger is put a mode which selects events randomly — without bias.

The most interesting B decay channels, exhibiting CP violation, have only a tiny branching fraction. For such decay channels, the bulk part of the events containing a $b\bar{b}$ pair should then also be regarded as background. It is generally expected that these so-called inclusive $b\bar{b}$ events are the most difficult to distinguish from the signal events containing the actual decay of interest. Inclusive $b\bar{b}$ events may differ only slightly from signal events as they both have displaced vertices with high-momentum tracks. Every second 10^5 $b\bar{b}$ pairs are created. As the branching fractions of most CP -violating B decay channels range between 10^{-4} – 10^{-6} , only 0.1–10 of these events contain the specific decay.

In the simulation, three event types can be distinguished: minimum-bias, $b\bar{b}$ inclusive, and signal events. The signal events are those events containing a specific B decay channel. In the data challenge of 2003, DC03, 10 million $b\bar{b}$ inclusive events were produced. This is equivalent to 4 minutes of normal LHC operation. In addition, 30 million minimum-bias events (equivalent to ~ 2 seconds) and 25 million signal events (equivalent to $\mathcal{O}(1)$ year) were generated. As will become clear in Chapter 7, these huge amounts are needed to obtain reliable estimates of the contamination of background in the selected signal events.

4.2 Framework and applications

A software framework that is common to all applications is an essential ingredient for a flexible and maintainable usage. The LHCb software is implemented within the object-oriented framework of GAUDI [51]. This framework is written in C++ and consists of services that allow sharing of basic functionality such as job steering, message logging, data access, and data analysis. GAUDI applications are composed of algorithms which exploit these services. Different applications are responsible for the different tasks as event generation, detector simulation, reconstruction, physics analysis, and visualisation. In fact, due to the flexibility of GAUDI, these tasks can be combined into one application, or subdivided into different applications. Below the subsequent tasks and their GAUDI applications are briefly described:

- **Event generation.** First, an event is generated by simulating the pp collision. This task is delegated to the external programme PYTHIA [52]. In Section 4.3 the features of this programme will be described, including the usage in LHCb. The output consists of the outgoing particles, represented by their four-momentum vectors. The decay of the B hadrons is controlled by another external programme

called EvtGEN [53]. Both programmes are steered by the GAUDI application known as GAUSS [54].

- **Detector simulation.** Second, the evolution of the particles in the detector is simulated. This task is performed by the GEANT4 toolkit [55], which is also controlled by GAUSS. It takes care of the interaction of particles with material inside the detector, the tracing of charged particles in the magnetic field, and the decay of the remaining unstable particles, such as, for instance, the K_s^0 . Details concerning the simulation will be given in Section 4.4.
- **Digitisation.** Next, the response of the detector electronics is simulated. Here, the hits, deposited by the particles in the sensitive materials of the detector, are “digitised” into an electrical signal. The application for this digitisation process is BOOLE [56]. For each subdetector, dedicated algorithms describe the detector response in detail. This response can typically be divided into a physical process of signal collection, such as electrons drifting to a wire, and the specific behaviour of the electronics. All subdetectors rely on results from test-beam data to calibrate these simulations. As an example the digitisation in the Outer Tracker will be explained in Chapter 5.
- **Trigger.** Then, the trigger [46] application is executed as an intermediate step between the digitisation and the offline reconstruction. Since it runs in real time, the trigger is often referred to as the online reconstruction. The lowest level trigger, Level-0, can be seen as part of the digitisation job, as it is fully implemented in (programmable) electronics. On the other hand, the higher level triggers (Level-1 and HLT) can be seen as part of the reconstruction job, as they are executed on a dedicated processor farm, running the same software that is used on MC data.
- **Reconstruction.** Subsequently, all data coming from the detector is processed by the reconstruction application BRUNEL [57]. Its main tasks are the reconstruction of tracks and the identification of particles. The track reconstruction algorithms will be presented in Chapter 6.
- **Physics analysis.** Finally, the event selection algorithms are executed using the DAVINCI [58] application. First, the particles are constructed from tracks and particle identification objects. Then, the primary vertices are searched and fitted. In the last step, specific B decays of interest are selected by making the appropriate particle combinations. The correct B decays can be found by cutting on the signal variables, such as the B mass and B lifetime. The LOKI toolkit [59] facilitates the looping over particles and the kinematic calculations common to all selections. In Chapter 7, the selection of the decays $B_s^0 \rightarrow D_s^- \pi^+$ and $B_s^0 \rightarrow D_s^{(*)\mp} K^{(*)\pm}$ will be explained.
- **Visualisation.** Additionally, events in the detector can be displayed using the visualisation application PANORAMIX [60]. This programme translates event objects and detector geometry into a graphical representation. It can be run after

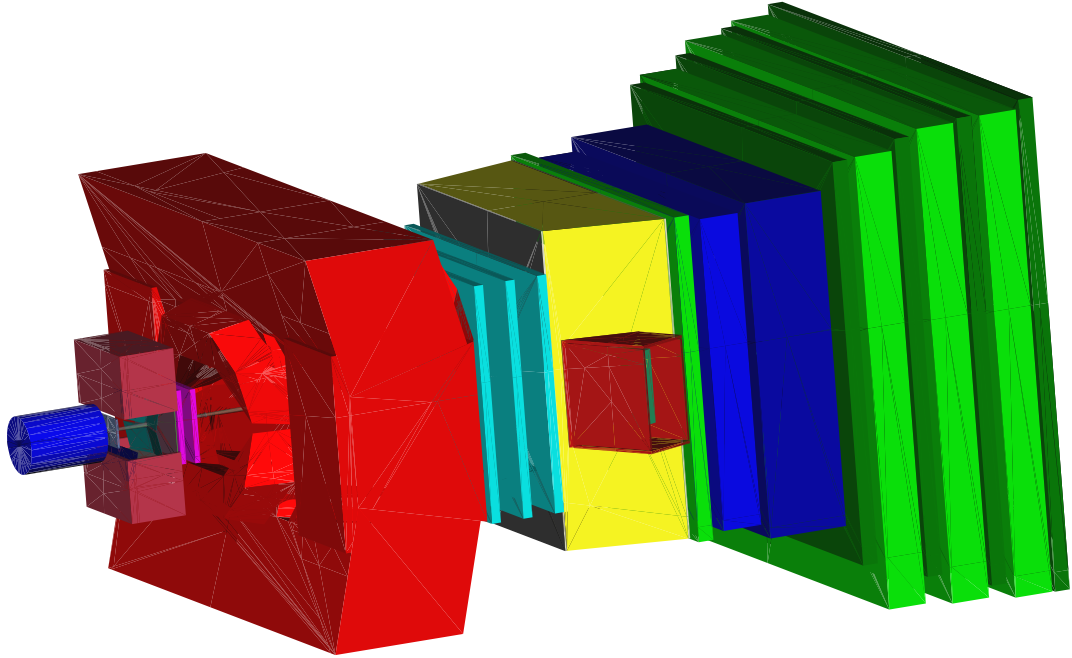


Figure 4.1: The LHCb detector visualised in PANORAMIX.

or in parallel with any application in the simulation and reconstruction sequence. In Chapter 6, the method of visualising tracks and hits will be explained. The visualisation plays an important role in the understanding of the detector and the data. Figure 4.1 shows a picture of the LHCb detector as seen by PANORAMIX.

An important service in the GAUDI framework, used by all applications, is the LHCb detector description [61]. It is designed to deal with all aspects of detector information about the detector, including geometry, materials, alignment, calibration, and controls. The database which describes the geometry of the detector is written in Extensible Markup Language (XML) [62]. It is a simple and flexible text format allowing for an easy conversion to the format needed by GEANT4. For this reason, the geometry description resembles the GEANT4 approach.

4.3 Event generation

The event generation programme simulates the physics processes in and right after the pp collisions in a bunch crossing. For the collisions in LHCb, PYTHIA version 6.2 is used. PYTHIA simulates all required event types, including minimum-bias, $b\bar{b}$ inclusive, and signal events. In the following, the pp collision processes in PYTHIA, the B production mechanisms and the final event building are discussed.

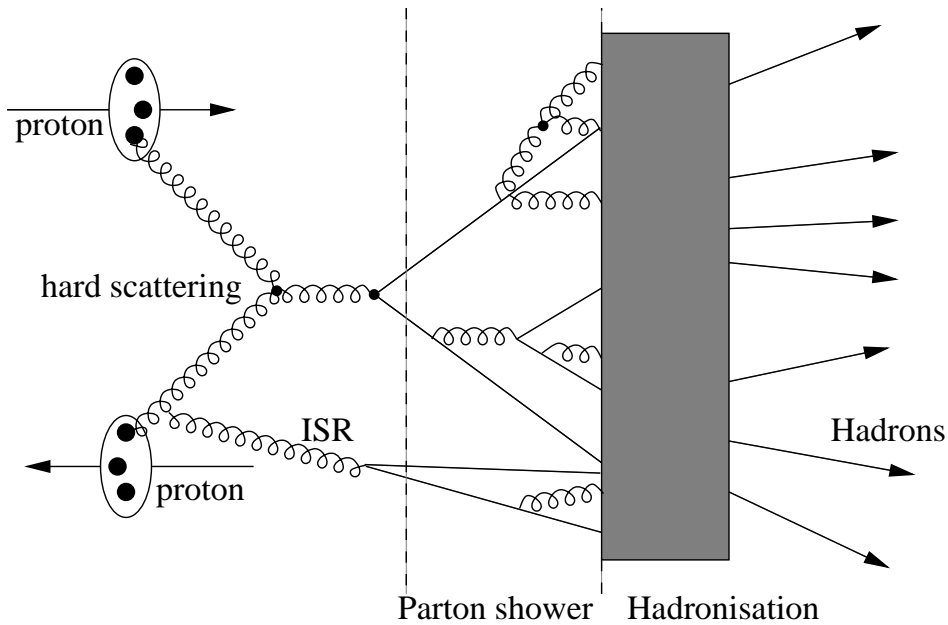


Figure 4.2: Schematic picture of a pp collision, including the initial state radiation (ISR), the hard scattering process, the parton shower, and the hadronisation.

4.3.1 Pythia

The PYTHIA event generator contains many aspects of which only a few are presented in this section. The majority of the processes during the pp collision are governed by QCD. PYTHIA includes short-distance, perturbative as well as many long-distance, non-perturbative QCD effects. Several models are used to account for the complex non-perturbative part, as e.g., the confinement of quarks and gluons (partons) inside the proton. The simulation of pp scatterings relies on the factorisation hypothesis: the inelastic pp collision is factorised into a hard scattering of the partons and the probability to find these partons inside the proton. In this way the non-perturbative confinement of the partons and the perturbative regime of QCD can be separated. The hard scatter determines many of the event characteristics. The full collision process can be divided into several steps, resembling the ordering in time (see Fig. 4.2):

- Two partons emerge from the protons in each of the beams, creating a hard interaction. This process is calculated with leading-order, QCD perturbation theory.
- Instead of calculating the next-to-leading order perturbative processes, the higher-order corrections are approximated in the parton-shower model. The leading-order process is modified by adding initial- and final-state parton showers to the hard parton-parton scattering.
- Besides the hard scattering of the initial partons, semihard interactions may occur between the other partons in the two protons. This process is described in PYTHIA

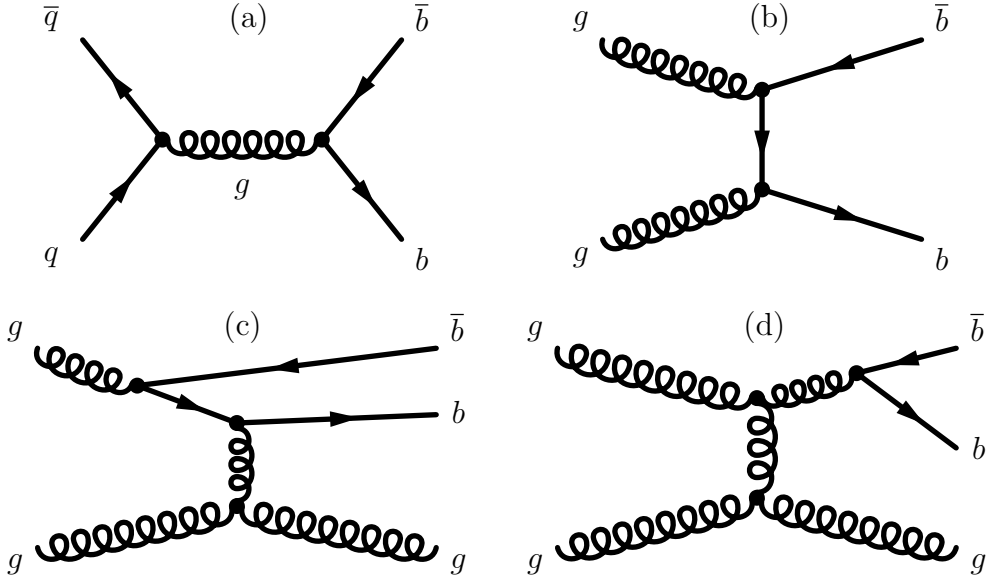


Figure 4.3: Examples of Feynman diagrams for B production. The two leading-order diagrams are pair creation through quark-antiquark annihilation (a) and gluon fusion (b). The next-to-leading order diagrams show examples of flavour excitation (c) and gluon splitting (d).

by the multiple interactions model (not shown in Fig. 4.2).

- Since the outgoing quarks and gluons are coloured, they cannot freely leave the interaction region: they must fragment to colourless hadrons. This fragmentation process has a phenomenological description, because perturbation theory breaks down as QCD becomes strongly interacting at the long-distance scale involved. By default, PYTHIA uses the Lund string fragmentation model [52].
- Finally, the produced hadrons that are unstable need to decay until only stable particles are left. The process of fragmentation and decay is commonly referred to as hadronisation.

4.3.2 B production

The processes in PYTHIA that contribute to $b\bar{b}$ production cross section can be summarised as follows [25]:

1. **Pair creation.** In these leading-order, hard $2 \rightarrow 2$ processes, the heavy flavours are produced by quark-antiquark annihilation ($q\bar{q} \rightarrow b\bar{b}$) and gluon fusion ($gg \rightarrow b\bar{b}$). The dominant contribution is from gluon fusion. Figure 4.3(a,b) shows two Feynman diagrams for these leading-order processes.
2. **Flavour excitation.** A virtual b quark from one of the protons is put on mass shell by the scattering with a parton from the other proton ($bq \rightarrow bq$ and $bg \rightarrow bg$). Since the b quark is not a valence quark, and thus comes from the sea, there must

Table 4.1: Contribution of the different B production processes in PYTHIA with at least one B in the LHCb acceptance.

Production process	Contribution (%)
(1) Pair creation ($q\bar{q}$ annihilation)	0.20 ± 0.04
(gluon fusion)	14.4 ± 0.4
(2) Flavour excitation	60.3 ± 0.5
(3) Gluon splitting	25.0 ± 0.4

be a \bar{b} quark from a previous branching $g \rightarrow b\bar{b}$. Likewise, the charge-conjugated process, with the b and \bar{b} interchanged, occurs with the same probability. Figure 4.3(c) gives a next-to-leading order Feynman diagram for flavour excitation.

3. **Gluon splitting.** Instead of in the hard scattering, the $b\bar{b}$ pair is created in a $g \rightarrow b\bar{b}$ branching in the initial- or final-state shower. A next-to-leading order Feynman diagram with a $b\bar{b}$ pair in final-state cascade is depicted in Fig. 4.3(d).

These processes are classified by the number of b and \bar{b} quarks involved the leading-order hard interaction, respectively 2, 1, and 0. It should be noted that in contrast with pair creation (1), where the production cross section is calculated with leading-order perturbation theory, the contributions from flavour excitation (2) and gluon splitting (3) to the $b\bar{b}$ cross section involve larger uncertainties, due to the uncertainties in the more phenomenological description. Simulations in PYTHIA with 14 TeV protons indicate [25], however, that flavour excitation and gluon splitting give significant contributions to the total $b\bar{b}$ cross section that cannot be neglected. As these production mechanisms lead to different kinematic distributions of the outgoing particles, it is important to include them in the simulation. Table 4.1 lists the contributions to the B production mechanism as simulated in PYTHIA.

After a pp collision most B mesons originating from the $b\bar{b}$ pair are expected to be emitted in the same forward (or backward) cone. This boost of the $b\bar{b}$ pair can be explained intuitively from the difference in momenta of the partons involved in the scattering. Each parton carries a fraction, x , of the total proton momentum. When the centre-of-mass energy of the pp collision increases, the momentum difference also increases, resulting in a larger boost of the $b\bar{b}$ pair in the detector frame towards $\sqrt{s} = 14$ TeV. Figure 4.4

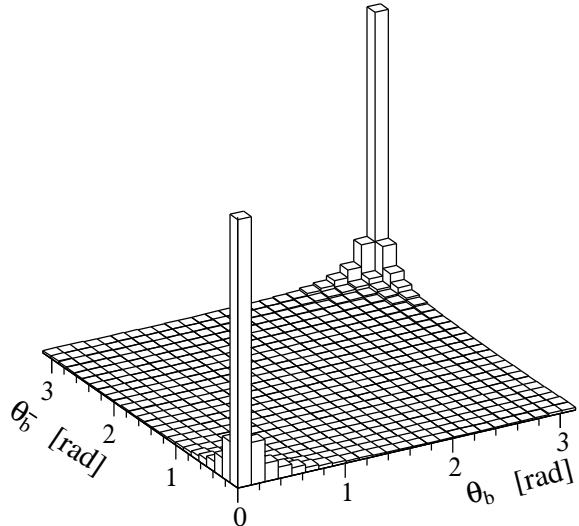


Figure 4.4: Correlation of the polar angles of the hadrons containing the b or \bar{b} quark at $\sqrt{s} = 14$ TeV.

shows the angular correlation of the produced B mesons in simulations with PYTHIA, motivating the choice to build LHCb as a forward spectrometer. About one third of the produced $b\bar{b}$ pairs decays within the acceptance of LHCb.

4.3.3 Multiple parton interactions

The other partons in the two colliding protons may cause additional, softer parton-parton interactions. This underlying event contributes to the observed particle multiplicity. The default multiple-parton interaction model (model 3) [63] in PYTHIA assumes varying impact parameters of the colliding protons and a Gaussian matter distribution inside the proton. The resulting particle multiplicity in this model is governed by a single parameter, $p_{T\min}$, as explained in the following.

The momentum transfer of the scattering partons determines the “hardness” scale of the interaction, conveniently expressed in terms of the transverse momentum, p_T , as measured in the detector. In a collision, the hardest parton interaction absorbs most of the available energy. The remaining partons have less energy at their disposal, corresponding to a lower p_T . In principle, the number of parton interactions can be calculated by taking out one parton at the time and adjusting the remaining available energy. However, the parton-parton cross section, σ_{part} , is divergent for $p_T \rightarrow 0$. The divergence can be regularised by introducing a cut-off, $p_{T\min}$, which is motivated by the fact that PYTHIA assumes partons to move freely, whereas, in reality, they are bound within the proton. A low- p_T parton cannot distinguish between the individual colour charges in the other proton. The cut-off is physically interpreted as the effective, inverse colour-screening distance.

The value of $p_{T\min}$ is tuned on the multiplicity of charged particles emerging from the collision. Figure 4.5(a) shows the average multiplicities at $\eta = 0^1$ measured by the UA5 and CDF experiments. The expected multiplicity at $\sqrt{s} = 14$ TeV is estimated from a quadratic fit in $\ln(s)$ [64] giving [26]

$$\left(\frac{dN_{ch}}{d\eta} \right)_{\eta=0} = 6.11 \pm 0.29 . \quad (4.1)$$

Figure 4.5(b) shows the corresponding $p_{T\min}$ values that reproduce these multiplicities in PYTHIA using the CTEQ4L [65] parton distribution functions and multiple interaction model 3. The energy dependence of $p_{T\min}$ can be described by a power law [66], resulting in

$$p_{T\min} = 3.47 \pm 0.17 \text{ GeV} , \quad (4.2)$$

at $\sqrt{s} = 14$ TeV. Simulations in PYTHIA with this value return an average charged particle multiplicity of

$$\left(\frac{dN_{ch}}{d\eta} \right)_{\eta=0} = 6.30 \pm 0.42 , \quad (4.3)$$

¹The pseudorapidity is defined as $\eta = -\ln[\tan \theta/2]$, where θ is the polar angle with respect to the beam axis.

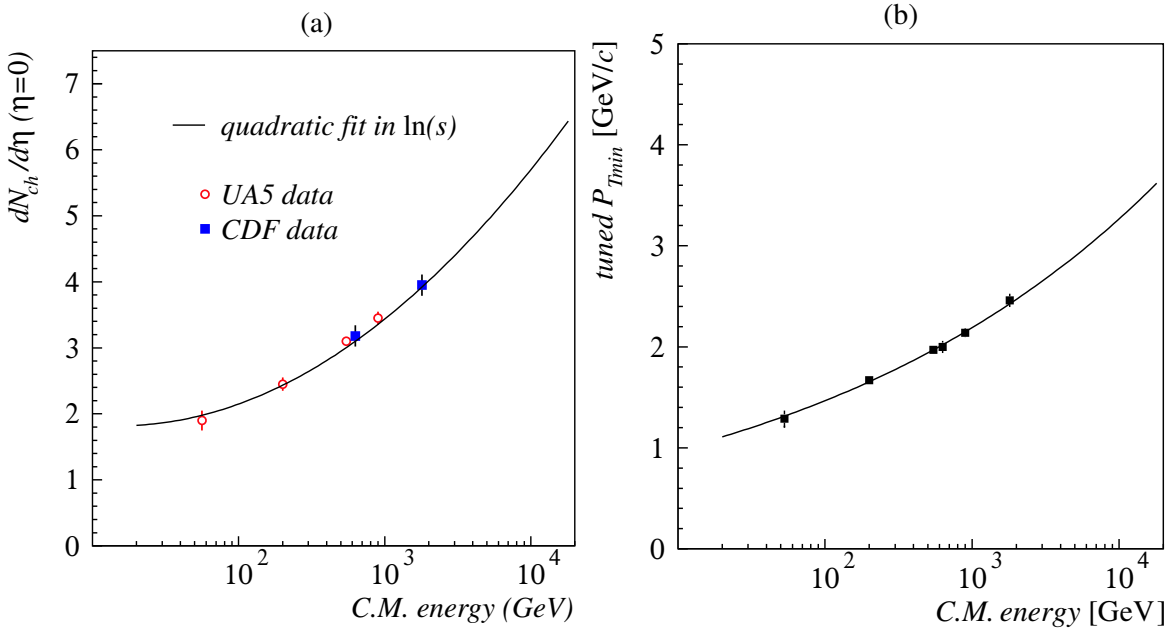


Figure 4.5: Charged particle density for inelastic, single collisions at $\eta = 0$ at the different collider energies at UA5 and CDF (a). And the tuned values for p_{Tmin} at these energies with a power law fit (b).

which agrees well with Eq. (4.1).

The parton-parton cross section that is obtained in PYTHIA with (4.2) is $\sigma_{\text{part}} = 550 \text{ mb}$, which is much higher than the total inelastic cross section of only 80 mb . Although this may seem like a contradiction, the ratio $\sigma_{\text{part}}/\sigma_{\text{inel}} = 6.9$ can simply be viewed as the average number of parton interactions in a proton-proton collision.

Figure 4.6 shows the charged particle density of inelastic, minimum-bias and $b\bar{b}$ inclusive collisions versus η with this tuning in PYTHIA. It can be seen that the central particle density in minimum-bias collisions reproduces roughly the expected value of Eq. (4.1).

The charged particle multiplicity in $b\bar{b}$ events is higher than in minimum bias. This is explained by the fact that events in which a $b\bar{b}$ pair is produced correspond to harder collisions. In Fig. 4.7, the multiplicity distributions of charged particles are depicted. On average, there are 58.6 ± 1.0 charged particles emerging from single collisions in minimum-bias of which there are 14.0 ± 0.3 inside the acceptance, while in $b\bar{b}$ inclusive collisions there are 139.7 ± 0.9 charged particles with 35.8 ± 0.3 inside the acceptance. As can be seen in Fig. 4.7(b), a large fraction ($\sim 32\%$) of the minimum-bias collisions does hardly produce particles in the acceptance of the detector. These collisions are mainly associated to elastic and soft diffractive pp collisions.

Besides the particle multiplicity, the transverse momentum of the emerging particles is another important kinematical parameter of the pp collision. Figure 4.8(a) shows the p_T spectrum for charged particles within the acceptance of the detector. Figure 4.8(b) shows only the highest p_T in the collision. Comparing the minimum-bias and $b\bar{b}$ inclu-

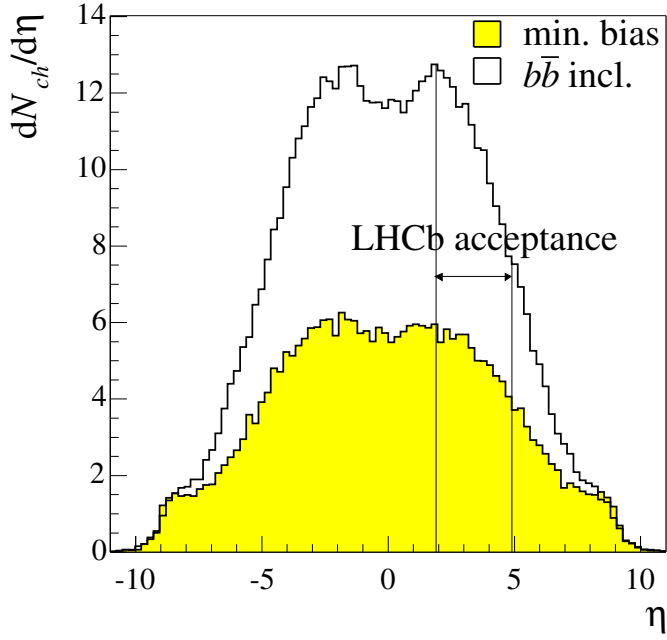


Figure 4.6: The charged particle density $dN_{ch}/d\eta$ versus η for inelastic minimum-bias and $b\bar{b}$ inclusive single collisions in PYTHIA. The vertical lines indicate the boundaries of the LHCb acceptance, covering the region $1.8 < \eta < 4.9$.

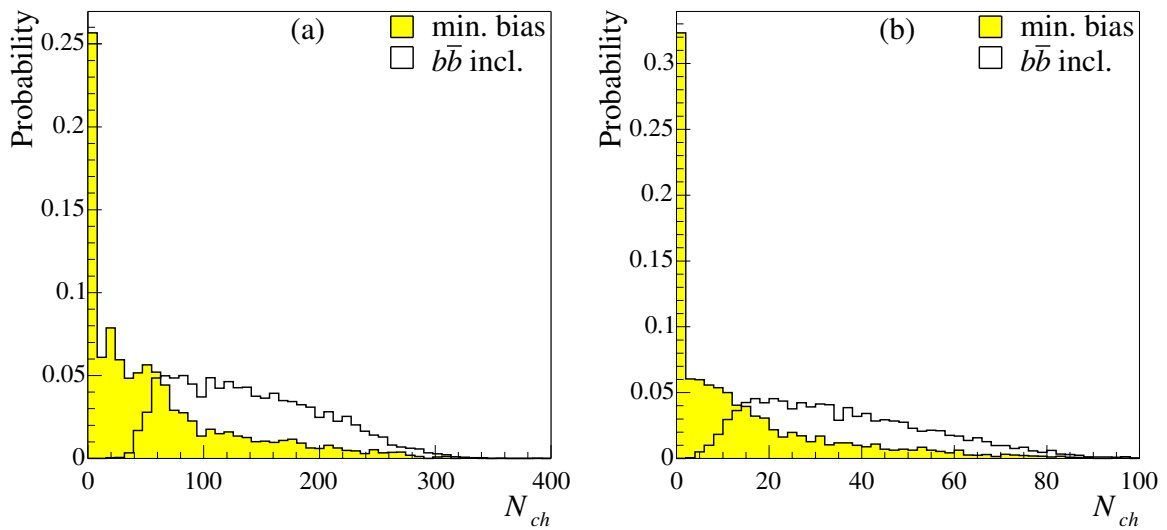


Figure 4.7: Charged particle multiplicity (N_{ch}) for minimum-bias and $b\bar{b}$ inclusive, single collisions in all directions (a), and only inside the LHCb acceptance (b).

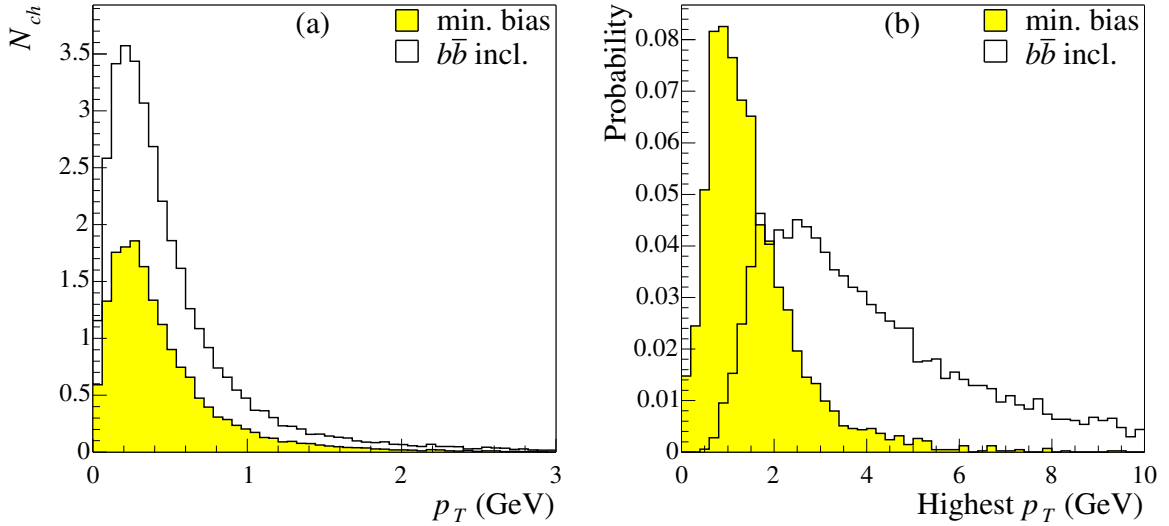


Figure 4.8: Transverse momentum (p_T) distributions for minimum-bias and $b\bar{b}$ inclusive collisions, for all charged particles in the LHCb acceptance (a) and for the one with the highest p_T in the collision (b).

sive collisions, it is clear that collisions with a high- p_T particle are more likely to have produced a $b\bar{b}$ pair. These high- p_T particles often correspond to the decay products of B hadrons. This feature is exploited in the trigger to select B events.

4.3.4 Fragmentation

At the final stage of the event generation, the outgoing, coloured quarks and gluons must hadronise to mesons and baryons. Up to this point, the PYTHIA settings are such that only minimum-bias events are generated. In order to obtain B events, the hard scattering process and parton shower evolution are repeated until a $b\bar{b}$ pair is produced. This approach is required to obtain a realistic underlying event structure, since the gluon splitting process, responsible for a significant fraction of the total B production, cannot be generated independently from the hard scattering.

For signal events, after the fragmentation of the $b\bar{b}$ pair, one B meson is selected to decay through the required B decay channel. This B meson is called the signal B . The other B meson, with the opposite b flavour, is called the opposite B , and is often used to determine (tag) the b flavour of the signal B . In signal events the b quark can be forced to hadronise in PYTHIA into the required B meson (B_d , B_u , B_s , etc.). The disadvantage of this “forced fragmentation” is that it does not consider the higher B resonances, which can also be used to tag the flavour of the signal B meson. For instance, the charge of the pion from the decays $B^{**+} \rightarrow B^{(*)0}\pi^+$ and $B^{**-} \rightarrow \bar{B}^{(*)0}\pi^-$ reveals the flavour of the B meson. A better approach is to allow the b quarks to hadronise via a higher B resonance, so that this tagging method can be studied. This means that the string fragmentation has to be repeated until — possibly through the B^{**} decay — the

required B meson is produced. This approach is referred to as “repeated hadronisation”, as opposed to forced fragmentation.

After the fragmentation, an acceptance cut is applied to signal events. Only events in which the angle of the signal B meson with respect to the positive z axis is less than 400 mrad are retained. This step saves processing time in the subsequent applications, because B mesons that decay outside the LHCb acceptance cannot be reconstructed. Events with B mesons travelling in the backward direction can be recycled after reversing the flight direction of all particles. This means that the z components of all momentum vectors are negated, before the acceptance cut is again applied. The fraction of events with the signal B meson inside the forward acceptance is $\varepsilon_\theta = (34.71 \pm 0.03)\%$, independent of the B meson type. This number is used in the calculation of the total selection efficiencies for the B decay channels (see Chapter 7). In case of $b\bar{b}$ inclusive events only one of both b hadrons needs to satisfy the acceptance cut. For these events a higher efficiency is found: $\varepsilon_\theta = (43.21 \pm 0.04)\%$. In case of minimum-bias events, no acceptance cut is applied.

4.3.5 B decay simulation

Since the decay of the B mesons in signal events is studied in detail, an accurate description of these decays is important. In LHCb, EVTGEN takes care of the simulation of the produced B meson into the desired B decay channel. This dedicated programme describes the physics processes relevant to B decays, using the actual decay amplitudes. It implements, for instance, the mixing of neutral B mesons, sequential decays, angular correlations, and time-dependent CP asymmetries. The resulting kinematic distributions have been verified [53] to correctly describe the observed data from different experiments.

4.3.6 Pile-up and spill-over

Multiple pp collisions in the same bunch crossing are referred to as pile-up (see also Chapter 3). They are simulated by running PYTHIA for each collision. The number of collisions per beam crossing is governed by a Poisson distribution with a mean of $\bar{n}_{pp} = 0.67$ as given by Eq. (3.2) using the total cross section $\sigma_{\text{tot}} = 100$ mb. Bunch crossings without any pp collision do not contribute to the minimum-bias sample. These ineffective bunch crossings amount to a fraction of $e^{-\bar{n}_{pp}} = 0.51$ of the total number of bunch crossings. Hence, the average number of collisions in a sample of minimum-bias events that have at least one collision is

$$\bar{n}_{pp}^{\text{mb}} = \frac{\bar{n}_{pp}}{1 - e^{-\bar{n}_{pp}}} = 1.37 \quad . \quad (4.4)$$

On the other hand, the situation for events with a cross section much smaller than the total cross section (e.g., $\sigma_{b\bar{b}} \ll \sigma_{\text{tot}}$) is different. The amount of pile-up increases because the probability to produce a rare event increases with the number of collisions. Hence, given an event with a rare process, it is likely that it has more pp collisions than a

minimum-bias event. Since the total cross section hardly changes when adding a rare process, such as B production, the probability that a rare process occurs is independent from the much more frequent pile-up collisions. In other words, given a rare $b\bar{b}$ collision, the number of pile-up collisions is equal to the number of collisions without a $b\bar{b}$ pair. Thus, the average number of pp collisions in $b\bar{b}$ events is

$$\bar{n}_{pp}^{b\bar{b}} = 1 + \bar{n}_{pp} = 1.67 . \quad (4.5)$$

Another effect which should be taken into account is spill-over. After 25 ns — the time between two bunch crossing — slow particles may still generate hits in the detector. In addition, some subdetectors require a readout window larger than 25 ns to be able to collect all the signals of that event. For instance, the maximum drift time in the Outer Tracker exceeds the 25 ns. These two so-called spill-over effects are simulated by adding bunch-bunch collisions with offsets at $t = -50$ ns, -25 ns, corresponding to the two previous bunch crossings, and at $t = +25$ ns, corresponding to the subsequent bunch crossing. The average number of pp collisions in each spill-over bunch crossing is $\bar{n}_{pp} = 0.67$. Both the spill-over and pile-up are regarded as background in the detector.

Finally, the positions of all primary interactions, including pile-up and spill-over, are smeared due to the extended size of the beam spot. Hereby, the interaction region obtains a Gaussian spread of $\sigma_x = \sigma_y = 70 \mu\text{m}$ and $\sigma_z = 5 \text{ cm}$ according to the LHC beam specifications.

4.4 Detector simulation

After event generation, the particles evolve in the detector. In this simulation, three physical processes can be distinguished, namely: (1) passage of particles through matter, (2) bending of the charged particles in the magnetic field, and (3) decay of the remaining unstable particles (e.g., K_S^0). The GEANT package consists of a set of algorithms simulating these processes. The algorithms are executed by the GAUSS application which controls the specific parameter settings for LHCb. In the detector simulation, the most complex part is the description of the passage of particles through matter. After an introduction to GEANT, the theory behind these material interactions is briefly reviewed in this section.

4.4.1 Geant

In GEANT, the passage through material is described by a large number of physical processes, covering a wide energy range for many types of particles. The final result of the GEANT simulation are hits, which are defined by the intersections of the particles with the sensitive parts of the detector. These hits are the starting point for the subsequent step in the simulation chain, namely the digitisation programme, discussed in the next chapter.

GEANT also deals with the interaction of the particles with the magnetic field. In a uniform field in vacuum, the trajectory of a charged particle can be represented by a

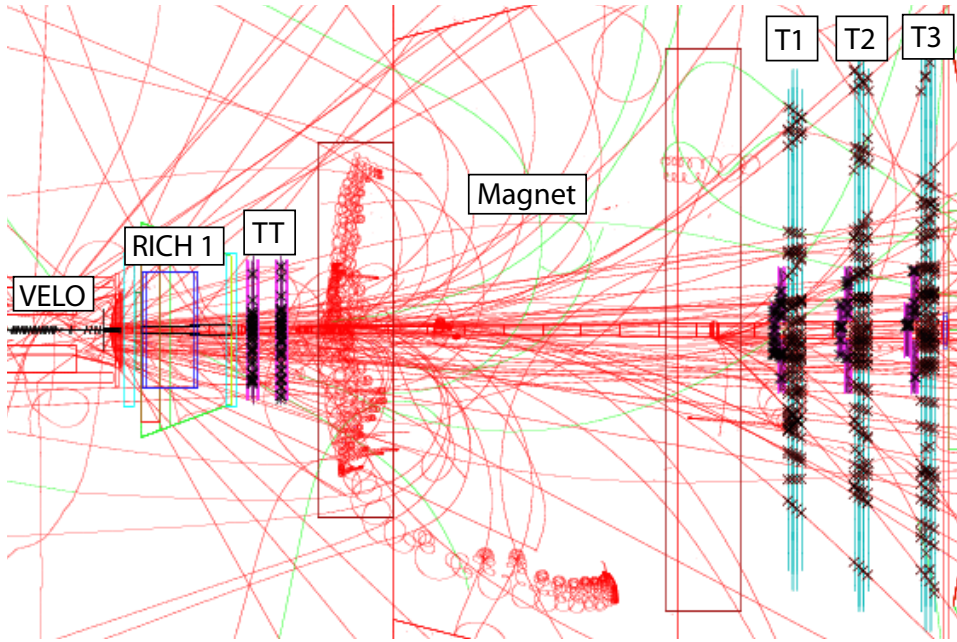


Figure 4.9: GEANT event display showing the trajectories of the charged particles in the tracking system of LHCb.

helix. However, the LHCb magnetic field is highly non-uniform (see Fig. 3.6). In this case, GEANT applies the method of Runge-Kutta integration [67] to solve the equation of motion numerically. By default, a fourth order Runge-Kutta method is used.

Figure 4.9 displays a typical GEANT simulation event in the tracking system of LHCb. It shows the trajectories of charged Monte Carlo particles. In the magnet region their curvature is clearly visible. The deposited hits are depicted as crosses in the sensitive tracker volumes.

The GEANT description can be adjusted for each subdetector separately. Naturally, the shower evolution in the calorimeters requires a different physical description than the simulation of Cherenkov photons in the RICH. The parameter settings can be modified for each detector region and for each material individually.

The simulation computing time can be reduced by introducing energy cut-offs. Particles with an energy below the threshold are then discarded. It has been shown [68] that many secondary, low-energy particles have no effect on the occupancy in the tracking stations. Accordingly, the threshold in the tracking stations is set to 10 MeV for hadrons and muons, and to 1 MeV for photons and electrons.

4.4.2 Passage of particles through matter

As a particle passes through a medium, it interacts with the atoms inside this medium. Most of these interactions are electromagnetic, thus only affecting charged particles. For high-energy particles, these phenomena are characterised depending on the distance of

closest approach to the atoms:²

- When the distance is large compared to the atomic radius, the particle reacts with the atom as a whole. This results in atomic excitation and ionisation.
- When the distance is of the order of the atomic radius, the particle interacts with the individual electrons. In this “knock-on” process, these electrons are ejected from the atom and form δ -rays which traverse the medium.
- When the distance is smaller than the atomic radius, the particle interacts with the electromagnetic field of the nucleus, causing a deflection of the particle’s trajectory. This phenomenon is called Coulomb scattering, or—when there is more than one—multiple scattering. If the traversing particle is an electron, it also loses energy due to bremsstrahlung. If it is a photon, pair production is the dominant process.
- When the distance is of the order of the nuclear radius, a nuclear interaction occurs. Similar to the pp collisions discussed in the previous section, this QCD process creates secondary particles.

Another type of particle interaction is Cherenkov radiation, which is associated to interaction with the bulk structure. This process does not contribute significantly to the energy loss, but is exploited in particle identification devices. Generally, particle detectors exploit the variety of interactions of particles with material. For example, tracking detectors use ionisation to measure the positions along the particle’s trajectory, electromagnetic calorimeters use the electromagnetic interaction (bremsstrahlung and pair production) to measure the energy of electrons and photons, and hadronic calorimeters use the nuclear interaction to measure the energy of hadrons.

In the context of this thesis, the focus is mainly on the physical processes important in tracking detectors, namely energy loss and multiple scattering. Finally, nuclear interactions, responsible for the total absorption of particles, are briefly discussed.

Energy loss

The main source of energy loss for relativistic, charged particles is ionisation. The energy loss per unit of distance is called the stopping power and is well described by the Bethe-Bloch equation [8],

$$-\frac{dE}{dx} = 4\pi N_A r_e^2 m_e c^2 z^2 \frac{Z}{A} \frac{1}{\beta^2} \left[\frac{1}{2} \ln \frac{2m_e c^2 \beta^2 T_{\max}}{(1 - \beta^2) I^2} - \beta^2 - \frac{\delta}{2} \right] , \quad (4.6)$$

in which N_A is Avogadro’s number, r_e the classical electron radius, m_e the electron mass, z the particle’s charge in units of e , Z the atomic number of the material, A the atomic mass, T_{\max} the maximum energy transfer in a collision, I the mean excitation potential and δ the correction for the density effect. Conventionally, dE/dx is expressed in energy per unit of distance per unit of density ($\text{MeV g}^{-1} \text{ cm}^2$). In Fig. 4.10, the energy loss rate

²A detailed introduction to this field can be found in Ref. [69].

as a function of the momentum of the particle is shown. When the momentum increases, it can be seen that the energy loss rate rapidly decreases as β^{-2} towards a minimum, before rising logarithmically. The energy loss rate of most relativistic particles is close to this minimum (about $2 \text{ MeV g}^{-1} \text{ cm}^2$). Therefore, those particles are referred to as minimum ionising particles (mip's).

The number of ionisations, and hence the amount of energy loss, depends much on the density of the material. For example, in gas a charged particle produces 2–4 primary ionisations per millimetre, while in silicon it produces 8×10^4 primary ionisations per millimetre. The Bethe-Bloch formula (4.6) describes the mean energy loss for a particle passing through material. The actual energy loss in individual collisions has statistical fluctuations, which are usually modelled by a Landau distribution. In Fig. 4.11 the energy loss distribution in GEANT of 1 GeV pions passing through the $220 \mu\text{m}$ thick VELO sensors is shown. The ionisations towards high ΔE in the tail of the distribution produce knock-on electrons (δ rays), which can have enough kinetic energy to produce secondary ionisations. For a gas, the number of secondary ionisations is 2–3 times that of the primary ionisations.

For high-energy electrons (above 100 MeV in carbon) the dominant contribution to energy loss is not ionisation, but bremsstrahlung. This effect, however, is not limited to electrons and positrons. All charged particles lose energy by bremsstrahlung, but for muons and hadrons it only becomes significant at energies in the TeV range. For electrons in the energy range of high-energy physics experiments, however, it is the dominant energy loss mechanism, since the transferred energy is inversely proportional to particle's mass squared. The energy loss for electrons is given by

$$-\frac{dE}{dx} = \frac{E}{X_0} , \quad (4.7)$$

where X_0 is the radiation length. The radiation length is a typical quantity for each material and is tabulated in Ref. [8]. For example, the radiation length in carbon is $X_0 = 18.8 \text{ cm}$ and in silicon $X_0 = 9.36 \text{ cm}$. Solving this differential equation, it follows

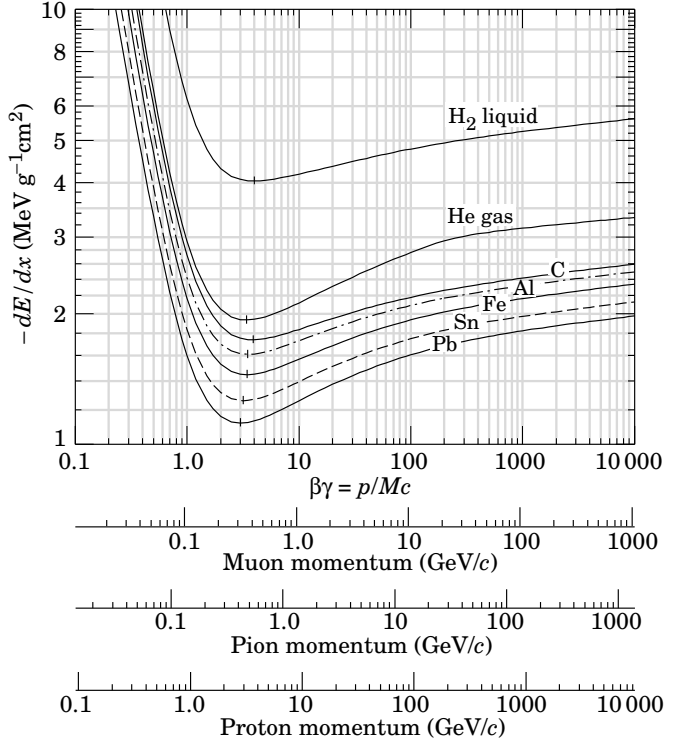


Figure 4.10: The energy loss rate for different materials as a function of the momentum. Figure taken from Ref. [8].

where X_0 is the radiation length. The radiation length is a typical quantity for each material and is tabulated in Ref. [8]. For example, the radiation length in carbon is $X_0 = 18.8 \text{ cm}$ and in silicon $X_0 = 9.36 \text{ cm}$. Solving this differential equation, it follows

that the energy decreases exponentially as a function of the distance traversed in the medium.

The energy loss due to bremsstrahlung has a significant effect on the mass resolutions in the reconstruction of B decay channels containing $J/\psi \rightarrow e^+e^-$. Fortunately, some of the missing energy can be recovered with bremsstrahlung photons found in the electromagnetic calorimeter [70].

A process related to bremsstrahlung is photon conversion ($\gamma \rightarrow e^+e^-$), also referred to as pair production. However, in contrast to bremsstrahlung, where the electron loses only a fraction of its energy, the photon is lost completely after conversion. In the reconstruction, some of the converted photons can be recovered using the e^+e^- pair. This is the case when the conversion occurred behind the magnet, because then the e^+e^- pair is still detected as a single cluster in the electromagnetic calorimeter.

Pair production is the main source of photon attenuation above a few tens of MeV. As pair production is governed by a Feynman diagram similar to that of bremsstrahlung, the characteristic mean free path for a photon is equal to $\frac{7}{9}X_0$. In Chapter 7, the reconstruction of photons and neutral pions ($\pi^0 \rightarrow \gamma\gamma$) is used in the reconstruction of $B_s^0 \rightarrow D_s^{(*)\mp} K^{(*)\pm}$ decays.

Multiple scattering

Multiple scattering is the result of many Coulomb scatterings off nuclei in a medium, thereby causing a deflection from the particle's original trajectory. Generally, multiple scattering is described in terms of the Molière–Bethe formalism [71]. This theory very accurately describes both small-angle scatterings as well as large-angle scatterings. Note that GEANT4 implements a more detailed model [55] for multiple scattering, slightly different from the Molière–Bethe formalism.

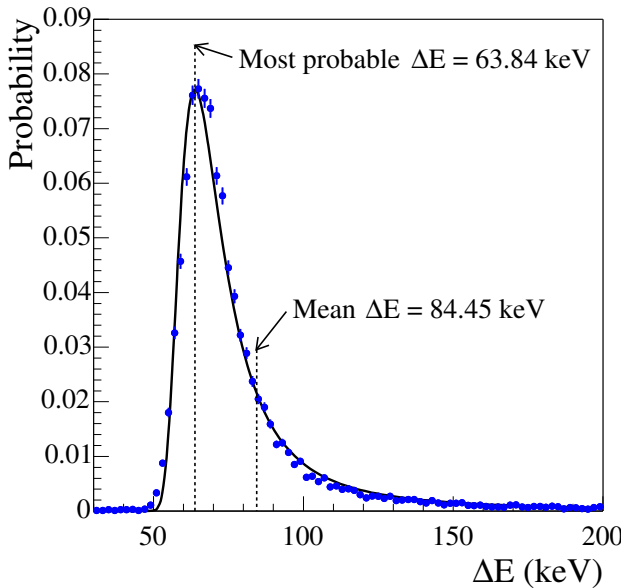


Figure 4.11: Energy loss (ΔE) distribution of 1.0 ± 0.1 GeV pions in the $220\text{ }\mu\text{m}$ thick silicon sensors of the VELO. A Landau curve is fitted with a most probable ΔE of (63.84 ± 0.06) keV and a width of (4.68 ± 0.04) keV. The mean ΔE for 99% of the pions equals 84.45 keV. Using the silicon density of $\rho = 2.33\text{ g cm}^{-3}$, this corresponds to a stopping power of $1.65\text{ MeV g}^{-1}\text{ cm}^2$.

Table 4.2: The material thickness d in terms of radiation lengths (X_0) and interaction lengths (λ_I) for the different subdetectors.

Subdetector	d/X_0 (%)	d/λ_I (%)
VELO	15.8	3.8
RICH 1	7.6	3.1
TT	3.5	1.1
Air in magnet	1.6	0.7
IT/OT	13.2	3.3
Total before RICH 2	41.7	12.0
RICH 2	12.4	4
SPD/PS	200	10
ECAL	2500	110
HCAL	-	560
Muon	-	2000

About 98% of the deflections can be modelled by a Gaussian distribution, thereby ignoring the tails. A Gaussian fit to the Molière angular distribution [72, 73] results in a standard deviation in the two-dimensional plane of

$$\theta_0 = \frac{13.6 \text{ MeV}}{\beta cp} z \sqrt{\frac{x}{X_0}} \left[1 + 0.038 \ln \frac{x}{X_0} \right] \quad . \quad (4.8)$$

This indicates that a 13.6 GeV particle has an average scattering of 1 mrad in one X_0 of detector material. In Chapter 6, the effect of multiple scattering in track reconstruction will be discussed.

Nuclear interactions

A nuclear interaction of a particle in a medium typically result in the creation of secondary particles. Often, the original particle is lost for detection. In GEANT different nuclear interaction models (i.e., physics lists) can be applied. The nuclear interaction length, λ_I , is the mean free path for hadrons and is related to the inelastic cross section. This parameter is commonly used in calorimetry to specify the absorption thickness of a material.

In the reoptimisation process [26, 50], it was shown that a number of detection planes (stations) could be removed without losing the ability to reconstruct the particles' trajectories. In addition, lighter materials were introduced in the design of, e.g., the beam pipe and the RF foil. This resulted in less particles being absorbed before or inside the tracking system. These particles would otherwise be lost for track reconstruction. In the reoptimisation process the total amount of material before RICH 2 was decreased from 20% of λ_I (60% of X_0) to 12% of λ_I (40% of X_0). Table 4.2 summarises the optimised thicknesses of the subdetectors in fractions of X_0 and λ_I . The optimisation improved the reconstruction efficiency for many B decays, in particular for the ones with many

final-state particles, because for each particle a factor $e^{\Delta\lambda_I}$ is gained. For example, the reoptimisation added 38% of statistics in the $B_s^0 \rightarrow D_s^\mp K^\pm$ channel, which has four particles in the final state. Moreover, a lower material budget evidently results in less multiple scattering and less energy loss (especially for electrons).

Chapter 5

Outer Tracker simulation

For a realistic event simulation in GEANT, an accurate description of the detector geometry is mandatory. Hence, the entire LHCb detector is modelled in detail in the simulation software. As explained in the previous chapter, GEANT uses this description to determine the interactions of the particles with the material and to locate the hits in the sensitive parts of the detector.

As a consequence of the use of different detector technologies, each subdetector in LHCb has its own dedicated digitisation programme, handling the response of the electronics to the traversing particles. The digitisation is the final stage of the simulation.

Here, in this chapter, the focus is on the simulation in the Outer Tracker (OT). First, in Section 5.1 the detector description is presented, including the geometry and the material distribution. Next, the particle and hit distributions in the OT stations, as a result of the GEANT simulation with the detector material, are discussed in Section 5.2. Then, in Section 5.3 the digitisation processes that are of influence to the detector performance are explained. Finally, in Section 5.4 the expected performance and hit occupancy of the detector are presented.

5.1 Detector description

Although simplified, the OT geometry description [74] follows as much as possible the actual design as explained in Section 3.6. Details about the technical design can be found in Ref. [34]. In this section, the geometry, as used in the software, is presented. Figure 5.1 displays a picture of the OT geometry, including the IT, TT, and beam pipe. The OT is described within the GAUDI detector description framework [61]. The location of the sensitive elements and the distribution of material is an important input for the GEANT simulation. Furthermore, this detector description is also used by the OT digitisation and reconstruction.

Figure 5.2 displays the modules and shows the numbering scheme of the readout in an OT station. As shown, the long modules are split in an upper and lower part to distinguish between the readout channels on the top and on the bottom of the long modules. The length of the short modules above and below the IT cross is chosen such that there is a small overlap between the sensitive detection volumes of the IT and

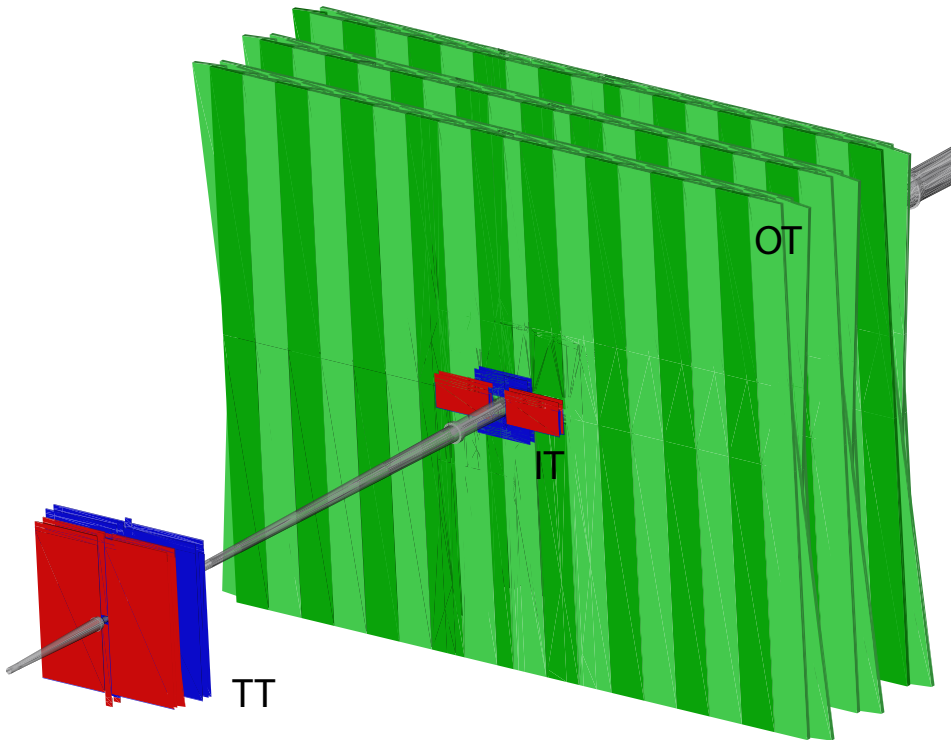


Figure 5.1: A PANORAMIX picture of the Outer Tracker including the Inner Tracker, Trigger Tracker, and beam pipe.

OT. This will facilitate the relative positioning and alignment of the OT detector with respect to the IT detector. Figure 5.3 shows the sensitive overlap in T1.

All material in the OT is located inside the modules. In the simulation a module is composed of three layers: a gas volume sandwiched between two panels (cf. Fig. 3.13). The gas volume, where the straws are located, is the sensitive part of the module. These sensitive volumes are used to inform GEANT to record the corresponding intersections of charged particles. The two enclosing, passive layers are the panels. They account for all material in the module. The panel material is described as a single fictitious mixture that includes contributions from the side panels, the straws, the wires, and of course the panels themselves. In terms of radiation (interaction) lengths, this mixture amounts to a total thickness of 3.0% (1.09%) per station. To simplify the detector description, the support structure and readout electronics, which are located outside the acceptance of LHCb, are not included in the simulation. Table 5.1 lists the main OT geometry parameters.

The individual straws are not described in the geometry database used in the GEANT simulation. Their contribution to the material budget is already taken into account in the panels. Nevertheless, the OT digitisation needs to determine which wires have actually been hit and the corresponding drift distances. The GAUDI detector description provides the possibility to define additional functionalities [75], which are able to address these detector-specific questions. These functionalities are used, for example, by the OT

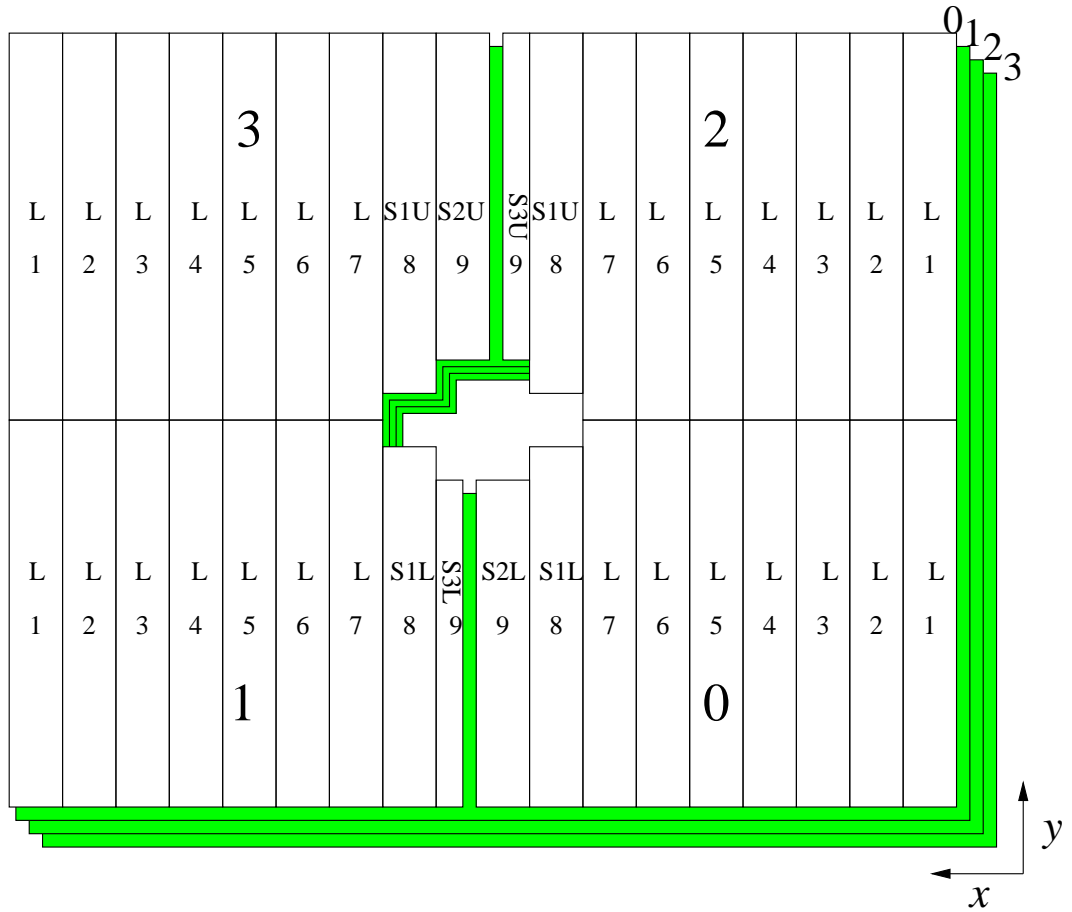


Figure 5.2: Module numbering scheme of the OT readout in the first x layer (layer 0). Also the layer and quarter numbering are drawn. Layer 1 has exactly the same module layout; however, in layer 2 and 3 the S2 and S3 modules are interchanged. The gap between the S2 and S3 modules is drawn to illustrate the boundary between the detector halves. The z axis is pointing into the paper, following a right-handed coordinate system.

digitisation algorithms, which will be described in Section 5.3. It is possible to include also the straws in the GEANT simulation. It would allow, e.g., an alignment of each straw individually. The price to pay, however, would be a slower simulation programme. In the current programme, it is not foreseen to align the individual straws; only the modules.

Not only is the detector description used in the GEANT simulation and in the digitisation, but also in the reconstruction. The use of the detector description in the track reconstruction will be explained in Chapter 6. The particle distributions resulting from the GEANT simulation and the digitisation procedure are discussed in the following sections.

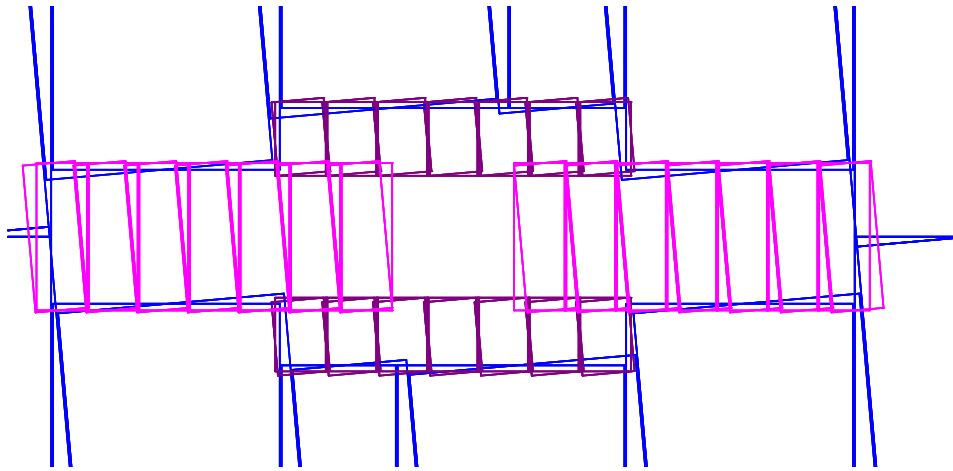


Figure 5.3: Picture of sensitive overlap in T1 between the IT and OT showing layers 0 and 1.

Table 5.1: The main OT geometry parameters.

Geometry parameter	Value
Straw pitch	5.25 mm
Straw cell size	5.0 mm
U stereo angle	-5°
V stereo angle	+5°
Readout modules per layer	36
Straws in standard module	128
Straws in S3 module	64
Total OT readout channels	52224
Module length (L)	4810 mm
Module length (S1)	2335 mm
Module length (S2,S3)	2243 mm
Module width (L,S1,S2)	338.625 mm
Module width (S3)	170.625 mm
Space between modules in x layers	2.625 mm
T1 central z position	7938 mm
T2 central z position	8625 mm
T3 central z position	9315 mm
Station thickness in X_0	3.0%
Station thickness in λ_I	1.09%

Table 5.2: Number of primary (N_{prim}), secondary (N_{sec}), and all particles (N_{all}) per event crossing T1, and the fraction (f_{prim}) of primary particles. Pile-up collisions are included (but no spill-over), and only charged particles are counted.

Events	Detector	N_{prim}	N_{sec}	N_{all}	$f_{\text{prim}}(\%)$
min. bias	IT	5.04 ± 0.07	6.58 ± 0.07	11.6 ± 0.1	43.4 ± 0.4
	OT	10.1 ± 0.1	20.5 ± 0.1	30.6 ± 0.2	33.0 ± 0.3
$b\bar{b}$ incl.	IT	10.8 ± 0.1	15.7 ± 0.1	26.5 ± 0.2	40.6 ± 0.3
	OT	23.1 ± 0.2	50.1 ± 0.2	73.2 ± 0.3	31.6 ± 0.2

5.2 Particle distributions

Armed with the material description in LHCb, GEANT simulations provide the expected particle and hit distributions in the detector. The most relevant quantities for the OT are the total number of charged particles traversing the T stations, the fraction of particles coming directly from the pp collision, their momentum distribution, and the resulting hit distributions. Since neutral particles do not create hits in the tracking stations, they are not considered in the detector response.

In the GEANT simulation, special care is taken for the creation of δ -rays in the energy loss process in the OT. In reality, these low-energy electrons would be stopped when traversing the straw tube walls inside a double layer. In the simulation, however, there is only gas in the sensitive volume where the straws are residing. In the absence of straws, δ -rays can travel much further, thereby artificially increasing the hit multiplicity. For this reason the energy loss in the material is simulated in GEANT without the explicit creation of δ -rays, but with the fluctuations in the energy loss of the original particle caused by the emission of δ -rays.

In Fig. 5.4 the spatial distribution of charged particles reaching T1 is shown. Towards the origin the particle flux increases, which justifies the choice for a detector with a higher granularity in this region: the IT. The central region of high particle flux is stretched along the x axis, because the magnetic field sweeps charged particles mainly in the horizontal plane.

Particles coming directly from a pp collision are referred to as primary particles. The ones created in a nuclear interaction with detector material are referred to as secondary particles. Table 5.2 gives the number of primary and secondary particles reaching T1. The other two stations, T2 and T3, show similar numbers. In general, the OT detects more than twice as many particles — both primary and secondary — as the IT. On the other hand, the IT covers only $\sim 1\%$ of the total detector area of T1. The number of primary particles reaching the T stations is about 15 for minimum-bias events and 34 for $b\bar{b}$ inclusive events. This number roughly correspond to the number of tracks that can be reconstructed in both the VELO and the T stations. Chapter 6 explains how most of these tracks are found and reconstructed.

Most particles that cross T1 are created in a secondary interaction. Only about

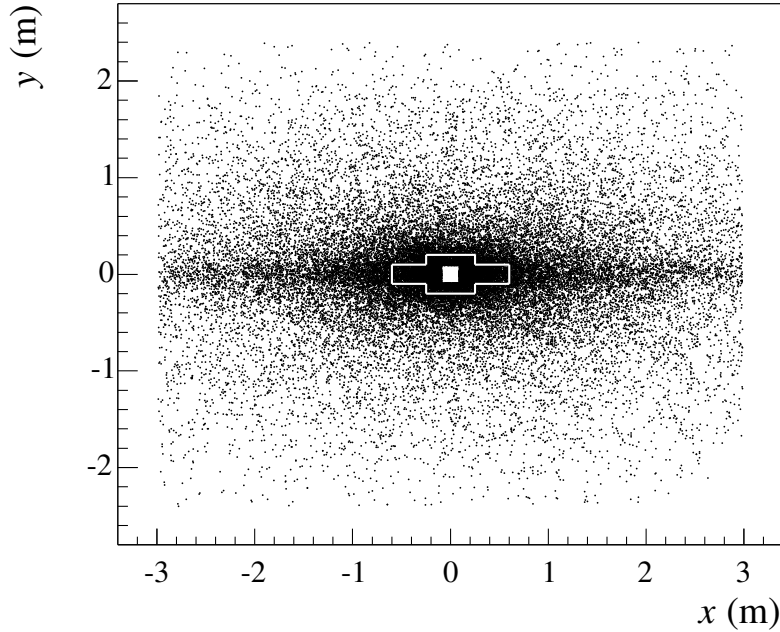


Figure 5.4: Spatial distribution of charged particles crossing T1, integrated over a large sample of events. The cross-shaped boundary between the IT and OT is indicated in white. Note the higher particle flux towards the beam axis.

Table 5.3: Average momentum of primary, secondary, and all particles crossing the IT and OT section of T1 for minimum-bias events and $b\bar{b}$ inclusive events.

Events	Detector	$\langle p_{\text{prim}} \rangle$ (GeV)	$\langle p_{\text{sec}} \rangle$ (GeV)	$\langle p_{\text{all}} \rangle$ (GeV)
min. bias	IT	22.7 ± 0.2	6.8 ± 0.1	13.7 ± 0.1
	OT	7.43 ± 0.08	2.17 ± 0.03	3.90 ± 0.03
$b\bar{b}$ incl.	IT	23.6 ± 0.2	7.9 ± 0.1	14.2 ± 0.1
	OT	7.76 ± 0.05	2.66 ± 0.02	4.27 ± 0.02

one third originates directly from a primary pp collision. The IT has a slightly higher fraction of these primary particles. This can be explained by the higher momentum of primary particles with respect to secondary particles. Low-momentum particles created in secondary interactions before the magnet are swept outside by the magnetic field and are thus more likely to cross the OT. The momentum distribution of charged particles in $b\bar{b}$ inclusive events is depicted in Fig. 5.5. The mean momentum in minimum-bias and in $b\bar{b}$ inclusive events is given in Table 5.3. The average momentum in the IT is almost three times as high as in the OT. The B decay products in $b\bar{b}$ inclusive events give rise to a slight increase in the average momentum compared to minimum-bias events (cf. Fig. 4.8).

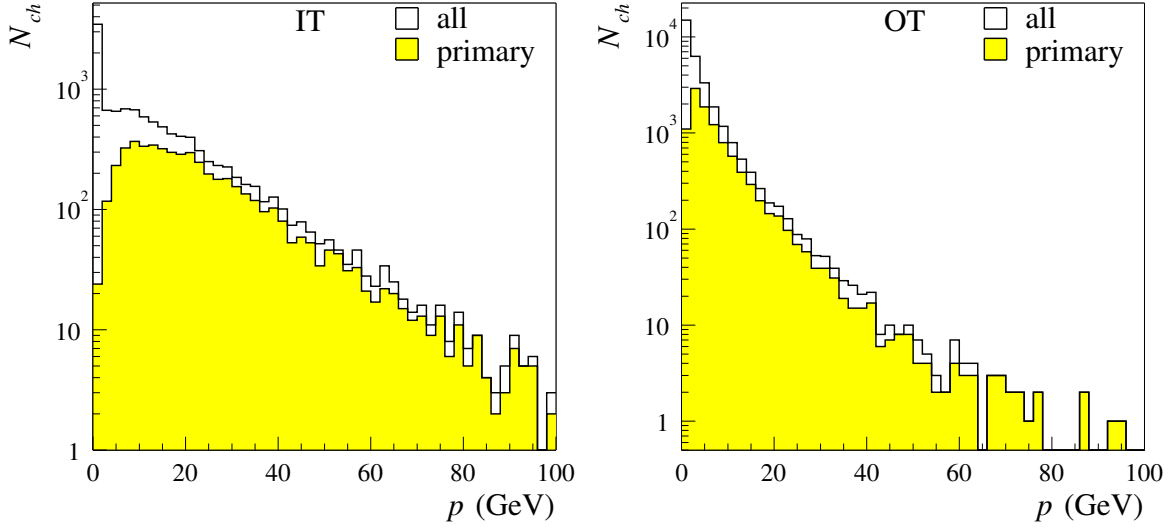


Figure 5.5: Momentum distribution of all (primary) charged particles leaving hits in the IT and OT section of T1 in bb inclusive events. Clearly, the average momentum in the IT is much higher than in the OT. The peak at $p \rightarrow 0$ in the IT spectrum for all particles is due to low-momentum particles coming from secondary interactions with the beam pipe.

5.3 Detector response

After the GEANT simulation, the detector response is simulated by dedicated digitisation algorithms. The OT detector response has been investigated extensively in test beam experiments using several module prototypes [36, 38, 76]. In this section, the observed performance parameters are used in the GAUDI digitisation programme. First, a general overview of the OT digitisation in the GAUDI framework is presented. Thereafter, the simulated detector response is discussed. Detailed information on the OT digitisation can also be found in Refs. [74, 77].

5.3.1 General overview

The OT digitisation process is part of the digitisation application BOOLE [56]. The starting point are the intersections of the particles with the OT modules. From this, the OT digitisation determines which wires are hit, the corresponding readout channels, and TDC times. Figure 5.6 gives an overview of the data flow in the simulation and reconstruction. The OT digitisation can be divided into different processes, listed in Table 5.4. They are discussed in detail in the following section.

As indicated in Fig. 5.6, there is a clear separation between the simulation and the reconstruction. Information from the simulation procedure is provided to the reconstruction algorithms only through the output of the digitisation. For a realistic simulation, this output is converted into the same format as that of the data acquisition buffer

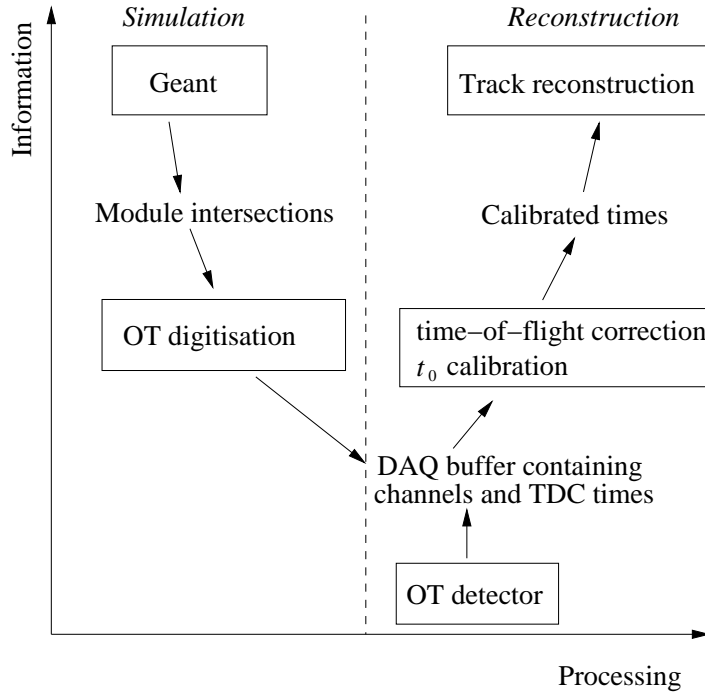


Figure 5.6: Overview of the data flow in the OT simulation and reconstruction chain. On the axes the amount of (physics) information and the processing flow are indicated.

Table 5.4: The processes treated in the OT digitisation.

1. distance calculation	6. cross talk
2. single cell efficiency	7. random noise
3. drift distance smearing	8. dead time
4. distance-to-time conversion	10. readout window
5. spill-over	11. TDC conversion

(DAQBuffer) [78]. In other words, the reconstruction algorithms do not distinguish between data generated by Monte Carlo simulation and data coming from the detector.

Before track reconstruction, the recorded times are corrected for the time offset (t_0) of the TDC and the time-of-flight of the particle. This correction is made in the BRUNEL reconstruction application [57].

5.3.2 Digitisation processes

Below, the different processes in the digitisation procedure and their effects on the OT performance are discussed.

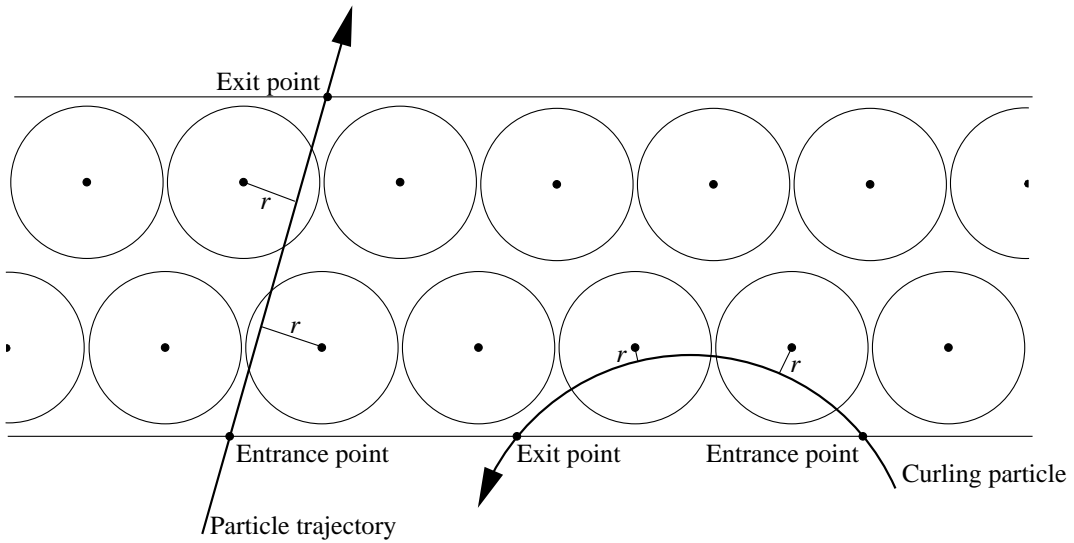


Figure 5.7: Sketch of two possible trajectories through the straws in a double layer. The left one traverses the whole module and is approximated by a straight line. The right one exits through the same plane as it entered the module and is approximated by a helix. From the entrance and exit points, the distance of closest approach (r) is calculated.

Drift distance calculation

As a particle travels through a gas-filled straw, several ionisations occur. Under influence of the electric field inside the straw, the released electrons drift to the wire. The recorded TDC time corresponds to the rising edge of the signal pulse, and thus to the first electrons that reach the wire. Consequently, the distance of closest approach between the wire and the particle's trajectory is a good estimate for the drift distance.

Figure 5.7 shows a sketch of two particles crossing a double layer of straws in a module. For a particle traversing the double layer, the distance of closest approach, r , is calculated by assuming that it travelled along a straight line between the entrance and exit points. Low-momentum particles, on the other hand, curl under influence of the magnetic field and some can even reverse direction inside a double layer. For these reversing particles, a helix-wise trajectory is assumed between the entrance and exit points. Their hits, which account for less than 0.5% of the total number hits, can be regarded background, because these trajectories cannot be reconstructed correctly.

The wire splitting halfway the long modules, located around the $y = 0$ plane, creates a 44 mm long, insensitive section in each straw. These insensitive sections are staggered in the two monolayers of a module in order to optimise for the tracking efficiency. The detailed motivation can be found in Ref. [79].

Figure 5.8 shows the distribution of the number of hits created by a particle traversing a double layer of straws in a module. Typically, in 72% of the cases, a particle creates two hits per double layer. For particles with $p > 2 \text{ GeV}$, this occurs in as

much as 80% of the cases, since they are less deflected by the magnetic field. Note that below 1 GeV, particles originating from the interaction point are bent out of the acceptance by the magnetic field before reaching the T stations. In general, most particles below 2 GeV that are seen in the T stations originate from a secondary interaction. They can have large incident angles and create much more than two hits.

Single cell efficiency

The number of ionisations depends on the path length through the straw. Nevertheless, not all primary electrons create enough secondary ionisations needed to accumulate a detectable signal on the wire. This effect is caused by electron attachment, and is explained in detail in Ref. [80]. Hence, only effective ionisation clusters contribute to the total signal. As the number of effective ionisations (n_{ions}) obeys a Poisson distribution, the probability that there are at least n_{\min} ionisation clusters equals

$$P(n_{\text{ions}} \geq n_{\min}) = 1 - \sum_{n=0}^{n_{\min}-1} \frac{\rho^n e^{-\rho}}{n!} . \quad (5.1)$$

where ρ is the average number of effective ionisations per unit of length and l is the path length through the straw. In case it is assumed that the first effective ionisation cluster accumulates enough charge on the wire (i.e., $n_{\min} = 1$), Eq. (5.1) simplifies to

$$P(n_{\text{ions}} \geq 1) = 1 - e^{-\rho l} . \quad (5.2)$$

It shows that when a particle passes a straw near the cell wall the detection efficiency drops, because the path length near the edge becomes too short to create any effective ionisation, resulting in cell inefficiency.

The single cell efficiency is identified as the probability for having at least one effective ionisation (Eq. (5.2)). Accounting also for overall effects as noisy channels, broken wires, etc., a constant factor ε_0 is inserted. The single cell efficiency is thus parameterised as [81]

$$\varepsilon(l) = \varepsilon_0 (1 - e^{-\rho l}) . \quad (5.3)$$

This parameterisation agrees well with test beam data [33], giving $\varepsilon_0 = 0.99$ and $\rho = 1.47 \text{ mm}^{-1}$.

Figure 5.9 displays the single cell efficiency as a function of the distance of closest approach, r . The path length, l , depends on r according to $l = 2\sqrt{R^2 - r^2}$, where

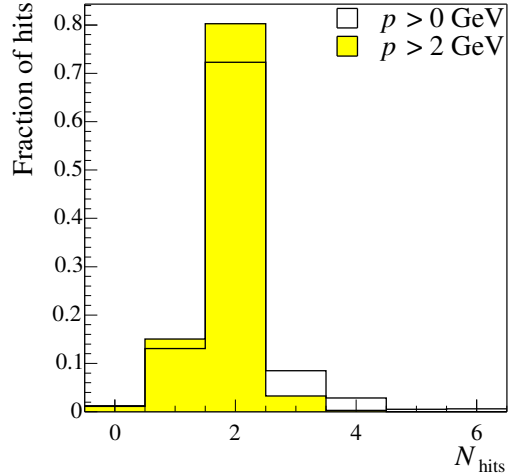


Figure 5.8: The number of hits in a double layer from a traversing particle. Averages are 2.12 for all particles and 1.87 for those with $p > 2 \text{ GeV}$.

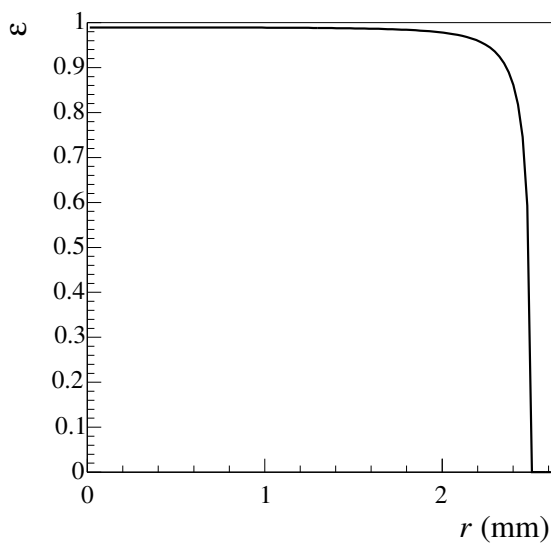


Figure 5.9: The single cell efficiency, ε , as a function of the distance to the wire, r . The average efficiency integrated over the inside of the cell ($r < 2.5$ mm) equals 97.0%.

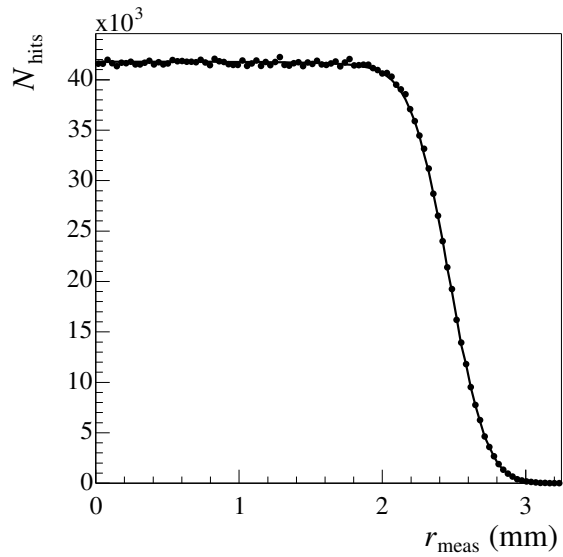


Figure 5.10: The drift distance distribution after applying the single-cell efficiency and the resolution smearing. The fitted curve is $\varepsilon(r)$ convolved with a Gaussian resolution function.

$R = 2.5$ mm is the inner radius of a straw. The average efficiency integrated over the full the cell ($r < R$) is 97.0%. Taking into account the 0.25 mm gap between the straws, the efficiency that a monolayer of straws detects a perpendicular incident particle equals 92.4%. The staggering of the two monolayers (see Fig. 5.7) optimises the efficiency for a double layer such that the probability that a particle does not produce any effective ionisation in a module is negligible.

Drift distance smearing

The uncertainty on the drift distance is measured in test beam experiments [36, 38, 76]. The resolution function could be well described by a single Gaussian distribution with a width of $\sigma = 200 \mu\text{m}$. The resolution was found to be relatively independent of the drift distance.

In the digitisation, the distance of closest approach, r , is smeared according to this Gaussian distribution. Figure 5.10 shows the smeared drift distance distribution. Although the distance of closest approach is known with a resolution of $200 \mu\text{m}$, it should be kept in mind that there remains an ambiguity on which side the particle passed the wire. This left-right ambiguity must be resolved in the process of track finding.

Distance-to-time conversion

The OT electronics registers the arrival time of the first drift electrons. The time at which the signal is detected, t_{det} , is composed of

$$t_{\text{det}} = t_{\text{tof}} + t_{\text{drift}} + t_{\text{prop}} , \quad (5.4)$$

where t_{tof} is the time-of-flight, t_{drift} is the drift time in the straw, and t_{prop} is the propagation time of the signal through the wire. The time-of-flight is the time, measured with respect to the time of the beam crossing, needed for the particle to reach the straw. It is obtained from the GEANT simulation. The signal propagation time is determined from the distance of the hit to the readout, assuming a propagation speed of 0.25 m/ns [82].

The $r(t)$ relation gives the drift distance as a function of the drift time. In the digitisation the inverse relation is used. For simplicity, a linear $r(t)$ relation is assumed:

$$r(t) = v_{\text{drift}} t = R \frac{t}{t_{\text{max}}} , \quad (5.5)$$

where v_{drift} is the drift velocity and $t_{\text{max}} = 32.5$ ns is the maximum drift time in a straw, found in test beam data [33]. Although these data also show some indications of a higher order $r(t)$ relation, the linear dependence was found to describe the data with reasonable accuracy. Nevertheless, the actual $r(t)$ relation has to be determined in the final LHCb setup.

Spill-over

The previous steps in the digitisation procedure are not only applied to the hits in the current bunch crossing, including those from pile-up collisions, but also to the spill-over hits in the neighbouring bunch crossings. Since the time to collect all signals in a given bunch crossing is more than the 25 ns between the bunch crossings, the effect of spill-over cannot be neglected in the OT.

Due to the tail in the time spectrum from particles with a large time-of-flight, not only the previous bunch crossing, but also the one before that must be included in the spill-over simulation. Furthermore, in order to collect most of the hits from the current bunch crossing, a 50 ns readout window is used. For this reason, also hits from the next bunch crossing are included.

Spill-over is simulated by adding hits from minimum-bias events to the hits in the current bunch crossing with the proper time offset. The calculation of t_{det} in (5.4) is modified accordingly

$$t_{\text{det}} = t_{\text{spill}} + t_{\text{tof}} + t_{\text{drift}} + t_{\text{prop}} , \quad (5.6)$$

where $t_{\text{spill}} = \{-50 \text{ ns}, -25 \text{ ns}, 0 \text{ ns}, +25 \text{ ns}\}$ is the time at which the bunch crossing occurred. The t_{det} time spectrum in T1 with the contributions from the different bunch crossings is displayed in Fig. 5.11(a). The current bunch crossing at $t_{\text{spill}} = 0$ ns contains a $b\bar{b}$ collision, which explains the higher hit multiplicity in the signal spill compared to that in the spill-over bunch crossings. In addition, the number of pp collisions in a

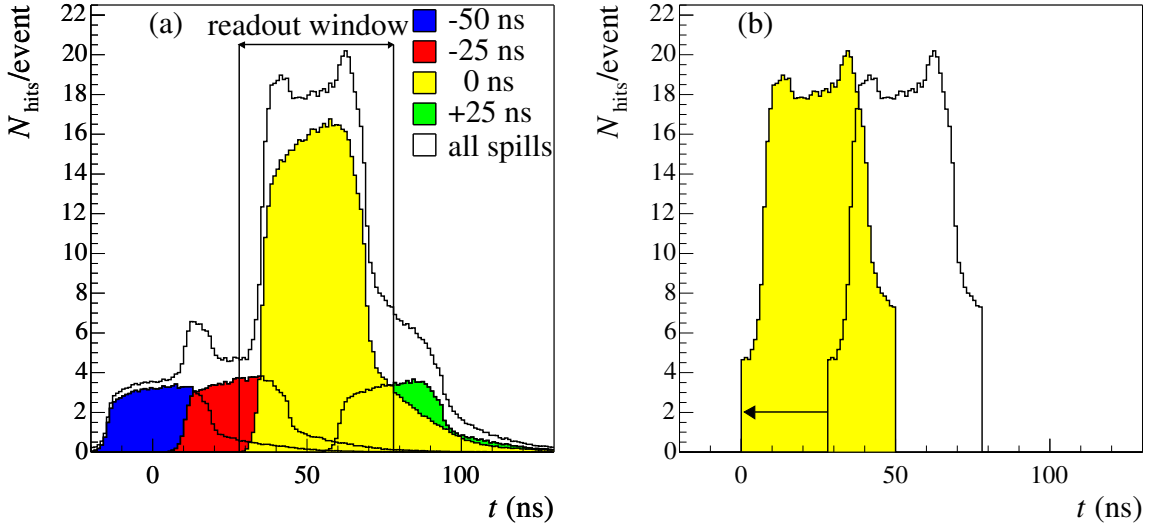


Figure 5.11: Time spectra in OT station T1. The left figure (a) shows the average distribution of t_{det} per event including the contribution from each spill (indicated with different shadings). The right figure (b) shows the distribution within the readout window (transparent) and after TDC conversion (filled).

spill-over bunch crossing is only $\bar{n}_{pp} = 0.67$, while it is $\bar{n}_{pp}^{bb} = 1.67$ in the signal spill (see Section 4.3.6). In the end, only the sum of the spills within the readout window in Fig. 5.11(b) is observed.

Although spill-over hits are created by real, physical particles, they are regarded as background noise in the detector. The background fraction of hits is defined as

$$f_{\text{bg}} = \frac{N_{\text{bg}}}{N_{\text{sig}} + N_{\text{bg}}} , \quad (5.7)$$

where N_{bg} is the number of background hits, and N_{sig} is the number of signal hits. In the 50 ns readout window, the average spill-over contribution in a $b\bar{b}$ event is $f_{\text{bg}} = (16.5 \pm 0.3)\%$. Note that in about a quarter of the events the spill-over background fraction is zero, due to bunch crossings without collisions.

Cross talk and random noise

The two other sources of background in the OT are cross talk and random noise. Cross talk is electrical pick-up from signals in neighbouring straws. The fraction of hits from pick-up is measured in a test beam experiment [36] to be 5%. It only affects the nearest-neighbouring straws inside a monolayer. There is no significant cross talk between the monolayers.

Random noise hits do not originate from real, physical particles. They are generated by instabilities in the straw and by noise in the electronics. A constant noise level of

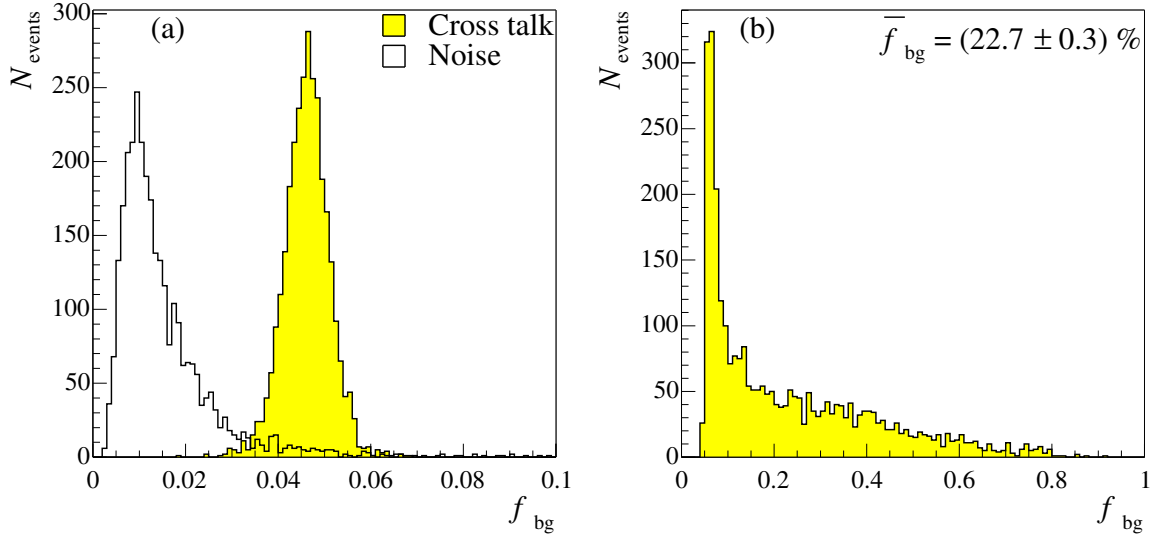


Figure 5.12: Contributions per event from cross talk and noise rate to the background fraction (a) and the distribution of the total background fraction including spill-over (b).

10 kHz per channel [83] is simulated, adding about 27 noise hits per event. In Fig. 5.12(a) the distributions of the background fraction from cross talk and random noise are shown. As expected, the contribution from cross talk is centred around 5%. The contribution from random noise hits is 1.2%.

Clearly, the largest contribution to the background fraction is from spill-over hits. In Fig. 5.12(b) the total background fraction per event is shown. The long tail originates from high occupancy spill-over events in combination with low occupancy signal events. The average total background fraction amounts to $(22.7 \pm 0.3)\%$.

Dead time

The fast rising time of the pulse, caused by electrons reaching the wire, allows an accurate time measurement. In contrast, due to the ion tail, the signal decreases slowly. This prevents a second hit from being recorded on the same channel during a certain (dead) time. In the simulation, these hits are discarded. Only the hit that arrives first is kept. The exact dead time of the electronics has not been determined yet. In the simulation studies, a conservative estimate of 50 ns is used.

The probability that a second hit is present on a wire having already a hit scales with the detector occupancy. In the ideal case — that means for a uniform and low hit occupancy, without spill-over — this probability is equal to the detector occupancy. Figure 5.13(a) shows the actual time difference, Δt , between two consecutive hits on the same channel. Here, the second hit is required to be from the signal spill and to be recorded within the readout window. The cases where this second hit occurs within the dead time lead to a detection inefficiency. Hence, the hit inefficiency is the integral from

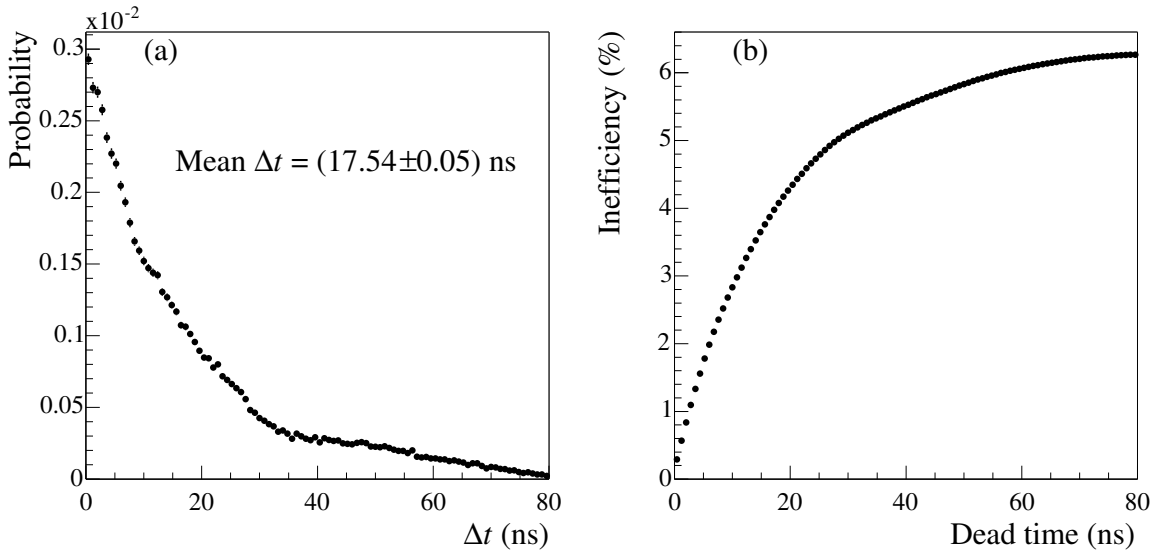


Figure 5.13: Time difference, Δt , between two consecutive hits on the same channel (a). The second hit is required to be from the signal spill and recorded within the readout window. The effect of dead time is that the entries up to 50 ns are not registered. Figure (b) shows this effect on the inefficiency as a function of the dead time. It is obtained by integrating the curve in (a).

zero up to the dead time value.¹ Figure 5.13(b) shows the integrated curve. For a dead time of 50 ns the average hit inefficiency amounts to 5.82%.

In spite of the loss of information due to dead time, this does not always imply a loss in terms of track reconstruction efficiency. When Δt is small enough, the first recorded hit fits the track just as well as the second hit, which is killed by dead time. Therefore, hits arriving within Δt_{accept} after the first recorded hit do not really contribute to the inefficiency. The cut is set at 3σ of the 200 μm intrinsic resolution, giving

$$\Delta t_{\text{accept}} = \frac{3\sigma_{\text{smear}}}{v_{\text{drift}}} = 7.8 \text{ ns} . \quad (5.8)$$

Taking this into account, the real inefficiency due to dead time is reduced to 3.51%.

With both the dead time and readout window set to 50 ns, there can only be one TDC time recorded per channel per event. Hence, the multiple hit capacity — the possibility of OTIS chip to register more than one TDC time on the same channel — is not effective. Recent estimates [83], however, indicate that a dead time of 30 ns is more realistic. In this case, the multiple hit capacity slightly reduces the average hit inefficiency from 2.92% to 2.78%. It should be noted that the reduction is more pronounced for a slower drift gas in combination with a larger readout window.

¹The data acquisition does not allow for more than one TDC time per 25 ns time interval. When the dead time is below 25 ns this effect should also be taken into account.

Readout window

On a trigger accept signal, all TDC times within a window of 50 ns are read out by the electronics. Figure 5.11 shows the effect of the finite readout window in the simulation: all TDC times outside the readout window are discarded. The time digitiser chip (OTIS) has an offset, t_0 , with respect to the LHC bunch clock. This offset defines the start of the readout window. It is set to the time at which the first hits from the signal spill (at $t = 0$) are expected (see Fig. 5.11(a)). In the simulation, t_0 is determined per station and the results are summarised in Table 5.5. Currently, the offset of the TDC clock is only caused by the delays due to the particle's time-of-flight and the signal propagation through the wire. In reality, it will also include delays due to the electronics and the length of the cables.

Apart from removing many spill-over hits, the readout window also removes hits from slow particles (see Fig. 5.11). The fraction of hits from the signal spill that are inside the readout window equals 90.1%. It should be noted, however, that the inefficiency is largely due to slow particles. For particles with $p > 2 \text{ GeV}$, 99.9% is recorded inside the readout window. In summary, for particles below 2 GeV the total inefficiency is mainly caused by the finite readout window, while for particles above 2 GeV the dead time of the electronics the main cause.

Table 5.5: Time offset (t_0) of the TDC chip for each station.

Station	t_0 (ns)
T1	28
T2	30
T3	32

TDC conversion

The final step in the digitisation procedure is the conversion of the recorded time into a 6-bit TDC time for each $\Delta t_{\text{spill}} = 25 \text{ ns}$. This implies that the time is measured in bins of $\sim 0.4 \text{ ns}$, which is well within the intrinsic resolution of $\sigma_{\text{smear}}/v_{\text{drift}} = 2.6 \text{ ns}$. Additionally, two bits are reserved to count the bunch crossing number. Before the digital conversion, the TDC offset, t_0 , is subtracted from Eq. (5.6). The final TDC time can thus be expressed as the nearest integer of

$$t_{\text{TDC}} = \frac{2^{n_{\text{bits}}}}{\Delta t_{\text{spill}}} (t_{\text{spill}} + t_{\text{tof}} + t_{\text{drift}} + t_{\text{prop}} - t_0) \quad , \quad (5.9)$$

where $n_{\text{bits}} = 6$ is the number of bits used to record the TDC time.

TDC offset calibration and time-of-flight correction

The first step in the reconstruction is to apply the corrections for the TDC offset (t_0) and the time-of-flight of the particle. The value for t_0 is simply taken from Table 5.5. Hence, it does not introduce an uncertainty in the calibrated TDC time. This can be justified, because the internal clock offset is expected to be well known.

In case of the time-of-flight correction, the time-of-flight depends on the particle's speed and the path length from the interaction point to the hit. For high-energy particles

Table 5.6: Fraction of $b\bar{b}$ inclusive events with an occupancy higher than the given occupancy. The quoted error are statistical.

Occupancy (%)	Fraction of events (%)
1	98.4 ± 0.4
2	88.0 ± 0.6
4	50.7 ± 0.9
4.3 (mean)	43.5 ± 0.9
8	7.0 ± 0.5
8.5 (2×mean)	4.5 ± 0.4
10	2.1 ± 0.3
12	0.7 ± 0.2

the assumption that they travel with the speed of light is a reasonable approximation. The path length is approximated by a straight line from the nominal interaction point $(0, 0, 0)$ to the centre of the wire (x_w, y_w, z_w) . In the next section it is shown that this is an accurate approximation for particles above 2 GeV. The calibrated time is thus expressed as

$$t_{\text{cal}} = t_{\text{TDC}} \frac{\Delta t_{\text{spill}}}{2^{n_{\text{bits}}}} + t_0 - \frac{\sqrt{x_w^2 + y_w^2 + z_w^2}}{c} . \quad (5.10)$$

5.4 Detector performance

After the digitisation procedure, the detector performance can be studied in terms of channel occupancy, detection efficiency, and hit resolution.

5.4.1 Occupancy

The hit occupancy has a considerable influence on the performance of the online and offline reconstruction. The higher the occupancy in an event, the more difficult it is to reconstruct this event. In Chapter 6, it is shown that the efficiency for track finding decreases with the number of hits, while the ghost rate increases. In addition, the computing time increases exponentially. The occupancy of an event is defined as the fraction of channels that has a hit recorded inside the readout window.

Figure 5.14 shows the distribution of the number of hits and the occupancy for $b\bar{b}$ inclusive events. On average there are about 2300 hits per event in the OT. As there are 53760 readout channels in total, this corresponds to an average channel occupancy of 4.3%.

Since the hottest events are the most difficult to reconstruct, it is interesting to consider the fraction of events with a high channel occupancy, i.e., the tail of the distribution in Fig. 5.14. Table 5.6 sums the fraction of events with an occupancy higher than a given occupancy. For instance, it follows that 4.5% of the events have an occupancy in the OT of twice the average.

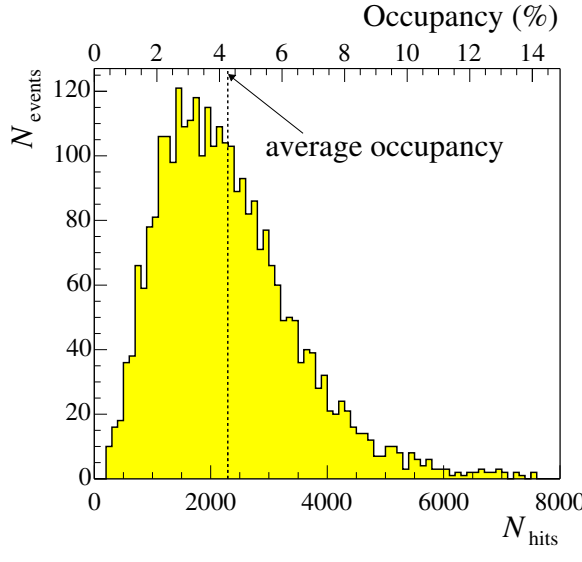


Figure 5.14: Distribution of the number of hits and occupancy averaged over all OT stations for $b\bar{b}$ inclusive events. The dashed line indicates the mean value.

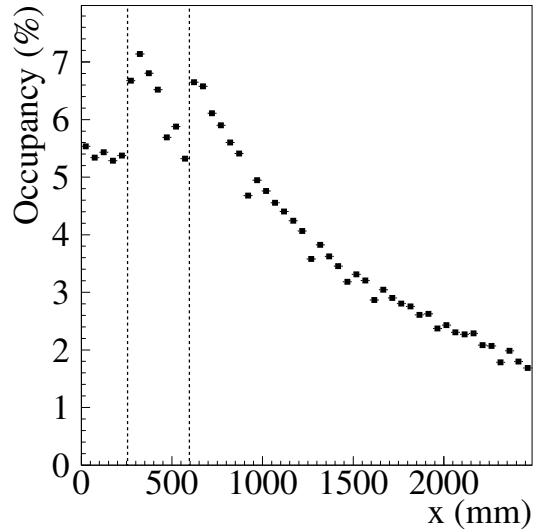


Figure 5.15: Event averaged occupancy in OT station T1, first x layer, as a function of x . The dashed lines represent the vertical boundaries between the cross-shaped IT and the OT.

As can be seen in Fig. 5.4, the particle flux in a station increases towards the beam pipe. The design and size of the IT has been chosen such that the occupancy of the OT in the central region does not become too high [50]. The cross shape was found to be the optimal design to keep the average channel occupancy in the hottest regions below the 7% level. With this design, the short module S1 and the adjacent long module obtain the highest occupancies. Figure 5.15 shows the average occupancy in the first OT layer as a function of x . The discontinuities are due to transitions between the different modules.

5.4.2 Efficiency

In the digitisation procedure, different sources of detector inefficiencies have been introduced. In summary, the final inefficiency is the result of single cell inefficiency, dead regions in the module, dead time of the electronics, and the finite readout window. The staggered arrangement of the two monolayers (see Fig. 5.7) maximises the probability to detect at least one hit. Therefore, the double layer efficiency is defined as the probability that at least one hit is recorded per traversing particle. As explained in the digitisation procedure, this efficiency depends on the momentum of the particle.

The average double layer efficiency for hits from particles with $p > 0$ GeV is 93.5%. The inefficiency is primarily due to low-momentum secondary particles falling outside the time window of the readout. Consequently, when considering only particles with $p >$

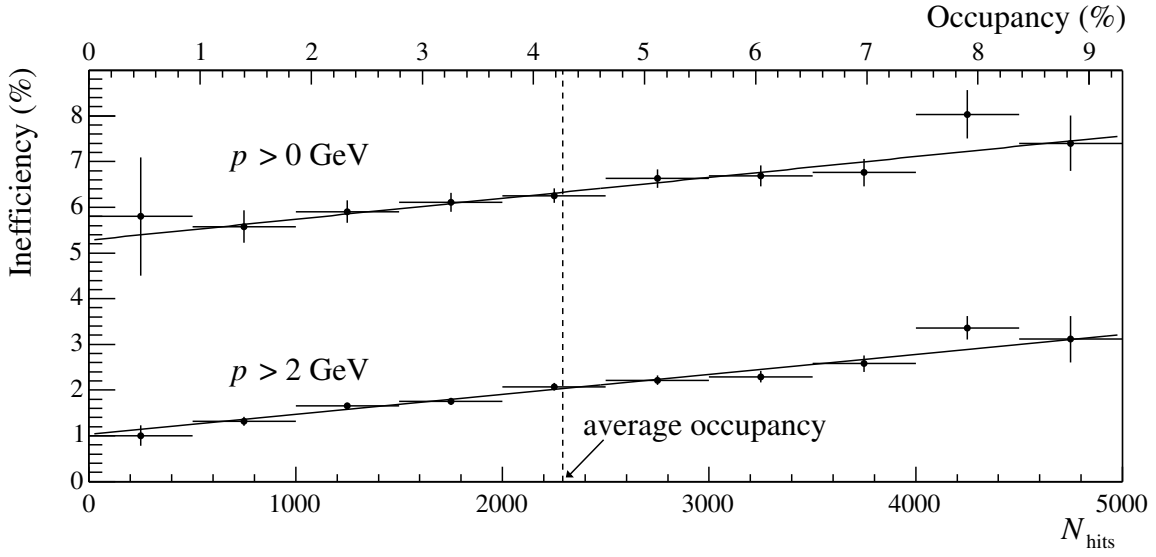


Figure 5.16: Double layer inefficiency as a function of the occupancy for hits from particles with $p > 0 \text{ GeV}$ and $p > 2 \text{ GeV}$. Straight lines are fitted to both sets of data points.

2 GeV, the efficiency rises to 97.9%. Figure 5.16 shows the inefficiency as a function of the occupancy. The dependence on the occupancy is due to dead time of the electronics. As the effect of dead time is negligible at zero occupancy, the remaining inefficiency of 1.0% for particles with $p > 2 \text{ GeV}$ can be attributed to dead regions in the detector. Hence, it follows that at average occupancy the dead time accounts for 1.1% of the inefficiency. In case of a 30 ns dead time, this contribution reduces to 0.7%.

5.4.3 Resolution

The track fit assumes that the uncertainty on the drift distance follows a Gaussian distribution. The width of this Gaussian is referred to as the resolution. In the Monte Carlo simulation, the error on the reconstructed drift distance can be obtained by comparing the reconstructed drift distance with the true distance of closest approach of the particle to the wire.

In the track reconstruction, the calibrated time in (5.10) needs to be converted back into a drift distance. The calibrated time contains contributions from the drift time, t_{drift} , as well as from the propagation time, t_{prop} . The propagation time, however, can only be calculated properly when the trajectory or an estimate for the trajectory is known. This information is only available during track reconstruction.

Figure 5.17(a) shows the error distribution without any knowledge about the trajectory. In this case, an average, constant t_{prop} is estimated such that the distribution is centred around zero. For particles with $p > 2 \text{ GeV}$, the resolution is about $230 \mu\text{m}$.

Figure 5.17(b) shows the error distribution for particles with $p > 2 \text{ GeV}$ when t_{prop} is obtained from the Monte Carlo truth. The resolution approaches the simulated resolu-

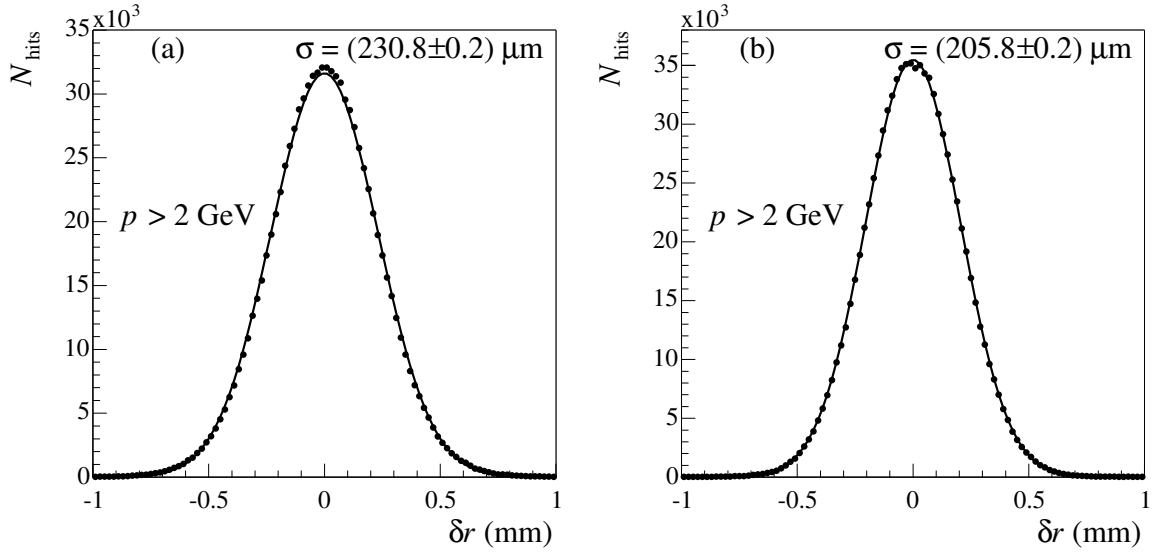


Figure 5.17: Error distribution of the reconstructed drift distance, δr , with t_{prop} assumed constant for all hits (a) and with t_{prop} extracted from the Monte Carlo truth (b). Only particles with $p > 2 \text{ GeV}$ are used. A single Gaussian, centred around zero, is fitted to both distributions.

tion of $200 \mu\text{m}$. It shows that the time-of-flight correction is a reasonable approximation for all particles with $p > 2 \text{ GeV}$. For low-momentum particles, the straight line approximation and speed of light assumption are less accurate, resulting in an overall resolution of $225 \mu\text{m}$.

Chapter 6

Track reconstruction

The reconstruction of tracks through the LHCb detector is a challenging task. To find the particle trajectories, the correct hits in different subdetectors (VELO, TT, IT, and OT) need to be combined. As shown in the simulation studies in Chapter 4 (see for example Fig. 4.9), a typical event contains a large number of tracks (~ 100). The challenge is not only to find all particle tracks, but also to accurately determine their track parameters. The best estimates of the track parameters are obtained from the track fit. In this chapter first the track fit is presented in Section 6.1. This helps to understand the pattern recognition methods used by the track finding algorithms, discussed in Section 6.2. In Section 6.3 the performance is presented in terms of track reconstruction efficiency and ghost rate, and also in terms of resolution and pull distributions. Finally, after having found and fitted the tracks, they can be visualised in an event display programme. The visualisation of the hits and the tracks in an event is a powerful tool in the understanding of the pattern recognition algorithms. The visualisation procedure is described in Section 6.4.

6.1 Track fit

The purpose of the track fit is to determine the most accurate estimates of the track parameters together with the corresponding covariances. In the event reconstruction, these estimates are used to efficiently match the tracks to particle identification objects, i.e., RICH rings, calorimeter clusters, and muon candidates. In the physics analysis, they are used to locate the primary and secondary vertices, and to calculate the invariant mass of particle combinations.

A track is modelled by a collection of straight line segments, tangent to the particle's trajectory. These straight line segments are called track states.¹ As all tracks in LHCb can be regarded as going either in the forward or in the backward direction, it is natural to parameterise the track states as a function of the z coordinate. A track state is

¹Instead of a straight line, other choices for the track states are, e.g., a helix or a parabola. In LHCb, however, most hits are in a region of low magnetic field, making the straight line locally an adequate approximation. Obviously, for the larger extrapolations between the measurements, the curvature due to the magnetic field has to be taken into account.

defined by a position and a tangent direction at a given z . This results in four track parameters. Furthermore, a fifth parameter, q/p , is added to include the momentum measurement obtained from the curvature in the magnetic field. In all cases, only single charged particles are considered, i.e., $q = \pm 1$. Conveniently, the state vector is chosen as follows

$$\vec{x} = \begin{pmatrix} x \\ y \\ t_x \\ t_y \\ q/p \end{pmatrix} \quad \text{with} \quad t_x = \frac{\partial x}{\partial z}, \text{ and} \quad t_y = \frac{\partial y}{\partial z}. \quad (6.1)$$

The corresponding errors on \vec{x} are given by a 5×5 state covariance matrix, C . The state vector and its covariance matrix are commonly referred to as the track state.

The location of the track states can be chosen anywhere along the trajectory. In the track fit, it is useful to determine the states at the measurement planes. The combination of a measurement and a track state is referred to as a *node*. In the track model, the transport of a state at node $k - 1$ to a state at node k is described by the propagation relation

$$\vec{x}_k = f_k(\vec{x}_{k-1}) + \vec{w}_k, \quad (6.2)$$

where f_k is the track propagation function, and \vec{w}_k is the *process noise*, for instance, as a result of multiple scattering. The actual function f_k depends on the chosen propagation method. For a straight line extrapolation, f_k simplifies to

$$f_k(\vec{x}_{k-1}) = F_k \vec{x}_{k-1}, \quad (6.3)$$

where F_k is the transport matrix given by

$$F_k = \begin{pmatrix} 1 & 0 & \Delta z & 0 & 0 \\ 0 & 1 & 0 & \Delta z & 0 \\ 0 & 0 & 1 & 0 & 0 \\ 0 & 0 & 0 & 1 & 0 \\ 0 & 0 & 0 & 0 & 1 \end{pmatrix} \quad \text{with} \quad \Delta z = z_k - z_{k-1}. \quad (6.4)$$

The measurements provide information about the trajectory at each node. The projection equation describes the relation between a measurement, m_k , and a track state as

$$m_k = h_k(\vec{x}_k) + \epsilon_k, \quad (6.5)$$

where h_k is the projection function, and ϵ_k the *measurement noise*. For example, in case a detector directly measures the x coordinate of a track state, h_k simplifies to

$$h_k(\vec{x}_k) = H_k \vec{x}_k, \quad (6.6)$$

where the measurement matrix, H_k , is given by

$$H_k = (1 \ 0 \ 0 \ 0 \ 0). \quad (6.7)$$

Since the detection planes in LHCb measure only one coordinate, the projection matrix, H , is a 1×5 matrix. Silicon pixel detectors, for example, would require a 2×5 projection matrix. The actual projection matrices for the LHCb tracking detectors are presented in Section 6.1.5.

In the track model, the process noise, \vec{w}_k , and the measurement noise, ϵ_k , are both regarded as unknown random disturbances with a zero expectation value. The uncertainties in \vec{w}_k and ϵ_k are described by the covariance matrices $Q_k \equiv \text{cov}(\vec{w}_k)$ and $V_k \equiv \text{cov}(\epsilon_k)$. In case of one-dimensional measurements, V_k is simply the measurement error squared.

6.1.1 Kalman formalism

The concept of regarding a track as a collection of measurements and track states sets the stage for the introduction the Kalman filter as a method to fit tracks. The principle of the Kalman filter is to add the measurements one-by-one to the fit, each time updating the local track state at the current node. The method is based on minimising the χ^2 of the measurements on the track, and therefore it is mathematically equivalent to a least-squares fit. However, the iterative Kalman procedure avoids the computationally slow inversion of large matrices that is common to a global least-squares fit, making it an attractive solution for fast applications.

The Kalman filter has many advantages. One is the possible use in pattern recognition algorithms. For instance, a track finding algorithm can decide to add a measurement to the track based on its contribution to the χ^2 without the need to refit the whole track. Another advantage is that after the fit, not only the track state at the primary interaction point, but the full trajectory of the particle is known, which is useful for matching tracks with RICH rings, calorimeter clusters, and muon candidates. Finally, it should be noted that the Kalman filter allows a natural way to include process noise, caused by multiple scattering.

Generally, the Kalman technique can be applied to any linear dynamic system where random disturbances are present in the evolution of the system as well as in the measurements. The method was developed in 1960 [84], and is nowadays used in a variety of different fields as, e.g., navigation systems, GPS, radar tracking, meteorology, and econometrics. Its first application in the field of particle physics was in 1983 in the DELPHI experiment (see Refs. [85] and [86]). Since then it has become a common procedure in many high-energy physics experiments.

The Kalman fit procedure recognises three distinct steps:

- **Prediction.** A prediction of the track state at a given node is made based on the track state at the previous node.
- **Filter.** This prediction is updated with information of the measurement in this node using the filter equations. The prediction and filter steps are repeated, until all measurements are added. The track state after each filter step is the best estimate of the trajectory based on the measurements incorporated so far.

- **Smoother.** When all measurements are added to the track, the track states at the previous nodes are updated in reverse direction using the smoother equations, such that the information from all measurements is properly accounted in every node, resulting in a more “smooth” track.

After the smoothing step, the best estimates of all track states along the trajectory are known. The result is independent of the direction in which the measurements are added. The Kalman filter can be run either in the downstream (towards positive z), or upstream direction (towards negative z). In LHCb, the default direction is upstream. Below the three steps in the Kalman filter procedure are explained in detail.

Prediction

The prediction for the state vector and its covariance matrix at the k^{th} node is obtained from the previous node, $k - 1$, using the propagation relation:

$$\vec{x}_k^{k-1} = f_k(\vec{x}_{k-1}) \quad , \quad (6.8)$$

$$C_k^{k-1} = F_k C_{k-1} F_k^T + Q_k \quad . \quad (6.9)$$

In this notation, \vec{x}_k^{k-1} refers to a predicted state vector, $\vec{x}_k^k \equiv \vec{x}_k$ refers to a filtered state vector, and \vec{x}_k^n refers to a smoothed state vector. In other words, the superscript denotes the amount of information (i.e., the number of measurements) used in this estimate. The process noise term, Q_k , is added to the predicted covariance matrix, C_k^{k-1} .

The track fit requires an estimate for the initial track state, \vec{x}_0 , in order to make the first prediction. In the absence of an estimate from any other subdetector, this prediction usually comes from an initial fit in the track finding algorithms. In order to suppress any bias from this prediction and to avoid the double-counting of measurements, the initial covariance matrix, C_0 , must have increased values for the errors on the diagonal.

The residual is the distance between the measurement, m_k , and the state vector in the measurement plane. The predicted residual and its covariance matrix are given by

$$r_k^{k-1} = m_k - h_k(\vec{x}_k^{k-1}) \quad , \quad (6.10)$$

$$R_k^{k-1} = V_k + H_k C_k^{k-1} H_k^T \quad . \quad (6.11)$$

The expected variance, R_k^{k-1} , has a contribution from both the covariance matrix of the track state, C_k^{k-1} , and the measurement variance, V_k . The predicted contribution of this measurement to the total χ^2 equals

$$(\chi^2_+)_k^{k-1} = r_k^{k-1} (R_k^{k-1})^{-1} r_k^{k-1} \quad . \quad (6.12)$$

The goal of the Kalman fit is to find the optimal track states that give a minimal χ^2_+ .

Filter

In the filter step, the track state is updated with information of the measurement at node k . In the gain matrix formalism, the filtered state vector and its covariance matrix

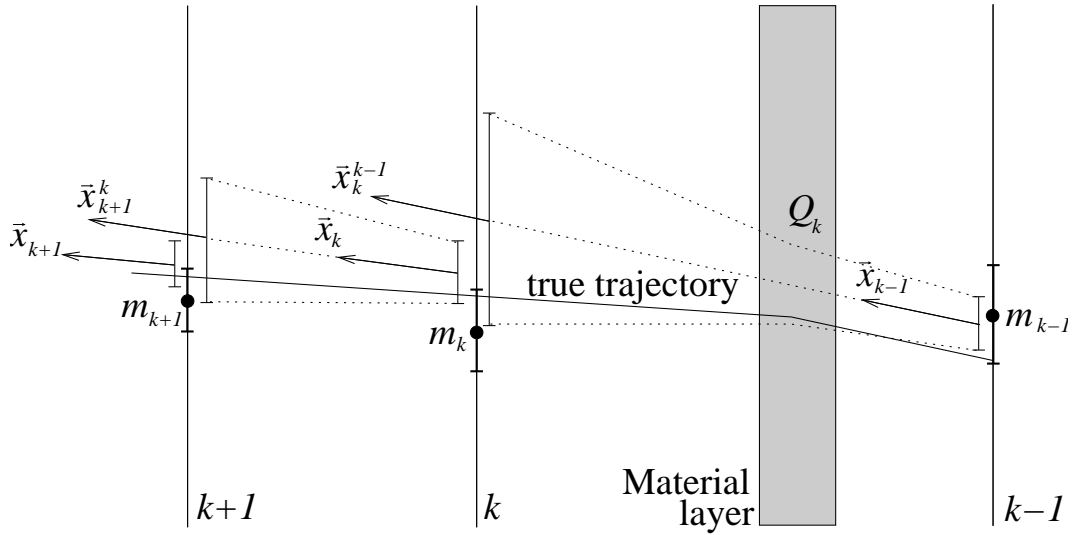


Figure 6.1: Schematic picture of the Kalman filter, showing evolution of a track state from node $k - 1$ to k to $k + 1$. The material layer increases the predicted error on \vec{x}_k^{k-1} , due to the (possible) scattering of the particle. The filtered state, \vec{x}_k , is pulled towards the measurements m_k .

are

$$\vec{x}_k = \vec{x}_k^{k-1} + K_k r_k^{k-1}, \quad (6.13)$$

$$C_k = (\mathbb{1} - K_k H_k) C_k^{k-1}, \quad (6.14)$$

where K_k is a 5×1 gain matrix, which equals

$$K_k = C_k^{k-1} H_k^T (V_k + H_k C_k^{k-1} H_k^T)^{-1} = C_k^{k-1} H_k^T (R_k^{k-1})^{-1}. \quad (6.15)$$

The appendix offers a complete derivation of the Kalman gain matrix. The filtered values for the residual and its covariance matrix are calculated as follows

$$r_k = m_k - h_k(\vec{x}_k) = (1 - H_k K_k) r_k^{k-1}, \quad (6.16)$$

$$R_k = (1 - H_k K_k) V_k = V_k - H_k C_k H_k^T. \quad (6.17)$$

Accordingly, the contribution to the total filtered χ^2 of this measurement is

$$(\chi^2_+)_k = r_k R_k^{-1} r_k. \quad (6.18)$$

Figure 6.1 gives a schematic overview of the prediction and filter steps. It shows the scattering of a particle at a material layer between node k and $k - 1$. The track fit accounts for this effect by increasing the predicted error on the state vector \vec{x}_k^{k-1} with Q_k . The measurement, m_k , pulls the state back to the true trajectory, resulting in a filtered track state, \vec{x}_k .

The prediction and filter steps are repeated until all measurements are added to the track. The filtered track state at the last node ($k = n$) is also the best estimate of this track state as it includes the information from all nodes. The other nodes ($k < n$) are updated in the smoother step.

Smoother

The smoother gives the best estimates of the tracks states at all previous nodes. A recursive method, known as the Rauch-Tung-Striebel smoother [87], is applied. In this method, the smoothed state vector and covariance matrix are given by

$$\vec{x}_k^n = \vec{x}_k + A_k(\vec{x}_{k+1}^n - \vec{x}_{k+1}^k) , \quad (6.19)$$

$$C_k^n = C_k + A_k(C_{k+1}^n - C_{k+1}^k)A_k^T , \quad (6.20)$$

where the 5×5 smoother gain matrix equals

$$A_k = C_k F_{k+1}^T (C_{k+1}^k)^{-1} . \quad (6.21)$$

The smoothed residual and the error on the residual are

$$r_k^n = m_k - h_k(\vec{x}_k^n) , \quad (6.22)$$

$$R_k^n = V_k - H_k C_k^n H_k^T . \quad (6.23)$$

Finally, the total χ^2 of the track fit is obtained by summation of the smoothed χ_+^2 increments

$$(\chi_+^2)_k^n = r_k^n (R_k^n)^{-1} r_k^n . \quad (6.24)$$

6.1.2 Resolution and pull

The performance of the fit is determined by comparing the fitted track states with true Monte Carlo information. The error on a parameter x is defined as

$$\delta x = x_{\text{rec}} - x_{\text{true}} , \quad (6.25)$$

where x_{rec} is the reconstructed, or fitted, value, and x_{true} is the true Monte Carlo value. The Gaussian width of the δx distribution is called the resolution. The pull is defined as

$$\Delta_x = \frac{x_{\text{rec}} - x_{\text{true}}}{\sigma_x} , \quad (6.26)$$

where σ_x is the estimated error, obtained from the covariance matrix of the fit. The pull distribution should have unit width and zero mean (i.e., no bias). The resolution and pull distributions of the track parameters are important measures for the performance of the fit. They are presented in Section 6.3.

6.1.3 Extended Kalman filter

Just as in a least χ^2 method, the Kalman filter assumes the propagation function, f_k , and projection function, h_k , to be linear, as suggested by the use of the transport matrix, F_k , and projection matrix, H_k , in the equations above. The examples of the propagation and projection functions given in (6.3) and (6.6) are linear relations. In reality, however, they are more complicated. Therefore, the propagation and projection functions are linearised using a Taylor expansion around a reference track state. In the Kalman approach, the linearisation of f_k and h_k is referred to as the extended Kalman filter [86, 88]. Its application in LHCb is described in the following two sections.

6.1.4 Propagation

The propagation relation describes the transport of a track state from a given z position to a new z position. It is applied in the prediction step (6.8) to the filtered track states of the previous node, \vec{x}_{k-1} . The propagation method has to take into account the magnetic field and the effect of the detector material. Since the magnetic field in LHCb is very inhomogeneous (cf. Fig. 3.6), the field strength at each position is determined from a measured field map. The transport through the magnetic field is evaluated using an adaptive, fifth-order Runge-Kutta method.² Consequently, the propagation function, f_k , is not a simple expression. Nevertheless, a first-order Taylor expansion around a reference track state, $\vec{x}_{k-1}^{\text{ref}}$, can still be calculated as

$$\vec{x}_k^{k-1} = f_k(\vec{x}_{k-1}) = f_k(\vec{x}_{k-1}^{\text{ref}}) + F_k(\vec{x}_{k-1} - \vec{x}_{k-1}^{\text{ref}}) \quad \text{with} \quad (6.27)$$

$$F_k = \frac{\partial f_k(\vec{x}_{k-1}^{\text{ref}})}{\partial \vec{x}_{k-1}^{\text{ref}}} . \quad (6.28)$$

The linearisation is a good approximation when the reference states are close to the true trajectory. In practise, the filtered states are already close enough to the true trajectory. Hence, it is not needed to determine additional reference states, but instead, the filtered states are evaluated *directly* in the Runge-Kutta extrapolation (i.e., $\vec{x}_{k-1}^{\text{ref}} = \vec{x}_{k-1}$). Also, this means that only one iteration of the fit is sufficient concerning the linearity of the propagation. The linearisation procedure is only needed to calculate the numerical derivatives in F_k required by the prediction and smoother equations.

The effect of the material in the detector is taken into account in the extrapolation procedure. The amount of material traversed along a segment of the trajectory is estimated from the material description (see Section 5.1). As a track passes through several layers of material, the state is transported from one layer of material to the next. At each layer, the effect of multiple scattering and energy loss is evaluated and the state vector and covariance matrix are updated. Below, both effects are described.

Energy loss

As discussed in Section 4.4.2, the dominant source of energy loss for relativistic particles is ionisation. The momentum precision in LHCb is high enough such that this effect cannot be neglected in the track fit. While propagating the state vector, the momentum component is adjusted at each material layer that is encountered. The correction is obtained from the Bethe-Bloch equation (4.6). In the track fit, the energy loss is approximated by regarding all particles as mip's, thereby neglecting the dependence on β :

$$-\frac{dE}{dx} = c_{\text{ion}} \frac{Z}{A} , \quad (6.29)$$

²The term adaptive means that the algorithm breaks up the stepping inside the field to achieve the required precision. This precision is set to $5\mu\text{m}$.

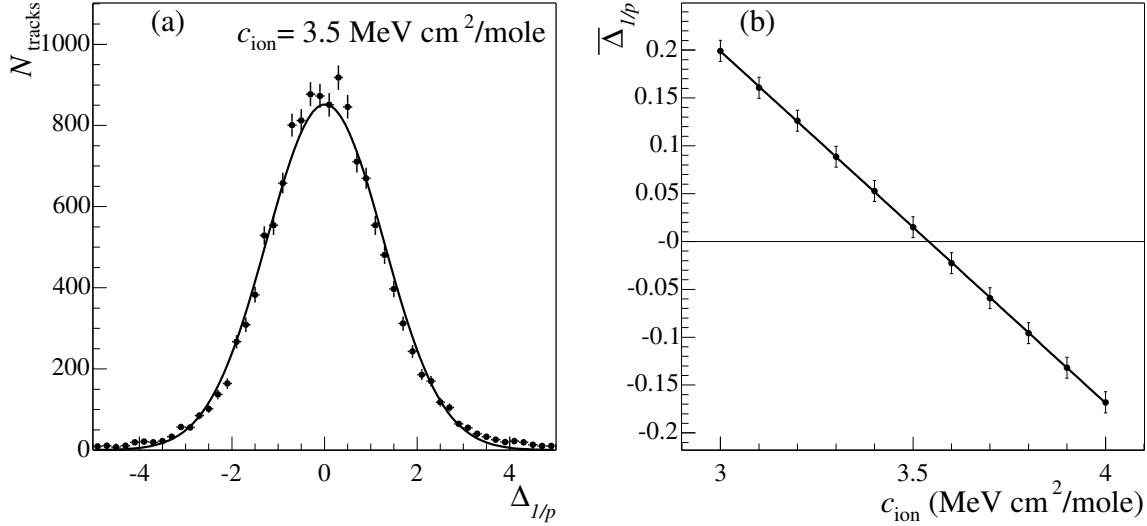


Figure 6.2: Pull distribution of $1/p$ at the vertex position for $c_{\text{ion}} = 3.5 \text{ MeV cm}^2 \text{ mole}^{-1}$ (a). The right plot (b) shows the Gaussian mean of these pull distributions for different values of c_{ion} . A straight line is fitted through the data points, intersecting the horizontal axis at $c_{\text{ion}} = (3.54 \pm 0.01) \text{ MeV cm}^2 \text{ mole}^{-1}$.

where c_{ion} absorbs all constant factors in (4.6). The difference in energy before and after a material layer is then given by

$$\Delta E = -c_{\text{ion}}\rho l \frac{Z}{A} , \quad (6.30)$$

where l is the distance travelled through the material layer, and ρ the material density. The minus sign refers to a downstream track fit, i.e., in the direction of the particle's flight. Accordingly, the minus sign must be omitted in case of an upstream track fit. In order to obtain the momentum change, the particle's mass is neglected. Since Landau fluctuations in the energy loss are small compared to the momentum resolution, no correction on the covariance matrix is required.

The value of c_{ion} is tuned such that there is no bias in the fitted momentum. Figure 6.2(a) displays the $1/p$ pull distribution for a given value of c_{ion} . The bias is defined as the mean of a Gaussian fit to the pull distribution. Figure 6.2(b) shows the bias as a function of c_{ion} . From a straight line fit through these data points, it is found that a value of $c_{\text{ion}} = (3.54 \pm 0.01) \text{ MeV cm}^2 \text{ mole}^{-1}$ gives an unbiased momentum estimate. For a material with $Z/A \simeq 0.5 \text{ mole g}^{-1}$, this corresponds with a stopping power of $dE/dx = 1.77 \text{ MeV g}^{-1} \text{ cm}^2$ (cf. Fig. 4.10).

For electrons, a different correction should be applied, as they lose their energy by bremsstrahlung (see Section 4.4.2). Solving (4.7), the energy loss equals

$$\Delta E = -E(1 - e^{-\frac{l}{x_0}}) , \quad (6.31)$$

where the first minus sign is again omitted in case of an upstream track fit. For electrons, not only a correction on the state vector, but also on its covariance matrix must be applied. The variance of the momentum in the noise matrix in (6.9) is given by [89]

$$Q_{55} = \left(\frac{q}{p} \right)^2 \left(e^{-\frac{\ln 3}{\ln 2} \frac{l}{X_0}} - e^{-2 \frac{l}{X_0}} \right) . \quad (6.32)$$

This correction increases the estimated momentum error at each material layer. Inside the magnetic field these corrections allow the fit to adjust for the uncertainty on the energy loss. Outside the magnetic field, where the fit cannot determine the momentum, they only increase the estimated momentum error. Nevertheless, in the final reconstruction of electrons, bremsstrahlung photons that are emitted before the magnet and detected in the electromagnetic calorimeter, can be added to the momentum to increase the momentum resolution of electrons. The effect of the electron correction in the track fit is described in detail in Ref. [70].

Multiple scattering

The simulation of multiple scattering in LHCb is described in Section 4.4.2. The uncertainty on the direction of the trajectory, introduced by this process, must be included in the track fit. Similar to energy loss, the amount of multiple scattering is estimated from the material encountered during the extrapolation. However, multiple scattering is not predictive: the multiple scattering correction only affects the noise matrix, Q . For a thin scatterer, the direction components are given by [90]

$$Q_{33} = (1 + t_x^2)(1 + t_x^2 t_y^2) \theta_0^2 , \quad (6.33)$$

$$Q_{44} = (1 + t_y^2)(1 + t_x^2 t_y^2) \theta_0^2 , \quad (6.34)$$

$$Q_{34} = t_x t_y (1 + t_x^2 t_y^2) \theta_0^2 , \quad (6.35)$$

where the projected scattering angle, θ_0 , is evaluated from (4.8).

In principle, the assumption of a thin scatterer is not valid for all material layers in LHCb. In a thin medium, the noise matrix, Q , is evaluated at the centre of each layer. In contrast, in a thick medium multiple scattering should not be regarded as a discrete, but rather as a continuous process. In this approach, the scattering also affects the position elements of the covariance matrix. The continuous multiple scattering along a straight line in a layer of thickness Δz (i.e., measured along the z axis) is given by the symmetric matrix [91]³

$$Q(\Delta z) = \begin{pmatrix} Q_{33} \frac{\Delta z^2}{3} & Q_{34} \frac{\Delta z^2}{3} & Q_{33} \frac{\Delta z}{2} & Q_{34} \frac{\Delta z}{2} & 0 \\ \dots & Q_{44} \frac{\Delta z^2}{3} & Q_{34} \frac{\Delta z}{2} & Q_{44} \frac{\Delta z}{2} & 0 \\ \dots & \dots & Q_{33} & Q_{34} & 0 \\ \dots & \dots & \dots & Q_{44} & 0 \\ \dots & \dots & \dots & \dots & 0 \end{pmatrix} , \quad (6.36)$$

³In the appendix of Ref. [91], the author derives the noise matrix for a continuous (thick) scatterer. Unfortunately, he integrates over a distance dl . Instead, he should have integrated over dz , since the linear propagation (6.3) is described as a function of Δz . His final result is correct if the total length, l , is substituted by Δz .

where Q_{33} , Q_{44} , and Q_{34} are given by (6.33)–(6.35). Note that for a thick scatterer, the noise term in (6.9) should not be added in the middle of the material layer, but, instead, at the exit point of the layer. The thick scatterer approximation is required when the thickness of the material is comparable to the extrapolation distance. In these cases, the thin scatterer approximation would underestimate the multiple scattering in the position matrix elements. In LHCb, the air in the magnet and the gas in RICH 1, are examples of thick scattering layers. Conservatively, only thick scattering layers are assumed in the track fit.

6.1.5 Projection

In order to determine the residual of a measurement, the state vector is projected onto the measurement space. In case of the TT, IT, and VELO ϕ silicon sensors, a measurement can be represented by a straight line corresponding to the central coordinate of the cluster of strips. The residual is the distance between this line and the intersection point of the track state with the sensor plane. This results in a linear projection function. For each of these measurements, which measure a coordinate in a plane at fixed z , the projection function can be expressed as

$$h_k(\vec{x}_k) = x \cos \alpha_s + y \sin \alpha_s , \quad (6.37)$$

where α_s is the rotation (stereo) angle with respect to the y axis.

On the other hand, the projection for r measurements cannot be represented by a linear relation. The VELO r clusters measure the radial distance, r , to the z axis. Hence, the projection of a state \vec{x} onto an r -measuring sensor reads

$$h_r(\vec{x}) = r = \sqrt{x^2 + y^2} , \quad (6.38)$$

which is clearly non-linear in x and y . In other words, the derivative matrix, H , depends on the predicted track parameters. Similarly, the projection onto an OT measurement, which depends on the distance of closest approach to the wire, is also given by a non-linear equation. The closest distance of a state \vec{x} to a wire in an x layer is given by the projection relation:

$$h_{\text{OT}}(\vec{x}) = (x - x_{\text{wire}}) \cos \theta = \frac{x - x_{\text{wire}}}{\sqrt{1 + t_x^2}} , \quad (6.39)$$

where x_{wire} is the x coordinate of the wire, and θ is the track angle with the z axis in the x - z plane. This expression is non-linear in the track parameter t_x .

As explained in the previous chapter, the OT actually measures calibrated times. Consequently, the state vector should be projected onto the space of calibrated times, giving

$$h_{\text{OT}}(\vec{x}) = A \frac{x - x_{\text{wire}}}{v_{\text{drift}} \sqrt{1 + t_x^2}} + \frac{|y - y_{\text{readout}}|}{v_{\text{prop}}} , \quad (6.40)$$

where v_{drift} is the drift velocity, $A = \pm 1$ is the solution of the left-right ambiguity, y_{readout} is the y coordinate of the readout electronics, and v_{prop} is the signal propagation

speed. It should be noted that the non-linearity originates only from the projection on the closest distance to the wire, already present in (6.39).

The non-linearity in (6.38) and (6.40) causes problems when the predicted state deviates too much from the true particle trajectory. In the prediction step, where the projection is applied to predicted track states, these problems may arise especially after long-distance extrapolations. Similar to the propagation relation, the solution is to linearise the projection relation using a reference track state.⁴ The first-order Taylor expansion around a reference track state, \vec{x}_k^{ref} , gives

$$h_k(\vec{x}_k) = h_k(\vec{x}_k^{\text{ref}}) + H_k(\vec{x}_k - \vec{x}_k^{\text{ref}}) \quad \text{with} \quad H_k = \frac{\partial h_k(\vec{x}_k^{\text{ref}})}{\partial \vec{x}_k^{\text{ref}}} . \quad (6.41)$$

Again, the reference track is required to be close to the true trajectory such that the linear approximation is valid. An initial estimate for the reference states is obtained from the track finding algorithms.

For r measurements, the projection relation (6.38) becomes

$$h_r(\vec{x}) = H\vec{x} = (\cos \phi_{\text{ref}} \quad \sin \phi_{\text{ref}} \quad 0 \quad 0 \quad 0) \vec{x} , \quad (6.42)$$

where ϕ_{ref} is the angle of the reference state with the x axis. As can be seen in Fig. 6.3, the r measurement is now effectively represented by a straight line, which touches the circular cluster at the nearest distance to the reference state. The predicted residual is the shortest distance between the predicted state and the straight line. As the r and ϕ sensors are mounted back-to-back inside one station, ϕ_{ref} can be estimated accurately. Similarly, for the OT measurements, the slope of the reference trajectory, t_x^{ref} , replaces t_x in (6.40), as illustrated in Fig. 6.4. A detailed discussion of the projection functions for different detector technologies is given in [80] and [92].

After the first iteration of the fit, the smoothed track states are used as reference states for the projection in subsequent iterations. In addition, the smoothed state at the first node can be used as initial track estimate, \vec{x}_0 . Of course, the initial covariance matrix, C_0 , should again be taken large, in order to avoid any bias. The fit should be repeated until it converges to a minimum χ^2 . Fortunately, the reference states obtained from the track finding algorithms are already close enough to the true trajectory, so that one iteration of the fit is sufficient. This can be explained by the configuration of the sensitive detection layers in LHCb. In the VELO stations, the r - ϕ configuration provides an accurate knowledge of the ϕ coordinate at each r sensor, while the x - u - v - x configuration in the OT stations provides an accurate estimate of the track slope t_x .

6.1.6 Outlier removal and refit

The χ^2 contribution (χ_+^2) of the measurements can be used to identify outliers. In the filter step, estimates of χ_+^2 for each measurement are already available. Removing outliers at this stage, can be done easily without the need to refit. However, the filtered

⁴The reference states in the projection are not necessarily the same as the ones in the propagation. Actually, Section 6.1.6 shows an example where they are chosen to be different to save processing time.

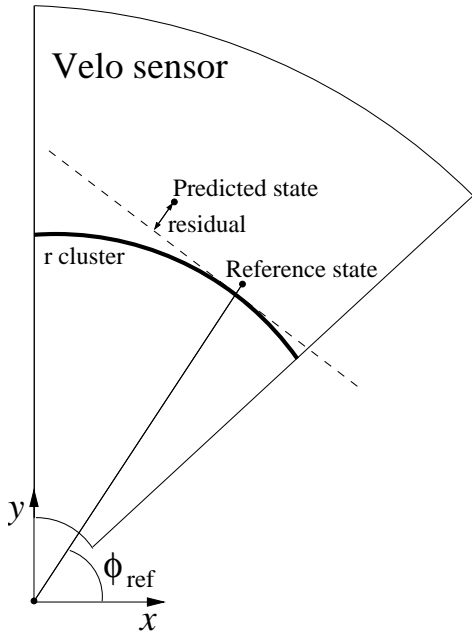


Figure 6.3: Sketch of the projection of a predicted track state onto an r measurement using a reference track state. The reference state fixes ϕ_{ref} , which is needed to linearise the projection.

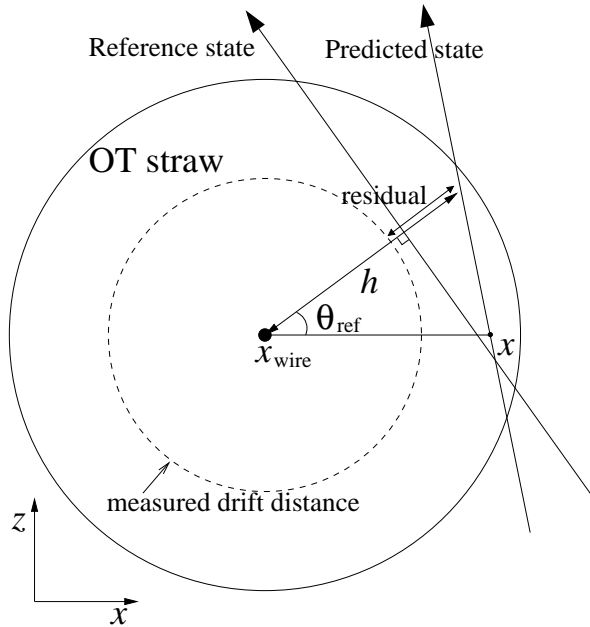


Figure 6.4: Sketch of the projection of a predicted track state onto an OT measurement using a reference track state. The reference state fixes θ_{ref} , and thus t_x^{ref} , which is needed to linearise the projection.

χ^2 contributions only take into account the measurements at the previous nodes. Therefore, the decision to remove a measurement depends on the direction of the fit and the number of measurements already added. The smoother, on the other hand, provides the best estimates of χ^2_+ , irrespective of the direction of the fit. Consequently, it is better to base the outlier removal on the smoothed χ^2_+ . The main disadvantage of this approach is the need to refit the whole track.

In order to reduce the processing time due to refitting, the filtered states of the first iteration are used as reference states for the propagation in the subsequent iterations. It should be noted that these reference states are different from the ones used to linearise the projection. The purpose of this approach is that the transport matrix, F_k , and the noise matrix, Q_k , which are calculated in the first iteration, can be reused in the subsequent iterations. The calculation of these matrices is the most time-consuming process in the fit, as it requires a fifth-order Runge-Kutta evaluation, and a calculation of the intersection points with the encountered detector material. When F_k and Q_k at each node are reused, these calculations need to be done only once, making the refitting approximately 10 times faster. In addition, also a transport vector, \vec{q}_k , defined as

$$\vec{q}_k = f_k(\vec{x}_{k-1}^{\text{ref}}) - F_k \vec{x}_{k-1}^{\text{ref}} , \quad (6.43)$$

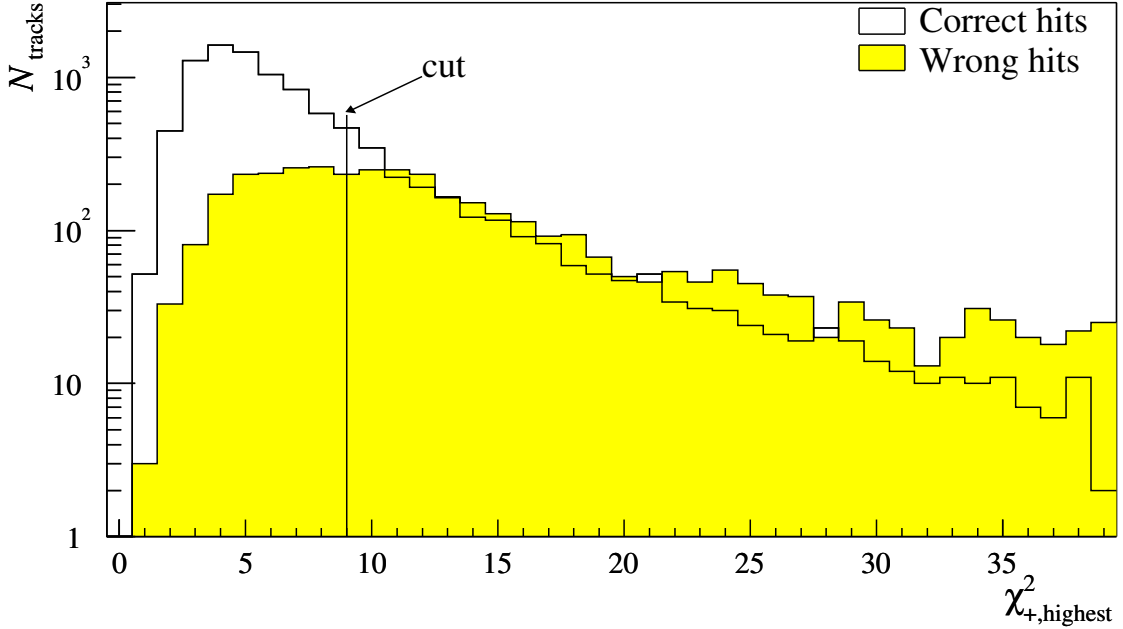


Figure 6.5: The distribution of measurements with the highest χ^2_+ for each track after the first iteration. The outlier rejection cut is set at 9.

is evaluated once and reused in the following iterations. Eq. (6.27) then becomes

$$f_k(\vec{x}_{k-1}) = \vec{q}_k + F_k \vec{x}_{k-1} . \quad (6.44)$$

After removing measurement k from the track, F_{k+1} , Q_{k+1} , and \vec{q}_{k+1} of the subsequent node need to be updated according to

$$F'_{k+1} = F_{k+1} F_k , \quad (6.45)$$

$$\vec{q}'_{k+1} = \vec{q}_{k+1} + F_{k+1} \vec{q}_k , \quad (6.46)$$

$$Q'_{k+1} = Q_{k+1} + F_{k+1} Q_k F_{k+1}^T . \quad (6.47)$$

Since outliers affect also the χ^2 contributions of the other, neighbouring measurements of the track, at most one measurement is removed during each iteration. This measurement is the one with the highest χ^2_+ above a certain cut-off value. Figure 6.5 shows the distribution of the highest χ^2_+ for each track after the first iteration. These are tracks with measurements in both the VELO and T stations, which are found by the forward tracking algorithm (see Section 6.2.2). Correct hits are defined as measurements on the track that originate from the true Monte Carlo particle; wrong hits are defined as those having a different origin. Beyond $\chi^2_+ \sim 9$ the contribution from wrong hits start to dominate.

The fit is only repeated when an outlier has been removed. Figure 6.6 shows the fraction of all tracks that is fitted in an iteration. Only 39% of the tracks is fitted more than once. It can be seen that after 5 iterations, only few tracks remain to be refitted.

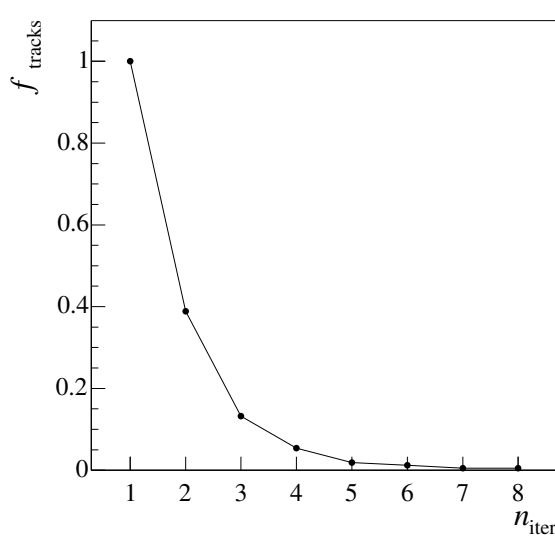


Figure 6.6: The fraction of all tracks, f_{tracks} , that is fitted in an iteration, with the χ^2_+ cut set at 9. After 5 iterations most outliers have been removed.

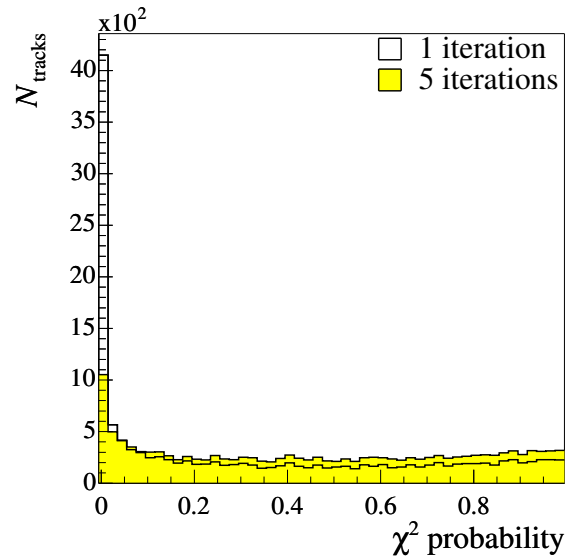


Figure 6.7: The total χ^2 probability distribution after 1 iteration and after 5 iterations.

Hence, the maximum number of iterations is limited to 5. In total about 1.6% of the measurements on the tracks are removed. The improvement in the total χ^2 probability distribution can be seen in Fig. 6.7. Clearly, the peak at zero probability, corresponding to a high χ^2 per degree of freedom, collapses.

Finally, the outlier removal procedure increases the fraction of correct hits on the track (hit purity), at the cost of a decrease in the fraction of correct hits found (hit efficiency). After 5 iterations, the average hit purity increases from 98.0% to 98.5%, while the average hit efficiency decreases from 95.1% to 94.3%. It should be noted that the optimal χ^2_+ cut and the number of iterations need to be determined for each track finding algorithm separately.

6.2 Pattern recognition

The first step in the track reconstruction, before the track fitting, is to find all tracks. This is the task of the track pattern recognition algorithms. Their goal is to efficiently assign the correct hits to the tracks. In addition, the number of reconstructed ghost tracks — i.e., tracks with (many) wrong hits — should be kept to a minimum.

6.2.1 Track types

The tracks are classified in different types, depending on their trajectories in the LHCb tracking system. They are schematically depicted in Fig. 6.8 and described as follows:

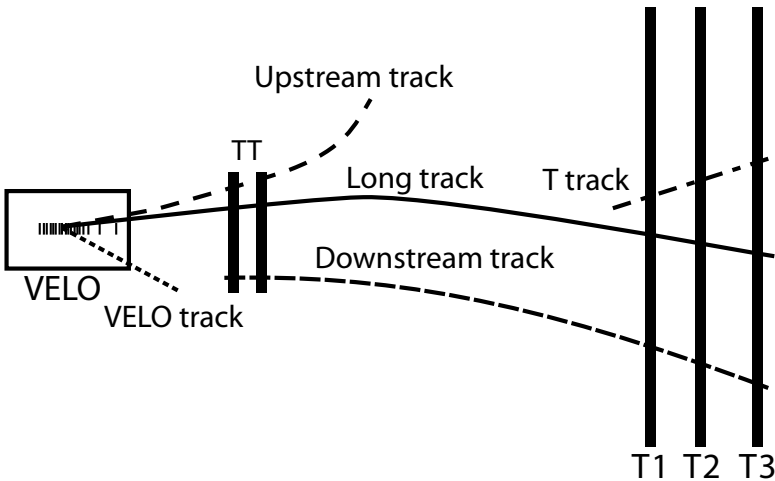


Figure 6.8: Sketch of the five different track types in the LHCb tracking system.

- **Long tracks** traverse the full tracking system, i.e., travelling from the VELO up to the T stations. Since they have an accurate momentum measurement, they are most useful for physics.
- **Upstream tracks** only traverse the VELO and TT stations. They are bent out of the acceptance before reaching the T stations. Their main use is in the RICH 1 reconstruction. Although their momentum resolution is reduced, they can be used in the reconstruction of several B decay channels.
- **Downstream tracks** only traverse the TT and T stations, and have no hits in the VELO. They allow reconstruction of K_s^0 's that decay outside the VELO acceptance.
- **VELO tracks** only traverse the VELO. They allow an accurate measurement of the primary vertex, because they typically have a large polar angle. Also, they often correspond to particles flying in the backward direction.
- **T tracks** only traverse the T stations. They are mainly used in the RICH 2 reconstruction.

The aim of the pattern recognition algorithms is to find as many tracks of each type as possible. In the following, the track finding strategy for the offline reconstruction is described. The corresponding algorithms have many similarities with the ones used in the online track reconstruction. Reference [48] offers a detailed overview of the online pattern recognition algorithms, used in the L1 and HLT trigger.

6.2.2 General strategy

In the following, the individual algorithms in the track finding procedure are described:

- **VELO seeding:** The magnetic field in the VELO is sufficiently low that tracks can be considered as straight lines here. The algorithm [93] starts by making three-dimensional space points, combining r and ϕ clusters. Then, triplets of space points are searched in the most downstream stations. Clusters in the more upstream stations are added by extrapolating the candidate track towards the interaction point. The resulting track segments serve as seeds for the other track finding algorithms.
- **Forward tracking:** This algorithm, which searches for long tracks, starts with these VELO seeds and tries to find continuations in the TT and T stations. The method is based on the idea [94] that for a given VELO seed and a single hit in either T1, T2, or T3, the trajectory of the track through the detector is determined (assuming no multiple scattering). The trajectory is parameterised by a second order (in y) and third order (in x) polynomial. Then, for the remaining hits the distance to this trajectory is plotted in a histogram. The track candidates with the most confirming hits are selected, and these hits are assigned to the track. Finally, a likelihood method is applied to confirm the correct tracks and reject the ghosts. This method finds already a large fraction of the long tracks. The hits used by the forward tracks are discarded for use in the subsequent track search algorithms, in order to reduce computing time.
- **T seeding:** Since the magnetic field in the T stations is sufficiently low to first order, this region is also well suited for finding tracks. The track seeding [95] is a stand-alone algorithm which searches for tracks in T1–T3. The algorithm starts to search for straight-line track candidates in the x - z plane, considering only hits in the x layers. In a second pass, the non-negligible magnetic field is taken into account by parameterising the trajectory as a parabola. The stereo-hits are added to confirm the 2D track candidates. Also here, a likelihood is calculated based on the expected and observed number of hits. It takes into account possible detector inefficiencies and insensitive regions. Ghost tracks are rejected by cutting on this likelihood.
- **Track matching:** This algorithm matches T seeds with VELO seeds that are not used by the forward tracking. It increases the reconstruction efficiency of long tracks. The method is explained further in Section 6.2.3.
- **Upstream tracking:** A dedicated algorithm [96] searches for upstream tracks. VELO seeds that are not used by the forward tracking or track matching algorithms are extrapolated as straight lines in the y - z plane to the TT stations. Then, for each hit that lies close to this extrapolated track, the corresponding momentum is calculated. When at least three hits in the four TT layers have a compatible momentum, the track is fitted with the Kalman filter. The candidate track is accepted when the χ^2 per degree of freedom is less than 5.
- **Downstream tracking:** There are two methods to find downstream tracks. Both methods use T seeds as a starting point and then try to add the correct TT hits.

The first algorithm is the default method and is the backward counterpart of the forward tracking. The second algorithm [97] first estimates the momentum of these T seeds assuming that the particle originated from the beam interaction point. This estimate is obtained from the p -kick method, which will be explained in the next section. Then, these candidate tracks are extrapolated to the TT stations and corresponding hits are selected based on the measurement's χ^2_+ obtained from the Kalman filter.

The VELO and T seeds that have not been used as part of either a long, upstream, or downstream track, are defined to be of type VELO or T track.

As described above, hits used by the forward algorithm are neglected in the hit search of any subsequent algorithm. Also, the VELO and T seeds that are used by either the forward or track matching algorithm are not considered by the upstream or downstream tracking algorithms. This cooperative strategy, referred to as the *filtered* mode, avoids as much as possible the creation of clone tracks, i.e., tracks which share a large fraction of their hits. The filtered mode is the default tracking strategy.

In contrast, the *concurrent* mode refers to the case in which each algorithm considers all possible hits and seeds. This means, for instance, that the T seeding will also find segments of long tracks that are already found by the forward tracking algorithm. Thereafter, the track matching algorithm will consider all these VELO and T seeds to find mostly the same tracks as the forward tracking.

6.2.3 Matching tracks

The track matching algorithm makes combinations of T seeds and VELO seeds in order to find long tracks. There are two approaches to match T seeds with VELO seeds. The first approach [98] extrapolates both track segments as straight lines towards a central plane in the magnet. The magnetic field appears to be homogeneous enough so that all the correct track combinations intersect in a focal plane at an almost fixed z position. Here, the tracks segments can be matched with good efficiency. This fast and robust method provided the first indication of the feasibility to reconstruct tracks in LHCb without making use of the stations in the magnet region. This insight finally led to the reoptimisation of the detector [26].

The second approach matches VELO and T seeds at a plane located just behind the last VELO station. Therefore, it first estimates the momentum of the T seeds using the p -kick method, described below. The momentum is then used to extrapolate the T seeds with a fifth-order Runge-Kutta method to the matching plane. The VELO seeds are extrapolated with a straight line to the same plane. There, a χ^2 criterion is used to select the correct match between the VELO and T seeds. For each successful match, TT hits are searched for and assigned to the track. In comparison with the first approach, which approximates the magnetic field by a single focal plane, the second approach is more efficient as it takes into account the full magnetic field shape. Especially for low-momentum particles there is a large gain. In the following, the second method, which is used by default in the current track reconstruction procedure, is discussed in more detail.

Momentum estimate

The momentum of a T seed can be estimated assuming that the particle originated from the interaction point. This method, known as the p -kick method, is based on the idea that the effect of the field can be described by an instant kick of the momentum vector in the centre of the magnet. In general, the actual momentum kick, $\Delta\vec{p}$, depends on the integrated magnetic field along the particle's trajectory:

$$\Delta\vec{p} = q \int d\vec{l} \times \vec{B} . \quad (6.48)$$

The main component, Δp_x , provides the highest precision on the momentum. In terms of the track parameters this relation becomes:

$$\Delta p_x = p_{x,f} - p_{x,i} = p \left(\frac{t_{x,f}}{\sqrt{1 + t_{x,f}^2 + t_{y,f}^2}} - \frac{t_{x,i}}{\sqrt{1 + t_{x,i}^2 + t_{y,i}^2}} \right) = q \int |d\vec{l} \times \vec{B}|_x , \quad (6.49)$$

where the subscript $t_{x,f}$ and $t_{y,f}$ are the slopes of the T seeds. They are known from the parabolic fit of the T seeds, and are evaluated at station T3. The slopes before the magnet, $t_{x,i}$ and $t_{y,i}$, as well as the integrated magnetic field need to be estimated. Note that the charge of the particle, q , is determined from the sign of curvature and the field polarisation.

The total integrated magnetic field along the z axis equals 4.2 T m. The centre of the magnet is defined by a plane at $z = z_{\text{magnet}}$ where the integrated field equals half the total value. This plane at $z_{\text{magnet}} = 5150$ mm serves as an initial focal plane for all T seeds. The particle's trajectory can be approximated by two lines intersecting at this focal plane, as illustrated in Fig. 6.9. This path starts from the T seed and is extrapolated up to z_{magnet} . At this point the path makes a kink towards the nominal interaction point $(0, 0, 0)$, giving a first estimate for the slopes before the magnet. Then, along this path, the integrated field is calculated and a second focal plane at $z = z_c$ is determined. The new values for $t_{x,i}$, $t_{y,i}$ and the integrated magnetic field are substituted in (6.49), resulting an estimate for p . However, a small systematic effect is observed in the momentum resolution, which depends on the slope $t_{x,f}$ as

$$\langle \delta p/p \rangle = -0.0092 - 0.112 t_{x,f}^2 . \quad (6.50)$$

After correcting for this effect, the final momentum from the p -kick method has a resolution of $\delta p/p = (0.6964 \pm 0.005)\%$, as illustrated in Fig. 6.10(a). The dependence of the resolution on the momentum of the particle is shown in Fig. 6.10(b).

Matching criteria

After applying the p -kick method, the T seeds are fitted with the Kalman filter, thereby accounting for multiple scattering and energy loss. The VELO seeds are also fitted, but without correcting for these effects, as the momentum of the VELO seeds is unknown. A good precision on the track parameters from these fits is required for an optimal track

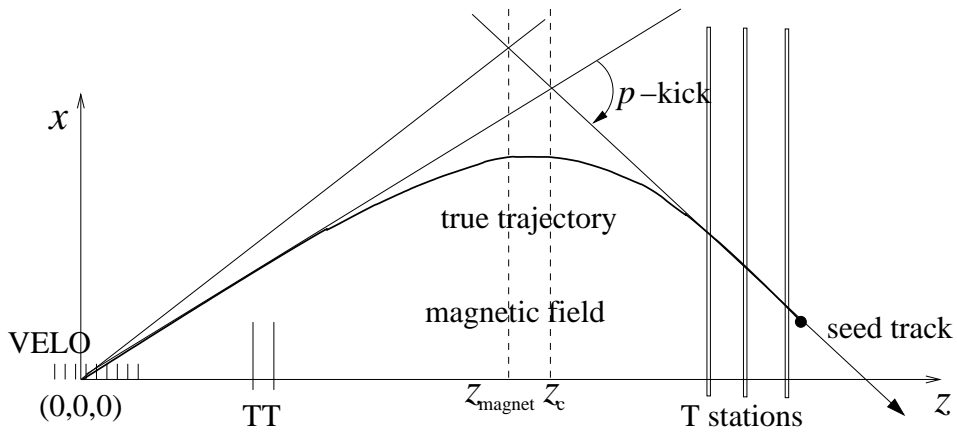


Figure 6.9: Schematic drawing of the p -kick method (not to scale). The effect of the magnetic field is approximated by an instant kick at z_{magnet} . Along this trajectory, the integrated magnetic field is estimated, and a new value for the centre of the magnetic field, z_c , for this trajectory is obtained. The difference in slopes and the updated value for the integrated field are used to estimate the actual momentum.

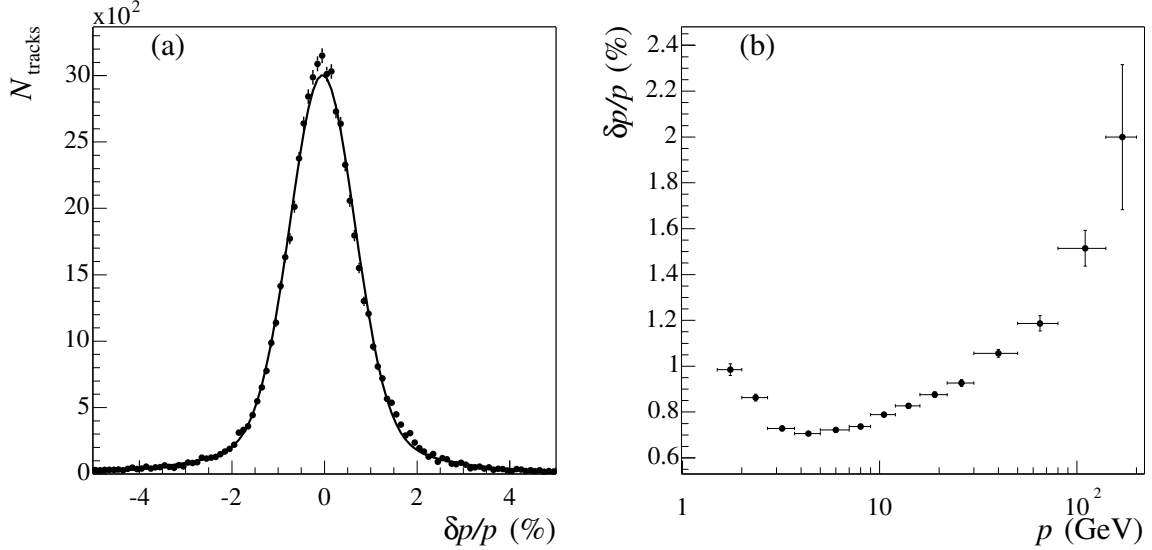


Figure 6.10: The distribution of the momentum resolution obtained with the p -kick method (a), fitted with a double Gaussian. The core resolution is $(0.6964 \pm 0.005)\%$; the fraction in the tail is 25%. The right figure shows the resolution, now fitted with a single Gaussian, as a function of the momentum.

matching efficiency. Using the momentum from the *p*-kick method, the T seeds are then extrapolated through the magnetic field to a plane, located just behind the last VELO station at $z_{\text{match}} = 752$ mm, where they are matched to the VELO seeds. For each combination, a χ^2_{match} is calculated as follows:

$$\chi^2_{\text{match}} = (\vec{x}_{\text{VELO}} - \vec{x}_T)(C_{\text{VELO}} + C_T)^{-1}(\vec{x}_{\text{VELO}} - \vec{x}_T) , \quad (6.51)$$

where \vec{x}_{VELO} and \vec{x}_T are the track parameters of the VELO and T seeds at z_{match} , and C_{VELO} and C_T are the corresponding covariance matrices. Since the momentum of the VELO seeds cannot be determined, the momentum component is not evaluated in (6.51). The combinations with χ^2_{match} below a certain cut are selected. When a VELO or T seed is selected more than once, only the combination with the lowest χ^2_{match} is kept. This requirement reduces the amount of wrong combinations.

When extrapolating the T seeds to the VELO, it is not needed to account for multiple scattering. The effect of multiple scattering is expected to be roughly the same for all T seeds. This means that the same efficiency can be obtained as in the case when multiple scattering is properly taken into account. It should be noted, however, that the values for χ^2_{match} will be much higher due to underestimated errors in the covariance matrix of the T seeds. The main advantage of neglecting the multiple scattering is the gain in processing speed of the matching procedure.

Figure 6.11 shows the distribution of χ^2_{match} in concurrent mode for correct and wrong matches. In order to reduce the number of wrong matches, a cut is placed at $\chi^2_{\text{match}} = 500$.

The matching efficiency is defined as

$$\varepsilon_{\text{match}} = \frac{N_{\text{correct}}}{N_{\text{MC}}} , \quad (6.52)$$

where N_{correct} is the number of correct matches found by the algorithm and N_{MC} is the number of true matches according to the Monte Carlo information. In addition, the wrong match fraction is defined as

$$w_{\text{match}} = \frac{N_{\text{tot}} - N_{\text{correct}}}{N_{\text{tot}}} = \frac{N_{\text{wrong}}}{N_{\text{tot}}} , \quad (6.53)$$

where N_{wrong} is the number of wrong matches and N_{tot} is the total number of matches found. Figure 6.12(a) shows the matching efficiency and wrong match fraction as a function of the seed multiplicity in the event. The seed multiplicity is defined as the number of reconstructed VELO and T seeds, $N_{\text{VELO+T}}$, which is 142 on average. Clearly, both the matching efficiency and wrong match fraction scale linearly with the multiplicity.

Figure 6.12(b) shows the matching efficiency and wrong match fraction as a function of the momentum (averaged over all tracks per momentum bin). The mean efficiency equals $(87.9 \pm 0.1)\%$ with a $(7.8 \pm 0.1)\%$ wrong match fraction. As can be seen in the figure, up to $p \approx 5$ GeV the efficiency rises steeply. For $p > 5$ GeV the mean efficiency equals $(91.2 \pm 0.1)\%$. The corresponding wrong match fraction equals $(4.8 \pm 0.1)\%$. In comparison, the first approach of track matching, which matches tracks with straight

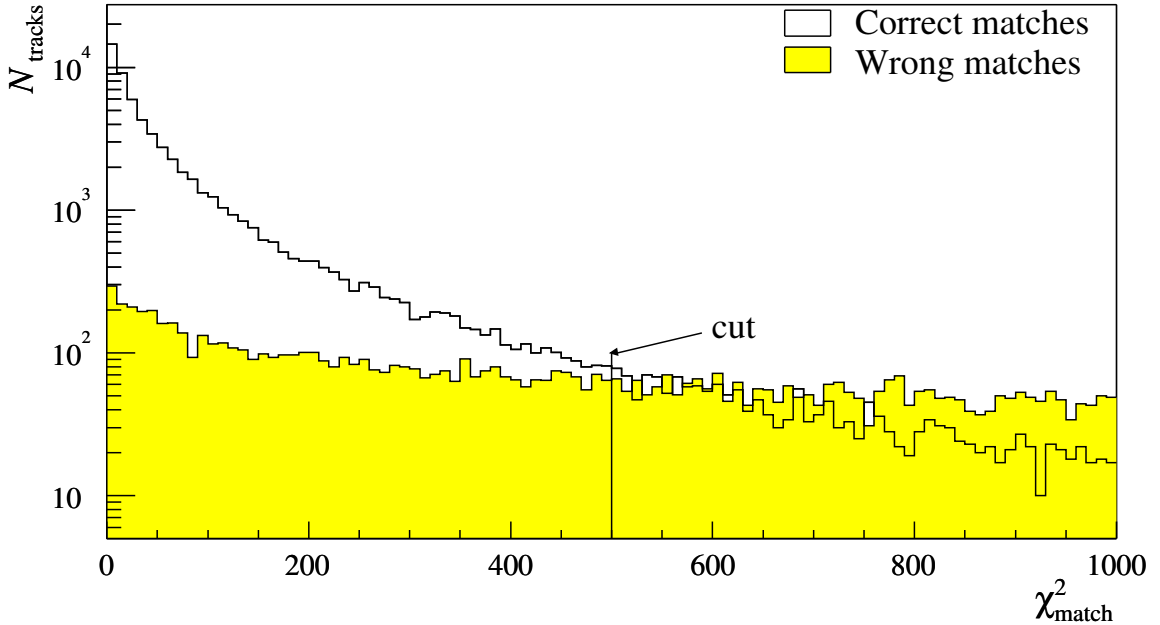


Figure 6.11: Distribution of χ^2_{match} for correct and wrong matches. Beyond $\chi^2_{\text{match}} \sim 500$ the contribution from wrong matches dominates. Consequently, the cut is placed at $\chi^2_{\text{match}} = 500$.

lines in the focal plane of the magnet, reaches efficiencies of $(76.5 \pm 0.2)\%$ for all tracks and $(88.3 \pm 0.2)\%$ for those with $p > 5 \text{ GeV}$. The wrong match fractions are comparable.

Adding TT hits

In the final step of the matching procedure, the corresponding TT hits must be added to each matched track. The hits in the silicon layers of the TT stations are actually clusters of neighbouring strips with a signal-over-noise ratio above threshold. The trajectory through the TT stations is estimated by extrapolating the VELO track to each TT layer, using the momentum from the T seed. Due to multiple scattering in RICH 1, the predicted trajectory may deviate from true trajectory. However, this deviation is approximately equal for all TT hits belonging to the same particle. The algorithm exploits this idea by searching for *groups* of TT hits having approximately the same distance from the predicted trajectory.

In the search, only one measurement per TT layer is allowed. This means that a group consist of maximally 4 TT hits. Only hits which have a distance smaller than 10 mm are considered in the search. The hits in a group are not allowed to differ in distance by more than 1 mm (in the same station) or 2 mm (in different stations). When 2 or more hits in the same layer are compatible with the group, a separate group is created for each hit. Furthermore, a group should have at least 3 TT hits.

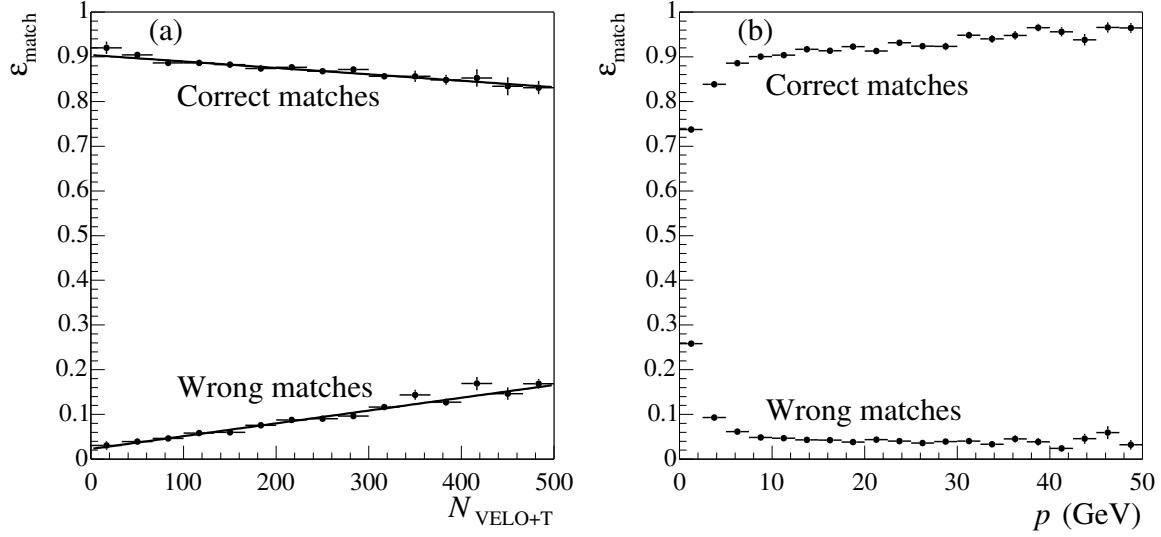


Figure 6.12: Matching efficiency and wrong match fraction versus event multiplicity (a) and versus momentum (b). The multiplicity, $N_{\text{VELO+T}}$, is calculated as the total number of VELO tracks and T seeds.

When a matched track has more than one group of TT hits, only the one with the smallest quality is selected. The quality of a group is defined as

$$q^2 = \bar{d}^2 + w_{\text{spread}}^2 s_d^2 , \quad (6.54)$$

where \bar{d} is the mean distance, w_{spread} is a weight factor, and s_d is the rms spread of the distances. The weight factor is tuned such that the TT hit efficiency is the highest. Figure 6.13(a) shows the hit efficiency as a function of w_{spread} . As can be seen, the efficiency quickly rises to a plateau, where it becomes insensitive for changes in the actual value of w_{spread} . For very large values of w_{spread} , the efficiency slowly decreases again. When the optimal value is chosen at $w_{\text{spread}} = 7$, the average hit efficiency equals $(88.5 \pm 0.3)\%$, and the fraction of wrong hits equals $(5.5 \pm 0.1)\%$. Figure 6.13(b) shows the efficiency and wrong hit fraction as a function of the seed multiplicity ($N_{\text{VELO+T}}$).

Finally, it should be noted that the addition of TT hits to the matched tracks affects the momentum resolution obtained from the track fit. These additional measurements after RICH 1 and in front the magnetic field, improve the Gaussian core of the momentum resolution from $(0.44 \pm 0.06)\%$ to $(0.33 \pm 0.04)\%$.

6.3 Overall tracking performance

The algorithms, discussed in Section 6.2.2, operate in a combined effort to reconstruct all possible tracks. The final goal of the track finding procedure is to obtain the highest efficiency for each track type, while keeping the ghost rate at a minimum. Since each track type has different applications in the event reconstruction and physics analysis, it

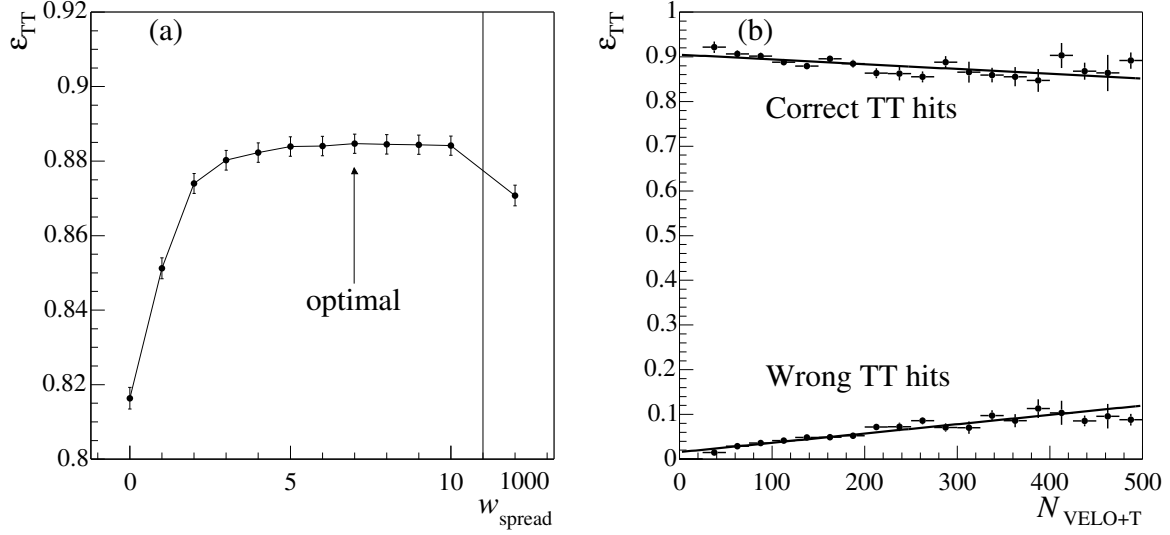


Figure 6.13: The efficiency (ε_{TT}) of adding the correct TT hits versus w_{spread} (a). After $w_{\text{spread}} = 5$ the efficiency reaches a plateau. The last data point at $w_{\text{spread}} = 1000$ is added for comparison on a separate scale. It indicates that the efficiency slowly drops for high values of w_{spread} . The right plot (b) show the hit efficiency and wrong hit fraction versus the seed multiplicity, $N_{\text{VELO+T}}$.

is convenient to define separate efficiencies. Therefore, the efficiency for each track type is normalised to a sample of “reconstructible” particles:

- **VELO tracks:** The particle must have at least 3 r and 3 ϕ hits.
- **T tracks:** The particle must have at least 1 hit in an x layer and 1 hit in a stereo layer (u or v) in each station T1–T3.
- **Long tracks:** The particle must be reconstructible as a VELO and as a T track.
- **Upstream tracks:** The particle must be reconstructible as a VELO track and have at least 3 hits in the TT stations.
- **Downstream tracks:** The particle must be reconstructible as a T track and have at least 3 hits in the TT stations.

Tracks found by a pattern recognition algorithm are defined to be successfully reconstructed (efficient) when at least 70% of the assigned hits originates from the same particle. Furthermore, long tracks must be successfully reconstructed both in the VELO and in the T stations. Upstream and downstream tracks must be successfully reconstructed in respectively the VELO or the T stations, and have at least 1 correct hit in the TT.

Finally, the track reconstruction efficiency can be expressed as

$$\varepsilon_{\text{track}} = \frac{N_{\text{correct}}}{N_{\text{MC}}} , \quad (6.55)$$

where N_{correct} is the number of reconstructed tracks that is associated to a reconstructible particle and N_{MC} is the total number of reconstructible particles. The error on the efficiency is given, according to a binomial distribution, by

$$\sigma_{\varepsilon} = \frac{\sqrt{N_{\text{correct}}(1 - \varepsilon_{\text{track}})}}{N_{\text{MC}}} . \quad (6.56)$$

Similarly, the ghost rate and corresponding error are given by

$$g_{\text{track}} = \frac{N_{\text{ghost}}}{N_{\text{tot}}} , \quad (6.57)$$

$$\sigma_g = \frac{\sqrt{N_{\text{ghost}}(1 - g_{\text{track}})}}{N_{\text{tot}}} , \quad (6.58)$$

where N_{ghost} is the number of reconstructed tracks that cannot be associated to a Monte Carlo particle and N_{tot} is the total number reconstructed tracks.

The average number of reconstructed tracks in $b\bar{b}$ inclusive events equals 106. This number is composed of 34 VELO tracks, 33 long tracks, 19 T tracks, 6 upstream tracks, and 14 downstream tracks. In the following, the performance for each track type is briefly discussed. The long tracks receive special attention, as they are the essential ingredient for the reconstruction of most B decays.

Long tracks

A reconstructed long track contains on average 35.6 measurements, of which 12.7 in the VELO, 3.0 in the TT, 2.4 in the IT, and 17.5 in the OT. It should be noted that these are average numbers. When traversing only the OT, a long track has on average 21.3 measurements in the T stations; when traversing only the IT, a long track has on average 11.8 measurements in the T stations. About 75% of the long tracks pass through the OT section and 12% through the IT section, while the rest has measurements in both detectors. Figure 6.14 shows the distributions of the number of VELO measurements and the total number of measurements on a long track. After outlier removal, the correct hits are found with an efficiency of about 94% and a purity of 99%.

The average efficiency for finding long tracks in $b\bar{b}$ events equals $(91.34 \pm 0.05)\%$ of which $(3.35 \pm 0.03)\%$ is from matched tracks. The dependence on the particle's momentum is illustrated in Figure 6.15(a). The efficiency rises as a function of the momentum, until it reaches a plateau. For $p > 5$ GeV the efficiency is $(94.31 \pm 0.08)\%$. For the decay products of B mesons, which typically have a high momentum, the track reconstruction efficiency is $(93.1 \pm 0.1)\%$.

The total ghost rate for long tracks equals $(11.53 \pm 0.06)\%$. Figure 6.15(b) shows the ghost rate as a function of the reconstructed momentum. The ghost rate decreases

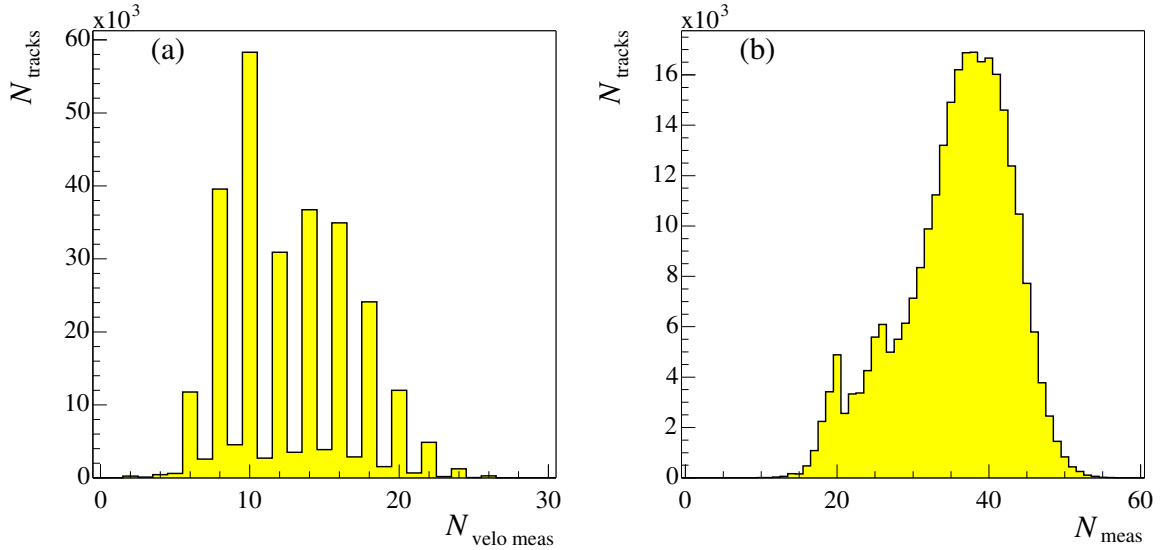


Figure 6.14: Distribution of the number of measurements on a long track, in the VELO (a) and in all tracking detectors (b). Due to the space-point track search, which combines the r and ϕ clusters, a track typically has an even number of VELO measurements. The small peaks at ~ 20 and ~ 25 in (b) are from long tracks that pass the IT only and long tracks that pass both the IT and TT.

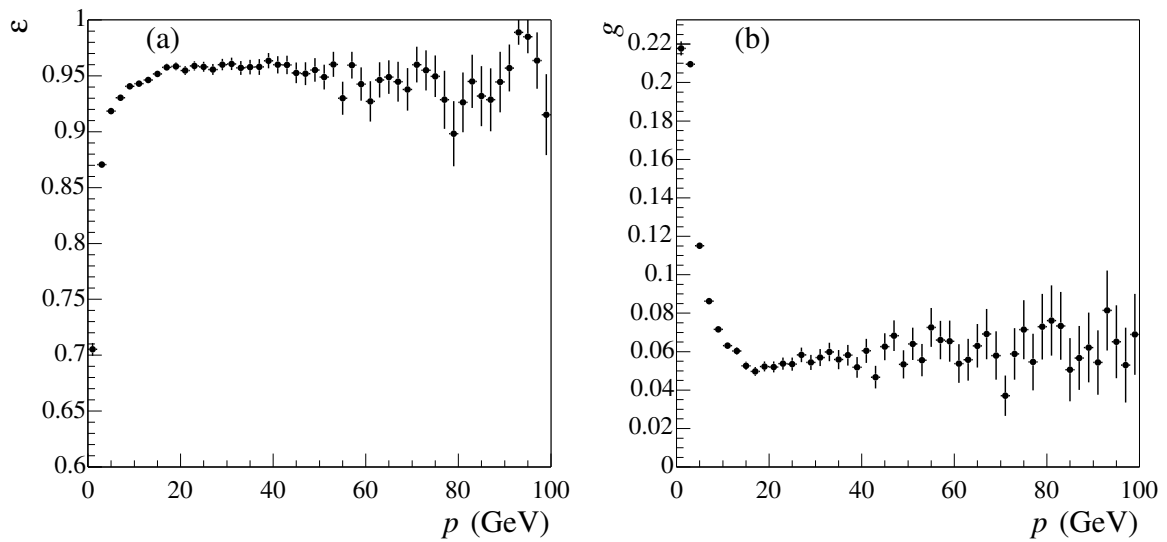


Figure 6.15: Tracking efficiency (a) and ghost rate (b) for long tracks as a function of momentum, p .

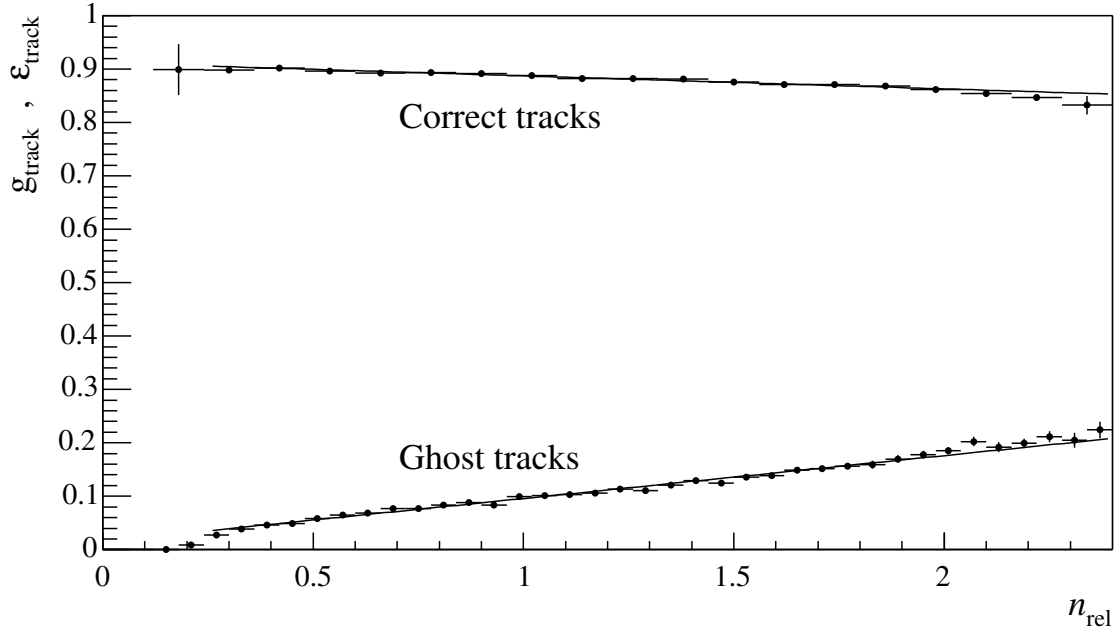


Figure 6.16: Track reconstruction efficiency and ghost rate for long tracks as a function of the relative hit multiplicity, n_{rel} .

towards higher momenta. For $p > 5 \text{ GeV}$ the corresponding ghost rate equals $(7.65 \pm 0.05)\%$.

There is a clear correlation between the multiplicity of an event and the track reconstruction efficiency and ghost rate. The higher the event multiplicity, the more difficult it becomes to assign the correct hits to the track candidates. The relative hit multiplicity, n_{rel} , in an event is defined as

$$n_{\text{rel}} = \frac{1}{4} \left(\frac{n_{\text{VELO}}}{\langle n_{\text{VELO}} \rangle} + \frac{n_{\text{TT}}}{\langle n_{\text{TT}} \rangle} + \frac{n_{\text{IT}}}{\langle n_{\text{IT}} \rangle} + \frac{n_{\text{OT}}}{\langle n_{\text{OT}} \rangle} \right) , \quad (6.59)$$

where n_{xx} is the number of hits in a given subdetector. Figure 6.16 shows the dependence of the efficiency and ghost rate⁵ as a function of n_{rel} . The figure indicates a linear dependence, which can be described by

$$\varepsilon_{\text{track}} = (91.2 - 2.4 n_{\text{rel}})\% , \quad (6.60)$$

$$g_{\text{track}} = (1.5 + 8.0 n_{\text{rel}})\% . \quad (6.61)$$

It is found that the efficiency decreases only slowly with increasing multiplicity. At the same time, the ghost rate rises more steeply. Nevertheless, the reconstruction of long tracks proves to be robust against higher hit multiplicities. It follows that even for high-multiplicity events of $n_{\text{rel}} = 3$, the ghost rate is still below 25%, while the efficiency is about 84%.

⁵In this case, the track reconstruction efficiency and ghost rate are averaged per event.

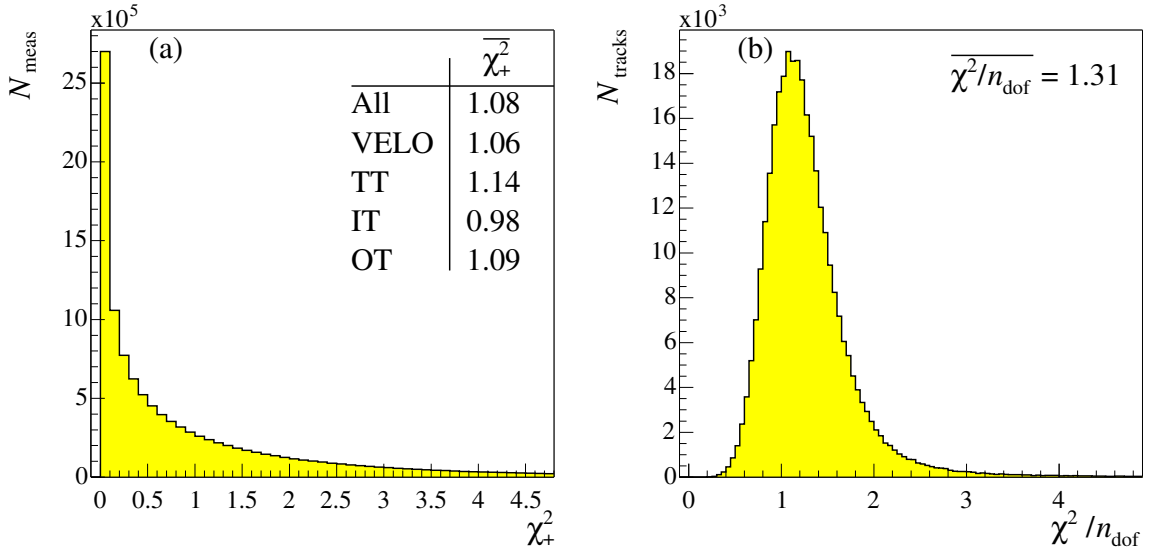


Figure 6.17: The χ^2_+ of all measurements from long tracks (a). Inserted is a table with the mean χ^2_+ for each subdetector. The right plot (b) shows the total χ^2 per degree of freedom (n_{dof}) for long tracks.

Table 6.1: Results of single Gaussian fits for the resolution and pull distributions of the track parameters at the first measurement and at the vertex location.

	x	y	t_x	t_y	$\delta p/p$
resolution at 1 st meas.	$9.4 \mu\text{m}$	$9.3 \mu\text{m}$	2.33×10^{-4}	2.03×10^{-4}	0.35%
resolution at vertex	$48.2 \mu\text{m}$	$46.7 \mu\text{m}$	3.39×10^{-4}	3.39×10^{-4}	0.35%
	x	y	t_x	t_y	q/p
pull at vertex	1.13	1.09	1.08	1.08	1.28

Finally, all reconstructed long tracks are fitted with the Kalman filter, described in this chapter. The distributions of the smoothed χ^2_+ of the measurements calculated from (6.24) and the total χ^2 per degree of freedom (n_{dof}) are shown in Fig. 6.17. In the ideal situation, the average χ^2 / n_{dof} should be one. The present deviation is ascribed to (a) differences in the transport of the track parameters in the simulation and reconstruction, (b) non-Gaussian tails in the multiple scattering distribution, (c) incomplete parameterisation of the measurement errors, and (d) wrong measurements on the track (hit impurity).

The accuracy of the estimated track parameters at the location of the vertex is an important measure for the performance of LHCb, because these parameters are directly used in the reconstruction of B vertices. The resolution and pull at the vertex and the resolution at the first measurement are listed in Table 6.1. It follows that the errors on the track parameters are overestimated, resulting in slightly larger pulls. This deviation

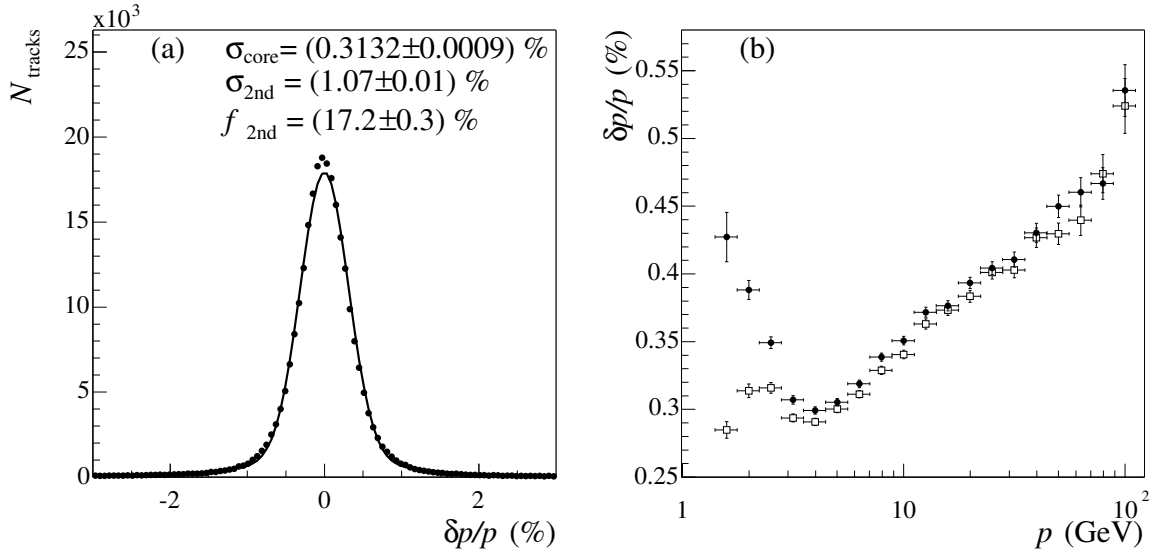


Figure 6.18: Momentum resolution of long tracks at the vertex (a). A double Gaussian is fitted to the distribution. The right plot (b) shows the momentum dependence of long tracks found by the matching and forward algorithms (filled circles) and of all particles reconstructible as long tracks (open boxes). In this case, the momentum resolution is determined from a single Gaussian fit in each momentum bin.

can be explained by the same arguments as mentioned above. The resolution at the vertex is mainly determined by the extrapolation of the track through the RF foil, which separates the primary beam vacuum from the silicon sensors. Only the error on the momentum is not affected by this extrapolation.

Long tracks have an accurate momentum estimate. On average, the momentum for long tracks has a core resolution of 0.31%, as shown in Fig. 6.18(a). Figure 6.18(b) shows the momentum dependence of the resolution for long tracks found by the matching and forward algorithms and for all particles reconstructible as long tracks (“cheated pattern recognition”). The rise in $\delta p/p$ towards low momenta in the curve for the real pattern recognition can be ascribed to the decrease in hit purity. Since the cheated pattern recognition does not suffer from wrong hits on the track, this rise is (almost) absent at low momenta. The increasing momentum resolution towards higher momenta is explained by the decrease in curvature of the track.

Another important measure for the performance of the track fit is the impact parameter with respect to the position of the true Monte Carlo vertex. The impact parameter is defined as the shortest distance from the track to the vertex. The corresponding distribution for long tracks from B decays is depicted in Fig. 6.19(a). The relation between the impact parameter and $1/p_T$ is illustrated in Fig. 6.19(b). The observed linear

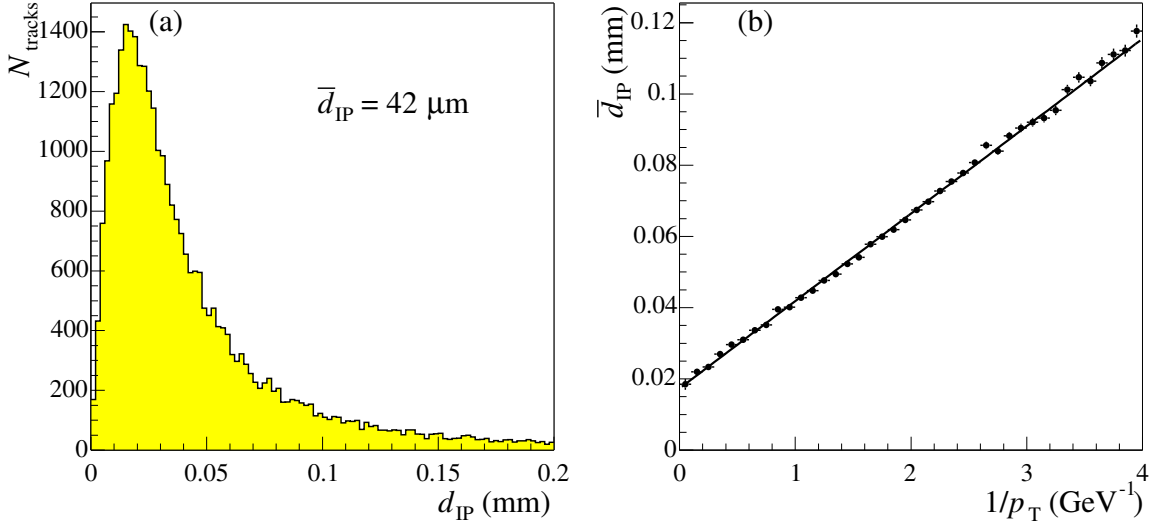


Figure 6.19: Distribution of the impact parameter, d_{IP} , of long tracks from B decays (a), and mean impact parameter versus $1/p_T$ for all long tracks.

dependence can be parameterised as

$$\bar{d}_{IP} = \left(17 + \frac{25 \text{ GeV}}{p_T} \right) \mu\text{m} , \quad (6.62)$$

with p_T expressed in GeV.

Upstream tracks

Upstream tracks have on average 11.3 hits in the VELO and 3.9 hits in the TT stations, while the hit purity is more than 99%. Below $p = 1 \text{ GeV}$ the search for continuations of VELO seeds in the TT results in many track candidates, leading to a high ghost rate and, as a consequence, a reduced efficiency. Above $p = 1 \text{ GeV}$, particles that are only reconstructible as upstream tracks are found with an efficiency of about 75% and a ghost rate of 15% [26]. The moderate B field between the VELO and TT provides, after applying the Kalman filter, a momentum estimate of $\delta p/p \sim 15\%$.

Downstream tracks

On average 3.2 TT hits are assigned to each downstream track. Downstream tracks are mainly used for enhancing the reconstruction efficiency of charged pions from K_s^0 's in B decays. Due to the long decay length of the K_s^0 , many of these pions will not leave (enough) hits in the VELO. Only about a quarter of these pions is reconstructible as either a long or upstream track. Half of all K_s^0 's decay outside the VELO, but before the TT. Their decay products are reconstructible as downstream tracks. The efficiency to find both pions from such a decay is 54%, corresponding to a single track efficiency

of about 74% [26]. The momentum of downstream tracks is measured with an average resolution of 0.39%. This is comparable to that of long tracks, since they also traverse through almost the full magnetic field.

VELO tracks

The remaining VELO seeds that have no continuation as either a long or upstream track are defined to be VELO tracks. They are mainly used for the reconstruction of the primary vertex. Typically, they have 9.3 hits, with a purity of more than 99%. The efficiency to reconstruct particles that are only reconstructible as a VELO track is $\sim 50\%$. The ghost rate is approximately 20%. The magnetic field in the VELO is too low to measure the momentum.

T tracks

The T seeds that have not been used in the track matching or downstream tracking are defined to be T tracks. They have on average 16.8 hits, of which 12.7 in the OT and 4.1 in the IT, with a purity of about 97%. The reconstruction efficiency of particles that are only reconstructible as T tracks equals 55%, with a corresponding ghost rate of 28%. The inefficiency is mainly due to low-momentum particles originating from secondary interactions with the material. For $p > 5 \text{ GeV}$ the efficiency rises to 72%. The fringe field in the T station provides a rough momentum estimate with a resolution of $\delta p/p \approx 12\%$.

6.4 Track visualisation

The LHCb event display, PANORAMIX, is well suited to visualise hits and reconstructed tracks in the tracking detectors. The location of the tracking stations is read directly from the GAUDI detector description service. All hits in the tracking detectors can be displayed as straight lines, except the hits in the VELO r sensors, which are drawn as circular lines. For hits in the VELO, TT, and IT, the line is defined by the centre-of-gravity of the cluster. For hits in the OT, the line is defined by the position of the wire. The endpoints of the line are determined by the dimensions of the corresponding sensor or module. Figure 6.20 shows a three-dimensional display of the tracking system with all hits and reconstructed tracks.

When a measurement is assigned to a track, a cross is drawn along the hit, at the location of closest approach with the track. In case of OT measurements, a circle representing the reconstructed drift distance is drawn in addition, as illustrated in Figure 6.21.

After the track fit, the states provide all the necessary information to draw the track through the detector. In the regions of low magnetic field (i.e., before $z = 2165 \text{ mm}$ and after $z = 9450 \text{ mm}$), the tracks are simply drawn as straight lines. Inside the magnetic field region, the curved trajectory is determined from the track states at 100 equidistant z positions. In the track fit, however, only the states before and after the magnetic field region are stored. In order to draw the full trajectory through the magnet, these

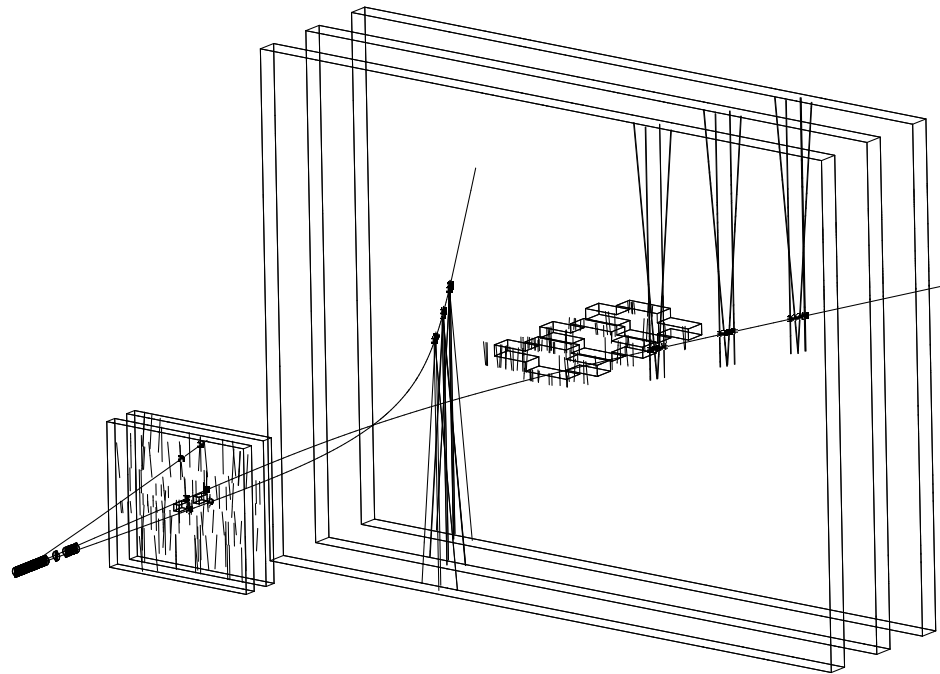


Figure 6.20: Display of the hits and tracks in a low-multiplicity minimum-bias event. From left to right, the VELO, TT, and T stations are drawn. Most of the hits that do not lie on a track are either noise hits or belong to (secondary) particles that are not reconstructible.

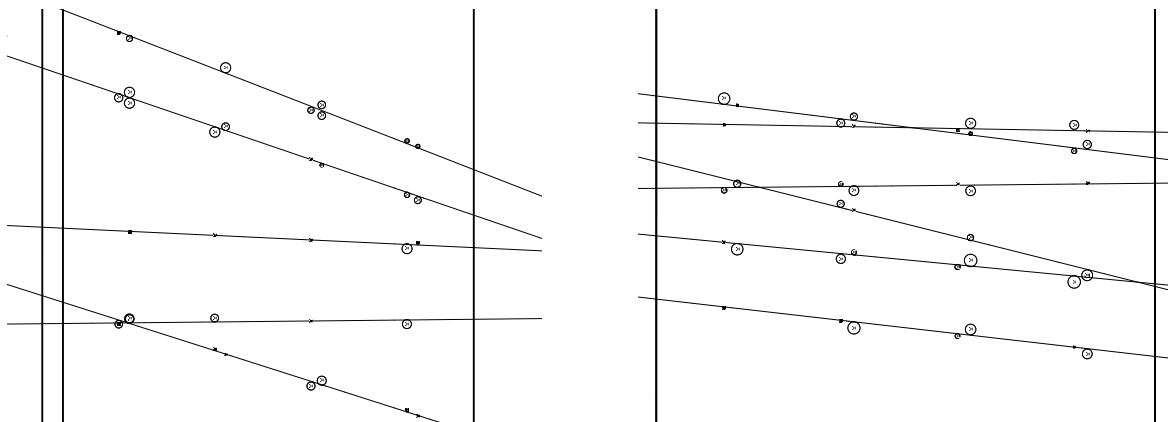


Figure 6.21: Two examples of intersections of an OT station, showing the tracks and their assigned hits. The assigned hits are displayed by small crosses, illustrating the location of the wire, and by circles, illustrating the reconstructed drift distance.

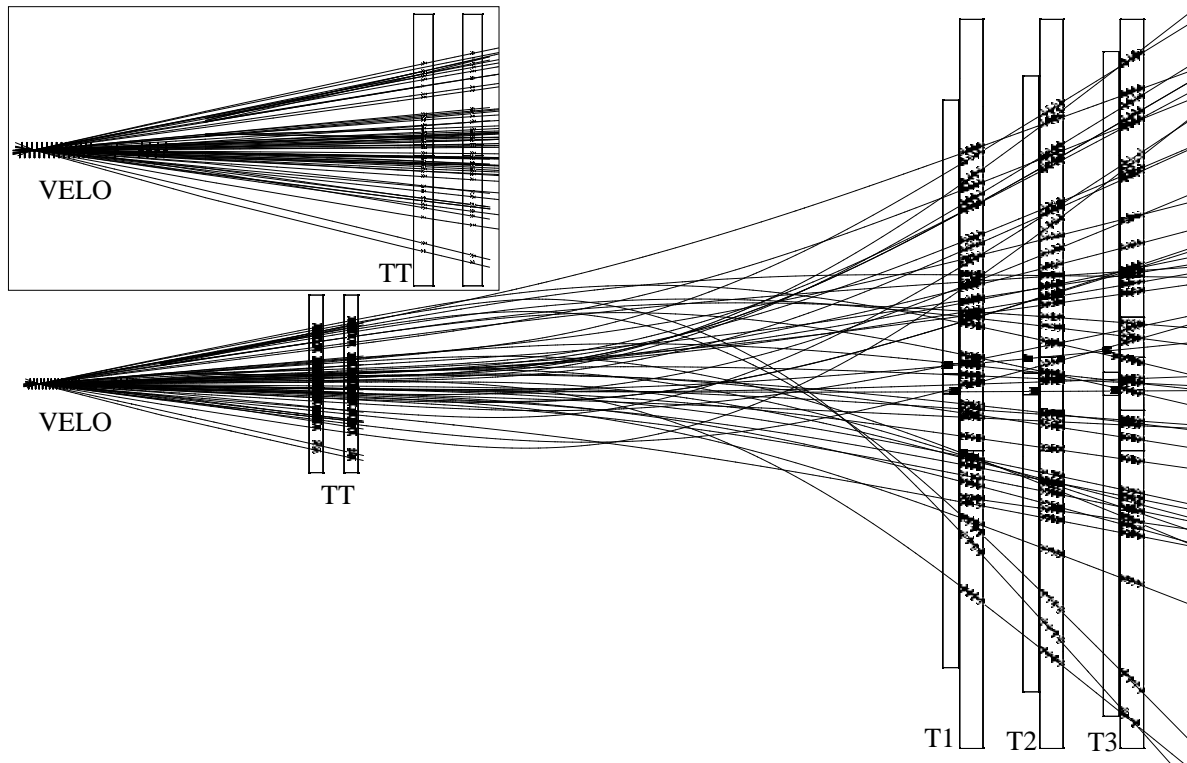


Figure 6.22: Display of an average-multiplicity event in the bending plane of the tracking system, showing the reconstructed tracks and their assigned hits. The insert is a zoom of the VELO–TT region.

100 intermediate states are obtained by interpolation. Hereby, the two track states at $z = 2165$ mm and $z = 9450$ mm are extrapolated with a fifth-order Runge-Kutta method. Then, at each z position, the weighted mean of these two states is calculated, giving the best estimate of the position along the trajectory. Figure 6.22 shows a typical event in the tracking event display including the different track types.

Chapter 7

Selection and sensitivity studies

The last step in the simulation, digitisation, and reconstruction chain is the selection of specific B decay channels. The reconstructed tracks and particle identities are important ingredients in this event selection. By selecting a set of tracks originating from a secondary vertex, which have the required particle identity, and together have an invariant mass corresponding to the B mass, B decays can be found. The selection of rare B decay events suffers from a potentially huge contamination of background events. Hence, for a reliable estimate of the background contamination, millions of background events need to be simulated. The aim is to reduce this background in the event selection in order to obtain a maximum sensitivity on the physics parameters. In this chapter, the selection of $B_s^0 \rightarrow D_s^- \pi^+$ and $B_s^0 \rightarrow D_s^\mp K^\pm$, two of LHCb's benchmark channels, is discussed. In addition, a study on two closely-related channels, namely $B_s^0 \rightarrow D_s^{*\mp} K^\pm$ and $B_s^0 \rightarrow D_s^\mp K^{*\pm}$, is presented.

The annual event yield and decay time resolution are obtained from the full Monte Carlo simulation. However, the final physics sensitivity is determined using a separate, fast Monte Carlo programme, which simulates the decay time distributions in LHCb. A combined likelihood fit on the decay time distributions of $B_s^0 \rightarrow D_s^- \pi^+$ and $B_s^0 \rightarrow D_s^{(*)\mp} K^{(*)\pm}$ is applied to extract the sensitivity on the oscillation frequency Δm_s and CP -violating weak phase $\gamma - 2\chi$.

7.1 Decays of interest

As explained in Chapter 2, the $B_s^0 \rightarrow D_s^- \pi^+$ decay is well suited to measure the $B_s^0 \leftrightarrows \bar{B}_s^0$ oscillations. The final state of this decay, either $D_s^- \pi^+$ or $D_s^+ \pi^-$, reveals the B flavour *at decay time*. The flavour *at the time of production* is determined with the flavour tagging method, which will be explained in Section 7.4. In the Standard Model, the oscillation frequency is predicted to be $\Delta m_s \simeq 20 \text{ ps}^{-1}$. This implies that a good time resolution is essential to resolve the fast B_s oscillations.

The interference terms in the four time-dependent decay rates (2.29) of $B_s^0 \rightarrow D_s^\mp K^\pm$ give access to the phases of λ_f and $\bar{\lambda}_{\bar{f}}$. As follows from Eq. (2.36), both phases are needed to extract the CP -violating weak phase $\gamma - 2\chi$. The same equations also hold

Table 7.1: The branching fractions used to estimate annual the event yield. The numbers are obtained from Ref. [8].

Decay channel	Branching fraction (BF)	Estimated from
$b \rightarrow B_s$	$(10.7 \pm 1.1)\%$	direct measurement
$B_s^0 \rightarrow D_s^- \pi^+$	$(2.76 \pm 0.25) \times 10^{-3}$	$B^0 \rightarrow D^- \pi^+$
$B_s^0 \rightarrow D_s^{(*)-} K^{(*)+}$	$(2.0 \pm 0.6) \times 10^{-4}$	$B^0 \rightarrow D^- K^+$
$B_s^0 \rightarrow D_s^{(*)+} K^{(*)-}$	$(2.7 \pm 1.0) \times 10^{-5}$	$B^0 \rightarrow D_s^+ \pi^-$
$D_s^\pm \rightarrow K^+ K^- \pi^\pm$	$(4.4 \pm 1.2) \times 10^{-2}$	direct measurement
$D_s^{*\pm} \rightarrow D_s^\pm \gamma$	$(94.2 \pm 2.5)\%$	direct measurement
$K^*(892) \rightarrow K\pi$	$\sim 100\%$	direct measurement
$K_S^0 \rightarrow \pi^+ \pi^-$	$(68.95 \pm 0.14)\%$	direct measurement

for the decays of $B_s^0 \rightarrow D_s^{*\mp} K^\pm$ and $B_s^0 \rightarrow D_s^\mp K^{*\pm}$.¹ Therefore, these decays may provide additional statistical sensitivity on $\gamma - 2\chi$. The branching fractions, BF, for all (sub)decays are listed in Table 7.1. It should be noted that the ratio $\text{BF}(B_s^0 \rightarrow D_s^+ K^-)/\text{BF}(B_s^0 \rightarrow D_s^- K^+)$ is equal to $|\lambda_f|^2$, as defined in (2.25). From Table 7.1 it can be deduced that $|\lambda_f| \approx 0.37$.

The D_s^\pm meson has a lifetime of ~ 0.5 ps, which is about one third of the B lifetime. Accordingly, the $B_s^0 \rightarrow D_s^- \pi^+$ and $B_s^0 \rightarrow D_s^{(*)\mp} K^{(*)\pm}$ decays have two separate decay vertices. The decay of $D_s^\pm \rightarrow K^+ K^- \pi^\pm$ has a significant branching fraction and provides a clear signal, since the final state contains only charged particles, of which two are kaons.² Other decay channels of the D_s^\pm are not considered in this thesis, although they might give additional sensitivity.

The decay of the $D_s^{*\pm}$ and $K^*(892)^\pm$ resonances gives rise to additional neutral particles in the final state. The $D_s^{*\pm}$ resonance decays mainly to a D_s^\pm and a photon (γ), while the $K^*(892)^\pm$ resonance decays either to $K^\pm \pi^0$ (33%), to $K_L^0 \pi^\pm$ (33%), or to $K_S^0 \pi^\pm$ (33%). In LHCb, K_L^0 mesons are not reconstructed. For this reason, the selection of $B_s^0 \rightarrow D_s^\mp K^{*\pm}$ is divided into two subsamples: one with $K^\pm \pi^0$ in the final state and one with $K_S^0 \pi^\pm$ in the final state.

The total branching fraction, BF_{tot} , takes into account the full decay of the B_s into the final state. Table 7.2 gives the total branching fraction and annual production for the five decays of interest. The annual production is obtained from the total branching fraction as

$$N_{\text{decay}} = \sigma_{b\bar{b}} \times \int \mathcal{L} dt \times 2 \times \text{BF}(b \rightarrow B_s) \times \text{BF}_{\text{tot}} , \quad (7.1)$$

where the factor 2 accounts for the fact that the b as well as the \bar{b} may hadronise into

¹Since the final state of these two decay channels has an angular momentum of $L = 1$, a subtle $(-1)^L$ factor [99] that arises in the expressions for λ_f and $\bar{\lambda}_f$ in (2.36) should be taken into account when extracting the weak phase from $B_s^0 \rightarrow D_s^{(*)\mp} K^{(*)\pm}$ decays.

²This decay channel also contains intermediate resonances such as the ϕ and the $K^*(892)^0$, which may provide an additional handle to reduce background. However, this possibility is not considered in this thesis.

Table 7.2: The total branching fractions for the five decays of interest. These numbers include the branching fractions of the subsequent decays, such as $D_s^\pm \rightarrow K^+K^-\pi^\pm$, taken from Table 7.1. The expected annual number of decays produced, including the charge-conjugate decays, is calculated from Eq. (7.1).

Decay channel	Total branching fraction	Annual production
$B_s^0 \rightarrow D_s^- \pi^+$	$(1.2 \pm 0.3) \times 10^{-4}$	26×10^6
$B_s^0 \rightarrow D_s^\mp K^\pm$	$(1.0 \pm 0.4) \times 10^{-5}$	2.1×10^6
$B_s^0 \rightarrow D_s^{*\mp} K^\pm$	$(9.4 \pm 3.9) \times 10^{-6}$	2.0×10^6
$B_s^0 \rightarrow D_s^\mp K^{*\pm} (\rightarrow K^\pm \pi^0)$	$(3.3 \pm 1.3) \times 10^{-6}$	7.1×10^5
$B_s^0 \rightarrow D_s^\mp K^{*\pm} (\rightarrow K_s^0 \pi^\pm)$	$(2.3 \pm 0.9) \times 10^{-6}$	4.9×10^5

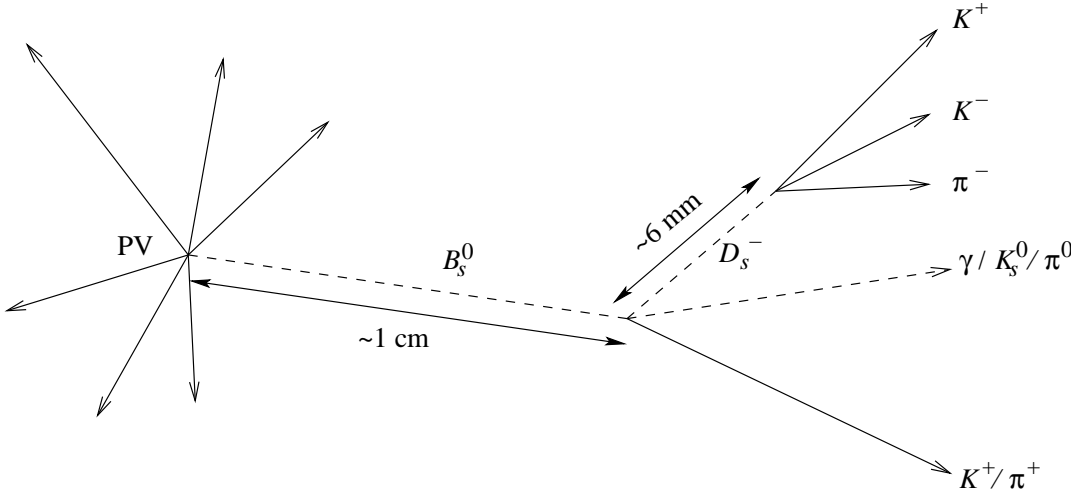


Figure 7.1: Common topology of the $B_s^0 \rightarrow D_s^- \pi^+$ and $B_s^0 \rightarrow D_s^{(\ast)\mp} K^{(\ast)\pm}$ decays.

a B_s . With a cross section of $\sigma_{b\bar{b}} = 500 \mu\text{b}$ and a luminosity of $2 \times 10^{32} \text{ cm}^{-2}\text{s}^{-1}$, a total of $10^{12} b\bar{b}$ pairs are expected per year (10^7 s).

The five decays of interest have similar topologies, depicted in Fig. 7.1. For instance, the $B_s^0 \rightarrow D_s^\mp K^\pm$ and $B_s^0 \rightarrow D_s^- \pi^+$ decays differ only in one particle. For convenience, this particle is referred to as the bachelor particle. Without the RICH detector these two decays would be almost identical. Since the branching ratio $\text{BF}(B_s^0 \rightarrow D_s^- \pi^+)/\text{BF}(B_s^0 \rightarrow D_s^\mp K^\pm) \sim 12$ (see Table 7.2), the $B_s^0 \rightarrow D_s^\mp K^\pm$ decay is overwhelmed by a background from $B_s^0 \rightarrow D_s^- \pi^+$ decays. The RICH detector is able to reduce the background from $B_s^0 \rightarrow D_s^- \pi^+$ in the selection of $B_s^0 \rightarrow D_s^\mp K^\pm$ decays.

In case of the decays of $B_s^0 \rightarrow D_s^{*\mp} K^\pm$ and $B_s^0 \rightarrow D_s^\mp K^{*\pm}$, additional neutral particles (i.e., γ , π^0 , and K_s^0) appear in the final state from the decay of the $D_s^{*\pm}$ and $K^{*\pm}$ resonances. The γ and π^0 ($\rightarrow \gamma\gamma$) are detected by the electromagnetic calorimeter, while the K_s^0 is detected in the tracking system through its decay into two charged pions. Note that all neutral particles originate from the B_s decay vertex.

7.2 Particle identification

Pions are most abundant in the LHCb detector. In $b\bar{b}$ inclusive events, they represent 73.4% of all charged particles that are reconstructed as long tracks. The fractions for the other particles are 15.9% for kaons, 4.0% for protons, 6.3% for electrons, and 0.5% for muons. This means, for instance, that for a clean selection of kaons, additional information on the particle identity must be available to reduce the contamination from pions. Particle identification (PID) in LHCb is provided by the RICH system, the calorimeters, and the muon system (see Sections 3.7–3.9). This section briefly describes the particle identification techniques.

The RICH detectors are mainly responsible for the identification of charged hadrons (i.e., K^\pm , π^\pm , and p), while it also offers some separation power between hadrons and leptons. The identification procedure [100] utilises the number of photons detected in each RICH ring as well as their Cherenkov angle. In the end, the significance of the K – π separation is converted into a likelihood ratio. The logarithm of this likelihood ratio is mathematically equivalent to a difference in the log-likelihood. Hence, the delta log-likelihood between the kaon and pion hypothesis equals

$$\Delta \ln \mathcal{L}_{K\pi} = \ln \mathcal{L}(K) - \ln \mathcal{L}(\pi) = \ln \frac{\mathcal{L}(K)}{\mathcal{L}(\pi)} . \quad (7.2)$$

The significance of the K – π separation can be expressed in terms of standard deviations as $N_\sigma = \sqrt{2|\Delta \ln \mathcal{L}_{K\pi}|}$. Similarly, the $\Delta \ln \mathcal{L}$ values for leptons and protons are determined.

The electromagnetic calorimeter (ECAL) identifies electrons, photons, and π^0 's [101]. Electron candidates are created when the energy and position of an ECAL cluster matches the extrapolated position and momentum of a track. The χ^2 of the matching procedure is required to be < 49 . In addition, the ECAL cluster must be compatible with an electromagnetic shower, which means that it must have a significant energy deposit in the preshower and a small deposit along the trajectory in the HCAL. Furthermore, bremsstrahlung photons emitted before magnet help to identify electron candidates by associating photon clusters with the track before the magnet. Each of these requirements provides an estimator, which are combined to provide the maximal electron–non-electron separation.

The identification of the neutral particles [102] γ and π^0 is exclusively made by the ECAL. Photons are found by searching for clusters that cannot be matched to a reconstructed track. The cluster–track matching procedure requires that $\chi^2 > 4$. The sample of candidate photons is divided into those that have converted ($\gamma \rightarrow e^+e^-$) and those that have not converted. Photons that have converted after the magnet (e.g., inside RICH 2 or M1) are still detected as a single cluster. These clusters are identified as converted, since the electron pair often leaves a hit in the SPD. After the photon reconstruction, π^0 's are found by searching for the decay $\pi^0 \rightarrow \gamma\gamma$. Low- p_T π^0 's leave two distinct photon clusters in the ECAL. These resolved π^0 's are found by combining all photon candidates and cutting on the invariant mass. High- p_T π^0 's give rise to a single, merged cluster in the ECAL. Nevertheless, in some cases the shape of the cluster

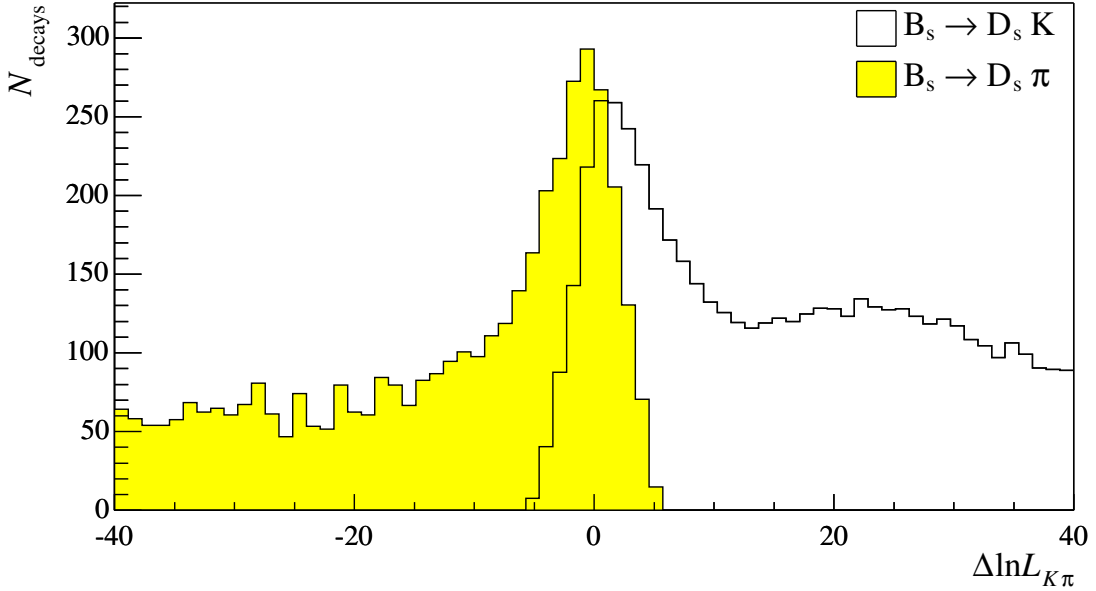


Figure 7.2: Delta log-likelihood between the kaon and pion hypothesis of the bachelor particle in $B_s^0 \rightarrow D_s^- \pi^+$ and $B_s^0 \rightarrow D_s^\mp K^\pm$ decays. The event yields are not normalised.

reveals two subclusters, allowing the π^0 to be still identified.

The muon detector provides the best muon–non-muon separation [103]. The search for muons starts with well-reconstructed tracks ($p > 3 \text{ GeV}$) which are extrapolated to each muon station. There, all hits within a field of interest (FOI) are assigned to the muon candidate. Muon candidates are selected when hits are found in enough different muon stations. The required number of muon stations depends on the momentum of the track.

Finally, the RICH, the calorimeters, and the muon detector express their PID estimate in terms of a likelihood ratio between the given PID hypothesis and the pion hypothesis. The likelihoods of the three different subdetectors are combined into a global likelihood as, e.g., for the K – π separation

$$\Delta \ln \mathcal{L}_{K\pi} = \sum_j \Delta \ln \mathcal{L}_{K\pi}^j , \quad (7.3)$$

where j sums over the three PID detectors. In the same way, the $\Delta \ln \mathcal{L}$ variables are calculated for the e , μ , and p hypotheses. It should be noted that any delta log-likelihood can be obtained from the combination of $\Delta \ln \mathcal{L}$ variables with respect to the pion, e.g.:

$$\Delta \ln \mathcal{L}_{Ke} = \Delta \ln \mathcal{L}_{K\pi} - \Delta \ln \mathcal{L}_{e\pi} . \quad (7.4)$$

In Fig. 7.2, the $\Delta \ln \mathcal{L}_{K\pi}$ distribution is shown for the bachelor particle in $B_s^0 \rightarrow D_s^- \pi^+$ and $B_s^0 \rightarrow D_s^\mp K^\pm$ decays. Obviously, the K – π separation provides a powerful selection

Table 7.3: Number of events produced for the $b\bar{b}$ inclusive background and signal decays after applying the acceptance cut (see Section 4.3.4).

Decay channel	Events produced
$b\bar{b}$ inclusive	10050950
$B_s^0 \rightarrow D_s^\mp K^\pm$	1210000
$B_s^0 \rightarrow D_s^- \pi^+$	207000
$B_s^0 \rightarrow D_s^{*\mp} K^\pm$	50500
$B_s^0 \rightarrow D_s^\mp K^{*\pm} (\rightarrow K^\pm \pi^0)$	50500
$B_s^0 \rightarrow D_s^\mp K^{*\pm} (\rightarrow K_S^0 \pi^\pm)$	49500

criterion to separate $B_s^0 \rightarrow D_s^- \pi^+$ and $B_s^0 \rightarrow D_s^\mp K^\pm$ decays. The maximum physics sensitivity is obtained by optimising these PID cuts for each decay channel individually.

7.3 Event selection

The event selection algorithms are part of the DA VINCI³ application. DA VINCI makes particle candidates based on the $\Delta \ln \mathcal{L}$ values, reconstructs primary vertices, K_S^0 's, and π^0 's, and provides flavour tagging. For each decay channel, or set of similar decay channels, there is an event selection algorithm. The event selection algorithm for $B_s^0 \rightarrow D_s^- \pi^+$ and $B_s^0 \rightarrow D_s^{(*)\mp} K^{(*)\pm}$ decays uses the LOKI toolkit [59], which provides tools to facilitate the event selection. For instance, it provides tools to calculate kinematical parameters (e.g., impact parameters), to loop over particle combinations, and to easily access MC truth information for monitoring purposes.

In general, the selection of signal decays is based on the presence of a detached B vertex and on the presence of high- p_T decay products with an invariant mass corresponding to the B mass. The B decays in $b\bar{b}$ inclusive events have the same properties, and, because the total branching fraction for a signal decay is tiny (see Table 7.2), $b\bar{b}$ inclusive events are considered as a main background source.

In Table 7.3, the number of simulated Monte Carlo events for $b\bar{b}$ background and signal decays are quoted. These numbers correspond to the number of events that survive the acceptance cut. The efficiency to pass the acceptance criteria is $\varepsilon_\theta = (34.71 \pm 0.03)\%$ for signal decays, and $\varepsilon_\theta = (43.21 \pm 0.04)\%$ for $b\bar{b}$ inclusive decays (see Section 4.3.4). The sample of 10 million $b\bar{b}$ background events is only a tiny fraction of the 10^{12} events expected per year. As will be shown in the following sections, the estimate for the background contamination thus suffers from large errors.

7.3.1 Overview of the selection variables

To separate the signal from the background, a number of selection requirements is applied to the reconstructed events. These requirements are divided into four groups:

³The event selection described in this thesis is done with DA VINCI version v9r3.

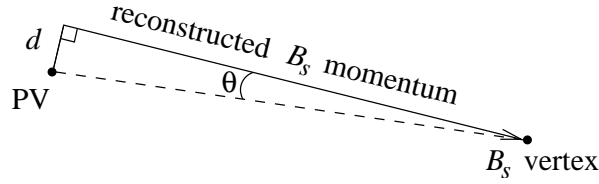


Figure 7.3: Definition of the impact parameter d and the angle θ of the B_s with respect to the primary vertex (PV). These two selection variables are used in the selection and preselection of $B_s^0 \rightarrow D_s^- \pi^+$ and $B_s^0 \rightarrow D_s^{(*)\mp} K^{(*)\pm}$ decays.

- **Vertex requirements.** The selected particles have to originate from a common point in space. For the D_s^\pm and B_s decay vertices, a simple cut is placed on the χ^2 from the vertex fit to the daughter particles. For the B_s origin vertex, the reconstructed B_s momentum is required to point back to the primary vertex. Three different selection variables are used. First, the angle θ between the B_s momentum direction and the line connecting the B_s vertex and primary vertex is used as a selection variable. The definition of θ is schematically depicted in Fig. 7.3. Second, also shown in this picture, there is the impact parameter significance of the B_s with the primary vertex, defined as d/σ_d , where σ_d is the uncertainty on the impact parameter d . In case of multiple primary vertices (pile-up), the minimal impact parameter significance, or $\min(d/\sigma_d)$, is used to select the correct primary vertex. Third, the pointing requirement can also be incorporated as a constraint into a lifetime fit. In this case, the pointing requirement is translated into a cut on the χ^2 from the lifetime fit. The advantage of such a method is that it simultaneously fits the B decay time.
- **Decay time requirements.** There should be a clear separation between the primary interaction vertex and (the tracks from) the secondary vertex. Requirements on the decay time can be applied to both the B_s and D_s^\pm particles. The decay time significance, τ/σ_τ , from the lifetime fit is used as selection variable. Other choices are the distance between the primary and secondary vertices, and the minimal impact parameter significance of the daughter particles with respect to the primary vertices.
- **Mass requirements.** The invariant mass of the daughter particles should correspond with the expected mass of the mother particle. Mass constraints are applied by selecting a mass window in the invariant mass spectrum. The large B mass also allows to put constraints on the minimal (transverse) momentum of the daughter particles. These momentum cuts are applied to reduce the combinatorics in the preselection procedure.
- **PID requirements.** The reconstructed PID should correspond with the required particle type. The $\Delta \ln \mathcal{L}$ variables, as discussed in Section 7.2, are used as selection variables.

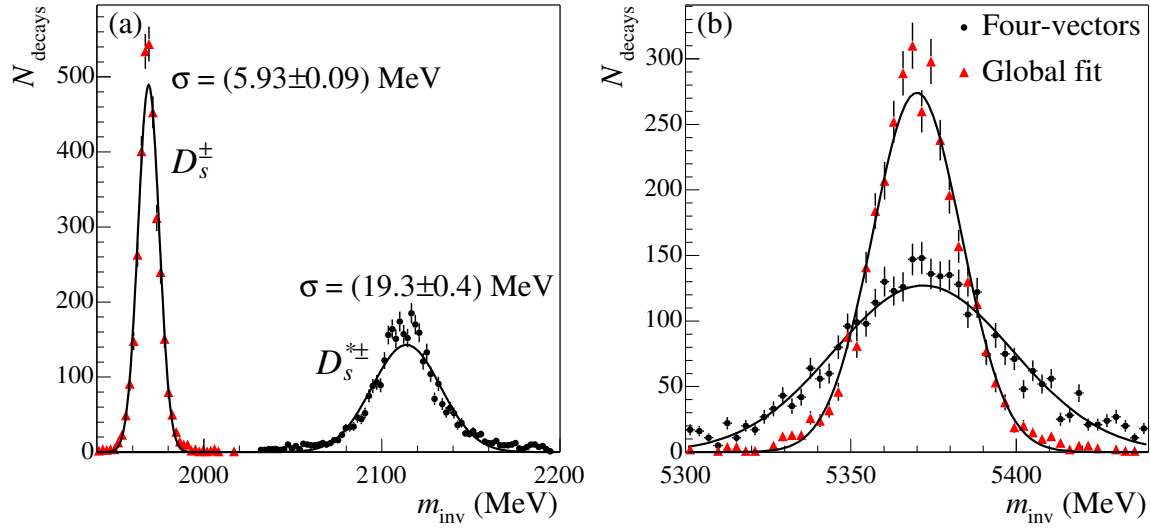


Figure 7.4: Invariant mass distributions of the D_s^\pm and $D_s^{*\pm}$ (a) and of the B_s (b) in $B_s^0 \rightarrow D_s^{*\mp} K^\pm$ events. The large uncertainty on the photon momentum degrades the $D_s^{*\pm}$ and B_s mass resolution. Fortunately, this is compensated by the $D_s^{*\pm}$ mass constraint in the global fit as shown in the right plot. The global fit improves the B_s mass resolution with respect to the regular four-vector sum from 27 MeV to 13 MeV.

Constrained vertex fits

The best estimates for the fitted parameters in a vertex fit are obtained when including as much information as possible. For instance, the mass of the mother particle can be incorporated as a constraint in the vertex fit. Such a *mass-constrained fit* improves the reconstructed vertex position and momentum of the mother particle. In addition, a cut on the χ^2 from the mass-constrained vertex fit implies a requirement both on the vertex and on the invariant mass, making the mass window cut obsolete. The D_s^\pm decay vertex is fitted in this way. On the other hand, a mass-constrained vertex fit cannot be used for the B vertex, since the side-bins in the invariant mass spectrum are needed to estimate the background contamination in the signal region.

The three, possibly mass-constrained, vertex fits, can also be replaced by a single *global fit*, which incorporates the mass and vertex constraints simultaneously. In principle, a single cut on the χ^2 from this fit could replace all vertex and mass requirements. On the other hand, as there are fewer selection variables, there is less freedom to cut away background. It is found that the χ^2 from the global fit is less efficient in reducing the background than the individual selection variables. Nevertheless, the global fit can be used to improve the B_s mass resolution. Figure 7.4 shows the improvement in the B_s mass resolution for $B_s^0 \rightarrow D_s^{*\mp} (\rightarrow D_s^\mp \gamma) K^\pm$ decays when using the global fit. In this case, the reconstructed photon energy, which has a relatively large uncertainty of $\sim 7\%$, is improved by the $D_s^{*\pm}$ mass constraint. Accordingly, the mass resolution

after the global fit is comparable to that of $B_s^0 \rightarrow D_s^\mp K^\pm$ decays. For $B_s^0 \rightarrow D_s^\mp K^\pm$ and $B_s^0 \rightarrow D_s^- \pi^+$ decays, a small improvement is observed when applying the global fit, namely from (13.71 ± 0.09) MeV to (12.10 ± 0.07) MeV for $B_s^0 \rightarrow D_s^\mp K^\pm$, and from (15.0 ± 0.2) MeV to (13.5 ± 0.1) MeV for $B_s^0 \rightarrow D_s^- \pi^+$.

In contrast, it is not possible to put a constraint on the $K^*(892)^\pm$ mass in the global fit, because the decay width of this resonance is as large as 51 MeV [8]. In decays of $B_s^0 \rightarrow D_s^\mp K^{*\pm} (\rightarrow K_S^0 \pi^\pm)$, the K_S^0 momentum resolution of 0.35% is accurate enough, such that the B_s mass resolution of (16.9 ± 0.6) MeV is only slightly worse. On the other hand, in decays of $B_s^0 \rightarrow D_s^\mp K^{*\pm} (\rightarrow K^\pm \pi^0)$, the poor π^0 momentum resolution of $\sim 6\%$ results in a poor B_s mass resolution of ~ 52 MeV. Accordingly, a larger mass window is required for this decay channel, which increases the background contamination. Figure 7.5 shows the invariant mass distributions of the π^0 , K_S^0 , $K^*(892)^\pm$, and B_s in $B_s^0 \rightarrow D_s^\mp K^{*\pm}$ decays.

7.3.2 Preselection

An initial event selection with loose cuts is applied to both signal and background events. This preselection reduces the background per decay channel by a factor ~ 100 , which facilitates the final tuning. On the other hand, the preselection cuts must not be too tight, otherwise it would restrict the optimisation of the final cuts. Loose cuts are applied on the (transverse) momentum, $\Delta \ln \mathcal{L}$, and $\min(d/\sigma_d)$ of the particles, and on the invariant mass and χ^2 of the vertices. In order to avoid any bias in the mass distribution, only unconstrained vertex fits are applied in the preselection. In general, the preselection uses mainly simple cuts, while the more sophisticated cuts are applied in the final selection. The preselection cuts for the five decays channels are listed in Table 7.4. In case a track satisfies both the pion and kaon hypothesis, then both PIDs are assumed for this particle candidate (inclusive particle selection). After the combined preselection for the five decays channels only 3.78% of the $b\bar{b}$ inclusive events remain. In this sample, 0.93% is selected as $B_s^0 \rightarrow D_s^- \pi^+$ candidates and 0.50% as $B_s^0 \rightarrow D_s^\mp K^\pm$ candidates.

Wide mass window method

In order to effectively simulate more background, the B_s mass window for background events is enlarged by a factor 10. Assuming that the invariant mass of the background has an approximately linear distribution, this method has the same effect as simulating 10 times more background. Hence, for signal events a mass window of ± 50 MeV around the nominal B_s mass is applied, while for background events a mass window of ± 500 MeV is applied.

7.3.3 Optimisation of final selection

For the final cut optimisation, not only $b\bar{b}$ inclusive background, but also specific sources of background are considered. In the selection of $B_s^0 \rightarrow D_s^\mp K^\pm$ events, this specific

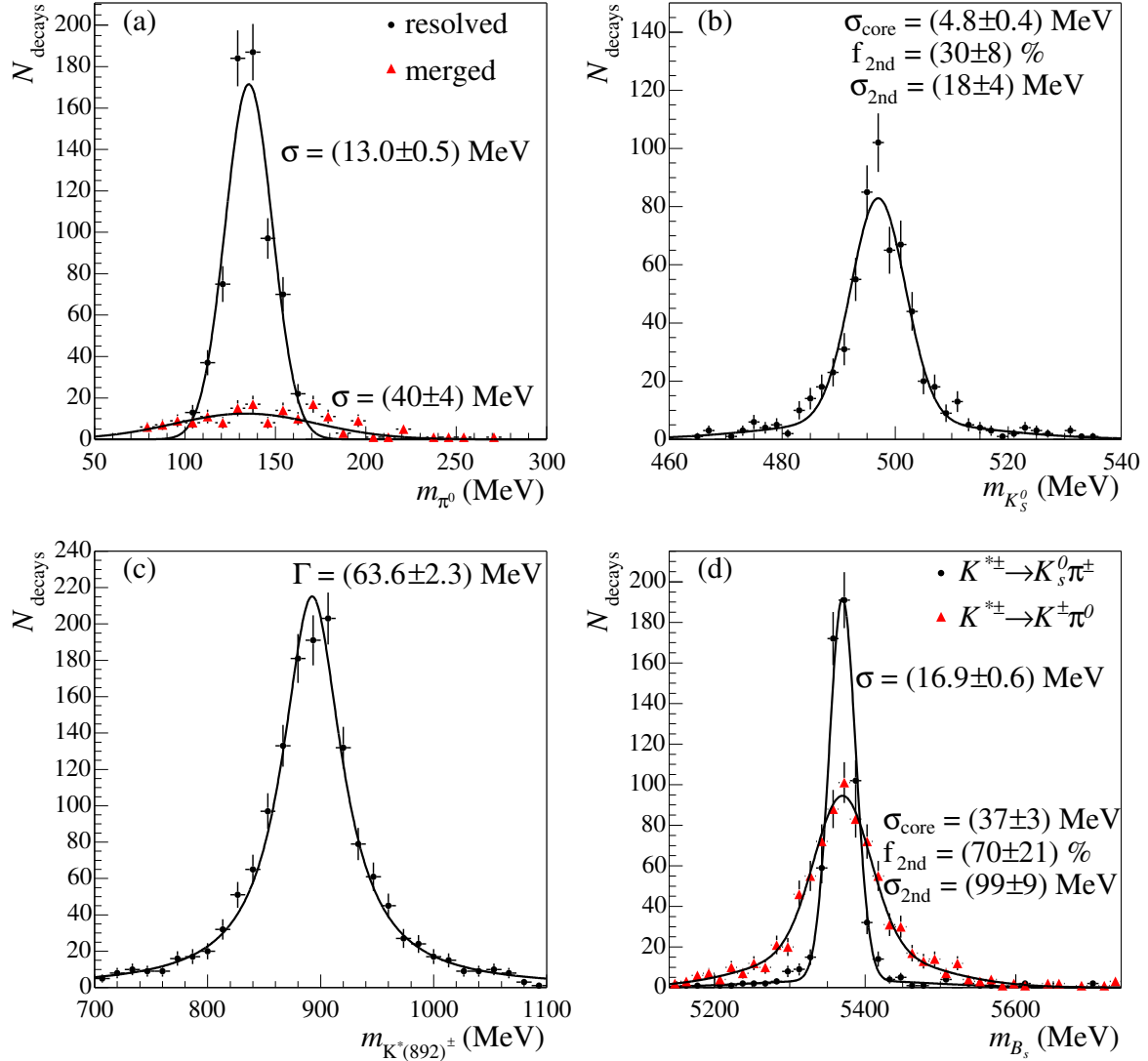


Figure 7.5: Invariant mass distributions of the π^0 (a), K_s^0 (b), $K^*(892)^\pm$ (c), and B_s (d) in $B_s^0 \rightarrow D_s^\mp K^{*\pm} (\rightarrow K^\pm \pi^0)$ and $B_s^0 \rightarrow D_s^\mp K^{*\pm} (\rightarrow K_s^0 \pi^\pm)$ decays. All distributions are fitted with a single or double Gaussian, except that of $K^*(892)^\pm$, which is fitted with a Breit-Wigner function.

background comes from $B_s^0 \rightarrow D_s^- \pi^+$ events. Often these specific backgrounds can be controlled by a single selection variable, thereby facilitating the optimisation. Thus, the strategy is to first optimise the selection with respect to these specific backgrounds, and then to tune the remaining cuts against the generic $b\bar{b}$ background. This procedure is iterated until the selection cuts converge to a global optimum.

Table 7.4: Preselection cuts for $B_s^0 \rightarrow D_s^- \pi^+$ and $B_s^0 \rightarrow D_s^{(*)\mp} K^{(*)\pm}$ decays. Most cuts are standard values used in the preselection of many other decay channels. They are responsible for a large reduction of the background, but are loose enough to perform an optimisation of the final selection.

Particle	Variable	requirement	Particle	Variable	requirement
all tracks	track type	long	π^0	momentum	$> 1 \text{ GeV}$
	momentum	$> 2 \text{ GeV}$		p_T	$> 500 \text{ MeV}$
	p_T	$> 200 \text{ MeV}$		$p_T \gamma$ (resolved)	$> 100 \text{ MeV}$
	χ^2/n_{dof}	< 4		$ \Delta m $ (resolved)	$< 30 \text{ MeV}$
all pions	detected in $\Delta \ln \mathcal{L}_{\pi K}$	RICH > -5		$ \Delta m $ (merged)	$< 60 \text{ MeV}$
	detected in $\Delta \ln \mathcal{L}_{K\pi}$	RICH > -5	K_s^0	p_T	$> 50 \text{ MeV}$
all kaons	detected in $\Delta \ln \mathcal{L}_{Ke}$	RICH > -5		χ^2 vertex fit	< 50
	detected in $\Delta \ln \mathcal{L}_{Kp}$	RICH > -5		$ \Delta m $	$< 110 \text{ MeV}$
	bachelor	$\min(d/\sigma_d) > 1$		$\min(d/\sigma_d) \pi'$ s	> 6 (long) > 3 (downstr)
D_s^\pm	$\min(d/\sigma_d)$	> 1	$K^{*\pm}$	$ \Delta m $	$< 200 \text{ MeV}$
	χ^2 vertex fit	< 20		B_s	$\min(d/\sigma_d) < 20$
	$ \Delta m $	$< 50 \text{ MeV}$		χ^2 vertex fit	< 20
	$\Delta z(D_s^\pm - \text{PV})$	$> 0 \text{ mm}$		$ \Delta m $	$< 500 \text{ MeV}$
γ	momentum	$> 1 \text{ GeV}$		$\Delta z(B_s - D_s^\pm)$	$> 0 \text{ mm}$
	p_T	$> 200 \text{ MeV}$		$\Delta z(B_s - \text{PV})$	$> 0 \text{ mm}$
$D_s^{*\pm}$	$ \Delta m $	$< 80 \text{ MeV}$		$1 - \cos \theta$	$< 2 \times 10^{-2}$

Specific backgrounds

For the selection of $B_s^0 \rightarrow D_s^\mp K^\pm$ decays, the cut on $\Delta \ln \mathcal{L}_{K\pi}$ of the bachelor particle removes a large fraction of the $B_s^0 \rightarrow D_s^- \pi^+$ background. Figure 7.6(a) shows the B_s invariant mass distribution in $B_s^0 \rightarrow D_s^\mp K^\pm$ events with $B_s^0 \rightarrow D_s^- \pi^+$ background. The PID cut is set at $\Delta \ln \mathcal{L}_{K\pi} = 3$ and the number of events is scaled to the expected annual yield (untriggered and untagged). The $B_s^0 \rightarrow D_s^- \pi^+$ background distribution is shifted to the right of the nominal B_s mass, because the bachelor particle is assumed to have the K^\pm mass in the invariant mass calculation. The total, observed distribution is fitted simultaneously with two Gaussians; one for the signal and one for the background. The statistical significance of the signal is defined as the number of signal events divided by its error (i.e., S/σ_S). The maximum significance is found by varying the PID cut, as is shown in Fig. 7.6(b). The optimal value is chosen at $\Delta \ln \mathcal{L}_{K\pi} = 3$. Similarly, the selection of $B_s^0 \rightarrow D_s^{*\mp} K^\pm$ decays faces a contamination from $B_s^0 \rightarrow D_s^{*-} \pi^+$ decays. The same PID cut for the bachelor particle is assumed in the selection of these decays.

Another specific background in the selection of $B_s^0 \rightarrow D_s^\mp K^\pm$ events is that of $B_s^0 \rightarrow D_s^{*\mp} K^\pm$. These events very much resemble $B_s^0 \rightarrow D_s^\mp K^\pm$ events in case the photon from the $D_s^{*\pm}$ decay is very soft. However, the $(-1)^L$ factor dilutes the observed interference.

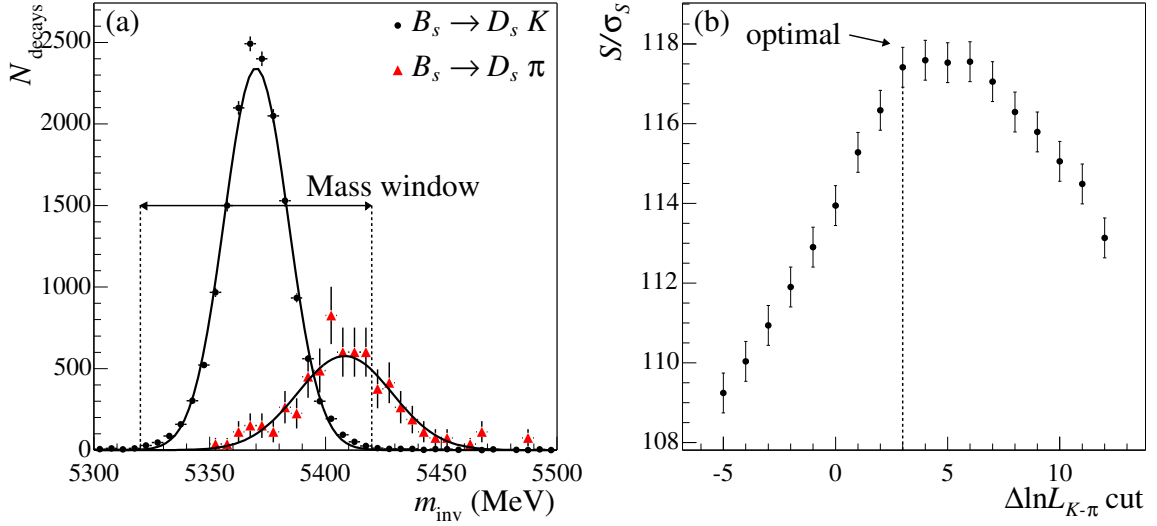


Figure 7.6: Invariant mass distribution for the B_s in $B_s^0 \rightarrow D_s^\mp K^\pm$ events with $B_s^0 \rightarrow D_s^- \pi^+$ background (a). The PID requirement for the bachelor particle is set at $\Delta \ln \mathcal{L}_{K\pi} = 3$. The signal distribution is centred around the nominal B_s mass (5370 MeV) with a sigma of 12.1 MeV, while the $B_s^0 \rightarrow D_s^- \pi^+$ background is centred around 5409 MeV with a sigma of 23.5 MeV. The significance of the signal distribution is determined from a simultaneous fit of both Gaussians. The right plot (b) displays this significance as a function of the PID cut of the bachelor. The optimal value is chosen at $\Delta \ln \mathcal{L}_{K\pi} = 3$.

The B_s mass spectrum can be estimated by considering the two extreme cases in the rest frame of the B_s meson: the case where the photon flies in the same direction as the bachelor kaon, and the case where the photon flies in the opposite direction as the bachelor kaon. It is then found that in case the photon is not reconstructed the B_s mass spectrum ranges between 5008 MeV–5313 MeV. Figure 7.7 shows the invariant mass distribution for $B_s^0 \rightarrow D_s^{*\mp} K^\pm$ events in case the photon is not reconstructed. Since the $B_s^0 \rightarrow D_s^{*\mp} K^\pm$ events are distributed over ~ 300 MeV, a negligible 0.5% of the events ends up in the ± 50 MeV mass window around the nominal B_s mass.

Optimisation tool

An optimisation tool [104] is used to simultaneously find the optimal requirements for the selection variables. Again, the optimum is defined as the point where the statistical significance of the signal is the highest. For a Poisson distribution this significance equals

$$\frac{S}{\sigma_S} = \frac{S}{\sqrt{S + B}} , \quad (7.5)$$

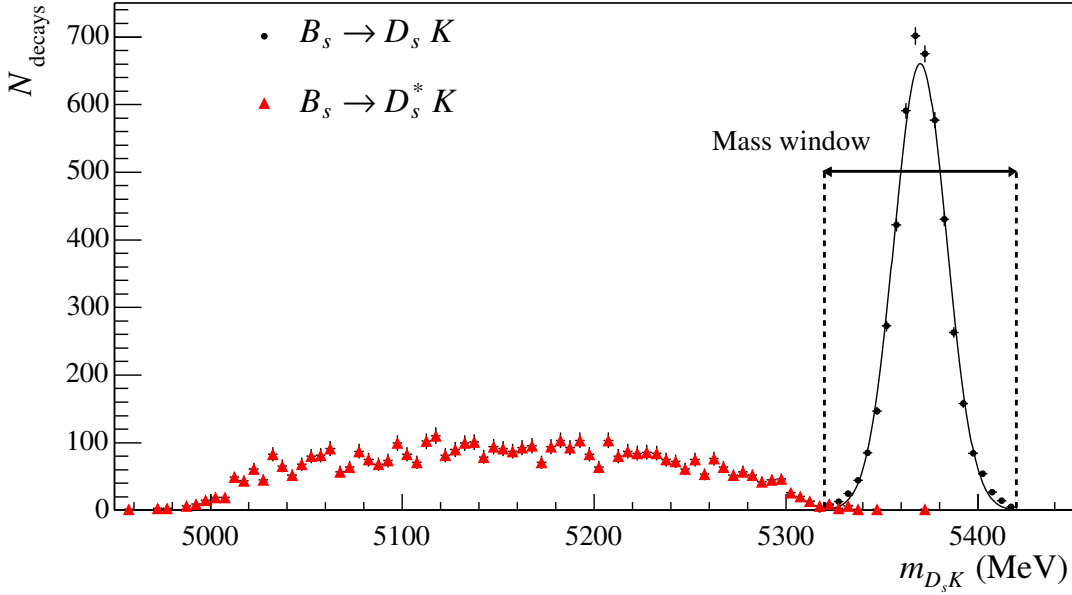


Figure 7.7: Invariant mass of the $D_s^\mp-K^\pm$ combination for $B_s^0 \rightarrow D_s^\mp K^\pm$ and $B_s^0 \rightarrow D_s^{*\mp} K^\pm$ events. Only 0.5% of the $B_s^0 \rightarrow D_s^{*\mp} K^\pm$ events ends up in the ± 50 MeV mass window of the $B_s^0 \rightarrow D_s^\mp K^\pm$ selection.

with S the number of signal events and B the number of background events. The cut values are placed at fixed intervals in a specified range. The n selection variables define an n -dimensional grid, and for each point the number of signal and background events passing the cuts is determined. The tool scans the space of selection variables and calculates $S/\sqrt{S+B}$ for each combination of cuts.

The number of generated $b\bar{b}$ background events is not enough to optimise all cuts simultaneously. When all final cuts are applied, only very few background events remain for the $B_s^0 \rightarrow D_s^- \pi^+$ selection, and none for the selection of the other decay channels. Therefore, a factorisation method, similar to the widening of the mass window for background events, is applied. The basic assumption is that the background distribution for a certain selection variable does not change when cutting on other selection variables. In case the standard efficiency is defined by

$$\varepsilon = \frac{N_{1+2+\dots+n}}{N_{\text{tot}}} , \quad (7.6)$$

where $N_{1+2+\dots+n}$ is the number of events passing selection 1 to n , and N_{tot} is the total number of events. Then, the factorised efficiency is

$$\varepsilon_{\text{fact}} = \varepsilon_1 \varepsilon_2 \dots \varepsilon_n = \frac{N_1}{N_{\text{tot}}} \frac{N_2}{N_{\text{tot}}} \dots \frac{N_n}{N_{\text{tot}}} , \quad (7.7)$$

where N_i is the number of events passing a single selection, and ε_i is the efficiency for this selection. The factorisation hypothesis assumes that $\varepsilon_{\text{fact}} = \varepsilon$. In other words,

Table 7.5: Final selection cuts in the decays of $B_s^0 \rightarrow D_s^- \pi^+$ and $B_s^0 \rightarrow D_s^{(*)\mp} K^{(*)\pm}$. The selection variables that are simultaneously optimised are grouped together.

Variable	$D_s^- \pi^+$	$D_s^\mp K^\pm$	$D_s^{*\mp} K^\pm$	$D_s^\mp K^{*\pm}$ ($\rightarrow K^\pm \pi^0$)	$D_s^\mp K^{*\pm}$ ($\rightarrow K_s^0 \pi^\pm$)
D_s^\pm mass-constr. χ^2	< 10	< 9	< 8	< 5	< 7
K^\pm from D_s^\pm $\Delta \ln \mathcal{L}_{K\pi}$	> 3.5	> 5	> 5	> 10	> 5
B_s unconstr. χ^2	< 2	< 1.5	< 2	< 2	< 2
$1 - \cos \theta$ ($\times 10^{-5}$)	< 6	< 3	< 1	< 0.5	< 1
B_s lifetime fit χ^2	< 16	< 8	< 6	< 10	< 20
D_s^\pm daughters min(d/σ_d)	> 5	> 7	> 7	> 8	> 10
bachelor $\Delta \ln \mathcal{L}_{K\pi}$	-	> 3	> 3	> 3	-
$D_s^{*\pm} \Delta m $ (MeV)	-	-	< 20	-	-
γp_T (MeV)	-	-	> 200	-	-
$K^* \Delta m $ (resolved) (MeV)	-	-	-	< 70	-
$\pi^0 p_T$ (resolved) (MeV)	-	-	-	> 1750	-
$\pi^0 p_T$ (merged) (MeV)	-	-	-	> 2000	-
$K^* \Delta m $ (MeV)	-	-	-	-	< 50
K^* vertex χ^2	-	-	-	-	< 2.5
$K_s^0 \Delta m $ (MeV)	-	-	-	-	< 15
K_s^0 vertex χ^2	-	-	-	-	< 30

it assumes that there are no correlations between the selection cuts. For the selection of $B_s^0 \rightarrow D_s^- \pi^+$ and $B_s^0 \rightarrow D_s^\mp K^\pm$ decays, possible correlations between the selection variables are minimised by dividing the selection variables into only two groups. For the $B_s^0 \rightarrow D_s^{*\mp} K^\pm$ and $B_s^0 \rightarrow D_s^\mp K^{*\pm}$ decays, a third group is added for the selection of the neutral particle.

The first group of selection variables contains the χ^2 from the mass-constrained D_s^\pm vertex fit, the χ^2 from the unconstrained B_s vertex fit, and the $\Delta \ln \mathcal{L}_{K\pi}$ for the kaons from the D_s^\pm . The second group contains the angle θ , the χ^2 from the B_s lifetime fit, and the minimal impact parameter significance of the D_s^\pm products. These two sets of cuts have been carefully selected to avoid possible correlations. Variables which have hardly any or no effect on the significance are left out in the final optimisation. For instance, a cut on the lifetime significance, τ/σ_τ , of both the D_s^\pm and B_s appears to have little impact on the significance of the signal. This is explained by the fact that the background consists of $b\bar{b}$ inclusive events, all having displaced secondary vertices. Table 7.5 lists the final cuts as a result of the optimisation.

7.3.4 Event yield

In Table 7.6, the annual event yield after applying the final selection cuts is given for each decay of interest. The total selection efficiency in Table 7.6 is subdivided as

Table 7.6: Breakdown of the total selection efficiency and annual yield of selected and triggered events for the listed decay channels (including the charge-conjugated decays). All efficiencies are quoted in percentages (%).

Decay channel	ε_{det}	$\varepsilon_{\text{rec/det}}$	$\varepsilon_{\text{sel/rec}}$	$\varepsilon_{\text{trg/sel}}$	ε_{tot}	Ann. yield
$B_s^0 \rightarrow D_s^- \pi^+$	5.1	80.3	30.4	30.4	0.379	85k
$B_s^0 \rightarrow D_s^\mp K^\pm$	5.0	80.9	20.3	28.3	0.232	4.6k
$B_s^0 \rightarrow D_s^{*\mp} K^\pm$	2.6	59.2	14.4	28.2	0.065	1.3k
$B_s^0 \rightarrow D_s^\mp K^{*\pm} (\rightarrow K^\pm \pi^0)$	1.7	57.1	5.1	42.5	0.021	142
$B_s^0 \rightarrow D_s^\mp K^{*\pm} (\rightarrow K_S^0 \pi^\pm)$	1.7	53.4	5.9	31.1	0.016	74

$$\varepsilon_{\text{tot}} = \varepsilon_{\text{det}} \times \varepsilon_{\text{rec/det}} \times \varepsilon_{\text{sel/rec}} \times \varepsilon_{\text{trg/sel}} , \quad (7.8)$$

where ε_{det} is the efficiency that all B decay products in the event are reconstructible, $\varepsilon_{\text{rec/det}}$ is the efficiency that these decay products are actually reconstructed, $\varepsilon_{\text{sel/rec}}$ is the efficiency that the event is selected, and $\varepsilon_{\text{trg/sel}}$ is the efficiency that the event is accepted by the Level-0 and Level-1 trigger algorithms.

The reconstructible efficiency includes the acceptance efficiency of $\varepsilon_\theta = (34.71 \pm 0.03)\%$. The remaining inefficiency is caused by decay products with not enough hits in the tracking systems to be reconstructible as a long track (charged particles), or decay products without a cluster in the calorimeter (neutral particles). Clearly, the additional neutral particle in the $B_s^0 \rightarrow D_s^{*\mp} K^\pm$ and $B_s^0 \rightarrow D_s^\mp K^{*\pm}$ decays decreases ε_{det} . This effect is enhanced since these decay products are relatively soft. Also, the reconstruction and selection efficiencies for these decay channels is lower. Nevertheless, it is interesting to note that the decay $B_s^0 \rightarrow D_s^{*\mp} K^\pm$ adds about 28% to the statistics of $B_s^0 \rightarrow D_s^\mp K^\pm$. In contrast, relatively few events are selected as $B_s^0 \rightarrow D_s^\mp K^{*\pm}$ decays, hardly contributing to the physics sensitivity.

The variation of the trigger efficiencies for the different decay channels is due to low statistics and is not significant (i.e., $< 3\sigma$). Therefore, in the remainder of this thesis a trigger efficiency of $(28.3 \pm 0.9)\%$, obtained from the large statistical sample of $B_s^0 \rightarrow D_s^\mp K^\pm$ events, is assumed to be valid for all decay channels.

Background analysis: $B_s^0 \rightarrow D_s^- \pi^+$

After applying the final $B_s^0 \rightarrow D_s^- \pi^+$ selection, but before applying the trigger selection, 21 $b\bar{b}$ inclusive events survive the cuts in the wide mass window and 4 in the tight mass window. In Table 7.7 the corresponding event types are listed. Due to the wide mass window, also $B_s^0 \rightarrow D_s^{*-} \pi^+$ events are selected. For the same reason that most $B_s^0 \rightarrow D_s^{*\mp} K^\pm$ events do not end up in the tight mass window in the selection of $B_s^0 \rightarrow D_s^\mp K^\pm$ events (see Section 7.3.3), $B_s^0 \rightarrow D_s^{*-} \pi^+$ events can safely be ignored in the selection of $B_s^0 \rightarrow D_s^- \pi^+$ events. This also holds for $B_s \rightarrow D_s^{*-} \rho^+ (\rightarrow \pi^+ \pi^0)$ events. Although similar arguments may be applicable to the other decay types, excluding these specific backgrounds requires a dedicated analysis. For instance, a reasonable fraction of $B_s^0 \rightarrow J/\psi (\rightarrow \mu^+ \mu^-) \phi (\rightarrow K^+ K^-)$ decays might end up in the tight mass window. Nev-

Table 7.7: Event types in $b\bar{b}$ background passing the $B_s^0 \rightarrow D_s^- \pi^+$ selection cuts before trigger. The last column denotes whether this decay type may end up in the tight mass window.

Selected decay	N_{sel}	Comment	possibly dangerous
$B_s^0 \rightarrow D_s^{*-} \pi^+$	8	γ not reconstructed	No
$B_s^0 \rightarrow D_s^{*-} \rho^+ (\rightarrow \pi^+ \pi^0)$	2	π^0, γ not reconstructed	No
$B_s^0 \rightarrow \nu \mu^+ D_s^{(*)-}$	2	μ^+ reconstructed as π^+	Yes
$B_s^0 \rightarrow D^- (\rightarrow K^+ \pi^- \pi^-) \pi^+$	1	π^- reconstructed as K^-	Yes
$B_s^0 \rightarrow D^- (\rightarrow K^+ \pi^- \pi^-) \pi^0 \pi^+$	1	idem and π^0 not rec.ted	Yes
$B_s^0 \rightarrow J/\psi (\rightarrow \mu^+ \mu^-) \phi (\rightarrow K^+ K^-)$	1	μ^\pm reconstructed as π^\pm	Yes
$\bar{A}_b^0 \rightarrow \bar{A}_c^- (\rightarrow \bar{p} K^+ K^-) \pi^+$	1	\bar{p} reconstructed as π^-	Yes
Combinatorics	5	-	Yes
Total	21	(4 in tight mass window)	

Table 7.8: Number of $b\bar{b}$ background decays selected (before trigger), annual background yield (after trigger), and the B/S ratio for the decays of interest. Both the number of events passing all cuts as well as the estimated number obtained from factorisation are given. Only statistical errors are quoted. In case no events are selected, the upper limit corresponds to a $CL > 90\%$. The B/S ratios are determined from the factorised background estimates.

Decay channel	Events selected		Annual yield		B/S
	all cuts	factorised	all cuts	factorised	
$D_s^- \pi^+$	21	22 ± 1	$(27 \pm 5)k$	$(29 \pm 1)k$	0.34
$D_s^\mp K^\pm$	0	0.9 ± 0.2	$< 2.9k$	$(1.1 \pm 0.2)k$	0.24
$D_s^{*\mp} K^\pm$	0	0.6 ± 0.1	$< 4.2k$	$(1.1 \pm 0.2)k$	0.85
$D_s^\mp K^{*\pm} (\rightarrow K^\pm \pi^0)$	0	0.021 ± 0.007	$< 17k$	$(0.13 \pm 0.05)k$	1.51
$D_s^\mp K^{*\pm} (\rightarrow K_S^0 \pi^\pm)$	0	0.04 ± 0.04	$< 2.9k$	$(0.05 \pm 0.05)k$	0.71

ertheless, a stronger cut on $\Delta \ln \mathcal{L}_{\pi\mu}$ should be able to reduce this specific background considerably. These types of background are thus expected to be well controlled. On the other hand, this is not the case for combinatorics. An event is classified as “combinatorics” when the decay products from both B hadrons or other non- B particles are selected. It is this type of background which is most dangerous, because it cannot be eliminated with a single cut.

Background analysis: $B_s^0 \rightarrow D_s^{(*)\mp} K^{(*)\pm}$

The number of $b\bar{b}$ events passing the final selection and expected annual yield are given in Table 7.8. In the selection of $B_s^0 \rightarrow D_s^{(*)\mp} K^{(*)\pm}$ decays, no $b\bar{b}$ background event survives

the final cuts in the wide mass window. The corresponding upper limits are obtained using the method of Feldman and Cousins [105] for the construction of confidence intervals. The annual background yield assumes the same trigger efficiency for the signal as for the background. Also note that the effective number of $b\bar{b}$ background events for the $B_s^0 \rightarrow D_s^{*\mp} K^\pm$ and $B_s^0 \rightarrow D_s^{\mp} K^{*\pm} (\rightarrow K^\pm \pi^0)$ selection is reduced to 7.2 million, because the calorimeter information was not available for all events. Furthermore, due to the broader mass peak in $B_s^0 \rightarrow D_s^{\mp} K^{*\pm} (\rightarrow K^\pm \pi^0)$ events, the wide mass window method adds only 2.5 times more background for this decay channel.

Using the factorisation hypothesis a better estimate of the background contamination can be made. In the example of the $B_s^0 \rightarrow D_s^- \pi^+$ selection, 132961 events pass the preselection. The selection efficiency with respect to these preselected events is $\varepsilon_1 = (4.89 \pm 0.06)\%$ for the first set of cuts, and $\varepsilon_2 = (0.34 \pm 0.02)\%$ for the second set of cuts. Hence, the factorised efficiency, $\varepsilon_{\text{fact}} = \varepsilon_1 \varepsilon_2 = (0.017 \pm 0.001)\%$, predicts that 22 ± 1 events pass the final selection. This is in good agreement with the 21 events that actually pass all cuts. The same method is also applied to $B_s^0 \rightarrow D_s^{(*)\mp} K^{(*)\pm}$ decays. The results are summarised in Table 7.8. The background over signal ratios (B/S) are obtained from the factorisation method.

7.3.5 B decay times

The B_s decay time resolution after the final selection in $B_s^0 \rightarrow D_s^{\mp} K^\pm$ events is shown in Fig. 7.8(a). The double Gaussian fit has a core resolution of (37.6 ± 0.6) fs. Similar resolutions are obtained for $B_s^0 \rightarrow D_s^- \pi^+$ and $B_s^0 \rightarrow D_s^{(*)\mp} K^{(*)\pm}$ events. The estimated errors from the lifetime fit describe the reconstructed lifetime reasonably well with a pull of 1.111 ± 0.007 , as can be seen in Fig. 7.8(b). In Fig. 7.8(c), the decay time error distribution is shown. The large variation in the errors is explained by the spread in the kinematic distributions of the B_s momentum and decay distance.

Figure 7.9 shows the distribution of generated B_s decay times for selected and triggered $B_s^0 \rightarrow D_s^{\mp} K^\pm$ decays. The shape of the exponential decay is modified towards shorter decay times due to a lower selection efficiency, which is the result of the requirements on the minimal B decay time, both in the trigger and in the offline event selection. The time-dependent selection efficiency, drawn in the same figure, is parameterised by the acceptance function defined as

$$\varepsilon_t(t) = C \times \frac{(at)^n}{1 + (at)^n} , \quad (7.9)$$

where C is the selection efficiency for large decay times, and a and n are two parameters which govern the time dependence. Their values are obtained from a fit to the data points, giving $a = (0.99 \pm 0.03) \text{ ps}^{-1}$ and $n = 2.24 \pm 0.07$.

7.4 Flavour tagging

Flavour tagging determines whether the selected B meson was produced as a b or \bar{b} quark. Without flavour tagging it is impossible to distinguish between the decay rates

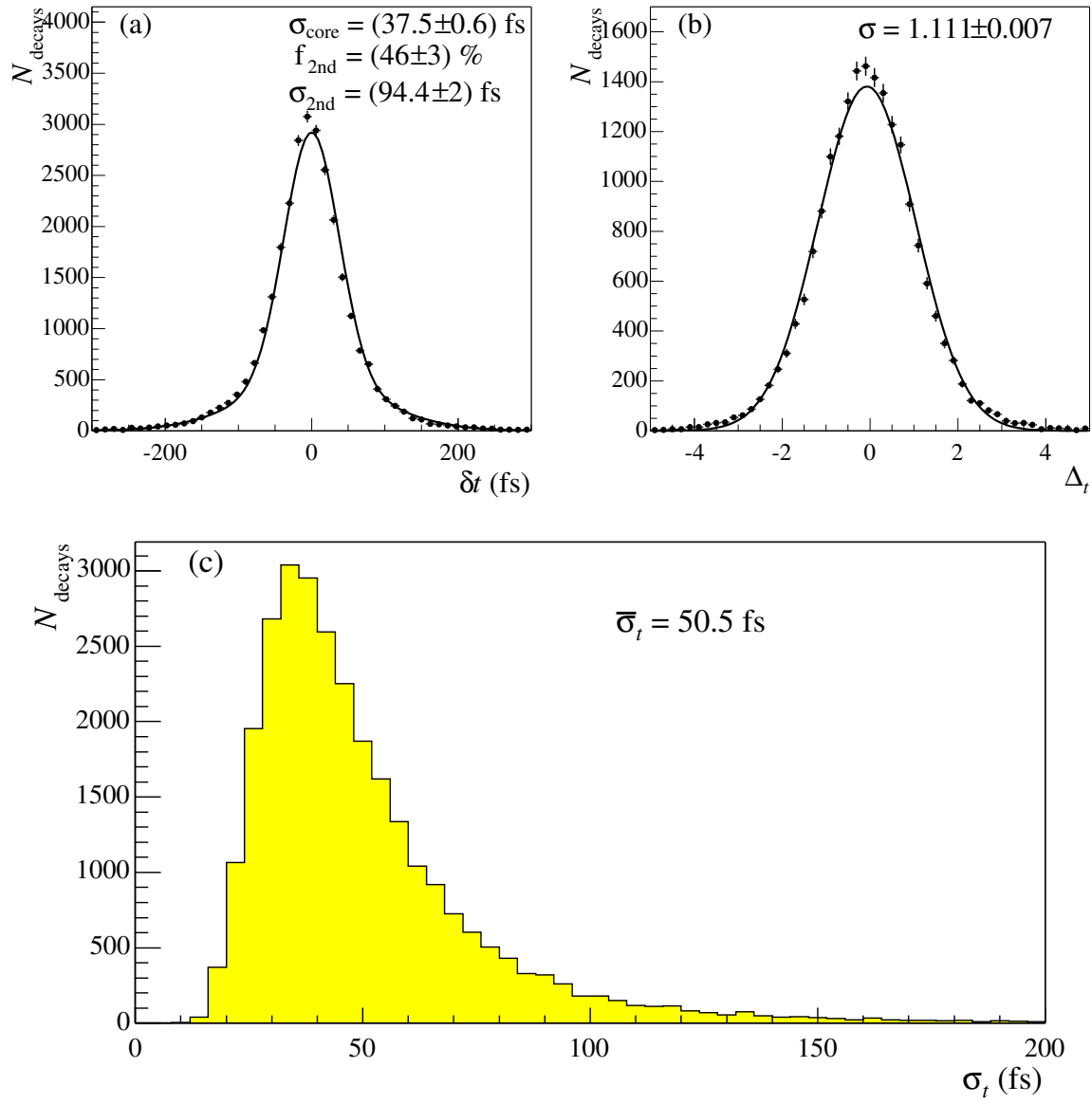


Figure 7.8: Decay time resolution (a), pull distribution (b), and error distribution (c) for reconstructed and selected $B_s^0 \rightarrow D_s^\mp K^\pm$ decays (untriggered). Note the large spread in the error distribution.

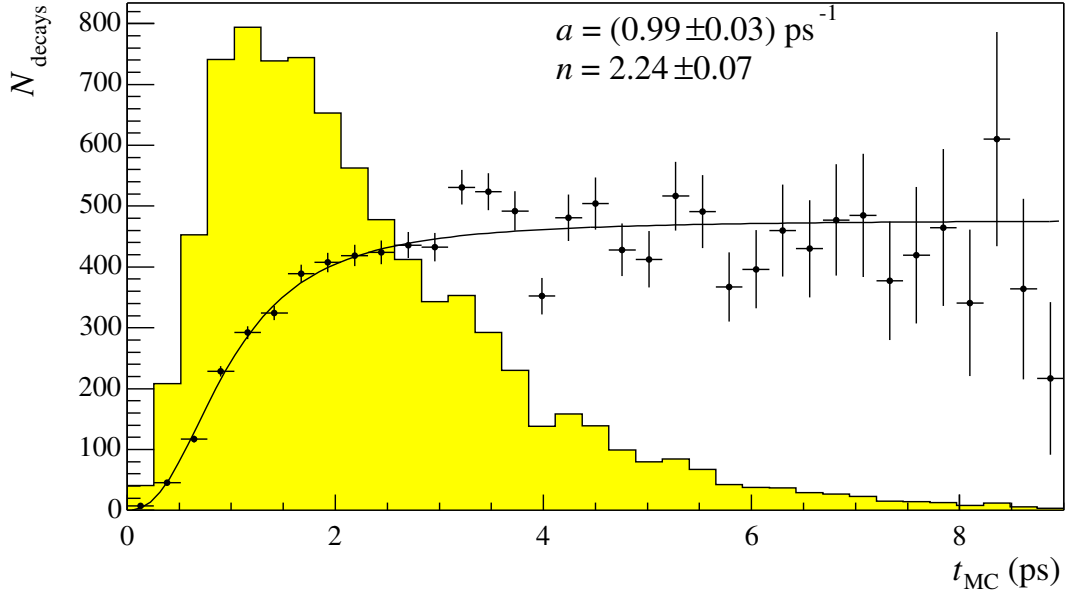


Figure 7.9: Distribution of the generated B_s decay times (t_{MC}) for selected and triggered $B_s^0 \rightarrow D_s^\mp K^\pm$ decays (filled histogram). The data points represent the selection efficiency (arbitrary scale) versus t_{MC} . The acceptance function (7.9) is fitted through the data points.

$\Gamma_{B \rightarrow f}$ and $\Gamma_{\bar{B} \rightarrow \bar{f}}$, and between the decay rates $\Gamma_{B \rightarrow \bar{f}}$ and $\Gamma_{\bar{B} \rightarrow f}$ in (2.29). The tagging performance is determined by two parameters: the tagging efficiency, ε_{tag} , which gives the fraction of selected decays that are tagged, and the wrong tag fraction, w_{tag} , which gives the fraction of tagged decays that are tagged incorrectly. The second parameter dilutes the observed asymmetry as

$$\mathcal{A}_{\text{obs}} = \mathcal{D} \mathcal{A}_{\text{phys}} \quad \text{with} \quad \mathcal{D} = (1 - 2w_{\text{tag}}) \quad , \quad (7.10)$$

where \mathcal{A}_{obs} is the observed asymmetry and $\mathcal{A}_{\text{phys}}$ the true asymmetry.

The error on \mathcal{A}_{obs} scales with $1/\sqrt{\varepsilon_{\text{tag}} N}$, where N is the number of untagged decays. Accordingly, the error on the asymmetry is proportional to

$$\sigma_{\mathcal{A}_{\text{phys}}} \propto \frac{1}{\mathcal{D} \sqrt{\varepsilon_{\text{tag}} N}} \quad . \quad (7.11)$$

It follows that the sensitivity on the asymmetry scales with the square root of the tagging power, Q_{tag} , defined as

$$Q_{\text{tag}} = \varepsilon_{\text{tag}} (1 - 2w_{\text{tag}})^2 \quad . \quad (7.12)$$

This equation shows that both a high efficiency and a low wrong tag fraction are required for a good sensitivity to observe B oscillations.

In the fragmentation process of the $b\bar{b}$ pair, both b quarks can hadronise into any B hadron. Afterwards, these hadrons evolve in an incoherent state. The flavour tagging

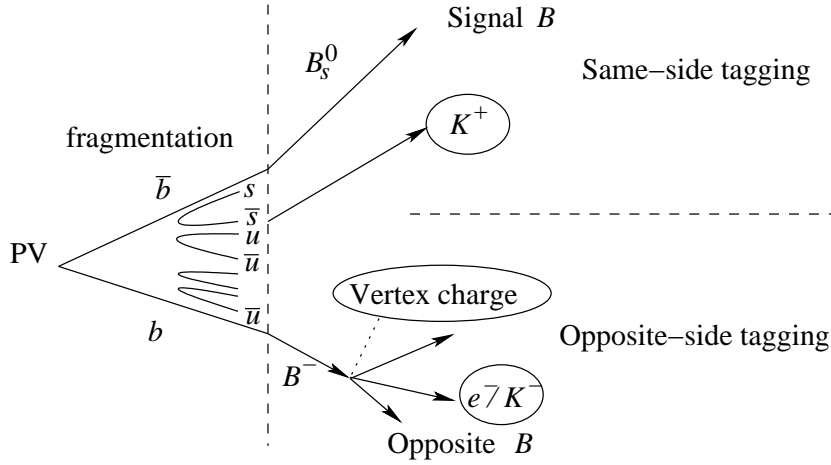


Figure 7.10: Schematic picture of the flavour tagging method, showing same-side tagging and opposite-side tagging. In this example the opposite b quark hadronises into a charged B^- .

probes the b quark flavour at time of production. There are two strategies to determine the flavour of the signal B meson: opposite-side tagging and same-side tagging [106]. They are schematically depicted in Fig. 7.10. In opposite-side tagging the flavour of the *other* B hadron from the $b\bar{b}$ pair is measured to deduce the flavour of the signal B . This can be done by measuring the charge of the lepton in semileptonic B decays (lepton tag) or the charge of the kaon in $b \rightarrow c \rightarrow s$ transitions (kaon tag). Also, by inclusive reconstruction of the secondary vertex, the charge of the tagging B hadron can be used to improve the tagging performance. The method of opposite-side tagging suffers from an intrinsic dilution, since, in case it is neutral, the tagging B itself can oscillate, leading to a wrong assumption for the B flavour at production. Furthermore, wrong tags also occur, e.g., when leptons from a $b \rightarrow c \rightarrow \ell$ transition are selected.

In same-side tagging the flavour of the signal B meson is measured directly. This method is mainly applied to B_s^0 mesons. When a B_s^0 ($\bar{b}s$) is created in a pp collision an \bar{s} quark becomes available in the $b\bar{b}$ fragmentation process. In case the \bar{s} quark hadronises into a K^+ ($\bar{s}u$), the positive charge of the kaon reveals the flavour of the B_s^0 meson. These tagging kaons originate from the primary vertex and, as they are produced adjacent to B_s^0 meson in the string fragmentation, these kaons are correlated in phase space with the B_s^0 meson. The same method can also be applied to tag B^0 mesons using charged pions. The high abundance of pions in the detector, however, makes this method less suitable for the B_d system. Another method under study uses the charge of the pion in the decay of a B resonance through $B^{**+} \rightarrow B^{(*)0}\pi^+$ to determine the B flavour (see also Section 4.3.4).

In order to obtain the best tagging performance, the methods of opposite-side and same-side tagging are combined. The final tagging efficiency for the $B_s^0 \rightarrow D_s^\mp K^\pm$ decay channel is $(53.5 \pm 0.6)\%$ with a wrong tag fraction of $(33.4 \pm 0.8)\%$ [106]. This results in a tagging power of $(5.90 \pm 0.16)\%$. For the $B_s^0 \rightarrow D_s^-\pi^+$ and $B_s^0 \rightarrow D_s^{(\ast)\mp}K^{(\ast)\pm}$ decay

channels the same tagging performance is assumed.

7.5 Sensitivity studies

The experimental sensitivity to measure the oscillation frequency Δm_s and the weak phase $\gamma - 2\chi$ is determined in a separate, fast Monte Carlo simulation [107]. This programme generates events according to the expected annual yield and B/S ratio obtained from the full Monte Carlo simulation as described in this thesis. For each event a final state f or \bar{f} is generated with a certain decay time, decay time error, and flavour tag. The final physics sensitivity is determined from an unbinned likelihood fit to the observed decay time distributions. The simulation and fit sequence is repeated for different settings of the input parameters. For each setting, 100 LHCb “experiments” are performed. All these jobs are executed using the DataGrid [108], which provides the required computing power.

The fast Monte Carlo programme can be divided into three steps:

- **Generator.** The four time-dependent decay rates $B \rightarrow f$, $\bar{B} \rightarrow f$, $B \rightarrow \bar{f}$, and $\bar{B} \rightarrow \bar{f}$ are calculated according to the master equations (2.29). Signal events are generated with a true decay time (t_{true}), according to these decay rates. In addition, background events are generated, but their decay rate follows a simple exponential decay. Their lifetime equals half the B lifetime [107], emulating the combinatorics from wrongly reconstructed events.
- **Simulator.** Several detector effects are simulated. First, an estimated error, σ_t , on the true decay time is assigned to each event. This error is taken from an event selected in the full Monte Carlo simulation with approximately the same t_{true} . This method properly accounts for the variations in the error distribution shown in Fig. 7.8(c). The reconstructed decay time, t_{rec} , is obtained by smearing t_{true} with a single Gaussian having a width of σ_t . Second, the acceptance function (7.9) is applied to the events. And finally, a flavour tag is assigned to each event taking into account the tagging efficiency and wrong tag fraction as given in Section 7.4.
- **Fitter.** A likelihood fit is performed on the four observed decay time distributions. The maximum sensitivity is reached by simultaneously fitting both the $B_s^0 \rightarrow D_s^- \pi^+$ and the $B_s^0 \rightarrow D_s^\mp K^\pm$ decays. The likelihood function \mathcal{L} is explained in the following.

7.5.1 Likelihood fit

The total likelihood is the product of the likelihoods for each event

$$\mathcal{L} = \prod \mathcal{L}_i . \quad (7.13)$$

The likelihood for an event i can be expressed as the convolution of the decay rates with the decay time resolution:

$$\mathcal{L}_i = \int_0^\infty [(1 - f_{\text{bg}})M_{\text{sig}}\mathcal{L}_{\text{sig}}(t) + f_{\text{bg}}M_{\text{bg}}\mathcal{L}_{\text{bg}}(t)] \varepsilon_t(t) G(t - t_{\text{rec}}, \sigma_t) dt , \quad (7.14)$$

where f_{bg} is the background fraction, $\mathcal{L}_{\text{sig}}(t)$ and $\mathcal{L}_{\text{bg}}(t)$ are the signal and background likelihoods, M_{sig} and M_{bg} are the mass probability functions for signal and background, and $\varepsilon_t(t)$ is the time-dependent acceptance function introduced in (7.9). The decay time resolution function is described by a Gaussian distribution

$$G(t - t_{\text{rec}}, \sigma_t) = \frac{1}{\sqrt{2\pi}\sigma_t} e^{-(t-t_{\text{rec}})^2/2\sigma_t^2} , \quad (7.15)$$

with t_{rec} the reconstructed time and σ_t the corresponding uncertainty, obtained from the full simulation.

The invariant mass distribution of the B_s provides statistical information on the probability that an event is signal or background. Therefore, for each event also a reconstructed mass, m_{rec} , is generated. The mass probability function for signal events follows a Gaussian distribution

$$M_{\text{sig}} = \frac{1}{\sqrt{2\pi}\sigma_m} e^{-(m_{\text{rec}} - m_{B_s})^2/2\sigma_m^2} , \quad (7.16)$$

where the mass resolution, σ_m , equals 12.10 MeV for $B_s^0 \rightarrow D_s^\mp K^\pm$ events and 13.5 MeV for $B_s^0 \rightarrow D_s^- \pi^+$ events. The mass distribution for $b\bar{b}$ inclusive background is assumed to be flat, i.e.,

$$M_{\text{bg}} = \text{constant} . \quad (7.17)$$

For a given event $B \rightarrow f$ the signal likelihood equals

$$\mathcal{L}_{\text{sig}}(t) = (1 - w_{\text{tag}})\Gamma_{B \rightarrow f}(t) + w_{\text{tag}}\Gamma_{\bar{B} \rightarrow f}(t) , \quad (7.18)$$

where w_{tag} is the wrong tag fraction. The signal likelihoods for $\bar{B} \rightarrow f$, $B \rightarrow \bar{f}$, and $\bar{B} \rightarrow \bar{f}$ events are obtained analogously. For untagged events, the value $w_{\text{tag}} = 0.5$ is inserted. The time-dependent decay rates, $\Gamma_{B \rightarrow f}(t)$ and $\Gamma_{\bar{B} \rightarrow f}(t)$, are given by the master equations (2.29). They introduce the sensitivity on Δm_s , $\Delta\Gamma_s$, λ_f and $\lambda_{\bar{f}}$ into the likelihood function. Note that for $B_s^0 \rightarrow D_s^- \pi^+$ decays, λ_f and $\lambda_{\bar{f}}$ are equal to zero, implying also that $D_f = S_f = 0$ and $C_f = 1$. Hence, only the $\cosh \Delta\Gamma_s t / 2$ and $\cos \Delta m_s t$ terms remain in (2.29) for these events. The background likelihood function is

$$\mathcal{L}_{\text{bg}}(t) = 2\Gamma_s e^{-2\Gamma_s t} , \quad (7.19)$$

such that the average lifetime of background events equals $\tau_s/2$.

The sensitivity on Δm_s and $\gamma - 2\chi$ is extracted from a simultaneous likelihood fit to the decay rates of $B_s^0 \rightarrow D_s^\mp K^\pm$ and $B_s^0 \rightarrow D_s^- \pi^+$. The combined analysis ensures a maximal precision on the values for the physics parameters. As an example, Fig. 7.11 shows the four decay rates for $B_s^0 \rightarrow D_s^\mp K^\pm$ observed after three years of data taking, assuming a constant luminosity. The result of the likelihood fit is superimposed.

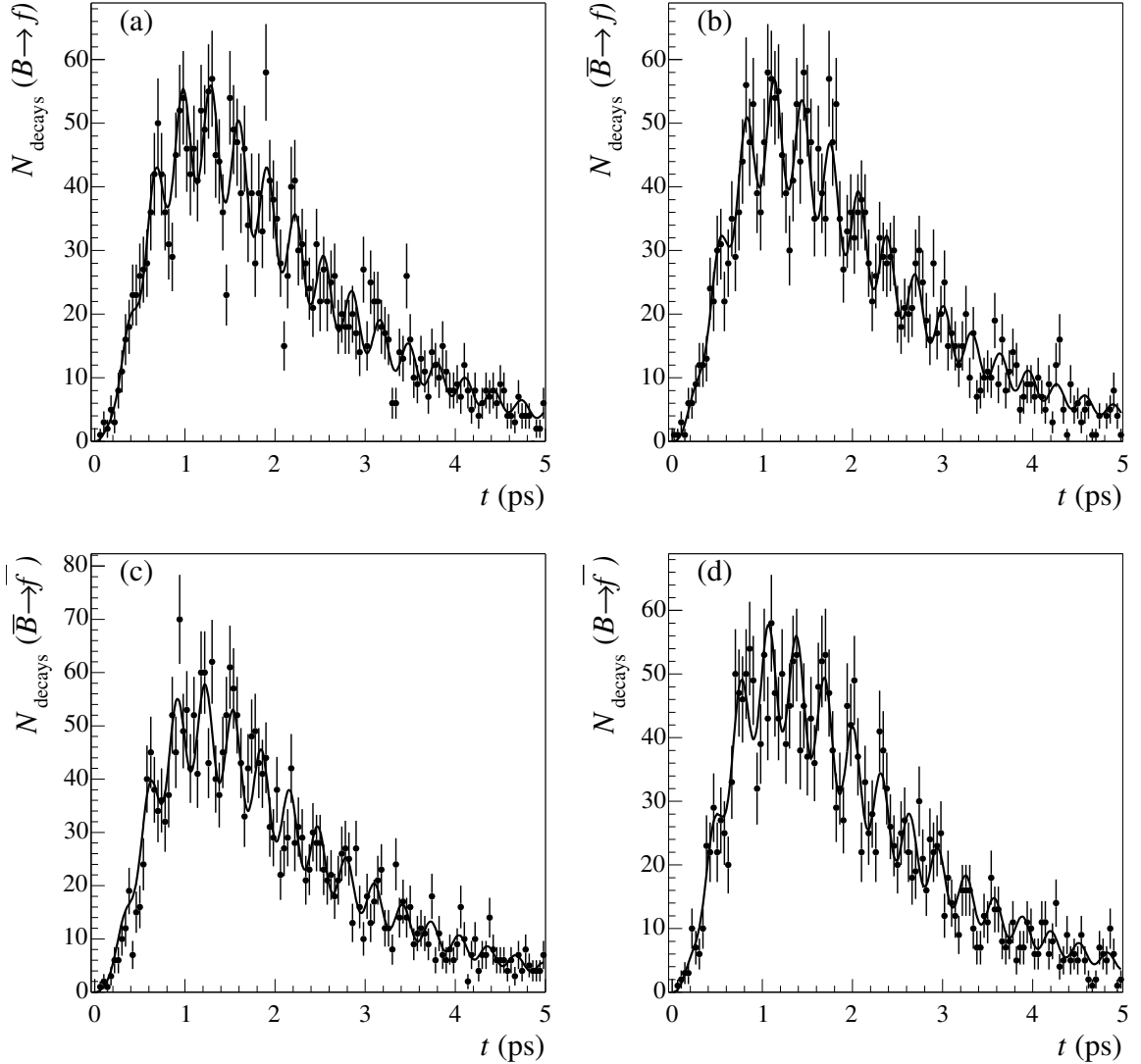


Figure 7.11: Observed decay rates for $B_s^0 \rightarrow D_s^- K^+$ (a), $\bar{B}_s^0 \rightarrow D_s^- K^+$ (b), $\bar{B}_s^0 \rightarrow D_s^+ K^-$ (c), $B_s^0 \rightarrow D_s^+ K^-$ (d) after three years of data taking. The corresponding decay rates from the likelihood fit are superimposed.

7.5.2 Sensitivity on Δm_s

Figure 7.12(a) shows the expected resolution of the Δm_s measurement for a value of $\Delta m_s = 20 \text{ ps}^{-1}$ after 1 year of data taking. The error on the oscillation frequency, $\delta(\Delta m_s)$, is determined from the difference between the value from the fit and the true value. The Gaussian width of this distribution gives a statistical precision on Δm_s of 0.010 ps^{-1} .

To find the maximum value of Δm_s that can be measured in LHCb, the amplitude method [109] is adopted. In this method, the $\cos \Delta m_s t$ term in (2.29) is multiplied by an

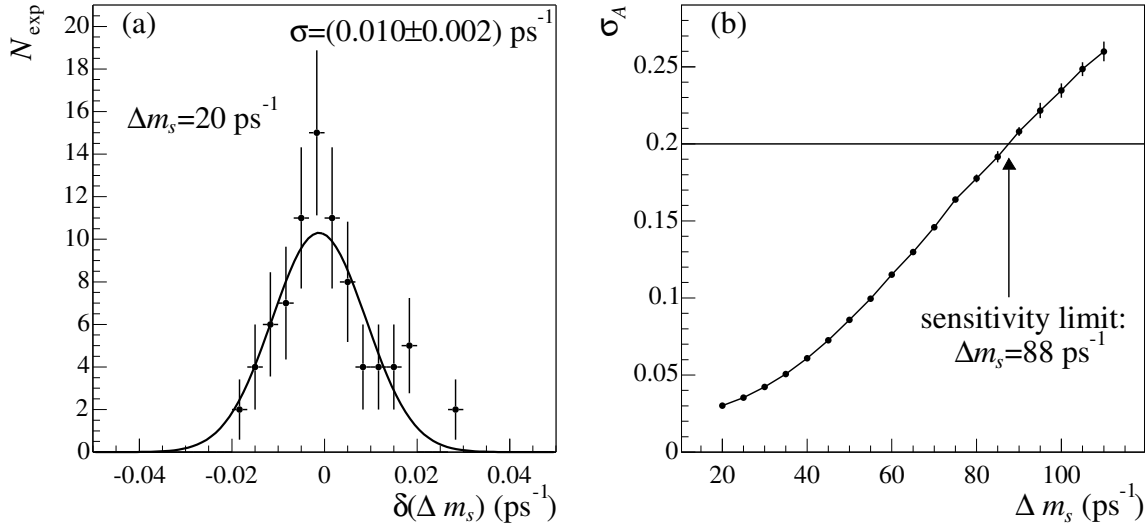


Figure 7.12: The Δm_s resolution for $\Delta m_s = 20 \text{ ps}^{-1}$ (a) and the uncertainty on the amplitude A versus Δm_s (b), both after 1 year of data taking. The sensitivity limit, satisfying $5\sigma_A = 1$, is $\Delta m_s = 88 \text{ ps}^{-1}$.

amplitude factor A . Subsequently, this amplitude is fitted for fixed values of Δm_s . When Δm_s is equal to the simulated or true value, the fit should return $A \approx 1$. The amplitude method is mathematically equivalent to a Fourier analysis on the time spectrum. The sensitivity of an experiment to the oscillation frequency is given by the uncertainty on the fitted value A . Figure 7.12(b) shows the sensitivity versus Δm_s in the “absence” of any oscillation (i.e., the data was generated with an “infinite” value of $\Delta m_s = 400 \text{ ps}^{-1}$). The sensitivity limit is defined as the value of Δm_s for which $5\sigma_A = 1$. It is found that in case there is no signal present in the data, values up to 88 ps^{-1} can be excluded at a 5σ confidence level.

7.5.3 Sensitivity on $\gamma - 2\chi$

For the simultaneous fit, $B_s^0 \rightarrow D_s^- \pi^+$ and $B_s^0 \rightarrow D_s^\mp K^\pm$ events are generated with the default input parameters as listed in Table 7.9. The number of generated events corresponds to three years of data taking. The number of $B_s^0 \rightarrow D_s^\mp K^\pm$ events includes the contributions from $B_s^0 \rightarrow D_s^{*\mp} K^\pm$ and $B_s^0 \rightarrow D_s^\mp K^{*\pm}$ decays. The default value for the weak phase is obtained from the Standard Model prediction of $\gamma = (60 \pm 14)^\circ$ [8]. The default value for the strong phase is set to zero, since QCD factorisation predicts small values for Δ_s [110]. The values of the other parameters have been discussed before.

The $B_s^0 \rightarrow D_s^\mp K^\pm$ events are sensitive to $|\lambda_f|$ and to the weak and strong phase. The two phases are not measured directly, but instead $\arg \lambda_f$ and $\arg \bar{\lambda}_{\bar{f}}$ are measured. Accordingly, the weak phase is determined from (2.36) as

$$\gamma - 2\chi = \frac{\arg \bar{\lambda}_{D_s^+ K^-} - \arg \lambda_{D_s^- K^+}}{2} . \quad (7.20)$$

Table 7.9: Default values for the input parameters in the generation of $B_s^0 \rightarrow D_s^- \pi^+$ and $B_s^0 \rightarrow D_s^\mp K^\pm$ events.

Variable	$B_s^0 \rightarrow D_s^- \pi^+$	$B_s^0 \rightarrow D_s^\mp K^\pm$
N_{years}	3	3
$N_{\text{events}}/\text{year}$	85k	6k
B/S	0.34	0.24
Δm_s	20 ps^{-1}	20 ps^{-1}
$\Delta \Gamma_s / \Gamma_s$	0.1	0.1
$ \lambda_f = \bar{\lambda}_{\bar{f}} $	0	0.37
$\gamma - 2\chi$	0°	60°
Δ_s	0°	0°

Similarly, the strong phase equals

$$\Delta_s = \frac{\arg \bar{\lambda}_{D_s^+ K^-} + \arg \lambda_{D_s^- K^+}}{2}. \quad (7.21)$$

The wrong tag fraction, which is assumed to be the same for both decay channels, is also fitted. The value for $\Delta \Gamma_s$ is fixed to the true value, since it can be obtained with more precision from decay channels as, e.g., $B_s^0 \rightarrow J/\psi \phi$.

The fast Monte Carlo programme is repeated for 100 “experiments”. The mean sensitivity on the weak angle after three years of data taking using the default settings equals 8.4° . Figure 7.13(a) shows the variations in the uncertainty on $\gamma - 2\chi$. An intrinsic fluctuation in the sensitivity with an rms of 1.1° is observed. This fluctuation can be interpreted as the *luck factor* and reduces with increasing statistics. The increase in the statistical precision with the number of years of data taking is illustrated in Fig. 7.13(b).

Figure 7.14 shows the sensitivity when varying the input parameters in Table 7.9. Each time, only one parameter is varied; the others are set to their default value. As can be expected from (2.29), the sensitivity increases towards smaller values for Δm_s , and towards higher values for $\Delta \Gamma_s$ and $|\lambda_f|$. Also, the sensitivity decreases for larger background values (only B is varied; S is fixed). Note that for convenience all $B_s^0 \rightarrow D_s^{(*)\mp} K^{(*)\pm}$ decay channels are assumed to have the same B/S ratio. The background dependence indicates that the higher B/S ratios for $B_s^0 \rightarrow D_s^{*\mp} K^\pm$ and $B_s^0 \rightarrow D_s^\mp K^{*\pm}$ events result in a slightly reduced overall sensitivity.

The actual values for the weak and strong phases seem to have less effect on the sensitivity. However, a final note should be made on the ambiguities in extracting the weak phase from $\arg \lambda_f$ and $\arg \bar{\lambda}_{\bar{f}}$. A two-fold ambiguity is introduced by (7.20), since there is an equally valid solution at $\pm 180^\circ$ from the true value of weak phase. In addition, in case $\Delta \Gamma_s$ is small, only the terms $S_f \propto \sin(\arg \lambda_f)$ and $S_{\bar{f}} \propto \sin(\arg \bar{\lambda}_{\bar{f}})$ in (2.29) are sensitive to the phases of λ_f and $\bar{\lambda}_{\bar{f}}$. Then, both $\arg \lambda_f$ and $\arg \bar{\lambda}_{\bar{f}}$ yield two solutions, and the two-fold ambiguity thus becomes an eight-fold ambiguity. An unwanted scenario arises when the ambiguous solutions start to overlap, which effectively results in a larger error on $\gamma - 2\chi$. The overlapping occurs when $\sin(\arg \lambda_f)$ or $\sin(\arg \bar{\lambda}_{\bar{f}})$ is close to unity.

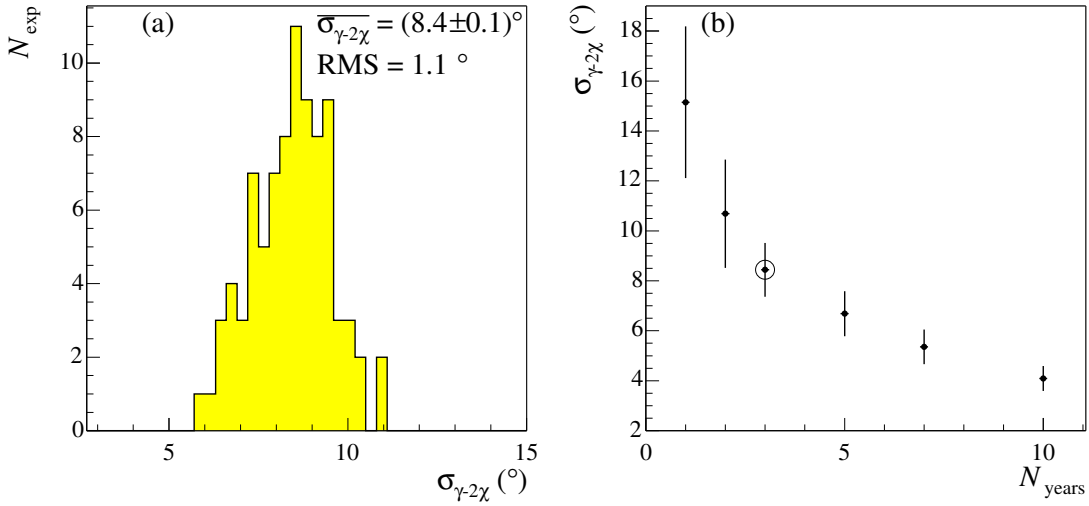


Figure 7.13: The distribution of the sensitivity on the weak phase $\gamma - 2\chi$ after three years of data taking for 100 experiments (a). There is an intrinsic fluctuation of the sensitivity of 1.1° . Also drawn is the sensitivity versus the number of years (b). The error bars indicate the rms fluctuation.

On the other hand, if $\Delta\Gamma_s$ is sizable, also the terms $D_f \propto \cos(\arg\lambda_f)$ and $D_{\bar{f}} \propto \cos(\arg\bar{\lambda}_{\bar{f}})$ in (2.29) contribute to the sensitivity on $\arg\lambda_f$ and $\arg\bar{\lambda}_{\bar{f}}$, in which case only two preferred solutions for $\gamma - 2\chi$ remain. To estimate the sensitivity due to these two terms only, a fit to the untagged decay rates with $\Delta\Gamma_s/\Gamma_s = 0.1$ is performed, resulting in an uncertainty on $\gamma - 2\chi$ of 17° after three years of data taking. For higher values of $\Delta\Gamma_s/\Gamma_s$ the sensitivity due to the untagged decay rates will become more important. Another approach to resolve the ambiguities, proposed in Ref. [99], relies on a combined U -spin analysis using $B^0 \rightarrow D^{(*)\mp}\pi^\pm$ decay channels.

7.6 Conclusion

Starting in 2007, the LHC will be a copious source of B mesons. The LHCb experiment is well equipped to accurately measure a large sample of decays of these B mesons, thereby providing access to CP -violating B decays with small branching fractions. This detector is modelled in detail, including a comprehensive description of the geometry, the interactions of the particles with the material, and the response of the detector to the traversing particles. An efficient track reconstruction, which determines the particles' momenta with high precision, is the input for the event selection and sensitivity studies.

The analysis presented in this thesis has shown the feasibility for an efficient selection of $B_s^0 \rightarrow D_s^-\pi^+$ and $B_s^0 \rightarrow D_s^\mp K^\pm$ events with a low background contamination using the LHCb detector. Additional statistics become available when including also $B_s^0 \rightarrow D_s^{*\mp}K^\pm$ events in the event selection. Due to the excellent decay time resolution in these

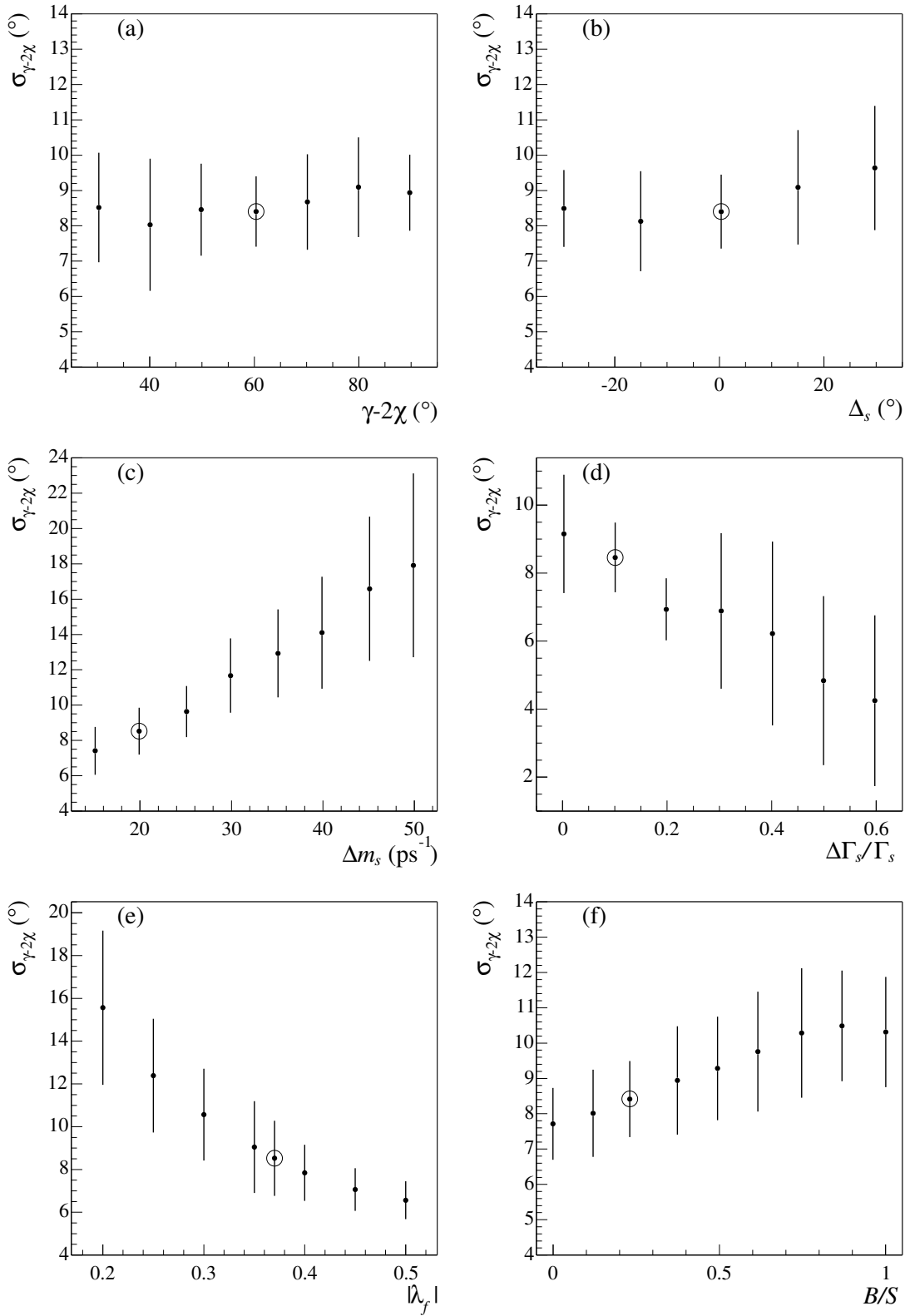


Figure 7.14: The sensitivity on the weak phase $\gamma - 2\chi$ versus $\gamma - 2\chi$ (a), versus the strong phase Δ_s (b), versus Δm_s (c), versus $\Delta \Gamma_s / \Gamma_s$ (d), versus $|\lambda_f|$ (e), and versus B/S (f). The default setting is indicated with a circle. The error bars show the rms fluctuation.

decays, a high sensitivity to measure the oscillation frequency up to $\Delta m_s = 88 \text{ ps}^{-1}$ can be achieved. Furthermore, assuming the expectation values for the physics parameters as given in Table 7.9, the weak phase $\gamma - 2\chi$ can be measured with an uncertainty of 8.4° after three years of data taking.

Appendix A

Kalman filter derivation

In order to derive the Kalman filter equations, it is assumed that the filtered state vector, \vec{x}_k , is a linear combination of the predicted state vector, \vec{x}_k^{k-1} , and the predicted residual in (6.10) as

$$\begin{aligned}\vec{x}_k &= \vec{x}_k^{k-1} + K_k r_k^{k-1} \\ &= \vec{x}_k^{k-1} + K_k(m_k - H_k \vec{x}_k^{k-1}) ,\end{aligned}\quad (\text{A.1})$$

where K_k is the gain matrix. The goal is to find the optimal value for K_k . First, the error on the predicted and filtered state vectors are defined as

$$\vec{e}_k^{k-1} = \vec{x}_k^{k-1} - \vec{x}_k^{\text{true}} ,\quad (\text{A.2})$$

$$\vec{e}_k = \vec{x}_k - \vec{x}_k^{\text{true}} ,\quad (\text{A.3})$$

where \vec{x}_k^{true} is the (unknown) true state vector. Now, by inserting (A.1) into (A.3) it is found that

$$\begin{aligned}\vec{e}_k &= \vec{x}_k^{k-1} + K_k(m_k - H_k \vec{x}_k^{k-1}) - \vec{x}_k^{\text{true}} \\ &= (\mathbb{1} - K_k H_k)(\vec{x}_k^{k-1} - \vec{x}_k^{\text{true}}) + K_k(m_k - H_k \vec{x}_k^{\text{true}}) \\ &= (\mathbb{1} - K_k H_k)\vec{e}_k^{k-1} + K_k \epsilon_k ,\end{aligned}\quad (\text{A.4})$$

where ϵ_k is the measurement noise, which has a corresponding covariance $\text{cov}(\epsilon_k) = V_k$. The filtered covariance matrix equals

$$\begin{aligned}C_k &= \text{cov}(\vec{e}_k) \\ &= (\mathbb{1} - K_k H_k)C_k^{k-1}(\mathbb{1} - K_k H_k)^T + K_k V_k K_k^T ,\end{aligned}\quad (\text{A.5})$$

which is known as Joseph's formula. The next step is to minimise this covariance matrix. This can be accomplished by first calculating the trace

$$\begin{aligned}\text{Tr}(C_k) &= \text{Tr}(C_k^{k-1}) - \text{Tr}(K_k H_k C_k^{k-1}) - \text{Tr}(C_k^{k-1}(K_k H_k)^T) \\ &\quad + \text{Tr}(K_k H_k C_k^{k-1}(K_k H_k)^T) + \text{Tr}(K_k V_k K_k^T) \\ &= \text{Tr}(C_k^{k-1}) - 2\text{Tr}(K_k H_k C_k^{k-1}) \\ &\quad + \text{Tr}(K_k(H_k C_k^{k-1} H_k^T) K_k^T) + \text{Tr}(K_k V_k K_k^T) ,\end{aligned}\quad (\text{A.6})$$

and then taking the derivative with respect to K_k

$$\frac{\delta \text{Tr}(C_k)}{\delta K_k} = -2(H_k C_k^{k-1})^T + 2K_k(H_k C_k^{k-1} H_k^T) + 2K_k V_k \quad , \quad (\text{A.7})$$

using the trace identities

$$\frac{\delta \text{Tr}(AB)}{\delta A} = B^T \quad , \quad (\text{A.8})$$

$$\frac{\delta \text{Tr}(ABA^T)}{\delta A} = 2AB \quad \text{for } B = B^T \quad . \quad (\text{A.9})$$

Finally, by setting (A.7) equal to zero,

$$-C_k^{k-1} H_k^T + K_k(H_k C_k^{k-1} H_k^T) + K_k V_k = 0 \quad , \quad (\text{A.10})$$

the result as given in (6.15) is derived

$$K_k = C_k^{k-1} H_k^T (V_k + H_k C_k^{k-1} H_k^T)^{-1} \quad . \quad (\text{A.11})$$

The filtered covariance matrix is calculated from Joseph's formula (A.5) using (A.10):

$$\begin{aligned} C_k &= (\mathbb{1} - K_k H_k) C_k^{k-1} (\mathbb{1} - K_k H_k)^T + (C_k^{k-1} H_k^T - K_k H_k C_k^{k-1} H_k^T) K_k^T \\ &= (\mathbb{1} - K_k H_k) C_k^{k-1} (\mathbb{1} - K_k H_k)^T + (\mathbb{1} - K_k H_k) C_k^{k-1} (K_k H_k)^T \\ &= (\mathbb{1} - K_k H_k) C_k^{k-1} \quad . \end{aligned} \quad (\text{A.12})$$

For further reading on the Kalman filter see for instance Ref. [88].

References

- [1] AMS Collaboration, J. Alcaraz *et al.*, *Search for antihelium in cosmic rays*, Phys. Lett. **B461** (1999) 387.
- [2] A.D. Sakharov, *Violation of CP invariance, C asymmetry, and baryon asymmetry in the universe*, Pisma Zh. Eksp. Teor. Fiz. **5** (1967) 32.
- [3] T.D. Lee and C.N. Yang, *Question of parity conservation in weak interactions*, Phys. Rev. **104** (1956) 257.
- [4] C. Wu *et al.*, *Experimental Test of Parity Conservation in Beta Decay*, Phys. Rev. **105** (1957) 1413.
- [5] J.H. Christenson, J.W. Cronin, V.L. Fitch, and R. Turlay, *Evidence for the 2π decay of the K_2^0 meson*, Phys. Rev. Lett. **13** (1964) 138.
- [6] F. Halzen and A.D. Martin, *Quarks and leptons: An introductory course in modern particle physics*, John Wiley & Sons, Inc., New York, 1984.
- [7] G.C. Branco, L. Lavoura, and J.P. Silva, *CP violation*, Oxford University Press, New York, 1999.
- [8] S. Eidelman *et al.*, *Review of Particle Physics*, Phys. Lett. **B592** (2004) .
- [9] S. L. Glashow, J. Iliopoulos, and L. Maiani, *Weak interactions with lepton - hadron symmetry*, Phys. Rev. **D2** (1970) 1285.
- [10] M. Kobayashi and T. Maskawa, *CP violation in the renormalizable theory of weak interaction*, Prog. Theor. Phys. **49** (1973) 652.
- [11] C. Jarlskog, *Commutator of the quark mass matrices in the standard electroweak model and a measure of maximal CP violation*, Phys. Rev. Lett. **55** (1985) 1039.
- [12] BABAR Collaboration, B. Aubert *et al.*, *Measurement of the CP-violating asymmetry amplitude $\sin 2\beta$.*, Phys. Rev. Lett. **89** (2002) 201802.
- [13] Belle Collaboration, K. Abe *et al.*, *Measurement of CP-violation parameter $\sin(2\phi_1)$ with 152 million B anti-B pairs*, hep-ex/0308036, 2003.

- [14] E. Fernandez *et al.*, *Lifetime of particles containing b quarks*, Phys. Rev. Lett. **51** (1983) 1022.
- [15] N. Lockyer *et al.*, *Measurement of the lifetime of bottom hadrons*, Phys. Rev. Lett. **51** (1983) 1316.
- [16] ARGUS Collaboration, H. Albrecht *et al.*, *Observation of $B^0 - \bar{B}^0$ mixing*, Phys. Lett. **B192** (1987) 245.
- [17] I. Dunietz, R. Fleischer, and U. Nierste, *In pursuit of new physics with B_s decays*, Phys. Rev. **D63** (2001) 114015.
- [18] CDF Collaboration, D. Acosta *et al.*, *Analysis of decay-time dependence of angular distributions in $B_s^0 \rightarrow J/\psi \phi$ and $B^0 \rightarrow J/\psi K^{*0}$ decays and measurement of the lifetime difference between B_s mass eigenstates*, Phys. Rev. Lett. **94** (2005) 101803.
- [19] R. Aleksan, I. Dunietz, and B. Kayser, *Determining the CP violating phase γ* , Z. Phys. **C54** (1992) 653.
- [20] P. Lefèvre and T. Pettersson, *The Large Hadron Collider: conceptual design*, CERN-AC-95-05-LHC, 1995.
- [21] LHCb Collaboration, S. Amato *et al.*, *LHCb Technical Proposal*, CERN-LHCC/98-4, 1998.
- [22] ATLAS Collaboration, W.W. Armstrong *et al.*, *ATLAS : Technical Proposal for a General-Purpose pp Experiment at the Large Hadron Collider at CERN*, CERN-LHCC/94-43, 1994.
- [23] CMS Collaboration, *Technical Proposal*, CERN-LHCC/94-38, 1994.
- [24] ALICE Collaboration, N. Ahmad *et al.*, *A Large Ion Collider Experiment - Technical Proposal*, CERN-LHCC/95-71, 1995.
- [25] P. Nason *et al.*, *Bottom production*, hep-ph/0003142, 1999.
- [26] LHCb Collaboration, R. Nobrega *et al.*, *LHCb Reoptimized Detector Design and Performance Technical Design Report*, CERN-LHCC/2003-030, 2003.
- [27] R. Lindner, *Definition of the coordinate system*, Techn. Note/LHCB-C-EN-0001, 2003.
- [28] LHCb Collaboration, S. Amato *et al.*, *LHCb Magnet Technical Design Report*, CERN-LHCC/2000-007, 1999.
- [29] LHCb Collaboration, P. Barbosa-Marinho *et al.*, *LHCb VELO Technical Design Report*, CERN-LHCC/2001-011, 2001.
- [30] J. Gassner, M. Needham, and O. Steinkamp, *Layout and expected performance of the LHCb TT station*, LHCb/2003-140, 2003.

- [31] M. Needham, *Silicon Tracker simulation performance*, LHCb/2003-015, 2003.
- [32] LHCb Collaboration, P. Barbosa-Marinho *et al.*, *LHCb Inner Tracker Technical Design Report*, CERN-LHCC/2002-029, 2003.
- [33] LHCb Collaboration, P. Barbosa-Marinho *et al.*, *LHCb Outer Tracker Technical Design Report*, CERN-LHCC/2001-024, 2001.
- [34] S. Bachmann and A. Pellegrino, *Geometry of the Outer Tracker (part I)*, LHCb/2003-035, 2003.
- [35] S. Bachmann, T. Haas, M. Walter, and D. Wiedner, *Construction of module boxes for the Outer Tracker in LHCb*, LHCb/2003-051, 2003.
- [36] I. Gouz, Th.S. Bauer, and L.B.A. Hommels, *Beam tests of a full-scale prototype of the LHCb Outer Tracker straw tube modules*, LHCb/2001-098, 2001.
- [37] G.W. Apeldoorn, Th.S. Bauer, and J. Steijger, *Aging studies of straw tube chambers*, LHCb/2001-003, 2001.
- [38] I. Gouz, B. Hommels, and G.W. van Apeldoorn, *Beam tests of LHCb Outer Tracker prototypes in 2000*, LHCb/2001-011, 2001.
- [39] B. Bevensee, F.M. Newcomer, R. Van Berg, and H.H. Williams, *An amplifier shaper discriminator with baseline restoration for the ATLAS transition radiation tracker*, IEEE Trans. Nucl. Sci. **43** (1996) 1725.
- [40] V. Gromov *et al.*, *Study of operational properties of the ASDBLR chip for the LHCb Outer Tracker*, LHCb/2000-054, 2000.
- [41] H. Deppe *et al.*, *Proposal for the LHCb Outer Tracker front end electronics*, LHCb/2001-015, 2001.
- [42] P. Moreira *et al.*, *A 1.25-Gbit/s serializer for LHC data and trigger optical links*, Prepared for 5th Workshop on Electronics for the LHC Experiments (LEB 99), Snowmass, Colorado, 20-24 Sep 1999.
- [43] LHCb Collaboration, S. Amato *et al.*, *LHCb RICH Technical Design Report*, CERN-LHCC/2000-037, 2000.
- [44] LHCb Collaboration, S. Amato *et al.*, *LHCb Calorimeter Technical Design Report*, CERN-LHCC/2000-036, 2000.
- [45] LHCb Collaboration, P. Barbosa-Marinho *et al.*, *LHCb Muon Technical Design Report*, CERN-LHCC/2001-010, 2001.
- [46] LHCb Collaboration, R. Nobrega *et al.*, *LHCb Trigger Technical Design Report*, CERN-LHCC/2003-031, 2003.

- [47] F. Legger, A. Bay, G. Haefeli, and L. Locatelli, *TELL1 : a common readout board for LHCb*, LHCb/2004-100, 2004.
- [48] O. Callot, *Online pattern recognition*, LHCb/2004-094, 2004.
- [49] LHCb Collaboration, P. Barbosa-Marinho *et al.*, *LHCb online system Technical Design Report: Data acquisition and experiment control*, CERN-LHCC/2001-040, 2001.
- [50] R.H. Hierck, *Optimisation of the LHCb detector*, Ph.D. thesis, NIKHEF, 2003, CERN-THESIS/2003-025.
- [51] G. Barrand *et al.*, *GAUDI - A software architecture and framework for building HEP data processing applications*, Comput. Phys. Commun. **140** (2001) 45.
- [52] T. Sjöstrand, P. Edén, C. Friberg, L. Lönnblad, G. Miu, S. Mrenna, and E. Norrbin, *High-Energy-Physics Event Generation with PYTHIA 6.1*, Comput. Phys. Commun. **135** (2001) 238.
- [53] D.J. Lange, *The EvtGen particle decay simulation package*, Nucl. Instr. and Methods A **462** (2001) 152.
- [54] I. Belyaev *et al.*, *Simulation application for the LHCb experiment*, physics/0306035, 2003.
- [55] GEANT4 Collaboration, S. Agostinelli *et al.*, *Geant4: A simulation toolkit*, Nucl. Instrum. Meth. **A506** (2003) 250.
- [56] M. Cattaneo, *Boole: The LHCb digitization program*, <http://lhcb-comp.web.cern.ch/lhcb-comp/Digitization>, 2004.
- [57] M. Cattaneo, *Brunel: The LHCb Reconstruction Program*, <http://lhcb-comp.web.cern.ch/lhcb-comp/Reconstruction/>, 2004.
- [58] P. Koppenburg, *DaVinci: The LHCb Analysis program*, <http://lhcb-comp.web.cern.ch/lhcb-comp/Analysis>, 2004.
- [59] I. Belyaev, *Python-based physics analysis environment for LHCb*, Prepared for CHEP 2004, Interlaken, Switzerland, 27 September 2004, 2004.
- [60] G. Barrand, *Data Visualization*, <http://lhcb-comp.web.cern.ch/lhcb-comp/Frameworks/Visualization/>, 2003.
- [61] S. Ponce *et al.*, *Detector Description Framework in LHCb*, physics/0306089, 2003.
- [62] S. Ponce, *The LHCb Detector description DTD*, <http://lhcb-comp.web.cern.ch/lhcb-comp/Frameworks/DetDesc/Documents/lhcBDtd.pdf>, 2001.
- [63] T. Sjöstrand and M. van Zijl, *A multiple interaction model for the event structure in hadron collisions*, Phys. Rev. **D36** (1987) 2019.

- [64] CDF Collaboration, F. Abe *et al.*, *Pseudorapidity distributions of charged particles produced in $\bar{p}p$ interactions at $\sqrt{s} = 630 \text{ GeV}$ and 1800 GeV* , Phys. Rev. **D41** (1990) 2330.
- [65] H.L. Lai *et al.*, *Improved parton distributions from global analysis of recent deep inelastic scattering and inclusive jet data*, Phys. Rev. **D55** (1997) 1280.
- [66] T. Sjöstrand, L. Lönnblad, and S. Mrenna, *PYTHIA 6.2: Physics and manual*, hep-ph/0108264, 2001.
- [67] W.H. Press, B.P. Flannery, S.A. Teukolsky, and W.T. Vetterling, *Numerical recipes*, Cambridge University Press (1986) .
- [68] M. Needham, *private communication*.
- [69] B. Rossi, *High-Energy Particles*, Prentice-Hall, Inc., Englewood Cliffs, NJ, 1952.
- [70] M. Needham, *Electron reconstruction studies*, LHCb/2001-102, 2001.
- [71] H.A. Bethe, *Molière's theory of multiple scattering*, Phys. Rev. **89** (1953) 1256.
- [72] V.L. Highland, *Some practical remarks on multiple scattering*, Nucl. Instr. Meth. **129** (1975) 497.
- [73] G.R. Lynch and O.I. Dahl, *Approximations to multiple coulomb scattering*, Nucl. Instrum. Meth. **B58** (1991) 6.
- [74] J. van Tilburg, *Outer Tracker Software*, LHCb/2003-062, 2003.
- [75] S. Ponce, *Extending detector elements and implications*, <http://lhcb-comp.web.cern.ch/lhcb-comp/Frameworks/DetDesc/Documents/detElemExtension.pdf>, 2001.
- [76] R. van der Eijk, *LHCb Outer Tracker prototypes*, LHCb/2000-057, 2000.
- [77] M. Merk *et al.*, *An Improved Digitization Procedure for the Outer Tracker*, LHCb/2001-055, 2001.
- [78] J. Nardulli, A. Pellegrino, and D. Wiedner, *Outer Tracker DAQ data format*, LHCb/2004-033, 2004.
- [79] M. Merk *et al.*, *Optimizing the Outer Tracker near the $y=0$ region*, LHCb/2003-019, 2003.
- [80] R.M. van der Eijk, *Track reconstruction in the LHCb experiment*, Ph.D. thesis, NIKHEF, 2002, CERN-THESIS/2002-032.
- [81] W. Hulsbergen *et al.*, *Calibration of the HERA-B Outer Tracker Chambers in a Cosmic Ray Setup at NIKHEF*, HERA-B/00-014, 2000.

- [82] V. Gromov and T. Sluijk, *Electrical properties of various types of straw tubes considered for the LHCb Outer Tracker*, LHCb/2001-001, 2001.
- [83] A. Pellegrino, *private communication*.
- [84] R.E. Kalman, *A new approach to linear filtering and prediction problems*, Trans. ASME J. Bas. Eng. **D82** (1960) 35.
- [85] P. Billoir, *Track fitting with multiple scattering: A new method*, Nucl. Instr. Meth. **A225** (1984) 352.
- [86] R. Frühwirth, *Application of Kalman filtering to track and vertex fitting*, Nucl. Instrum. Meth. **A262** (1987) 444.
- [87] H.E. Rauch, F. Tung, and C.T. Striebel, *Maximum likelihood estimates of linear dynamic systems*, AIAA Journal **3(8)** (1965) 1445.
- [88] P.S. Maybeck, *Stochastic models, estimation, and control*, Academic Press, Inc. 111 Fifth Avenue, New York, 1979.
- [89] D. Stampfer, M. Regler, and R. Frühwirth, *Track fitting with energy loss*, Comput. Phys. Commun. **79** (1994) 157.
- [90] E.J. Wolin and L.L. Ho, *Covariance matrices for track fitting with the Kalman filter*, Nucl. Instrum. Meth. **A329** (1993) 493.
- [91] R. Mankel, *Ranger - A pattern recognition algorithm for the HERA-B main tracking system. Part IV: The object-oriented track fit*, HERA-B note 98-079, 1998.
- [92] R. Mankel, *Application of the Kalman filter technique in the HERA-B track reconstruction*, HERA-B note 95-239, 1995.
- [93] O. Callot, *Improved robustness of the VELO tracking*, LHCb/2003-017, 2003.
- [94] M. Benayoun and O. Callot, *The forward tracking, an optical model method*, LHCb/2002-008, 2002.
- [95] R. Forty, *Track seeding*, LHCb/2001-109, 2001.
- [96] Y. Xie, *Short track reconstruction with VELO and TT*, LHCb/2003-100, 2003.
- [97] R. Hierck, *Track following in LHCb*, LHCb/2001-112, 2001.
- [98] J. van Tilburg, *Matching VELO tracks with seeding tracks*, LHCb/2001-103, 2001.
- [99] R. Fleischer, *New strategies to obtain insights into CP violation through $B_s^0 \rightarrow D_s^\mp K^\pm, D_s^{*\mp} K^\pm, \dots$ and $B_d \rightarrow D^\pm \pi^\mp, D^{*\pm} \pi^\mp, \dots$ decays*, Nucl. Phys. **B671** (2003) 459.
- [100] R. Forty and O. Schneider, *RICH pattern recognition*, LHCb/2000-064, 2000.

-
- [101] H. Terrier and I. Belyaev, *Particle identification with the LHCb calorimeters*, LHCb/2003-092, 2003.
 - [102] O. Deschamps, F.P. Machefer, M.H. Schune, G. Pakhlova, and I. Belyaev, *Photon and neutral pion reconstruction*, LHCb/2003-091, 2003.
 - [103] J.R.T. de Mello Neto and M. Gandelman, *Muon ID performance with the reoptimized LHCb detector*, LHCb/2003-089, 2003.
 - [104] S. Klous, *LHCb: Vertex detector and read out chip, computing challenge and $B_s \rightarrow J/\psi \phi$ analysis*, Ph.D. thesis, NIKHEF, 2005.
 - [105] G.J. Feldman and R.D. Cousins, *A unified approach to the classical statistical analysis of small signals*, Phys. Rev. **D57** (1998) 3873.
 - [106] M. Calvi, O. Dormond, and M. Musy, *LHCb flavour tagging performance*, LHCb/2003-115, 2003.
 - [107] R. Hierck, J. van Hunen, and M. Merk, *The sensitivity for Δm_s and $\gamma + \phi_s$ from $B_s^0 \rightarrow D_s^- \pi^+$ and $B_s^0 \rightarrow D_s^\mp K^\pm$ decays*, LHCb/2003-103, 2003.
 - [108] *The DataGrid Project*, <http://eu-datagrid.web.cern.ch>.
 - [109] H. G. Moser and A. Roussarie, *Mathematical methods for $B^0 \bar{B}^0$ oscillation analyses*, Nucl. Instrum. Meth. **A384** (1997) 491.
 - [110] M. Beneke, G. Buchalla, M. Neubert, and Christopher T. Sachrajda, *QCD factorization for exclusive, non-leptonic B meson decays: General arguments and the case of heavy-light final states*, Nucl. Phys. **B591** (2000) 313.

References

Summary

The apparent absence of antimatter in the Universe leads to the assumption that the symmetry between matter and antimatter must be broken. In fact, measurements of the decay of kaons and B mesons have demonstrated that this so-called CP symmetry is violated. The Standard Model provides an accurate description of the fundamental interactions between elementary particles. In the Standard Model, CP violation is incorporated in the CKM matrix, which describes the quark transitions in the weak interaction.

The decay of B mesons is well suited to measure the CP -violating parameters of the CKM matrix. B mesons are particles containing the heavy b quark. When evolving in time, neutral B mesons oscillate between the particle state and antiparticle state. The time-dependent decay of $B_s^0 \rightarrow D_s^- \pi^+$ can be used to measure the oscillation frequency, Δm_s . The current experimental lower limit is determined to be $\Delta m_s > 14.4 \text{ ps}^{-1}$ at a CL > 95%. The time-dependent decay of another channel, $B_s^0 \rightarrow D_s^{(*)\mp} K^{(*)\pm}$, can be used to measure the CP -violating parameter $\gamma - 2\chi$.

The Large Hadron Collider (LHC), due to start operating in 2007, accelerates proton bunches in opposite directions in a ring of 27 km circumference. Every 25 ns, these protons collide with a centre-of-mass energy of 14 TeV. LHCb is one of the four experiments along the ring and is dedicated to measure the decay of B mesons, receiving as much as $10^{12} b\bar{b}$ pairs per year. Since these $b\bar{b}$ pairs are frequently produced in a cone along the beam axis, the experiment is designed as a forward spectrometer. The subdetectors of LHCb can be divided into tracking detectors and particle identification detectors. The first tracking detector, the Vertex Locator or Velo, is closely built around the interaction point to accurately measure the vertex positions. The other tracking detectors are the Trigger Tracker (TT), placed just before the magnet, and three large T stations, placed just behind the magnet. They measure the momentum of particles based on the curvature due to a magnetic field with an integrated strength of $\int B dl = 4.2 \text{ T m}$. Each T station contains two detector technologies: the Inner Tracker (IT), covering the high-flux region around the beam pipe, is made from silicon sensors, and the Outer Tracker (OT), covering the rest of the acceptance, is made from gas-filled straw tubes. Particle identification is provided by the Cherenkov detectors (RICH 1 and RICH 2), the electromagnetic and hadronic calorimeters (ECAL and HCAL), and the muon detector. Finally, a trigger system reduces the output data volume by reconstructing and selecting signal events online.

Simulation studies play an important role during the design of the detector. First, the event generation, based on PYTHIA, simulates the processes in the proton collisions.

The expected B production cross section and particle multiplicity obtained from other experiments are in good agreement with this simulation. Next, the detector simulation, based on GEANT, simulates the passage of the particles through the detector material, including processes such as ionisation, multiple scattering, and nuclear interactions. It is important to minimise the amount of detector material that a particle needs to traverse. Up to the last tracking station a particles sees on average only 12% of an interaction length and 40% of a radiation length.

From the GEANT simulation, it follows that in B events on average 73 charged particles pass through the OT and 27 though the IT. However, in the IT their average momentum is more than three times higher (14 GeV) than in the OT (4 GeV). Several effects are included in the simulation of the OT detector response (digitisation). Background hits are added to simulate random noise (1.2%), cross talk (5%), and hits from neighbouring bunch crossings (17%). Detector inefficiencies are simulated by accounting for a single cell efficiency (97%), a 50 ns dead time, and dead regions in the detector. For high-momentum particles ($p > 2$ GeV), dead time and dead regions each cause a 1% loss in the double-layer detection efficiency. The average channel occupancy in B events amounts to 4.3%. In the hottest regions of the OT, the occupancy is still below the 7% level, due to the convenient IT shape.

The tracks that are found are fitted using the Kalman filter approach. Hereby, the track fit is viewed as a linear dynamic system where process noise as a result of multiple scattering and measurement noise are naturally included. In the propagation of the track parameters, the magnetic field, continuous multiple scattering, and energy loss are properly taken into account. Since the propagation and projection relations are actually not linear, the extended Kalman filter method is applied, which linearises both relations. To linearise the projection relation, the use of a reference trajectory is required. Outlier hits are removed based on their contribution to the χ^2 of the fit. Before each iteration of the fit, the hit with the highest contribution satisfying $\chi^2_+ > 9$ is removed. After five iterations, the hit purity for long tracks is increased from 98.0% to 98.5%. To make the refitting less time consuming, the propagation matrices calculated in the first iteration are reused in the subsequent iterations.

The tracks are subdivided into different track types, depending on their trajectory through the detector. The most important for physics purposes are the long tracks, which extend from VELO up to the last T station. The matching algorithm finds long tracks by combining the tracks found in the VELO with the tracks found in the T stations. The matching efficiency for high-momentum long tracks ($p > 5$ GeV) is 91%. Afterwards, TT hits are added to the track with an efficiency of 89% and a wrong hit fraction of 6%. The combined performance of the long track algorithms shows a 94% efficiency and 8% ghost rate for $p > 5$ GeV. The momentum resolution of long tracks equals 0.35%.

The event selection of the $B_s^0 \rightarrow D_s^- \pi^+$ and $B_s^0 \rightarrow D_s^\mp K^\pm$ decays is very similar; these decays only differ in one particle. Due to the higher branching fraction of $B_s^0 \rightarrow D_s^- \pi^+$, the $K-\pi$ separation capability of the RICH detector is utilised to remove the $B_s^0 \rightarrow D_s^- \pi^+$ background in the $B_s^0 \rightarrow D_s^\mp K^\pm$ selection. The corresponding cut is set at $\Delta \ln \mathcal{L}_{K\pi} > 3$. In comparison with the $B_s^0 \rightarrow D_s^\mp K^\pm$ decay, the decays of $B_s^0 \rightarrow D_s^{*\mp} K^\pm$

and $B_s^0 \rightarrow D_s^\mp K^{*\pm}$ have an additional neutral particle in the final state (γ , π^0 , or K_S^0). The expected annual yield equals 85000 for $B_s^0 \rightarrow D_s^- \pi^+$ and 4600 for $B_s^0 \rightarrow D_s^\mp K^\pm$ with background fractions of 0.34 and 0.24, respectively. In addition, 1300 $B_s^0 \rightarrow D_s^{*\mp} K^\pm$ events and 200 $B_s^0 \rightarrow D_s^\mp K^{*\pm}$ events are expected. A standalone Monte Carlo simulation programme generates the observed decay time distributions for different settings of the input parameters. An unbinned likelihood fit to the distributions for the $B_s^0 \rightarrow D_s^- \pi^+$ and $B_s^0 \rightarrow D_s^{(*)\mp} K^{(*)\pm}$ decays determines the sensitivity on the physical parameters of interest. It follows that, after 1 year of data taking, the oscillation frequency can be accurately measured up to 88 ps^{-1} (sensitivity limit) and that, after 3 years of data taking, a precision on $\gamma - 2\chi$ of $8.4^\circ \pm 1.1^\circ$ can be reached.

Summary

Samenvatting

Spoorsimulatie en -reconstructie in LHCb

De schijnbare afwezigheid van antimaterie in het heelal leidt tot de aannname dat de symmetrie tussen materie en antimaterie gebroken moet zijn. Metingen aan het verval van kaonen en B -mesonen hebben aangetoond dat deze zogenaamde CP -symmetrie inderdaad geschonden is. Het Standaard Model geeft een nauwkeurige beschrijving van de fundamentele wisselwerkingen tussen elementaire deeltjes. In het Standaard Model is CP -schending opgenomen in de zogenaamde CKM matrix, die de quarkovergangen in de zwakke wisselwerking beschrijft.

Het verval van B -mesonen is erg geschikt om de CP -schendende parameters van de CKM matrix te meten. B -mesonen zijn deeltjes die de zware b -quark bevatten. Als neutrale B -mesonen zich in de tijd ontwikkelen, oscilleren ze tussen de deeltjestoestand en de antideeltjestoestand. Het tijdsafhankelijke verval van $B_s^0 \rightarrow D_s^- \pi^+$ kan worden gebruikt om de oscillatiefrequentie, Δm_s , te meten. De huidige, experimentele ondergrens hiervan is vastgesteld op $\Delta m_s > 14.4 \text{ ps}^{-1}$ voor een $\text{CL} > 95\%$. Het tijdsafhankelijke verval van een ander kanaal, $B_s^0 \rightarrow D_s^{(*)\mp} K^{(*)\pm}$, kan worden gebruikt om de CP -schendende parameter $\gamma - 2\chi$ te meten.

De Large Hadron Collider (LHC), die in 2007 in werking treedt, versnelt protonbundels in tegengestelde richting in een ring van 27 km in omtrek. De protonen botsen iedere 25 ns met een zwaartepuntsenergie van 14 TeV op elkaar. LHCb is een van de vier experimenten langs deze ring en is met $10^{12} b\bar{b}$ -paren per jaar gewijd aan het meten van het B -verval. Omdat $b\bar{b}$ -paren meestal worden geproduceerd in een kegel langs de bundelas, is het experiment ontworpen als een voorwaartse spectrometer. De subdetectoren van LHCb kunnen worden onderverdeeld in spoordetectoren en identificatiedetectoren. De eerste spoordetector is de Vertex Locator (VELO) en is dicht rondom het interactiepunt gebouwd om de vertexposities nauwkeurig te kunnen meten. De overige spoordetectoren zijn de Trigger Tracker (TT), vlak voor de magneet, en drie grote T-stations, vlak achter de magneet. Zij meten de impuls van de deeltjes aan de hand van de kromming van hun banen in een magnetisch veld met een geïntegreerde sterkte van $\int B dl = 4.2 \text{ T m}$. Elk T-station bevat twee detectietechnologieën: de Inner Tracker (IT) bestrijkt het hoge-fluxgebied rondom de bundelpijp en is gemaakt van silicium sensoren en de Outer Tracker (OT) bestrijkt de rest van het gebied en is gemaakt van strootjes gevuld met gas. De identificatie van deeltjes wordt verzorgd door de Cherenkov-detectoren (RICH 1 en RICH 2), de elektromagnetische en hadronische calorimeters (ECAL en HCAL) en de muondetector. Uiteindelijk reduceert een triggersysteem de hoeveelheid

uitvoerdata door de gebeurtenissen direct te reconstrueren en te selecteren.

Simulatiestudies spelen een belangrijke rol tijdens het ontwerpen van de detector. Allereerst simuleert de *event generation*, gebaseerd op PYTHIA, de protonbotsingen. De verwachte werkzame doorsnede voor B -productie en de verwachte deeltjesmultipliciteit verkregen uit andere experimenten komen goed overeen met deze simulatie. Daarna simuleert de *detector simulation*, gebaseerd op GEANT, de doorgang van de deeltjes door het materiaal van de detector, met inachtneming van processen als ionisatie, meervoudige verstrooing en nucleaire interacties. Het is van belang om de hoeveelheid materiaal waar een deeltje doorheen gaat te minimaliseren. Tot aan het laatste T-station ziet een deeltje gemiddeld slechts 12% van een interactielengte en 40% van een stralingslengte.

Uit de GEANT simulatie volgt dat in B -gebeurtenissen gemiddeld 73 geladen deeltjes de OT passeren en 27 de IT. Echter, in de IT is hun gemiddelde impuls meer dan drie keer zo hoog (14 GeV) als in de OT (4 GeV). Tijdens de simulatie van de OT detectorrespons (digitalisatie) worden verschillende effecten meegenomen. Achtergrondsignalen worden toegevoegd om ruis (1.2%), overspraak (5%) en signalen van naburige bundelkruisingen (17%) te simuleren. Detectieverlies worden gesimuleerd door een detectie-efficiëntie van 97%, een dode tijd van 50 ns en dode gebieden in de detector in acht te nemen. Voor deeltjes met een hoge impuls ($p > 2 \text{ GeV}$) zorgen de dode tijd en de dode gebieden elk voor een verlies van 1% in de detectie-efficiëntie van een dubbele laag strootjes. De gemiddelde bezettingsgraad van de uitleeskanalen in B -gebeurtenissen is 4.3%. In de heetste gebieden van de OT is deze bezettingsgraad nog beneden de 7% dankzij de vorm van de IT.

De gevonden sporen worden gefit met behulp van het Kalman filter formalisme. Hierbij wordt een spoor voorgesteld als een lineair dynamisch systeem waar procesruis als gevolg van meervoudige verstrooing en meetruis op een natuurlijke manier worden meegenomen. Tijdens de voortplanting van de spoorparameters wordt rekening gehouden met het magnetische veld, continue meervoudige verstrooing en energieverlies. Aangezien de voortplantings- en de projectievergelijking eigenlijk niet lineair zijn, wordt de uitgebreide Kalman filter methode, die beide vergelijkingen lineair maakt, toegepast. Voor het lineair maken van de projectievergelijking is het gebruik van een referentiepad noodzakelijk. Metingen die afwijken van het gefitte spoor worden verwijderd op basis van hun bijdrage aan de χ^2 van de fit. Voor iedere iteratie van de fit wordt de meting met de hoogste bijdrage die voldoet aan $\chi^2_+ > 9$ verwijderd. Na vijf iteraties is het percentage correcte metingen verhoogd van 98.0% naar 98.5%. Om het herfitten sneller te laten verlopen worden de voortplantingsmatrices, berekend tijdens de eerste iteratie, hergebruikt in de daaropvolgende iteraties.

De sporen kunnen worden onderverdeeld in verschillende spoortypes, afhankelijk van hun pad door de detector. Het meest belangrijk voor de fysica zijn de lange sporen, die zich uitstrekken van de VELO tot aan het laatste T-station. Het *matching* algoritme zoekt naar deze sporen door sporen gevonden in de VELO te koppelen aan sporen gevonden in de T-stations. De efficiëntie van de matching voor sporen met $p > 5 \text{ GeV}$ is 91%. Naderhand worden de TT-metingen toegevoegd aan het spoor met een efficiëntie van 89% en met 6% aan verkeerde metingen. Gecombineerd leveren de algoritmen die naar lange sporen zoeken een efficiëntie van 94% met een *ghost rate* van 8% voor $p >$

5 GeV. De resolutie op de impuls van deze lange sporen is 0.35%.

De selecties van gebeurtenissen met $B_s^0 \rightarrow D_s^- \pi^+$ en $B_s^0 \rightarrow D_s^\mp K^\pm$ vervallen komen grotendeels overeen; ze verschillen slechts in één deeltje. Aangezien het $B_s^0 \rightarrow D_s^- \pi^+$ verval veel vaker voorkomt, moet het $K-\pi$ scheidingsvermogen van de RICH detector worden benut om de $B_s^0 \rightarrow D_s^- \pi^+$ achtergrond in de $B_s^0 \rightarrow D_s^\mp K^\pm$ selectie te verwijderen. De bijbehorende snede staat op $\Delta \ln \mathcal{L}_{K\pi} > 3$. In vergelijking met het $B_s^0 \rightarrow D_s^\mp K^\pm$ verval hebben de vervallen van $B_s^0 \rightarrow D_s^{*\mp} K^\pm$ en $B_s^0 \rightarrow D_s^{*\mp} K^{*\pm}$ een extra neutraal deeltje in de eindtoestand (γ , π^0 , of K_S^0). De jaarlijkse opbrengst is 85000 $B_s^0 \rightarrow D_s^- \pi^+$ vervallen en 4600 $B_s^0 \rightarrow D_s^\mp K^\pm$ vervallen met achtergrondbijdragen van respectievelijk 0.34 en 0.24. Daarbij komen 1300 $B_s^0 \rightarrow D_s^{*\mp} K^\pm$ en 200 $B_s^0 \rightarrow D_s^{*\mp} K^{*\pm}$ vervallen. Een apart Monte Carlo simulatieprogramma simuleert de gemeten verdelingen van de vervalstijd voor verschillende waarden van de invoerparameters. Met een *unbinned likelihood fit* aan de verdelingen van de $B_s^0 \rightarrow D_s^- \pi^+$ en $B_s^0 \rightarrow D_s^{(*)\mp} K^{(*)\pm}$ vervallen wordt de verwachte gevoeligheid op de te meten fysische parameters bepaald. Hieruit volgt dat met 1 jaar aan data oscillatiefrequenties tot aan 88 ps^{-1} nauwkeurig kunnen worden gemeten (gevoelighedslimiet) en dat met 3 jaar aan data een nauwkeurigheid op $\gamma - 2\chi$ van $8.4^\circ \pm 1.1^\circ$ kan worden bereikt.

Dankwoord

Hoewel het schrijven van een proefschrift soms een eenzame lijdensweg lijkt, is dit boekwerk zeker ook tot stand gekomen met de hulp van anderen. Ik ben iedereen die hieraan een bijdrage heeft geleverd dan ook zeer dankbaar. Een aantal personen wil ik in het bijzonder bedanken.

Allereerst wil ik mijn promotor en dagelijkse begeleider bedanken. Marcel, de afgelopen jaren heb je mij geholpen met allerlei problemen die ik tegenkwam bij mijn onderzoek. Daarnaast zorgde je met jouw vrolijkheid elke dag weer voor een prettige omgeving. Jouw suggesties en correcties tijdens het schrijven hebben dit proefschrift enorm verbeterd en ik ben er trots op om, nu je zelf professor bent, jouw eerste promovendus te mogen zijn.

Tijdens mijn tijd in Genève kon ik altijd rekenen op de gezelligheid van mijn kameren naamgenoot, Jeroen van Hunen. Uiteraard leidde dit feit bij de buitenlanders tot de nodige verwarring en kregen we regelmatig mailtjes bestemd voor de *andere Jeroen*. Jeroen, ik ben erg blij dat je in mijn leescommissie zit. Ook Jo van den Brand ben ik dankbaar als mijn aanvankelijke promotor tijdens de eerste jaren van het onderzoek. Voor een enthousiaste en zeer gedetailleerde uitleg over de *B* fysica, spoorreconstructie, software of een willekeurig ander onderwerp kon ik altijd terecht bij Gerhard Raven. Gerhard, jouw correcties voor mijn proefschrift waren erg nuttig.

Met mijn collega's heb ik een fijne tijd beleefd op het NIKHEF. De combinatie van wetenschappelijke discussies en gezelligheid tijdens koffie- en lunchpauzes is mij uitstekend bevallen. De ervaringswijscheden van mijn voorgangers, de Rutgers (van der Eijk en Hierck), Sander en Niels van Bakel, waren voor mij van onschatbare waarde. Mijn kamergenoten Iouri, Jacopo en Edwin hebben ervoor gezorgd dat het met de eenzaamheid wel mee viel, maar waren bovenal een garantie voor een goede sfeer. De overige promovendi, Bart, Gabriël, Marko, Hernan (you have finished your thesis just before me), Antonello, Max, Hella, Peter, Aras, Eduard, Jan en Besma wens ik uiteraard veel succes met hun onderzoek of het afronden hiervan. Verder wil ik Eduardo, Niels Tuning, Matthew en alle overige collega's van LHCb bedanken voor de goede samenwerking in de afgelopen jaren.

Naast het onderzoek hebben mijn vrienden eraan bijgedragen dat ik niet alleen maar met natuurkunde bezig was. Matthijs, ik ben blij dat jij als paranimf mij terzijde zal staan. Tom en Inge (en familie), bedankt voor het zoeken naar de laatste foutjes in dit proefschrift. Aan mijn voormalige huisgenoten van de Burgemeester Reigerstraat 62^{bis} heb ik te danken dat ik regelmatig kon genieten van hun culinaire hoogstandjes en nog meer van hun gezelligheid. Mijn belangrijkste tijdverdrijf, het basketball bij de

Dankwoord

studenten van SBU en daarna bij de club voor afgestudeerden, de Utrecht Bull's, zorgde niet alleen voor inspanning, tijdens trainingen en wedstrijden, maar daarnaast ook voor de nodige ontspanning.

Als laatste wil ik de mensen bedanken die het dichtste bij mij staan. Mijn schoonfamilie, Kommer, de doctorstitel erft dit keer schuin over. Mijn eigen familie, waarvan oma Luiten dit helaas niet meer mee mocht maken. Mijn broertje en paranimf, Roderick, ik hoop jou nog eens bij een andere gelegenheid in je eigen galakostuum te mogen aanschouwen. Mijn ouders, aan wie ik zo veel te danken heb, waaronder ook de foto's voor de omslag van dit proefschrift. En natuurlijk mijn grootste liefde en belangrijkste steun tijdens het schrijven van dit proefschrift, Rianne.

